Computational and Experimental Investigations of Biologically Interesting Molecules

Thesis submitted for the degree of

Doctor of Philosophy

in the

School of Engineering and Science,
Faculty of Health, Engineering and Science,

Victoria University

by

Matthew Blair Stewart

May 2009

ABSTRACT

The reconciliation of experimental and computational data is an on-going challenge in many fields of scientific enquiry. This is particularly true in chemistry, especially with respect to biologically interesting molecules, given the myriad of problems that now lend themselves to theoretical investigation. This work sampled several areas of this greater landscape using various computational methods, and compared these results to relevant, experimentally derived data.

Firstly, the experimentally determined antioxidant activities of a range of hydrxoyquinoline derivatives were examined and compared to their homolytic O-H bond dissociation energies (BDEs) that were calculated using density functional theory (DFT) methods. A single experimental parameter was developed that could be correlated with a range of computed BDEs. The problem of "intrinsic" versus "non-intrinsic" BDE, relating to whether or not the O-H group is involved in intramolecular hydrogen bonding, has been explored. The 5-hydroxyquinoline derivative was demonstrated both experimentally and computationally to have enhanced antioxidant capacity. An attempt has been made to provide an explanation for this in terms of the relative dipole moment orientations and the subsequent effect on the electronic distribution within the molecules.

Secondly, Electrospray Ionisation Mass Spectroscopy (ESI-MS) was coupled with various computational methods, including relativistic methods, in order to facilitate the development of a model for a possible mode of action of 5-chloro-7-iodo-8-hydroxquinoline (Clioquinol, CQ) towards Parkinson's disease. In this regard, a 3:1 Fe-CQ radical cation was discovered as a relevant species in the ESI and this species was validated computationally. It was demonstrated that the precursor to this species could act as a potent radical scavenger *in vivo*. This antioxidant activity does not invoke the redox chemistry of the iron.

Thirdly, the phenomenon of “magic numbers”, when metal ions/species interact with nucleic acid constituents in preferred clusters, has been further explored by ESI-MS/MS for the interaction of platinum species with the nucleoside deoxyguanosine. Thus, for species of general formula [Pt(L)(dG)n]2+, where L = diethyltriammine (dien) or 2,2’:6’2’’-terpyridine (terpy), this phenomenon is apparent for n = 5 for terpy and n = 4 for dien. This phenomenon has been successfully rationalized *in silico* via molecular dynamics calculations. The simulated collision calculations predict with fidelity both the experimental profiles of the collision induced dissociation experiments and the correct magic numbers for the respective ligands.

Finally, platinum(II) and palladium(II) species with judiciously designed carrier ligands have been reacted with various nucleic acid constituents within the ESI spectrometer in order to ascertain to what extent carrier ligand design influences steric selectivity. Such selectivity for coordination to different nucleobase moieties has been clearly demonstrated. The steric interactions have been modelled using semi-empirical quantum chemical calculations.

ACKNOWLEDGEMENTS

I would like to thank my supervisor, Prof. John Orbell, for his steadfast dedication to this project. I appreciate all of the skills gained from him over the past five years of post-graduate study and look forward to future collaborations.

Thanks are due to Victoria University for supplying the research scholarship that allowed me to complete this degree. Also, thanks to the staff of the School of Molecular Sciences for their assistance, particularly Joe Pelle and Min Nyugen for their help with analytical instrumentation and equipment.

Thanks also to Professor Richard O'Hair and Dr. George Khiarallah of the Bio21 Institute at The University of Melbourne and Dr. Elizabeth Yuriev of the Victorian College of Pharmacy at Monash University for their assistance and guidance with the work on platinum-dG clusters. Also, I would like to thank Dr. David Wilson of La Trobe University for his assistance with the Fe-CQ chelate calculations, as well as the donation of his allotted time on the APAC National Supercomputer Facility at ANU.

Finally, I would like to thank my family and friends for their unwavering support and tolerance, particularly Aimee who has had to endure me through every single day of my candidature. This would not have been completed without your tireless dedication.

DECLARATION

"I, **Matthew Blair Stewart**, declare that the PhD thesis entitled "Computational and Experimental Investigations of Biologically Interesting Molecules" is no more than 100,000 words in length including quotes and exclusive of tables, figures, appendices, bibliography, references and footnotes. This thesis contains no material that has been submitted previously, in whole or in part, for the award of any other academic degree or diploma. Except where otherwise indicated, this thesis is my own work".

Signature Date

Table of Contents

Abstract i
Acknowledgments iii
Declaration iv

Preamble 1

Chapter 1 Experimental and Computational Investigations of the Relative Radical Scavenging Ability of Phenolics

1.1 Introduction 6
1.1.1 Experimental (in vitro) methods for assaying antioxidant activity 10
1.1.1.1 Lipid peroxidation inhibition 10
1.1.1.1.1 Thiobarbituric acid-reactive species (TBARS) assay 11
1.1.1.1.2 LDL oxidation assay 11
1.1.1.2 Spectroscopic methods utilizing DPPH 12
1.1.1.2.1 EC 50 and variations 13
1.1.1.2.2 % scavenged 14
1.1.1.2.3 k determination 15
1.1.1.2.4 Log(Z) determination 16
1.1.1.3 Spectroscopic methods utilizing other probes 16
1.1.1.3.1 Chemiluminescence quenching method 17
1.1.1.3.2 Fluorescence quenching method 18
1.1.1.3.3 Trolox Equivalent Antioxidant Capacity (TEAC) 19
1.1.1.4 Other antioxidant methods 20
1.1.1.4.1 Folin-Ciocalteu assay 20
1.1.1.4.2 Differential Scanning Calorimetry (DSC) 21
1.1.2 A single descriptor for antioxidant activity 22
1.1.3 Overview of Density Functional Theory 22
1.2 Methods 24
1.2.1 Materials and equipment 24
1.2.2 UV/Vis measurements – DPPH assay 25
1.2.2.1 Log(Z) calculation 26
1.2.3 Computational methodology 27

1.2.3.1 BDE calculation 28
1.2.3.2 Rotational allowance 28
1.3 Results and discussion 28
1.3.1 Benchmarking of the Log(Z) methodology – comparison with previously published results 28
1.3.2 Log(Z) results 32
1.3.3 BDE calculation 33
1.3.3.1 Effect of Ar-OH rotation on BDE 37
1.3.4 Towards a greater understanding of antioxidant activity 38
1.3.4.1 The x-hydroxyquinoline (x-HQ) series, x = 2 – 8 39
1.3.4.2 The 1-naphthol analogues 40
1.3.5 Summary 43

Chapter 2 - ESI/MS and Quantum Chemical Investigations of Iron(III)–Hydroxyquinoline Species

2.1 Introduction 45
2.1.1 Neurodegenerative disease 45
2.1.1.1 Current treatments for Alzheimer's disease and Parkinson's disease 47
2.1.2 New therapeutic targets 48
2.1.2.1 Alzheimer's disease 49
2.1.2.2 Parkinson's disease 52
2.1.3 Basis of this work 55
2.2 Methods 56
2.2.1 Chemicals and equipment 56
2.2.2 ESI-MS methodology 56
2.2.2.1 Preparation of solutions for ESI/MS 56
2.2.2.2 ESI-MS analysis 57
2.2.3 Computational methodology 58
2.3 Results and discussion 60
2.3.1 ESI/MS Investigations 60
2.3.1.1 8-hydroxyquinoline 61
2.3.1.2 5,7-dichloro-8-hydroxyquinoline (DCHQ) 66
2.3.1.3 5-chloro-7-iodo-8-hydroxyquinoline (CQ) 69

2.3.2 Computational investigations 73
2.3.2.1 Semi-empirical PM3 characterization of the 2:1 and 3:1 iron hydroxyquinoline systems 74
2.3.2.2 Hindrance to the addition of a third ligand 76
2.3.2.3 High level quantum chemical calculations 77
2.3.2.3.1 Iron species 77
2.3.2.3.2 Free ligands 79
2.3.3 Significance of the discovery of the radical cation 81
2.3.3.1 Possible explanation of Fe-CQ toxicity 81
2.3.3.2 Impacts on current research in this area 83

Chapter 3 - "Magic Numbers" for Metal-Nucleoside Clusters – Molecular Dynamics Simulation of ESI-MS/MS Results

3.1 Introduction 86
3.1.1 Metal ion interactions with nucleic acid constituents 86
3.1.2 Clusters 87
3.1.3 Concept of "magic numbers" in mass spectrometry 88
3.1.4 Overview of molecular mechanics 89
3.1.5 The AMBER force field 93
3.1.6 Missing parameters 94
3.1.6.1 Adding transition metal complexes to AMBER99 95
3.2 Methods 96
3.2.1 ESI-MS/MS 97
3.2.2 Computational methods 98
3.2.2.1 AMBER99 atom types and parameters 99
3.2.2.2 Cluster construction 101
3.2.2.2.1 Linear conformation 101
3.2.2.2.2 Electrostatic partial charges 102
3.2.2.2.3 Cluster formation 104
3.2.2.3 'Selection' of atoms 105
3.2.2.4 Collision simulation and analysis 106
3.2.2.4.1 Statistical analysis 107

3.3 Results and discussion 110

3.3.1 Collision induced dissociation of clusters using ESI-MS/MS 110
3.3.1.1 Relative cluster abundances for the dien system 111
3.3.1.2 Relative cluster abundances for the terpy system 112
3.3.2 In search of the origin of magic numbers 113
3.3.3 Analysis of the MM collision simulations 116
3.3.3.1 Computational Results 117
3.3.3.1.1 Dien results 117
3.3.3.1.2 Terpy results 121
3.3.3.2 Comparison of both ligands 124
3.3.3.3 Summary 125

Chapter 4 - ESI-MS and Computational Investigations of the Interaction of Sterically Restrictive Platinum(II) and Palladium(II) Complexes with Nucleobases and Nucleosides

4.1 Introduction 128
4.1.1 Preamble 128
4.1.2 Platinum(II) – DNA interactions 129
4.1.2.1 Binding modes 129
4.1.3 Manipulation of the steric features of carrier ligands 132
4.1.3.1 Steric influences of nucleobases 133
4.1.3.2 Initial investigations – [PtII(bpe)Cl2] and [PtII(bmpe)Cl2] 134
4.1.3.2.1 ESI-MS Methodology and results 136
4.1.3.2.2 Analysis of bpe results 137
4.1.3.2.3 Analysis of bmpe results 138
4.2 Methods 140
4.2.1 Preparation of the Palladium species 140
4.2.1.1 Determination of metal concentration and speciation 141
4.2.2 Analysis of binding selectivity to nucleic acid constituents 143
4.2.3 Computational methodology 144
4.3 Results and discussion 145
4.3.1 Experimental ESI-MS results 145
4.3.1.1 Characterisation of the “diaquo” solution 145
4.3.1.2 Competition experiments – ESI-MS 155

4.3.1.2.1 Pd-bbmm 155
4.3.1.2.2 Pd-bbme 156
4.3.1.2.3 Pd-bbmp 158
4.3.2 Computational results 160
4.3.2.1 Benchmarking studies 160
4.3.2.2 Comparison of computational modelling with experimental ESI-MS data 165
4.3.2.2.1 Di-aquo species – above- and below-the-plane hindrance 167
4.3.2.2.2 Disclaimer affecting the analysis of the following data 168
4.3.2.2.3 Mono-substituted considerations 169
4.3.2.2.4 Bis-substituted considerations 170
4.3.3 Summary 174

References 176

Appendices

Appendix I – ESI-MS spectra 192
Appendix II – Identification tables for ESI-MS spectra 223
Appendix III – Auxiliary benchmarking case studies 231
Appendix IV – Molecular structures and raw data CD

PREAMBLE

With a burgeoning increase in computational power (software and hardware) and the ever increasing evolution and sophistication of scientific instrumentation, the reconciliation of computational and experimental data is an imperative, as evidenced by numerous review articles published across a variety of discipline areas including materials science[1-5], nuclear science[6-9], aeronautical engineering[10-12] and astronomy[13] - to mention but a few.

Chemistry in particular, lends itself to computational enquiry and hence to comparison with experimental data. To date, the large majority of such comparisons have tended to focus on small molecules and (generally) their physical chemistry characteristics, which have been extensively investigated using a variety of computational models. An example of such comparisons is the NIST Computational Chemistry Comparison and Benchmark Database (CCCBDB)[14]. Release 14 of the NIST CCCBDB contains comparisons between experimental and computational data for 788 atoms and small molecules, with parameters relating to structure (i.e. bond lengths and angles, vibrational frequencies, rotational constants and barriers to internal rotation), energetics (i.e. enthalpy of formation, entropy and heat capacity) and electronic properties (i.e. dipole moments and polarizabilities). Furthermore, the computational data in this database covers the full range of computational techniques available today. However, probably due to computational limitations, no such databases appear to contain more than what can be described as the basic fundamental properties of *small* organic and/or inorganic systems. In this regard, they are of limited assistance when studying the larger and more complex molecules of biological interest.

Given the size and complexity of biological systems in general, current computational chemistry methods are still somewhat challenged when it comes to the *ab initio* modelling of entities such as nucleic acids, carbohydrates and

proteins. For this reason, it is not surprising that extensive databases of *ab initio* computational data for such systems are not available. In fact, most computational studies of larger systems such as these are *semi-empirical* and/or depend on reported crystal structures or other experimentally determined information.

Therefore, due to the inherent difficulties in studying macromolecular structures of biological interest, much of the work on biologically interesting molecules focuses on their smaller constituents, such as peptides and nucleoconstituents such as nucleobases, nucleosides and nucleotides; as well as on smaller molecules that have known or potential biological profiles (drug candidates for example). Thus processes such as docking/binding to a known or modelled receptor[15-19], pharmacological profiles[20-24] and antioxidant potential[25-27], have all been previously studied computationally and subsequently compared to experimental data.

There remain a multitude of gaps in the literature with respect to the comparison of experimental data to computation models; not just in order to develop predictive models, but also to be descriptive regarding the mechanisms at play in various experimental processes. Therefore, this thesis focuses on using computational chemistry methods to model experimental results (particularly those derived from ESI-MS investigations) with the objective of obtaining further insights into biologically important phenomena. Four such areas, relating to the reconciliation of computational data with experimental investigations, have been selected; namely, the prediction of antioxidant propensity, the elucidation of possible mechanisms of action for non-receptor specific drug candidates, the origin of the phenomenon of "magic numbers" in metal nucleic acid chemistry and the role of steric effects in molecular recognition. These specific areas of interest are briefly outlined as follows:

The pursuit of a single descriptor for antioxidant activity in phenolics

Numerous studies have attempted to devise a computational method for the prediction of antioxidant activity in phenolics. These previous investigations have centered predominantly on the computation of O-H homolytic bond dissociation energies (BDE)[25-27], with lower BDE values corresponding increased antioxidant potentials. Given that the experimental BDE value for the same molecule can vary greatly depending on the particular method[28], this approach is currently less than ideal.

The approach taken in this thesis, as described in Chapter 2, is to use an alternative experimental measurement of antioxidant ability (i.e. a kinetic assay) to compare a single calculated descriptor (the computed O-H homolytic BDE) with the experimental data for a range of different phenolic compounds. This approach appears to be unique, in that a direct single measurement of antioxidant activity is being correlated with a computationally obtained value. An attempt is also made to negate the effects of the polar solvent used.

Clues towards elucidating the mode of action of a non-receptor specific drug candidate for the treatment of Parkinson's disease

Whilst computational chemistry methods are gaining a foothold in the drug development setting, these investigations relate principally to the docking of molecules to defined receptors or active sites of proteins[15-19], or the prediction of pharmaceutical properties of drug leads (i.e. ADMET profiles such as Absorptivity, Distribution, Metabolism, Elimination and Toxicity, oral availability, pKa, etc.)[20-24]. Biologically active synthetic metal chelators, as treatments for neurodegenerative disorders, are non-specific regarding their site of action and therefore have not been so vigorously examined theoretically.

Chapter 3 is concerned with exploring this area. The ESI-MS investigation of a potential neurodegenerative disease inhibitor, which may act via ferric ion chelation, was further probed computationally. A proposed mechanism, which may relate to an enhanced therapeutic effect for this compound was formulated by a consideration of the ESI-MS data and this hypothesis was then buttressed by the subsequent theoretical calculations.

In search of the origin of "magic numbers" in metal – nucleic acid systems

The phenomenon of "magic numbers" (where an unusually stable clustering of nucleic acid constituents per metal ion is observed) is an area of increasing interest. The first indication of such magic numbers was via the discovery of the G-quartet, a hydrogen bonded ionophore consisting of four guanine moieties, which self-aggregates around Na^+ and K^+ ions - but interestingly, not with Li^+ and Cs^+ ions[29]. The G-quartet structure has since been located in various DNA and RNA sequences[30-32], including the telomeres of nuclear DNA, indicating that these aggregates may have a significant biological influence.

Recent work has involved the study of such guanine-based aggregates in the gas phase, via ESI-MS and tandem mass spectrometry (ESI-MS/MS). These studies show that a range of clusters are formed, of varying sizes, in the gas phase, but when fragmented using ESI-MS/MS, an unusually stable cluster is consistently produced following the dissociation of larger clusters[33]. For the Na^+, K^+, Li^+ and Cs^+ ions, this magic number is four, as in the G-quartet[33-35].

To determine if this aggregation and subsequent magic number phenomenon extended to transition metal complexes, platinum(II) species were chosen for investigation, given the extent of knowledge already in existence with respect to its interaction with nucleoconstituents, especially guanine derivatives.

Two amine-based tridentate carrier ligands were selected, with and without aromatic characteristics.

Thus Chapter 4 employs molecular dynamics calculations in order to rationalize the magic number phenomenon, in relation to the gas-phase (ESI-MS/MS) clustering of deoxyguanosine with platinum(II) species. The modelling of this phenomenon, where the experimental ion trap has been effectively simulated, has been found to describe the experimental results with fidelity.

Exploring the role of steric effects in site selectivity by manipulating the carrier ligand in platinum (II) and palladium (II) species

Since the discovery in the 1960s of the DNA-binding anticancer drug cisplatin[36-38], the interaction platinum(II) species with nucleic acid constituents has been an area of ongoing interest. The nature of the "carrier ligand" of platinum (II) species can dramatically influence its binding characteristics and this can be exploited to design species that are site specific or site preclusive. In particular, the steric attributes of the carrier ligand may be varied with a view to achieving desired molecular recognition outcomes. Designing such molecules, tailored to bind, or not to bind, to specific sites, is greatly assisted by molecular modelling and the results may be tested experimentally by conducting competition experiments using ESI-MS.

Thus Chapter 5 explores both computationally and experimentally (in the gas phase) the interactions between judiciously designed platinum(II) and palladium(II) complexes (with sterically hindered carrier ligands) and a range of nucleoconstituents in order to delineate sterically-controlled site selectivity.

Chapter 1

Experimental and Computational Investigations of the Relative Radical Scavenging Ability of Phenolics

1.1 INTRODUCTION

The chemistry of destructive radical species is of interest with respect to a number of different discipline areas including biology[39], medical science[40], polymer science[41] and environmental science[42]. Biochemically, free radical damage (oxidation) has been implicated in various pathophysiologies, such as aging[43, 44], cancer[45] and neurodegeneration[46, 47].

Aerobic organisms are constantly exposed to, and possibly adversely affected by, free radicals. Sources of these oxidants can be both exogenous and endogenous[48]. Biological oxidants can arise from environmental sources, such as UV light and ionising radiation, or through internal processes, with the majority of endogenous oxidants escaping from the electron transport pathway[48]. An example of this escape is the release of superoxide ($O_2^{\bullet -}$) by mitochondria during ordinary oxidative metabolism, Fig. 1.1.

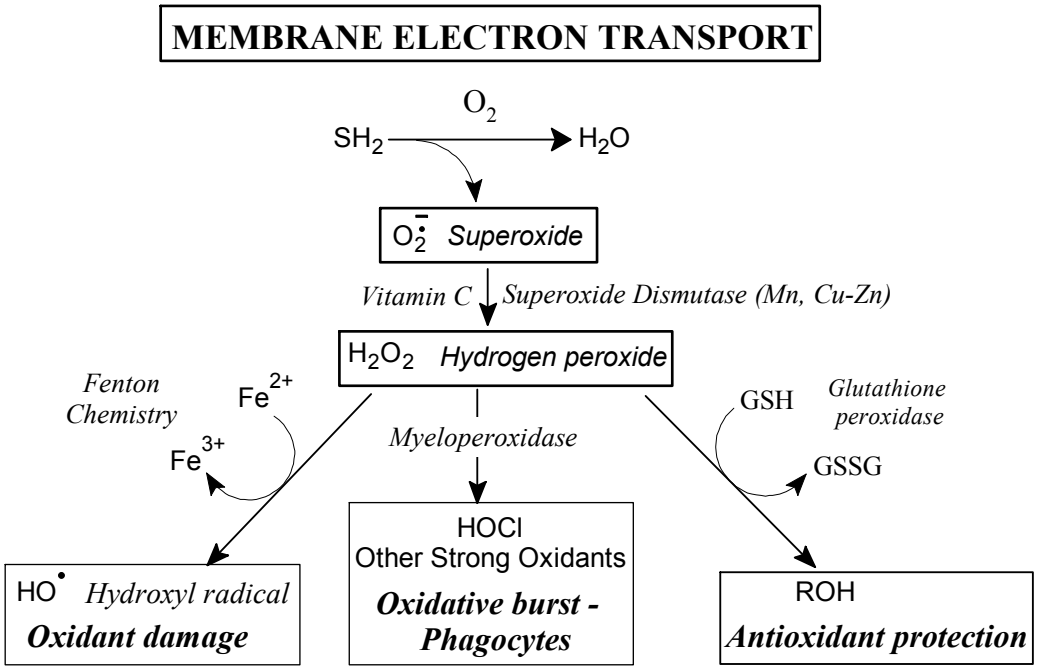

Figure 1.1 – Possible fates of superoxide generated by mitochondrial respiration. Radicals from the oxidative burst of phagocyte attacks may be an important source of oxidants in chronic infection, further increasing inflammation. Superoxide can also act as a powerful oxidant without prior conversion to a hydroxyl radical. Figure is adapted from Ref.49.

Superoxide, as shown in Fig 1.1, can produce hydroxyl radicals ($HO^{\bullet}$), which are responsible for initiating one of the most damaging oxidative processes known to biology, that of lipid peroxidation[49], Fig. 1.2. This process causes major damage to cellular membranes, as well as producing by-products that themselves can cause further damage[50]. Given that lipid peroxidation is a chain reaction, extensive damage can be done if left unchecked[49].

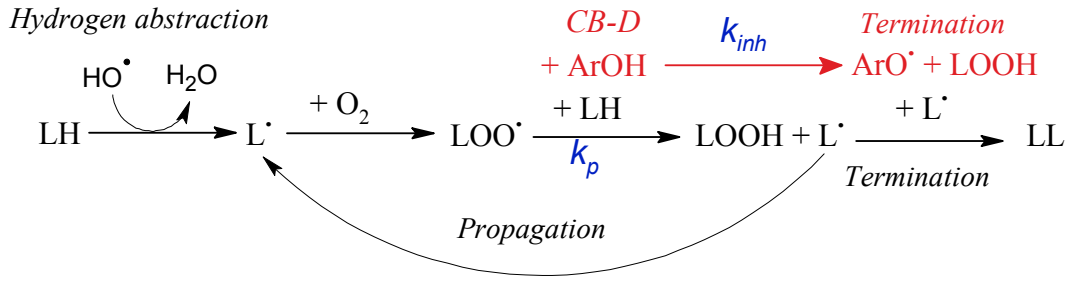

Figure 1.2 – Schematic of the major steps of lipid peroxidation. Initiated by a hydroxyl radical (*hydrogen abstraction*) attacking a polyunsaturated fatty acid (LH), a chain reaction proceeds (*propagation*) until two lipid radicals ($L^{\bullet}$) react, creating a dimer. In the presence of a chain-breaking donor (CB-D) antioxidant, the highly reactive lipid peroxyl radical ($LOO^{\bullet}$) reacts with the antioxidant (shown as a phenolic, ArOH) to form a stable radical species that terminates that chain reaction. The chain reaction would only be inhibited by the antioxidant if $k_{inh} > k_p$ [51].

Due to the potential for vast damage, antioxidant protection has evolved in biological systems. These defences include specific enzymes for neutralising oxidant threats, such as superoxide dismutase (SOD), which facilitates a reaction involving superoxide to produce hydrogen peroxide (H_2O_2). A number of other enzymes, can then react with H_2O_2 to produce less toxic alcohols (peroxidase) or to form O_2 and H_2O (catalase)[49].

Another aspect of antioxidant defence is the vitamins and other relatively small molecules that are well known for their biological antioxidant activity. Compounds such as vitamin E (α-tocopherol) and vitamin C (ascorbic acid) are potent antioxidants, with α-tocopherol being the major chain-breaking antioxidant (CB-D) in lipid peroxidation, Fig. 1.2 above. A chain-breaking

antioxidant acts by reacting with the propagating radical ($LOO^{\bullet}$ in Fig. 1.2) faster than that of chain propagation[51].

Given the implications of oxidant damage in various pathophysiological systems, recent research has focussed on the area of natural antioxidant compounds which may be obtained from dietary sources. These include the numerous polyphenols found in green tea[52] and a wide range of fruits, vegetables, herbs and spices[53-58] including compounds such as curcumin, as isolated from tumeric[59-61]. Not only is the identification of these various naturally occurring compounds important, but the development of methods to determine their relative antioxidant potential can provide insights into their relative potency and could lead to the development of enhanced therapeutic agents for the treatment of a range of disorders related to cellular oxidative stress.

Another aspect of the current work in this area involves the theoretical examination of antioxidant ability, particularly for phenolics. This is generally done through the calculation of the homolytic bond dissociation energy (BDE) parameter[25, 26, 62]. This method is the theoretical equivalent of the process of radical scavenging via hydrogen abstraction, as it attempts to describe the energy required to achieve homolytic cleavage of the phenolic O-H bond of the antioxidant. Generally, a decrease in calculated BDE is associated with an increase in antioxidant efficacy[51]. This calculation is performed as follows:

$$BDE = (E_{ArO^{\cdot}} + E_{H^{\cdot}}) - E_{ArOH} \qquad \textbf{(1.1)}$$

This theoretical approach can be used to study existing antioxidants and to develop new synthetic varieties with enhanced antioxidant activity. Such research is relevant to a variety of areas (such as polymer chemistry) and not just in areas of biological importance. However, in order to establish confidence in this technique, it is desirable for the theoretical results to be benchmarked to corresponding experimental values, obtained using one of a multitude of

antioxidant assays available in the literature. Here, a review of such experimental assays that are used to study antioxidant activity is presented, followed by a brief discourse on theoretical methods.

1.1.1 Experimental (*in vitro)* methods for assaying antioxidant activity

There is no accepted 'gold standard' method for the experimental determination of antioxidant activity, with numerous variations existing within the literature. Many of these methods are reviewed here. Notably, whilst some methods focus on a single species as the analyte, other methods measure the total antioxidant capacity of an extract, where a specific analyte is not necessarily defined.

This review is conducted in light of the fact that the methodology used in this thesis requires single compounds, of known concentration, as the analyte; various published methods were developed for use on plant extracts without a known concentration or composition. As such, these methods have inherent problems when attempting to analyse pure substances, but shall be discussed where appropriate.

1.1.1.1 Lipid peroxidation inhibition

One approach to the quantification of protective antioxidant behaviour is the ability to protect lipids from peroxidation. The ability to quantify protection from lipid peroxidation is particularly sought after by chemists in various fields, from food chemistry to medicine and biochemistry. Oxidation of lipids causes the rancidity of fats and oils in foods, as well as being linked to several pathological effects, including arteriosclerosis, a leading cause of heart disease[63, 64]. Currently, there are two major approaches for the experimental determination of lipid peroxidation inhibition in the literature.

1.1.1.1.1 Thiobarbituric acid-reactive species (TBARS) assay

The TBARS method involves the incubation of a lipid, both with and without the compound/extract of interest, in the presence of generated free radicals (from either a Fe^{2+}/ascorbate system, or H_2O_2 generation) as well as 2-thiobarbituric acid (TBA)[65, 66]. As the lipid is oxidised, substances that form adducts with TBA, especially malondialdehyde, are produced. These adducts strongly absorb visible radiation between 515 nm and 540 nm. Therefore, the difference in absorbance at the analytical wavelength between the control and sample can yield a quantitative value for lipid oxidation inhibition.

However, this assay, by reputation, is known to lack specificity[67]. When plant extracts are studied using this method, other substances that are not products of lipid oxidation can form adducts with TBA. Since these non-oxidatively produced adducts absorb at similar wavelengths, this can lead to an overestimation of antioxidant effects, where the sample being analysed is not a single, pure compound. Such interferences can be accounted for, an example is the addition of butylated hydroxytoluene (BHT) to reduce additional chromophore production[66].

1.1.1.1.2 LDL oxidation assay

The low-density lipoprotein (LDL) oxidation assay is an important tool in a modern medical research laboratory, given that oxidation of LDL is related to a number of disease states including coronary heart disease[68], one of the biggest killers in developed nations[69].

This assay is a relatively simple assay to perform, involving the addition of a known quantity of low density lipoprotein (LDL), in buffered saline, to a sample that is spiked with a known amount of $CuSO_4$[64]. The resulting oxidation of LDL is measured continuously for several hours at 234 nm, using UV/Visible spectrophotometry. An increase in the absorption at this wavelength indicates a

higher concentration of peroxyl radicals, which indicates greater oxidation of the LDL and less free radical protection by the sample.

The extent of antioxidative activity is compared to a control assay, generally (-)-epigallocatechin-3-gallate (ECGC), a known LDL oxidation inhibitor. The activity of the sample is presented as ECGC equivalents per gram of sample (μmol/g).

In some cases, the time involved in conducting this assay may be a limiting factor, as the sample requires continual monitoring for several hours. This can be negated by using a multi-cell automatic sample analyser, with regular readings made of many samples[64].

1.1.1.2 Spectroscopic methods utilizing DPPH

While lipid peroxidation-based assays are important in determining the specific effects of antioxidants on structures such as cell membranes and arterial plaques, more general approaches to determining the overall antioxidant capacity of a compound, or extract, also exist within the literature. Numerous methods to determine antioxidant capacity utilize the compound 1,1-diphenyl-2-picrylhydrazyl (DPPH).

DPPH (Fig. 1.3) is a stable, nitrogen-centered radical capable of being scavenged by an antioxidant. As a radical, DPPH strongly absorbs visible light with a λ_{max} of approximately 515-550 nm, depending on the particular solvent used[64, 70-74]. The reduced, neutral species of DPPH, which is also stable in solution, is present as a pale yellow solution and as such has no absorbance at the analytical wavelength[75]. Hence, antioxidant capacity is proportional to the loss of absorption at the appropriate analytical wavelength. This allows for a simple, stable and reproducible assay that can be quickly and easily performed to determine the antioxidant ability of both plant extracts and pure compounds[70, 76].

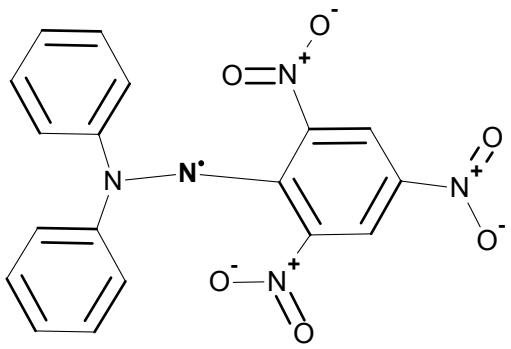

Figure 1.3 – Structure of the stable radical of DPPH.

However, the precise method of data collection and subsequent analysis varies throughout the literature. As each method, and subsequent experimental parameter, is different, results from one DPPH method are not always easily compared to others. This creates a problem when attempting to benchmark a method or compare results from different studies. To illustrate these differences, methods of analyses utilizing DPPH will be described in more detail.

1.1.1.2.1 EC 50 and variations

The EC50 parameter, broadly defined as the effective concentration of an analyte to elicit an effect of 50%, is a parameter derived from medicinal chemistry. In the context of measuring antioxidant activity with DPPH, the EC50 value obtained refers to the ratio of antioxidant to DPPH concentration required to reduce the steady state absorbance to 50% of the control, in this case being only DPPH[75]. Therefore, the compounds or extracts with a lower EC50 are more efficient antioxidants.

The EC50 measurements are achieved by recording the absorption as a function of time at λ_{max} until a steady state is achieved[75]. By repeating this method over a range of concentrations of the same antioxidant, a plot of [antioxidant]/[DPPH] versus % remaining DPPH at steady state can be constructed[75]. From the trendline of this plot, an approximate value for 50% remaining DPPH can be reached[75].

Whilst a useful parameter, there are several issues with the use of EC50 in the study of antioxidants, one of which is the application of steady state measurements. When analysing weak antioxidants, time periods of seven hours or greater to obtain a steady state are not unusual[75]. Also, how much variation constitutes a steady state may be open to interpretation, depending on the differences in sensitivity between instruments, or the time periods between readings. Furthermore, the suitability of steady state measurements has not been adequately demonstrated, as the *rate* of reaction can be a more important factor, given the speed of radical reactions. For example, with respect to superoxide scavengers, rate constants of around 10^8 M^{-1} s^{-1} are required for effective action[39].

1.1.1.2.2 % scavenged

The % scavenged approach uses two UV/Vis absorbance readings, one before the addition of the antioxidant and the second after a predetermined incubation period[39, 63, 66, 73]. The difference in absorbances gives a value for the effectiveness of the antioxidant, as a relative % scavenged (equation 1.2). This method is generally repeated with several concentrations of antioxidant, whilst holding the concentration of DPPH constant. However, the period of incubation between studies can differ immensely, with periods ranging from 1 to 30 minutes[63, 66, 73]. This will greatly affect any attempt to compare results between published values, given that values will be obtained at different sections of a non-linear decomposition curve, given this reaction is second-order with respect to the rate constant.

$$\% \text{ scavenged} = (Abs_{control} - (Abs_{antioxidant} / Abs_{control})) \times 100 \qquad \textbf{(1.2)}$$

Whether the value is given as % scavenged or the alternative, interchangeable terms DPPH scavenging effect[73], or Rs[63], the underlying chemical process is still the same. Furthermore, the different methods in the literature make comparison difficult, as some studies use a standard molar-based concentration (such a mmol/L) of compound or extract, while other studies use a

mass-based unit (such as μg/mL), depending on the particular field that the study was completed in.

While this method is a fast and simple assay, caution needs to employed when comparing publications or during benchmarking methods.

1.1.1.2.3 **k** *determination*

A purely kinetic method that involves singular determinations of the absolute second-order rate constant, *k*, for the reaction of DPPH with an antioxidant has been described[71, 77]. This is achieved by recording the decrease in absorption as a function of time[71]. The second-order integrated rate equation is given by the equation:

$$\frac{1}{[A]} - \frac{1}{[A]_0} = akt \qquad \textbf{(1.3)}$$

where A = reactant, A_0 = reactant at time zero, a = stoichiometry of A, k = rate constant and t = time.

A plot of $1/[A]$ versus time (or, in the case of this reaction where absorbance ≡ concentration, a plot of 1/Abs vs time) yields a gradient of ak and a y-intercept of $1/[A]_0$. Therefore, this value can be obtained with a single analysis of a compound at a known concentration.

With respect to the use of this assay, the term ‘rate constant’ can be a misnomer, as the solvent has been proven to alter this ‘constant’, after having been commonly assumed to be independent of DPPH-based radical abstractions[77]. Such solvent effects have been previously shown to effect the rate constant 67-fold for α-tocopherol and 106-fold for phenol[77]. Therefore, only results obtained using the same solvent are directly comparable.

1.1.1.2.4 Log(Z) determination

This method involves the calculation of a kinetic parameter, designated Log(Z). Initially, *k* values are calculated as above, for a range of relative molar concentration ratios ([antioxidant]/[DPPH])[70]. These initial *k* values (i.e. second-order reaction rates), are plotted against the concentration ratio, with the gradient of the linear regression equal to Z[70]. The logarithm of this value, designated Log(Z), is the value used to quantify radical scavenging[70].

This method was originally designed to be a sound option for the study of antioxidant activity, as it decreases experimental error by incorporating several *k* values, themselves produced with numerous data points. These *k* values, when plotted, also require linearity, again significantly negating errors in single samples.

For most of the other methods described in this section, an estimation of steady state, where the absorbance of the analyte remains constant as a function of time, is required. This steady-state estimation may differ between researchers and/or equipment. Also, with measurements at a steady state, the specific mechanisms behind antioxidant activity, either Single Electron Transfer (SET) or Hydrogen Abstraction (HAT) remain unclear, as total antioxidant potential is essentially measured. With Log(Z) calculated using the *initial* rates of reaction, the only mechanism possible is HAT[70]. The use of several correlated values of *k* also decreases the likelihood of error affecting the outcomes, which may occur if only one *k* measurement is made on a compound. Due to these advantages, this is the method that will be used in the experimental section of this work.

1.1.1.3 Spectroscopic methods utilizing other probes

Other probes specifically developed for the measurement of antioxidant behaviour are also available, with three such methods discussed in this section.

These methods are similar to those discussed above, but use a different species to track antioxidant activity.

1.1.1.3.1 Chemiluminescence quenching method

The chemiluminescence (CL) quenching method relies on the complexation of a hydroxyl radical ($OH^{\bullet}$) and a compound known as luminol (5-aminophthalazine-1,4-diol). When the hydroxyl radical reacts with luminol, a burst of light is produced, with the overall light intensity being proportional to the number of hydroxyl radicals present[78]. Scavenging of the hydroxyl radical is therefore measured as a loss of chemiluminosity between a control without antioxidant, and an analysis with an antioxidant present. This can be calculated using the area under the curve (AUC) of luminosity versus time, with a lower area indicting a higher antioxidant activity[78]. The other option for quantifying antioxidant activity is to use an IC50 method identical to that discussed earlier; that is, determination of the concentration of antioxidant required to achieve a 50% reduction in measured light, therefore 50% inhibition of hydroxyl radicals[79].

As this CL quenching method requires a supply of hydroxyl radicals, and hydroxyl radical reaction rates are so fast[39], the radicals need to be generated during the analysis. Two popular methods for generating these radicals are the hydrogen peroxide (H_2O_2) – horseradish peroxidase system[80], or a Fenton-type reaction involving H_2O_2 and EDTA-bound Fe^{2+} [79].

This CL method has an added advantage, in that the ability to determine *pro*-oxidant behaviours is present[79]. With an excess of luminol, if a compound is prone to pro-oxidation, the luminol intensity increases above control levels. A difficulty with this method can be in the determination of the order of addition, as well as quantity, of the reactants, that provides maximum luminosity. However, once this is determined, this assay is reproducible and effective.

1.1.1.3.2 Fluorescence quenching method

This fluorescence quenching method, whilst similar to the above chemiluminescence method, is different enough to be discussed separately. The major point of difference between the CL quenching method above and this fluorescence quenching method is that fluorescent probes are used to measure antioxidant behaviour. This method was first published by Cao *et al*, and has also been referred to as the Oxygen Radical Absorbance Capacity (ORAC) assay. With this assay, peroxyl ($ROO^{\bullet}$) radicals are generated by a compound known as AAPH (2,2`-azobis(2-amidinopropane)dihydrochloride)[81]. The peroxyl radicals negatively react with the fluorescence probe, causing a decrease in the measured fluorescence. The relative antioxidant ability is a measure of the inhibition of the fluorescence loss, and is generally compared to a standard, such as Trolox – a water soluble analogue of vitamin E[82].

There are two probes commonly used for this assay, namely β-phycoerythrin and fluorescein[81, 82]. β-Phycoerythrin was the first-generation probe used by Cao *et al* in developing the original methodology. A hydrophilic protein isolated from *Porphyridium cruentum*, β-phycoerythrin absorbs visible light with a high fluorescence yield and sensitivity to $ROO^{\bullet}$[83]. However, protein inconsistency, instability of the probe when exposed to the excitation wavelength for long periods of time and polyphenol interactions through non-specific protein links, all lead to the development of another fluorescent probe, fluorescein and its derivative, 6-carboxyfluorescein[83, 84]. These probes are small molecules, so the quality and quantity of the probe can be more closely controlled. These probes, especially 6-carboxyfluoroscein, show high quantum yield, high molar absorptivity, as well as good thermal and photochemical stability[84].

As peroxyl radicals are generated in lipid peroxidation, this method can be used as an alternative to the lipid peroxidation method examined earlier. A disadvantage of this fluorescent assay, however, is the hydrophilicity of the probes, such that lipophilic compounds cannot easily be examined. However,

lipophilic compounds can still be examined with the LDL oxidation method, as discussed previously.

1.1.1.3.3 Trolox Equivalent Antioxidant Capacity (TEAC)

The functional aspects of the TEAC method are very similar to several of those involving DPPH. This technique utilizes the radical cation $ABTS^{+\bullet}$ (2,2'-azino-bis-(3-ethylbenzthiazoline-6-sulfonic acid) to spectroscopically measure antioxidant activity as a decrease in absorbance at the λ_{max}, 734 nm[85-87].

However, unlike DPPH, ABTS is not as stable a radical as DPPH. A major downfall of this technique is that the ABTS radical needs to be generated before use, as it is not a naturally stable radical like DPPH. With the reactants and products of this radical generation present during the assay, this could possibly lead to the regeneration of the scavenged radicals during analysis. Further, the ABTS radicals can react with scavenged parent molecules, leading to greater than expected results. An example of this is the reaction of Trolox with ABTS. The structure of Trolox, a water-soluble analogue of α-tocopherol, has a single hydroxyl group, yet reacts with a stoichiometry of 1.9:1, rather than the 1:1 expected[86]. It is suspected that this is due to the Trolox radical involved in a fast reaction with another ABTS molecule[86].

The data analysis of the TEAC method requires determining the moles of ABTS molecules scavenged per moles of antioxidant, as measured after 6 minutes of incubation time as a loss of absorbance[85, 86]. Comparisons of antioxidants are carried out by comparing the ratio of moles scavenged by the antioxidant to moles scavenged by a standard.

When compared to the results of other antioxidant activity studies, the TEAC assay shows little or no correlation, and as such is unsuitable for structure activity relationship (SAR) studies[85]. This is due to the fact that the TEAC assay measures the antioxidant capacity of the parent compound as well as any active

products of this scavenging reaction, while SAR studies require a single molecular identity[85]. The TEAC assay is useful, however, for the study of complex mixtures such as extracts[85].

It must also be noted at this point that the ABTS radical species can be used to replace DPPH in all of the previous methods, such as *k* determination and EC50 studies[87]. However, the problem of secondary reactions still persists.

1.1.1.4 Other antioxidant methods

This section presents several methods that do not fit neatly into any of the above categories regarding antioxidant behaviour. This is due to the fact that these methods do not use an organic radical probe, as all methods discussed to this point have. Instead, processes such as transition metal reduction and calorimetry are used in the methods presented here.

1.1.1.4.1 Folin-Ciocalteu assay

The Folin-Ciocalteu assay was originally developed in 1912 to react specifically with phenols[88]. This was further extended to the determination of tyrosine concentrations in proteins[89], as well as vanillin in vanilla extracts[90]. The power of this reagent was such that the Folin-Denis reagent (a precursor to the Folin-Ciocalteu reagent) became an AOAC standard for the analysis of tannins in alcoholic beverages[91].

The Folin-Ciocalteu reagent is essentially a phosphomolybdic-phosphotungstic acid reagent, containing "complex polymeric ions formed from phosphomolybdic and phosphotungstic heteropoly acids"[91]. This yellow, acidic reagent oxidizes phenolates, partially reducing the heteropoly acid from a +6 oxidation state, to a mixture of +5 and +6[91]. This produces the complex molybdenum-tungsten blue, a reaction that is monitored spectroscopically at 765 nm[91].

This reagent, however, can also react with other reductants, yielding abnormally high results[92]. Also, given the generally slow speed of reaction completion, information regarding the strength of the O-H bond cannot be collected. As such, this method is occasionally referred to as a 'total reducing power' assay.

This method is predominately used for examining botanical samples and extracts, however, this assay can be affected by a variety of non-phenolics, such as nucleotides, sugars, organic acids, iron(II) and metal chelators, to name a few[92]. With respect to using this assay to examine known quantities of pure compounds for antioxidant activity, this assay would not yield information pertinent to SAR studies and is relatively slow, therefore this method would not be recommended.

1.1.1.4.2 Differential Scanning Calorimetry (DSC)

DSC is a physical chemistry technique, which has been used in this case to quantify the antioxidant behaviours of additives to oil products[93, 94]. This approach involves dispersing known amounts of chosen antioxidants into samples of a standard mineral oil, applying heat in an ambient environment, and measuring the heat flow of the sample. Antioxidant ability is measured as the temperature at which oil oxidation, an exothermic process, is delayed compared to an unadulterated control sample[93, 94]. This method was designed for petrochemical research, rather than the analytical assessment of antioxidants.

Following this review, the method chosen for the experimental work presented later in this Chapter is the Log(Z) parameter method, which uses the DPPH radical probe. This method allows for accurate determinations of, specifically, hydrogen abstraction ability, which therefore provides information regarding the strength of the O-H bon. This is important, as this allows for a targeted computational study of this abstraction process only, without factoring in any effects of SET.

1.1.2 A single descriptor for antioxidant activity

The second aspect of the work to be presented later in this Chapter is the attempt to correlate experimental antioxidant activity with a *single* computationally derived descriptor. With a good theoretical model, antioxidant activity could therefore be predicted for any compound, allowing for the design of synthetic antioxidants or study of natural products with suspected antioxidant properties. A current literature search shows that this outcome is yet to be adequately reached.

The advantage of using a single descriptor is that, when comparing computational results to experimental results, less data points are required for statistical significance. It has been previously reported that, for a statistically significant relationship to exist, five data points per theoretical descriptor is required[95]. Another advantage is that, with less data manipulation involved, a more logical argument describing the significance of a correlation can be made, rather than relying on multiple linear regression (MLR) analysis to identify positive relationships between the experimental data and a multitude of chemical descriptors (which may number up to 600 or more). Further, any correlation discovered may only be class-specific[96].

As the experimental process to be modelled in this work is hydrogen abstraction, homolytic bond dissociation energy (BDE), calculated using Density Functional Theory (DFT), is the descriptor chosen for this modelling. This choice is justified below.

1.1.3 Overview of Density Functional Theory

DFT is a computational method for calculating the electronic density of atoms and molecules[95]. The essential idea behind DFT is the presence of a relationship between the total electronic energy and the overall electronic

density[95]. An approximate model of this idea was developed in the late 1920's and was known as the Thomas-Fermi model. The discovery that the ground-state energy of a system, amongst other properties, are uniquely defined by electron density, was published in 1964[95, 97]. This allowed for a general improvement over the existing Hartree-Fock method, with an explosion of interest and development since the late 1980's[95].

The major improvement achieved with DFT specifically relates to the treatment of the electronic environment. In Hartree-Fock theory, a Slater determinant is calculated from the set of *N* single-electron wavefunctions, where *N* is the number of electrons in the molecule[95]. Whilst DFT also uses single-electron wavefunctions, these are used to calculate not just the total electronic energy, but the overall electronic energy distribution as well.

Without resorting to an in-depth discussion of the finer workings and equations of DFT, the major premise of DFT is that the total electronic energy functional is the sum of two terms. The first term describes the Coulombic interaction of electrons with the positively charged nuclei, and the second term relates to the kinetic energy of the electrons and energetic contributions from interelectronic interactions[95].

It is this second term that is the most relevant to the application of this theory to the work presented in this Chapter. Given that radical scavenging, as mentioned above, involves the homolytic breaking of bonds, interelectronic interactions are of vital importance to this process. As the procedure of bond breaking is a purely electronic exercise, accurate representations of the electronic energy and density, before and after abstraction, are required.

This work attempts to correlate an experimental parameter (Log(Z)) with a theoretically derived descriptor, BDE. A range of compounds will be examined in this process, including various known antioxidants as well as molecules only

sparingly studied previously for radical scavenging ability. An attempt to account for significant outliers will also be presented where applicable.

1.2 METHODS

1.2.1 Materials and equipment

All reagents were used as obtained from the suppliers without further purification, Table 1.1. Ethanol was supplied by CSR.

The UV/Vis spectrophotometer that was used in the spectroscopic analyses was a Cary 1E UV/Visible Spectrophotometer at room temperature. Measurements were made via a dedicated personal computer. The Cary WinUV software suite was used, Version 2.00. The kinetics program within this suite was used to record the absorbance as a function of time at 5-second intervals.

Table 1.1 – List of reagents used in UV/Vis assay. All compounds, except for DPPH, are phenolic reagents.

Chemical	Supplier
2-hydroxyquinoline	Fluka
4-hydroxyquinoline	Fluka
5-hydroxyquinoline	Aldrich
6-hydroxyquinoline	Fluka
7-hydroxyquinoline	Acros
8-hydroxyquinoline	BDH
5-chloro-7-iodo-8-hydroxyquinoline (Clioquinol)	Sigma
5,7-dichloro-8-hydroxyquinoline	Sigma
Phenol	BDH
Butylated hydroxytoluene (BHT)	Sigma
Butylated hydroxyanisole (BHA)	Sigma
1,1-diphenyl-2-picrylhydrazyl (DPPH)	Sigma

1.2.2 UV/Vis measurements – DPPH assay

Standard solutions of all phenolic reagents from Table 1.1 were quantitatively dissolved in ethanol. The stable radical used as a probe in this assay, DPPH (1,1-diphenyl-2-picrylhydrazyl, Fig. 1.3) was also quantitatively dissolved in ethanol and left to equilibrate at room temperature for 24 hours. This standard stock solution was refrigerated between uses, and returned to room temperature before each use. A fresh stock was prepared every three days. The assay method, as well as the mathematical treatment described in the next section, were developed from a method published by Ancerewicz[70].

Sets of reactions of known concentrations of DPPH and antioxidant were prepared. These reaction sets involved a fixed concentration of DPPH, and varied concentrations of the phenolics, with a range of ratios of [antioxidant]/[DPPH] covering 0.5 to 4 for all antioxidant candidates except for α-tocopherol, which required ratios between 0.2 and 1 due to the extremely rapid rate of reaction. Appropriate volumes of the phenolic solutions were added to small reaction vessels and were diluted with a volume of ethanol that would obtain a volume of 5.25 mL. To this, 0.75 mL of a 0.4 mM ethanolic DPPH solution was added, rapidly mixed, transferred to a quartz cuvette, and placed within the incidence beam of the UV/Vis spectrophotometer. The UV/Vis was set to measure the absorbance of the reaction at 515.2 nm, the observed λ_{max} of the DPPH radical when dissolved in ethanol.

The kinetics program within the UV/Vis software was used to make periodic measurements of the absorbance at 5-second intervals. Each reaction was analysed until an approximately steady state was achieved, where only a small decrease in absorbance was recorded over a relatively large time period. This indicated that enough data points for second-order rate kinetics could be calculated. The achievement of a steady state is not essential to the analysis, however.

1.2.2.1 Log(Z) calculation

Once the raw kinetic data was collected, the Log(Z) values, as measurements of antioxidant activity, could be calculated. Given that the DPPH$^{\bullet}$ + ArOH $\rightarrow$ DPPH-H + ArO$^{\bullet}$ reaction displays second-order rate kinetics, the rate constant, *k*, for all spectra were calculated. This was achieved by plotting time (secs.) vs 1/Abs[a], as example of which is Fig. 1.4. The gradient of the linear portions of these graphs were calculated using the regression module of the Data Analysis pack included with Microsoft Excel 2000. These *k* values were then plotted against the ratio of initial [antioxidant]/[DPPH] concentrations, Fig. 1.5. Linear regression, again calculated in the same way as previously mentioned, gives a Z value for that antioxidant candidate. The logarithm of this value, Log(Z), was then used to compare these empirical results to the computational values described below.

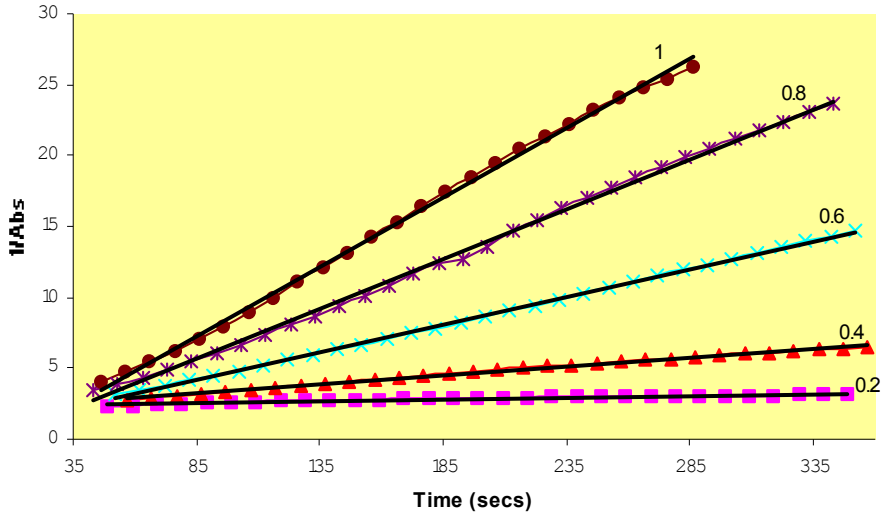

Figure 1.4 – Graph showing the vitamin E data for the calculation of the k values. The annotations are the ratios of antioxidant to DPPH for each set of data. The gradients of the trendlines are the k values.

[a] Normally, this would be a plot of Time vs 1/[A], where A is the analyte being measured. In this case, due to the Beer-Lambert Law, as well as the linearity of the Beer-Lambert law at these concentrations (data not shown), [A] ≡Abs.

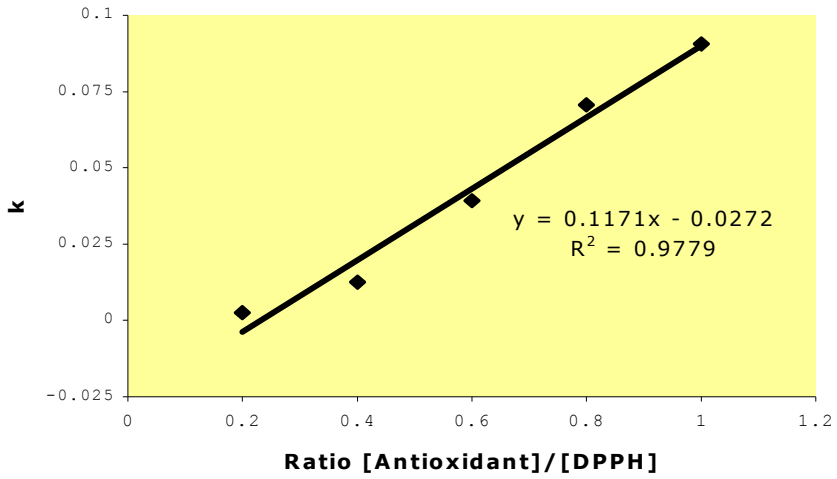

Figure 1.5 – Corresponding k values from the data in Fig. 1.4. The gradient of this trendline is the Z value, the logarithm of which is the Log(Z) parameter. In this case, Log(0.1171) = -0.9314.

1.2.3 Computational methodology

All phenolics that were assayed using the Log(Z) parameter method were subsequently modelled using DFT, as employed by Spartan '04[98]. All molecules were built and initially subjected to a conformer search to locate likely global minimum structures. Geometry optimisation using the B3LYP hybrid functional with the 6-31G(d,p) basis set was then carried out. The formation energies of the optimised structures were recorded, and these optimised structures were used as starting points for the optimisation of the radical analogues. The radical forms of the phenolics were optimised under the same scheme, with the exception being a change in multiplicity from singlet to doublet. Again, the energies of these molecules were recorded. The energy of the extracted hydrogen radical was also calculated using B3LYP/6-31G(d,p) as a neutral doublet.

1.2.3.1 BDE calculation

The calculated energies for both the complete, as well as the reduced, structures were used to calculate a homolytic Bond Dissociation Energy (BDE) value for each phenolic. BDE was calculated as in equation 1.1 above.

BDE was chosen as the single descriptor, due to the fact that DPPH, unlike several other radical scavenging probes, is accepted to act solely through hydrogen abstraction rather than single electron transfer (SET)[70]. As such, homolytic BDE is analogous to the process occurring *in vitro*, where SET would be described through ionisation potentials.

1.2.3.2 Rotational allowance

Calculations were repeated for all phenolic molecules, with the aim of locating a *local* minimum. Whilst a couple of the phenolics studied contained several degrees of freedom, hence several possible local minima, only one degree of freedom was examined in these molecules, namely that related to the rotation of the hydroxyl group. Starting with the previously optimised structures, a manual rotation of the hydroxyl group through 180°, followed by the geometry optimisation of this structure, achieved these local minima structures. BDE calculations, as described in equation 1.1 above, were repeated, with the energies of the local minima structures used as the E_{ArOH} value.

1.3 RESULTS AND DISCUSSION

1.3.1 Benchmarking of the Log(Z) methodology – comparison with previously published results

To ensure the validity of the experimental method, a comparison of the data to previously published antioxidant results is desirable. Following an extensive literature search, however, no pure substances had been previously analysed using the Log(Z) parameter with ethanol as the solvent, the medium of choice for the investigations presented in this Chapter.

The identity of the solvent with respect to the reaction of phenolics with DPPH is vital, especially when the solvent can form hydrogen bonds with the reactants[99]. Large differences in observed antioxidant activities for various compounds, as measured using DPPH in different solvent systems, have been previously reported[99]. Therefore, relative kinetic measurements such as Log(Z) cannot be compared between different solvent systems. The original work by Ancerewicz *et al.*, upon which the Log(Z) method used experimentally in this thesis is based, used methanol as the solvent. Therefore, the published Log(Z) values for α-tocopherol and BHT obtained by the Ancerewicz group cannot be directly compared with the present work.

In order to have confidence in this method, some benchmarking was required. This was achieved via a comparison between the observed Log(Z) values obtained in this work with corresponding values from the literature for that compound in the same solvent (also employing the DPPH probe) but utilizing an alternative parameter to Log(Z)[73].

Thus, a publication by Oktay *et al* was chosen, which assayed three compounds, in ethanol, using the DPPH radical and the '% scavenged' method as discussed in section 1.1.1.2.2 above. These standards were BHA, BHT and α-tocopherol[73]. These results allowed for a comparison to be made regarding the relative antioxidant activities in ethanol for these well-studied compounds. These results, when compared on a molar scale, display a reported order of antioxidant activity, such that α-tocopherol > BHA > BHT[73]. The Log(Z) values obtained in this thesis for these compounds are - α-tocopherol = -0.93, BHA = -1.81 and BHT = -3.82, thereby supporting the qualitative order of activity reported in the literature. This encouraging finding shows that the DPPH$^{\bullet}$ probe, as applied to the Log(Z) method, produces analogous results to those previously published using an alternative parameter.

However, to thoroughly benchmark the Log(Z) method, a more defined, quantitative relationship is desirable. In particular, a benchmark is required that involves a different method entirely and that includes a wider range of antioxidant activities. In this regard, previous work was uncovered in which BHT, 1-naphthol, 5-HQ and 8-HQ were investigated for their ability to enhance the thermal stability of oil, using Differential Scanning Calorimetry (DSC)[93].

The DSC method, as discussed in section 1.1.1.4.2 above, involves controlled heating of the samples, with continuous measurement of the temperature of the samples. The analytically important value is the inflection point, defined as the onset temperature, of the exothermic process of oil oxidation[93]. The delay in the onset temperature is directly proportional to the relative antioxidant activity of that particular antioxidant. A direct comparison of the literature values with the Log(Z) values obtained show a very good agreement, as shown in Fig. 1.6.

As demonstrated in Fig 1.6, at low concentrations of additive, the DSC experiments correlate very well with the quantitative Log(Z) measurements presented in this thesis. The reason for the drift from this correlation at the highest concentration of antioxidants (Fig. 1.6c) is unknown.

The quality of the correlations achieved between these two very different methods indicates that results obtained using the Log(Z) method is quantitatively reflective of antioxidant activity. This is important for two reasons; firstly, the purely kinetic measurement reflected by Log(Z) is directly related to actual activity, and secondly, the Log(Z) method is sensitive enough to separate similar species and activities (i.e. 5-HQ and 1-naphthol), yet is robust enough to cover several orders of magnitude of activity (i.e. difference between 5-HQ and 8-HQ). This concordance with previously published results suggests that the method is a valid, viable method for the study of antioxidant activity.

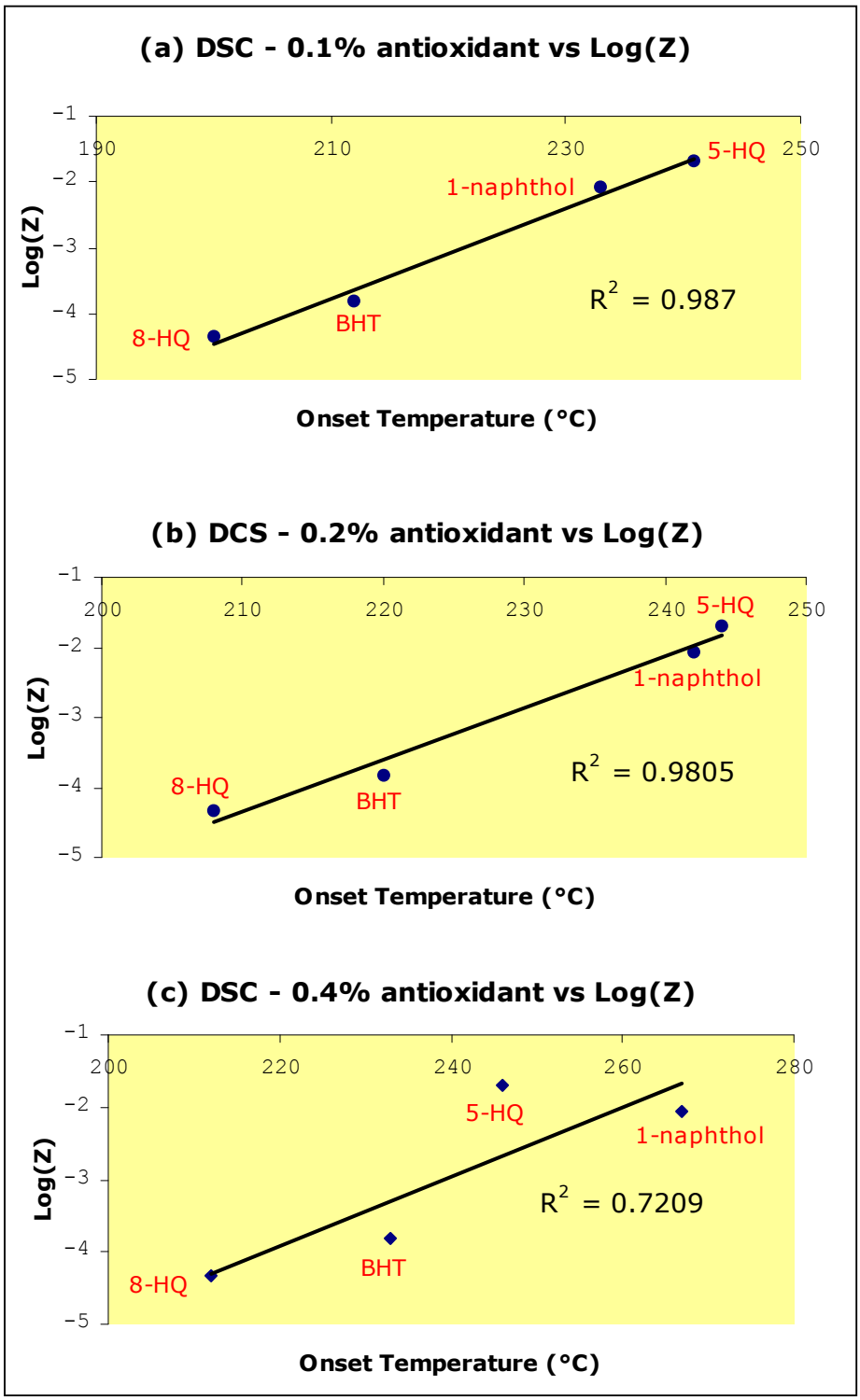

Figure 1.6 – Comparison of results from literature[93] versus experimentally obtained Log(Z) results. DSC experiments contained (a) 0.1% antioxidant additive (b) 0.2% antioxidant additive (c) 0.4% antioxidant additive.

1.3.2 Log(Z) results

As mentioned in section 1.1.1.2, DPPH is a suitable antioxidant probe due to several characteristics. Firstly, it is relatively stable and exists as a free radical reagent. This allows for a controlled, quantifiable amount of the reactive species to be added to a reaction milieu without requiring an activation reaction process, as some scavenging methods require[85, 86]. Secondly, the stable radical species is strongly coloured, with a high extinction coefficient, allowing accurate measurements to be made with small amounts of both probe and sample. Thirdly, once reacted, the diamagnetic species shows no absorbance at the λ_{max} of the radical species, therefore all absorbance at the analytical wavelength is due to the species of interest. No further corrections are required, and, due to the Beer-Lambert Law, the concentration is equivalent to absorbance (Beer-Lambert behaviour data can be found in Appendix IV – the attached CD).

The results obtained using the Log(Z) assay on thirteen compounds are summarised in Table 1.2. Raw data can be found in Appendix IV. Antioxidant activity is proportional to the magnitude of Log(Z); greater activity is represented by larger (less negative) Log(Z) values.

Table 1.2 – Log(Z) values obtained for the phenolic compounds studied

Phenolic substrate	Log(Z)
Phenol	-4.59
BHT	-3.82
BHA	-1.81
α-tocopherol (Vitamin E)	-0.93
1-naphthol	-2.07
2-hydroxyquinoline	-5.88
4-hydroxyquinoline	-4.84
5-hydroxyquinoline	-1.71
6-hydroxyquinoline	-4.92
7-hydroxyquinoline	-5.08
8-hydroxyquinoline	-4.34
5,7-dichloro-8-hydroxyquinoline (DCHQ)	-4.32
5-chloro-7-iodo-8-hydroxyquinoline (CQ)	-4.29

This set of antioxidant activities provide a sufficient data set for the attempted correlation with calculated BDE values (described below), given that the aim of this chapter is to explore the use of a single computational descriptor to describe experimental antioxidant ability. As only one descriptor is to be used and statistical significance is generally accepted to be a minimum of five compounds per descriptor[95], the set of data in Table 1.2 allows for a meaningful correlation of these experimental values to computationally derived results. In addition, this data is fundamentally useful, given that a number of these compounds have not been previously characterized with respect to their relative antioxidant potential.

1.3.3 BDE calculation

As mentioned in the methodology (section 1.2.3.1), the descriptor chosen to attempt to describe antioxidant activity is BDE (equation 1.1). Table 1.3 contains a summary of the BDE results for each compound studied, together with the corresponding Log(Z) values. In order to quantify how well the BDE descriptor describes antioxidant ability, the Log(Z) values were plotted against the corresponding BDE values, Fig 1.7.

As can be seen from Fig. 1.7 below, a satisfying correlation is found between BDE and Log(Z). Where R^2 values greater than 0.8 are usually referred to as "strong"[100], the R^2 value obtained indicates a reasonably strong correlation. Therefore, with an aim of predicting antioxidant activity computationally using BDE as the sole descriptor, this approach seems to have some promise. However, some investigation is required in order to ascertain why the correlation is not higher.

In an attempt to improve the relationship between Log(Z) and BDE, the data has been thoroughly scrutinized. Upon close inspection of Fig. 1.7, a dislocation with respect to two groups of data is observed; one above the

trendline with four data points (10-13), and another below it with five data points (5-9). This might be suggestive of systematic errors (particularly in the calculation of the BDEs) in one group or the other. In order to examine this in more detail, the features of the compounds in each group were reassessed.

Table 1.3 – BDE results obtained, with corresponding Log(Z) values for each compound studied.

Compound	BDE (kcal/mol)	Log(Z)
Phenol	85.96	-4.59
BHT	83.70	-3.82
BHA	77.71	-1.81
α-tocopherol (Vitamin E)	74.44	-0.93
1-naphthol	79.18	-2.07
2-hydroxyquinoline	96.60	-5.88
4-hydroxyquinoline	85.82	-4.84
5-hydroxyquinoline	80.21	-1.71
6-hydroxyquinoline	85.12	-4.92
7-hydroxyquinoline	86.78	-5.08
8-hydroxyquinoline	91.34	-4.34
5,7-dichloro-8-hydroxyquinoline (DCHQ)	89.44	-4.32
5-chloro-7-iodo-8-hydroxyquinoline (CQ)	89.58	-4.29

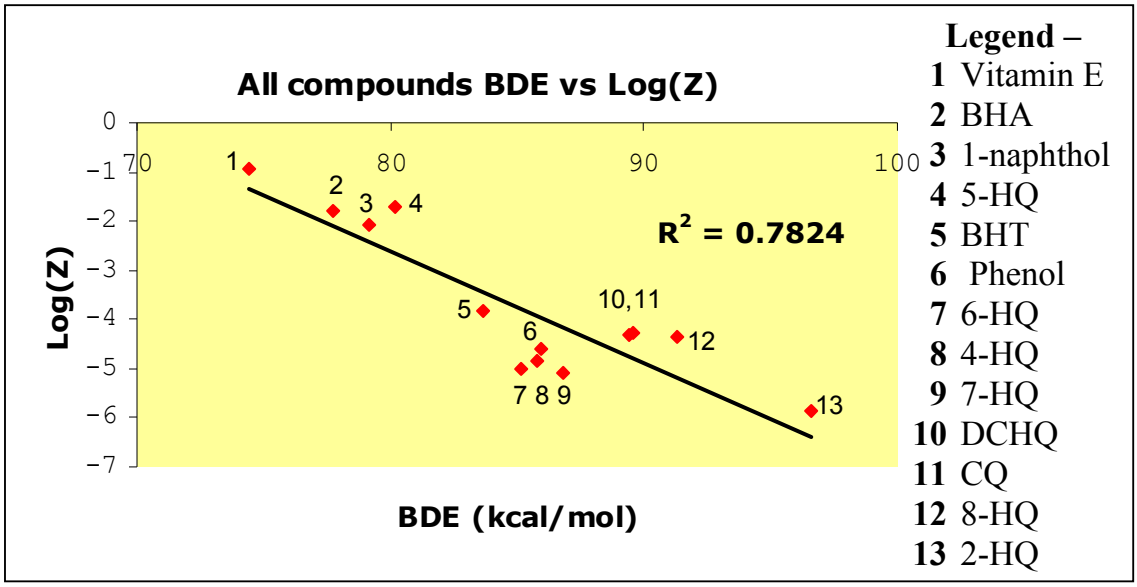

Figure 1.7 – Graph of BDE vs Log(Z) for all compounds studied.

Notably, when each group is plotted separately, together with the highly active compounds (1-4), two very strong correlations are obtained, Fig. 1.8. This suggests that the two separate groupings might differ at a molecular level in a specific way. Upon close examination of the structures of the molecules in these two respective groups, it can be observed that, in the group affecting trendline 2, that the OH moiety is involved in an intramolecular hydrogen bond to the endocyclic nitrogen atom, but not in the group affecting trendline 1, Fig. 1.9. Where an intramolecular hydrogen bond exists, this interaction would be required to be broken prior to, or concomitant with, hydrogen atom abstraction.

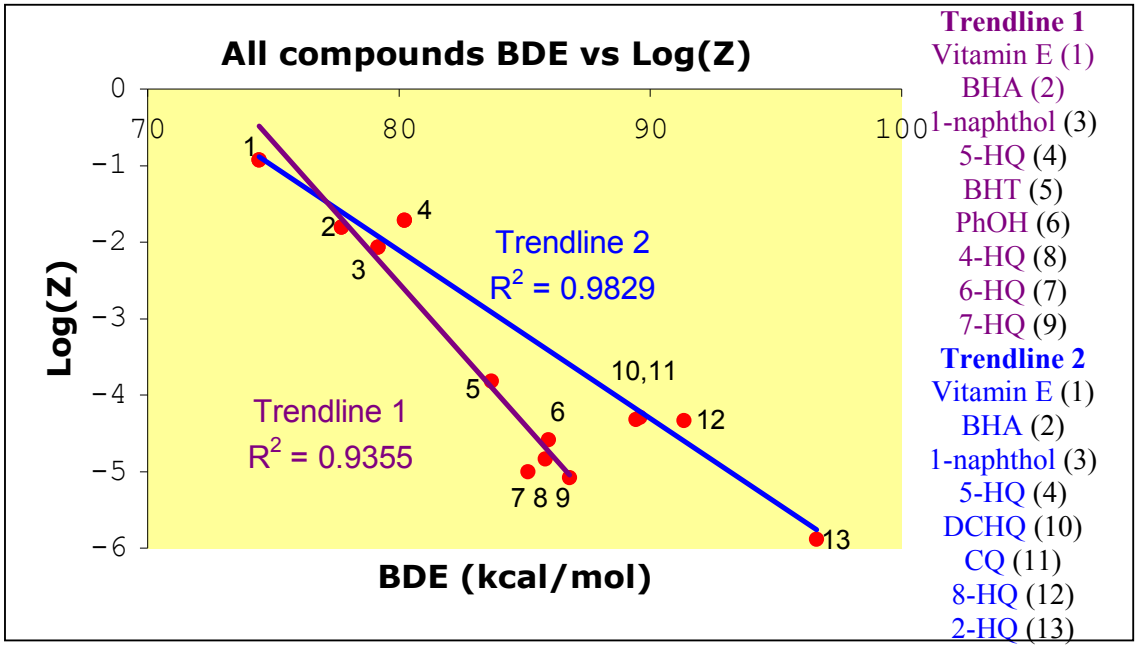

Figure 1.8 – Plots highlighting the two separated groups of compounds. The identities of the compounds involved are above each plot.

With an extra interaction occurring at the site of reactivity for radical scavenging, it is expected that such intramolecular hydrogen bonding, if not properly accounted for, could be the source of the systematic error in the BDE calculation. The effect of an extra interaction involving the atom to be abstracted, would be to increase the calculated BDE by up to 8.5 kcal/mol, as this hydrogen bond would also need to be overcome. As the suspected source of error in this subset of compounds is in the BDE calculation, a correction of the relevant data

points would need to be carried out, which allows for the energy required to break the intramolecular H-bond for a given molecule.

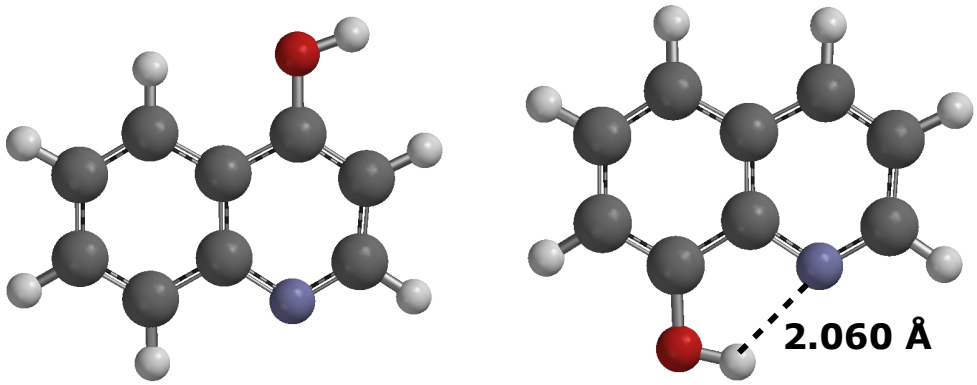

Figure 1.9 – Representative structures of the two groups from Fig. 1.7. Molecules are 8 (4-hydroxyquinoline) and 12 (8-hydroxyquinoline), respectively. Note an absence of hydrogen bonding in the first molecule (8), and a strong intramolecular H-bond in the other (12).

Whilst these studies suggest that the abstraction of the hydrogen atom is influenced by the involvement of this atom in hydrogen bonding, specifically intramolecular hydrogen bonding, the influence on the data of *intermolecular* hydrogen bonding, involving the OH moiety and the solvent (in this case ethanol), is also of interest. It is likely that, due to other considerations such as steric effects, each molecule is subtly different in this regard. Therefore, errors arising in the calculation of the Log(Z) values from the DPPH experiments due to intermolecular hydrogen bonding effects are difficult to address and have not been accounted for in this study.

In order to remove the influence of the intramolecular H-bond in the calculation of the BDE, the OH moiety is rotated by 180 degrees about the C-O bond and is subsequently optimised in this configuration, such that no intramolecular hydrogen bond can form. This energy is then used in the calculation of a corrected BDE as described earlier.

1.3.3.1 Effect of Ar-OH rotation on BDE

The initial BDE values were obtained for the global minimum conformer of each compound in the gas phase. For the compounds that can form an intramolecular hydrogen bond, this global minimum conformer did include this bond in all four optimised structures. Therefore, geometry optimisation was performed on structures without this hydrogen bond, using the B3LYP/6-31G(d,p) model, Table 1.4 and Fig 1.10.

Table 1.4 – Tabulation of computed BDE parameters and their corresponding experimental Log(Z) values. The BDE values highlighted in red have been corrected for the presence of an intramolecular hydrogen bond. The uncorrected value is given in brackets and Δ is the energy difference between the uncorrected and corrected values, indicting the energy required to break the intramolecular H-bond. This data is plotted in Fig. 1.10.

Compound	BDE (kcal/mol)	Log(Z)
Phenol	85.96	-4.59
BHT	83.70	-3.82
BHA	77.71	-1.81
α-tocopherol (Vitamin E)	74.44	-0.93
1-naphthol	79.18	-2.07
2-hydroxyquinoline	90.45 (96.60); Δ = 6.15	-5.88
4-hydroxyquinoline	85.82	-4.84
5-hydroxyquinoline	80.21	-1.71
6-hydroxyquinoline	85.12	-4.92
7-hydroxyquinoline	86.78	-5.08
8-hydroxyquinoline	82.76 (91.33); Δ = 8.57	-4.34
5,7-dichloro-8-hydroxyquinoline (DCHQ)	83.43 (89.43); Δ = 6.00	-4.32
5-chloro-7-iodo-8-hydroxyquinoline (CQ)	82.69 (89.58); Δ = 6.89	-4.29

The marked improvement, in Fig. 1.10, of the correlation between BDE and Log(Z) (0.73 to 0.91) when corrections are made for the presence of an intramolecular H-bond, is suggestive that, in order for hydrogen abstraction to occur, the intramolecular hydrogen bond needs to be broken.

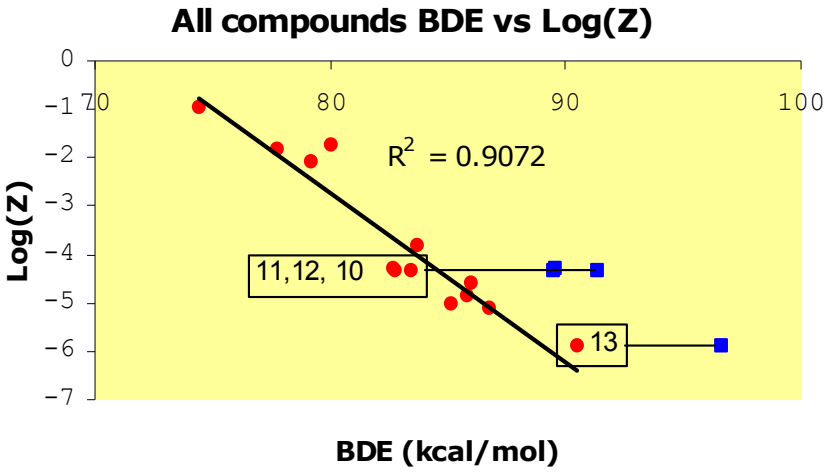

Figure 1.10 – Plot of BDE vs Log(Z). The data points in blue represent the uncorrected BDE values described in Table 1.4.

Therefore, it is important to consider intramolecular hydrogen bonding (and also intermolecular hydrogen bonding), along with other factors, as being determinative of the relative efficacy of a molecule as a radical scavenger. This is especially vital with respect to current research into natural antioxidant compounds, which are best described as polyphenolics, where several intramolecular hydrogen bonds can occur between adjacent hydroxyl groups. Such hydrogen bond interactions should be appropriately considered before a model can possibly become predictive.

1.3.4 Towards a greater understanding of antioxidant activity

As mentioned in section 1.3.2 above, the Log(Z) data set itself is inherently useful due to the fact that several of the compounds investigated have not previously been examined for relative antioxidant capacity, namely, 4-, 6-, and 7-hydroxyquinoline. Given the long-standing interest in hydroxyquinolines as a class of molecule[101], it is of interest to fully characterize the relative molecular characteristics of this particular scaffold.

1.3.4.1 The x-hydroxyquinoline (x-HQ) series, x = 2 – 8

All members of the hydroxyquinoline series, except for 3-HQ, were examined for antioxidant activity using Log(Z). The results of the experimental Log(Z) investigations of the x-HQ series, along with 1-naphthol (a structurally similar compound), are represented in Figs. 1.11a and 1.11b. Note the unusual activity of 5-HQ, compared to the other members of the x-HQ series.

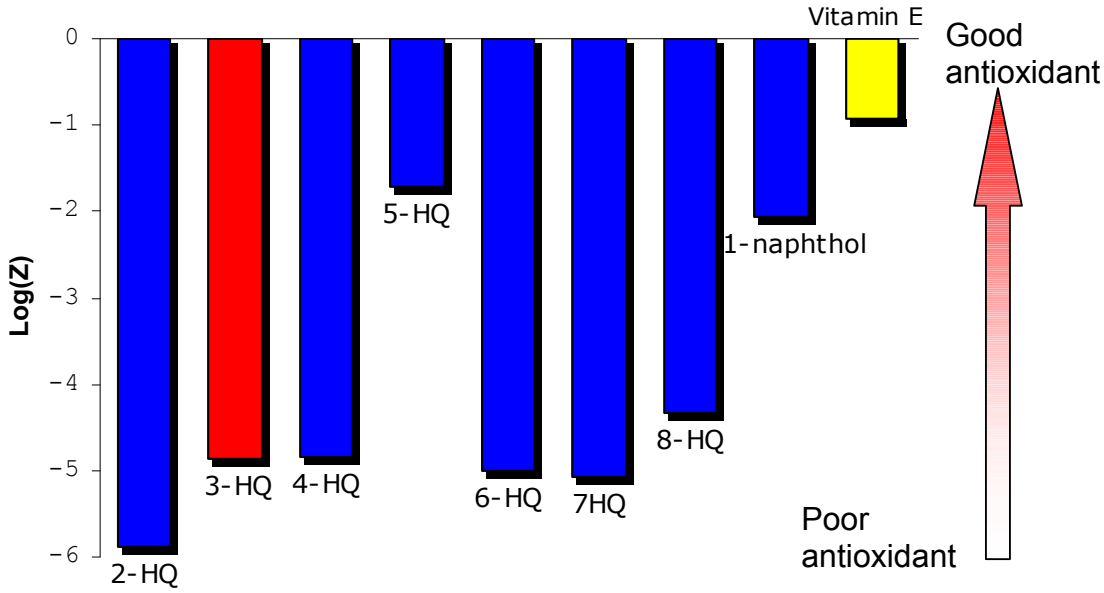

Figure 1.11a – Histogram of Log(Z) values of the x-HQ series. Note the unique activity of 5-HQ compared to the other HQ derivatives. Vitamin E has been included as a benchmark for relative activity and 3-HQ activity has been predicted from the BDE calculations.

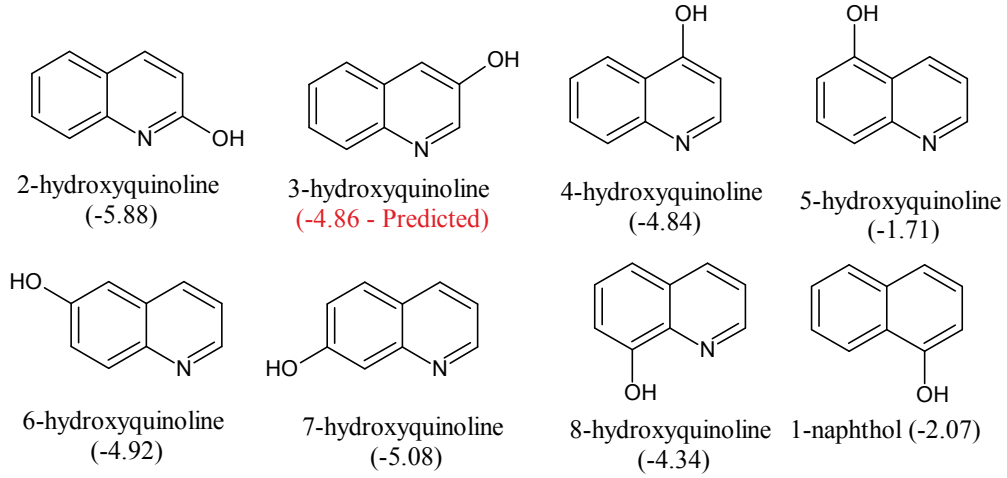

Figure 1.11b – The x-HQ series that was analysed for antioxidant activity, as well as the structure of 1-naphthol. Log(Z) values, as plotted in the histogram above, are in brackets

3-HQ was unable to be obtained due to a lack of availability from commercial sources, however, the BDE for 3-HQ has been calculated to be 86.13 kcal/mol. By interpolation of Fig. 1.8, we would expect a Log(Z) value for 3-HQ of approximately -4.86.

1.3.4.2 The 1-naphthol analogues

To further investigate the unique antioxidant ability of 5-HQ, a subset of the x-HQ series was used. This subset of compounds uses 1-naphthol as a starting point, and probes the addition of a heterocyclic nitrogen atom into the naphthalene scaffold as a function of position. Therefore, the molecules examined here are 1-naphthol, 4-HQ, 5-HQ and 8-HQ. As can be seen from the structures below, (Fig. 1.12) all molecules are similar in structure, with the location of the heterocyclic nitrogen, relative to the hydroxyl, being the only difference.

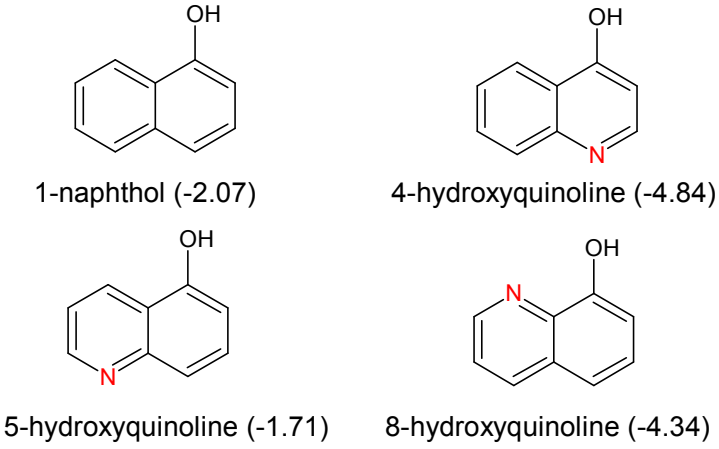

Figure 1.12 – Investigative set of 1-naphthol analogues. Note the position of the heterocyclic nitrogen (red). Relative Log(Z) values are in brackets.

The important aspects of this data set are (1) the large retardation in activity of 4-HQ and 8-HQ when compared to 1-naphthol, and (2) a slight increase in activity of 5-HQ when compared to 1-naphthol. These differences were thought to be electronic in nature, and so the electronic environment of all four compounds was probed, using the optimised structures that were produced as part of the BDE calculations.

An analysis using several descriptors of the electronic environment of these compounds failed to illuminate the unique activity of 5-HQ compared to the rest of the x-HQ series. Standard descriptors such as E(HOMO), E(LUMO) and the polarity of the O-H and C-O bonds of the hydroxyl group of these compounds were tried, and were subsequently unsuccessful, in elucidating the source of the enhanced 5-HQ activity.

Given that the molecules of interest here are built upon a naphthalene scaffold, they contain two fused aromatic rings. This allows for an effective diffusion of charge across the molecule. From the comparison of Log(Z) values for these four compounds, it appears as though the location of the heterocyclic nitrogen atom is of vital importance.

This is demonstrated in the comparison between 4-HQ and 5-HQ. In both molecules, the endocyclic nitrogen is on the opposite side of the molecule to the OH group. The only structural difference between 4-HQ and 5-HQ is that, in 4-HQ, the nitrogen is located on the same ring as the hydroxyl; in 5-HQ, the nitrogen is on the other ring. This reasoning became the basis of the development of a novel descriptor, which evaluates the polarity of each ring in a fused aromatic ring system. This descriptor, of which no previous evidence can be found, involves the summation of the electrostatic potentials of the atoms on the ring containing the hydroxyl group. An example is shown in Fig. 1.13.

When the electrostatic charge of the ring with the hydroxyl group is examined for 4-HQ, 5-HQ and 1-naphthol, values of -0.279, -0.147 and -0.141 are obtained, which was suggestive of discrimination. In order to determine whether the relationship between this descriptor and antioxidant activity existed for the entire x-HQ series, these values were calculated and plotted against Log(Z), Fig 1.14.

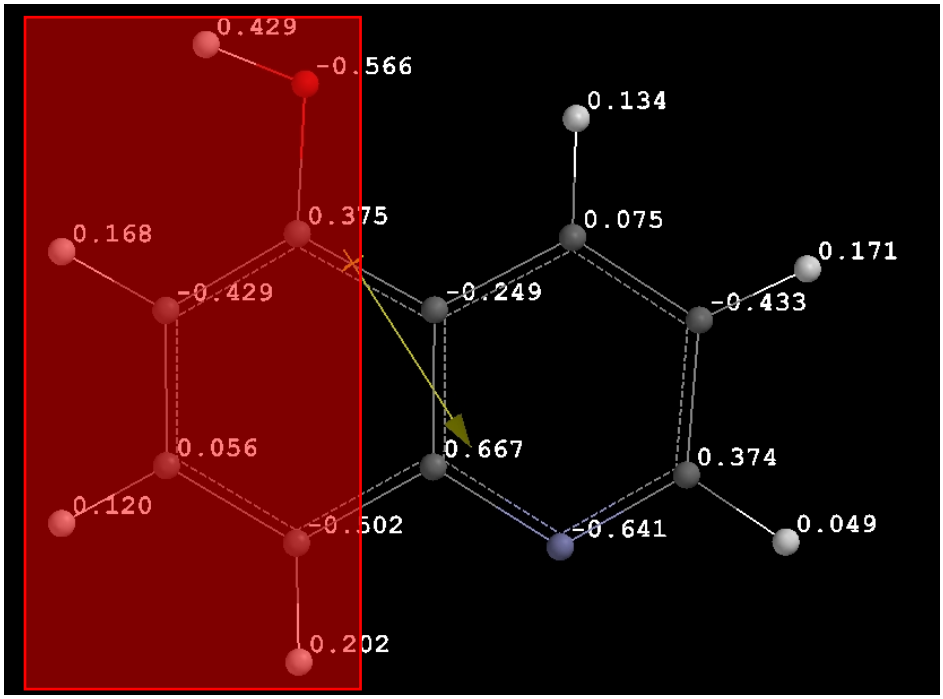

Figure 1.13 – Example of the separation of charges into electrostatic charges of the ring with the hydroxyl (Red). The charges on the atoms that straddle the rings are not involved in the calculation of this descriptor. The charges of the hydrogen atoms are included.

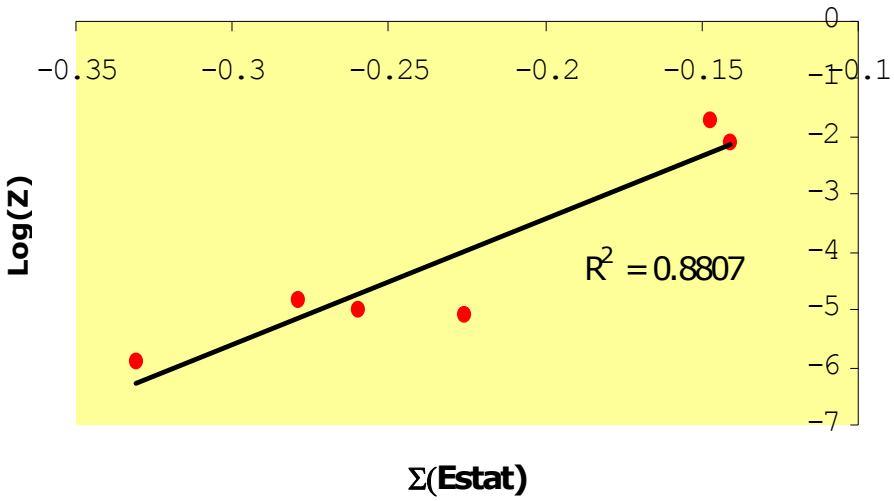

Figure 1.14 – Plot of electrostatic parameter against Log(Z). 8-HQ has been omitted due to the presence of the intramolecular hydrogen bond 'leaking' charge across the rings. 2-HQ as included due to the fact that the hydrogen bond in this compound is between atoms on the same ring.

As can be seen from Fig 1.14, a strong correlation was achieved between this descriptor and antioxidant ability, Log(Z). A rationalisation for this effect is that, with less electrostatic charge on the hydroxyl-containing aromatic ring, the

immediate environment contains a greater capacity to delocalise the lone electron produced following homolytic bond cleavage.

A possible alternative rationalisation, involving the withdrawal of electrostatic potential away from the oxygen, and as such weakening the O-H bond, is not valid here, as a difference in polarity of this bond did not show significant correlation with Log(Z), as mentioned previously.

1.3.5 Summary

BDE has been shown here to correlate strongly to a kinetic experimental measurement of antioxidant ability, Log(Z). BDE is most effective when the effects of intramolecular hydrogen bonding have been accounted for. The enhanced activity of 5-HQ, compared to the other members of the hydroxyquinoline series, was also examined; a novel descriptor was developed, and this illustrated that the enhancement is due to electronic effects present in the fused aromatic ring system.

Following from the investigations presented here, it would be expected that further work would possibly involve several streams. Firstly, to expand the number of compounds examined by both Log(Z) and BDE, involving different classes of compounds such as anthocyanins, flavonols and various other polyphenols of botanical origin, which are of current interest. Many of these natural compounds include intramolecular hydrogen bonding, and so this work could improve predictions of antioxidant ability from calculated BDE alone. Secondly, a fundamental study, experimentally and computationally, of the effects of the intermolecular hydrogen bonding by the solvent to the reagents could be carried out. Experimentally, by changing the solvent composition and/or temperature, the intramolecular hydrogen bonds - where formed - could be controlled to some degree. This could lead to either reduced or enhanced hydrogen bonding, depending on the specific circumstances. Computationally,

molecular dynamic simulations could be carried out to further characterise the nature of the intermolecular, and intramolecular, hydrogen bonding.

Chapter 2

ESI-MS and quantum chemical investigations of iron(III)–hydroxyquinoline species

2.1 INTRODUCTION

2.1.1 Neurodegenerative disease

Age-related neurodegenerative disorders are an emerging health challenge in many developed countries[102, 103]. These disorders are devastating for sufferers and their families due to their insidious and intractable nature[104]. Of the various diseases associated with neurodegeneration, considerable attention has been directed towards Alzheimer's disease (AD) and Parkinson's disease (PD), especially with respect to the potential role of metals in these conditions[a].

AD is characterised by initial subtle memory loss, leading to progressive dementia, as well as a decline in language skills[102, 103, 105]. PD is characterised by the presence of a resting tremor, rigidity, bradykinesia (slowed ability to start or continue movements), and postural instability[106]. Whilst dementia is not always associated with PD, factors influencing the development of dementia in PD include advanced age at diagnosis and the duration of the disease[107].

Pathologically, AD is characterised as involving metallo-stabilized β-amyloid plaques and neurofibrillary tangles[108] throughout the cerebral cortex, initially appearing in the hippocampus[109]. PD is characterised by the selective loss of doparminergic neurons, the presence of Lewy bodies and, significantly, increased levels of iron within the substantia nigra (SN)[106, 110].

At present, few treatment options are available to sufferers, and those that are available alleviate symptoms rather than address the pathophysiological processes.

[a] A SciFinder search displayed 86120 references for "Alzheimer's disease", 52934 references for "Parkinson's disease", 1893 references for "Alzheimer's disease and metals" and 890 references for "Alzheimer's disease and metals".

2.1.1.1 Current treatments for Alzheimer's disease and Parkinson's disease

Two classes of drugs are currently used for the treatment of AD. The most commonly used drug class involves increasing the levels of the neurotransmitter acetylcholinesterase (ACh) by inhibiting the enzyme that breaks down ACh in the neuronal synapses[111]. Recently, a new class of drug was authorised for use which acts by antagonising the glutamatergic system, which decreases the excitotoxicity related to AD[112-114]. Neither class of drug attempts to resolve the underlying cause of Alzheimer's, rather a reduction of symptoms is achieved through these treatments[113-116].

With PD, the outlook is slightly better, as several classes of drugs are used to treat the symptoms associated with the disorder, and these therapies can be used in conjunction for greater effect[111]. All classes of drugs focus on increasing the levels of dopamine in the brain, as these levels are greatly reduced in PD. Fig. 2.1 is a schematic indicating the classes of drug treatments and their effect on the dopamine system.

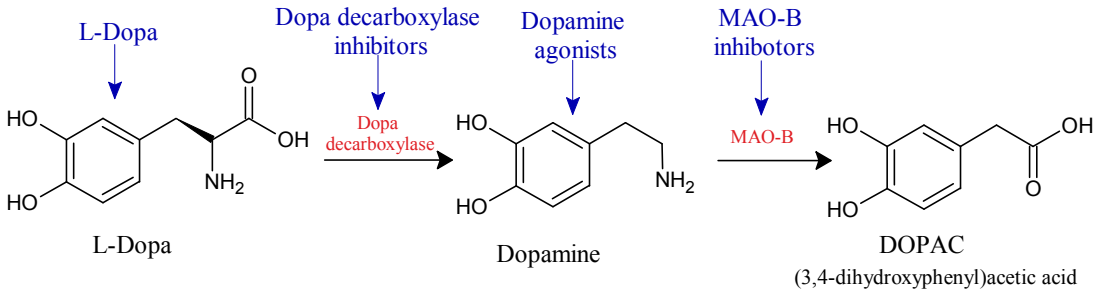

Figure 2.1 – Schematic of the dopamine pathway that is the focus of current PD drugs. Enzymes are in red and drug classes are in blue, with an arrow indicating the target for each class.

L-Dopa. Dopamine in its active form is unable to cross the Blood-Brain Barrier (BBB) and is also a systemic neurotransmitter. Therefore, one method of increasing dopamine levels in the brain is to increase the levels of the precursor, l-dopa. This treatment is generally inefficient, as much of the administered l-dopa

is converted to dopamine before reaching the brain, and has many and varied side effects associated with its use.

Dopa decarboxylase inhibitors. This class of drugs are generally used in combination with l-dopa to reduce the systemic conversion of l-dopa to dopamine, therefore increasing the amount of l-dopa available to the brain. However, the side effects of this approach can be more severe than administering l-dopa alone.

Dopamine agonists. Compounds in this class of treatment bind directly to the dopamine receptors, by-passing the need to produce increased amounts of dopamine. However, this approach leads to a decrease in the sensitivity of the dopamine receptors, effectively increasing the onset of symptoms after prolonged use.

MAO-B inhibitors. These drugs act in a similar way to the AD drugs outlined previously, as the breakdown of dopamine in the neuronal synapses are inhibited. However, this treatment can lead to insomnia, amongst other side effects.

While the treatments briefly discussed here for AD and PD may be able to treat the symptoms of these diseases, there is currently no cure for either disease. An important area of on-going research is the search to find new therapeutic targets that may stop the neurological damage associated with these diseases.

2.1.2 New therapeutic targets

Given that an absolute cause of these diseases has eluded researchers for some time, a definite receptor for therapeutics has been missing. However, in both AD and PD, physical artefacts associated with localized neuronal damage, namely the plaques that form in the brains of AD sufferers[108, 109] and the iron

deposits in the substantia nigra of PD sufferers[106, 110], can be targeted. The history of research into targeting the metal imbalances in both of these diseases is explored as follows.

2.1.2.1 Alzheimer's disease

Focussing on the distinctive β-amyloid plaques of AD pathophysiology, two important initial discoveries were made which indicated that these plaques might be useful therapeutic targets. Firstly, that the plaques themselves are neurotoxic, meaning they destroy local neurons[117]. Secondly, a zinc ion imbalance in the plaques was detected[118].

Subsequently, Zn^{2+} ions were found to stabilise a non-soluble conformation of a normally soluble protein, known as amyloid[118]. Further work indicated that in the neurological regions affected by these plaques, the overall Zn concentration was higher than normal[119], suggesting a possible cause was abnormal metal ion homeostasis, rather than protein over-expression or protein folding problems, as had been previously postulated[119].

With the discovery of increased Zn levels, the effect of other biometals on the precipitation of amyloid protein was also examined. Cu and Fe ions were also found to be present, in higher than normal concentrations, in the areas where these plaques form, and were subsequently found in post-mortem plaques[109, 120]. An attomolar-affinity copper binding site was located on the amyloid protein, separately from the zinc binding site[121]. A possible iron binding site was also located in the mutated region of amyloid precursor protein (APP) mRNA as found in familial AD. This region includes an iron regulatory element (IRE)-like sequence similar to that found in ferritin, an iron regulation protein[109].

With these metal ions as targets, *in vitro* studies probing the effects of treating these plaques with metal ion chelators, to determine if the plaque-

forming precipitation could be reversed, were carried out[122]. This work found that the post-mortem plaques could be solubilized *in vitro* by removing those ions implicated in the precipitation of amyloid, as long as the chelator used did not remove Mg^{2+} or Ca^{2+}, which seem to stabilise the soluble protein conformation[122]. The chelators selected for study were well studied hydrophilic copper and zinc chelators[122].

An *in vivo* study by Cherny *et al* involving a transgenic mouse model of AD was carried out to probe this solubilization. A known drug, Clioquinol (5-chloro-7-iodo-8-hydroxyquinoline, CQ), was used in this study, as this compound was a known chelator, via the 8-hydroxyquinoline scaffold, with a known toxicology profile. The results of this initial study showed a 49% decrease in amyloid plaque mass against the controls in post-mortem analysis of the mice models after just nine weeks of treatment. No adverse reactions or systemic depletion of any metal ions were recorded[123]. CQ was further shown to decrease the production of damaging reactive oxygen species (ROS)[124].

A pilot phase 2 clinical trial of CQ was proposed to study a small group of patients with moderately severe Alzheimer's disease[125], given the success of the mouse model experiments. For this trial, however, the shady history of CQ needed to be re-examined, especially with respect to why it was withdrawn from the marketplace in the 1970's.

CQ chelates were thought to be the causative agents in an unusual condition affecting the central nervous system[126]. The condition, known as Subacute Myelo-Optic Neuropathy (SMON), affected 10,000 Japanese patients taking CQ as either an antiparasitic, or to increase absorption of intestinal zinc in a genetic disorder known as acrodermatitis enteropathica[126]. Epidemiological studies tentatively linked CQ with the prevalence of SMON, which is characterised initially by abdominal pain and/or diarrhoea, leading to sensory and motor disturbances and occasionally progresses to blindness[127]. Another study

suggested that an iron-CQ chelate was to blame, as this green-coloured chelate was found in the tongue and urine of suspected SMON sufferers[128].

However, another interpretation of the SMON symptoms was that an accelerated, subacute vitamin B_{12} deficiency was produced, given that this vitamin contains a cobalt(II) ion[123]. At the time of the SMON outbreak in post-war Japan, residents of other countries were consuming greater quantities per capita of CQ, yet only 220 cases were recorded outside of Japan. It was suggested that this was due to a general vitamin deficiency in the population at this time. As a precaution, all patients in the double blind pilot phase 2 trial received vitamin B_{12} supplementation[123]. No adverse systemic, neurological, or cognitive effects were recorded during this phase 2 trial, suggesting that the ingestion of CQ as an AD treatment over a short-term period is safe when used with vitamin B_{12} supplementation[123].

Another finding of the phase 2 trial was the confirmation of the hypothesis that oral CQ would improve the moderately severe symptoms of the patients in the trial. The cognitive test used was the Alzheimer's disease Assessment Scale (ADAS-cog score)[125]. Blood samples were also taken from the patients during the trial, with various parameters tested for, such as plasma levels of amyloid, copper and zinc[125].

Even with such a small sample size (32 patients in total with significant data), a cognitive improvement was seen in the CQ group, compared to the placebo, but only for the more severely affected patients[125]. The patients with less severe symptoms showed no statistically significantly improvement. Blood tests also showed that the therapeutic effect was not due to systemic chelation, as metal levels in the blood increased, suggesting that metal ions were being mobilised from the brain. These blood test results, coupled with the reduced cognitive decline, suggests that CQ does have a positive effect in human AD

patients, providing a proof of concept for metal ion chelation as a viable treatment option for this disease[125].

With regard to the safety of CQ in this phase 2 trial, one of the patients in the CQ group developed impaired visual acuity and colour vision between weeks 31 and 36 of the trial[125]. The patient had a history of visual migraines and glaucoma, and the visual impairment symptoms were resolved on CQ treatment cessation[125]. No other patients recorded symptoms related to their CQ treatment.

Hence, a new class of drug compounds was born, with the evidence that CQ and CQ-like metal chelators could be beneficial in neuroprotection. Due to their suspected mode of action, these compounds were to become known as metal-protein-attenuating compounds (MPAC)[125].

With the evidence of the proof of concept provided by the pilot phase 2 clinical trial, the use of MPAC-type drugs for other neurodegenerative diseases was explored. In fact, no less than 19 neurological disorders or afflictions have been associated with abnormal levels of these transition metal ions[129]. One such neurodegenerative disorder which implicates metal ions, specifically Fe, is Parkinson's disease[110, 129-131].

2.1.2.2 Parkinson's disease

An abnormal iron accumulation is known to occur in the substantia nigra in the brain, which is the site of doparminergic neuron loss in PD etiology[110, 132-140]. Whether such iron accumulation is of consequence, or is causative, is subject to some debate[47, 109, 110, 141]. There certainly seems to be a systemic Fe and Zn homeostasis issue, as both metal ions have been shown to be elevated in the blood of PD patients[131].

Only one trial, to this point, seems to have tested the theory that MPAC treatment can relieve Parkinsonism, using in a mouse model[110]. This trial was constructed to determine if iron accumulation was causally linked to cellular degeneration[110]. The compound 1-methyl-4-phenyl-1,2,3,6-tetrapyridine (MPTP) was fed to the mice[110]. This compound induces Parkinson's disease in the subject, so that various treatments can be studied in a controlled setting.

The treatments examined using this mouse model involved either the transgenic expression of the human version of ferritin, an iron binding protein, or the administration of CQ for 8 weeks before treatment with MPTP, to assess neuroprotective ability[110]. The findings of this study show that there was a protective effect, with considerable decreases in MPTP toxicity, loss of dopamine, loss of glutathione, neuronal death and motor dysfunction when compared to control mice[110, 129]. The conclusions from this study were that CQ can remove excess iron from the brain without apparent interference to the normal function of the nervous system[110].

To date, AD and PD are the only neurodegenerative disorders to have been clinically studied using metal chelators, even though up to 19 neurological disorders may be pathologically attributed to metal ion imbalances[129]. As research into biochelators progresses, more clinical studies are expected into a range of neurological afflictions.

Recent work with MPAC's has attempted to increase the efficacy of these compounds. As mentioned earlier, one of the ways that metal ions are implicated in neurodegenerative diseases is by generating ROS[142, 143], and treatment with antioxidants have yielded positive results in AD trials[144]. It would be expected that analogous treatment in PD patients would yield similar results, especially given the prevalence of redox-active iron species in the SN. One theoretical study has previously attempted to combine both metal chelation properties with antioxidant ability[145].

Using purely computational methods to evaluate various compounds, loosely based on the superoxide dismutase (SOD) binding moiety, an attempt was made to design a compound with both metal chelation and radical scavenging abilities[145]. The aim of the study was to show that one or some of these chelates could act as Cu^{2+}(or Zn^{2+} in some cases)-based SOD mimics, with several descriptors calculated[145]. Each chelate was examined for Binding Energy (BE) and Electron Affinity (EA)[145]. The BE was used to show that the chelate was stable in that configuration, and to give a quantitative measure as to how strong the metal binding is[145]. The EA was calculated to describe the possible radical scavenging, or SOD activity, of the chelate[145]. These values were compared to those calculated for the active SOD site of the enzyme[145]. Both Zn^{2+} and Cu^{2+} chelates of CQ were used in this study, as well as various other known chelators[145].

The results of this study suggested that none of the chelators studied were as effective as SOD in binding metal ions or scavenging radicals; however, some were certainly better than others[145]. CQ chelates faired quite well with respect to theoretical metal ion sequestering, but faired quite poorly with respect to EA[145]. Two of the compounds studied, both based on the same moiety, faired the best, with high BE's and EA's similar to SOD[145]. These compounds were 1-BYT and 1,4-BYT (Figure 2.2). This study gives an alternative method of developing effective, neurologically protective compounds. However, the activity of these compounds *in vitro* or *in vivo* has not been shown; these results are purely theoretical[145]. Indeed, an effective metal-scavenging SOD-mimic may have uses therapeutically in familial amyotrophic lateral sclerosis (FALS) in which defective SOD mutants have been directly implicated in the specific etiology[146].

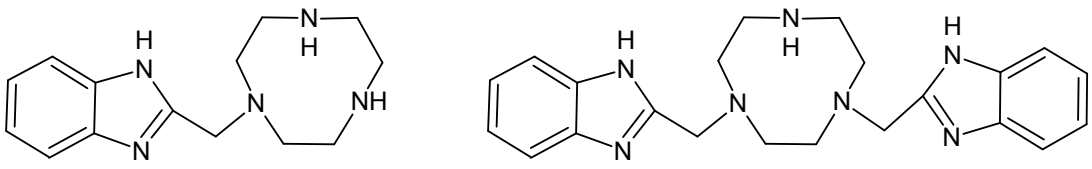

Figure 2.2 – Structures of 1-BYT (L) and 1,4-BYT (R), theoretical SOD mimics.

2.1.3 Basis of this work

The work presented in this chapter follows on from tantalising hints obtained previously within the Orbell group. This work found possible traces of a radical cation, of identity $[Fe(CQ)_3]^{+\bullet}$ [147]. However, at the time, the mass spectrometer being used did not have the resolution or accuracy required to confirm the appearance of a radical species. This was due to the fact that the ESI-MS being used by previous workers was seemingly accurate to approximately 0.4 m/z, therefore the possible 'evidence' for a radical cation was a deviation from 'ideal m/z' (that is, the calculated mass ratio expected calculated from the formula) of 0.6 m/z. This was unsatisfactory at the time, with further characterisation following acquisition of a newer instrument.

Given the apparent role of iron in both AD and PD and the possible therapeutic effects of hydroxyquinoline derivatives in both conditions, it was decided that a detailed ESI-MS investigation of the possible species formed between iron(III) and three 8-hydroxyquinoline based compounds: 8-hydroxyquinoline (HQ), 5,7-dichloro-8-hydroxyquinoline (DCHQ) and 5-chloro-7-iodo-8-hydroxyquinoline (CQ), Fig. 2.3, could provide useful information on how such ligand scaffolds might sequester iron(III) and what species are of significance.

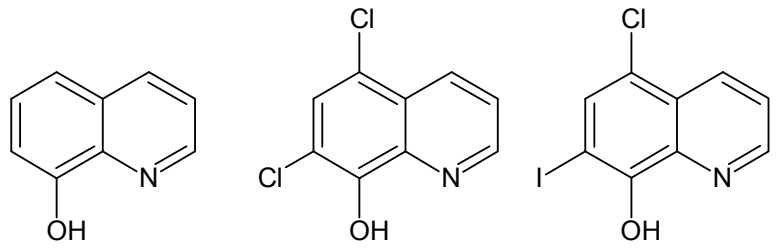

Figure 2.3 – Structures of the ligands used, namely (L-R) 8-HQ, DCHQ and CQ.

These experiments have been designed to explore the effect of varying the iron:ligand mole ratio from a deficiency to an excess of iron. The species of interest have been fully characterized by molecular modelling using semi-

empirical and ab initio quantum chemical methods and attempts have been made to relate the results to a possible mode of action for drugs of this type.

2.2 METHODS

2.2.1 Chemicals and equipment

High purity (99.8%) $[Fe(NO_3)_3]$**.**$9H_2O$ was sourced from Aldrich. AR grade 8-HQ, DCHQ and CQ were sourced from BDH and Sigma-Aldrich. Methanol was supplied by BDH. MilliQ deionized water was prepared on site as required. Samples were analysed using a Finnegan LCQ Deca XP MAX ESI-MS.

2.2.2 ESI-MS methodology

2.2.2.1 Preparation of solutions for ESI-MS

In order to investigate the speciation of Fe^{3+} with 8-HQ, CQ and DCHQ (Fig. 2.3) in a systematic way, which takes into account the effect of varying the ligand to iron mole ratio, a series of solutions were prepared as follows:

A 100 mL aqueous stock solution of 100 μM $[Fe(NO_3)_3]$**.**$9H_2O$ and 100 mL stock solutions of each ligand was prepared, in methanol, at concentrations of 400 μM.

By combining appropriate aliquots of the above stock solutions, a range of solutions of varying mole ratios were produced, whereby the Fe(III) concentration remains constant and the amount of ligand varies. Thus, ligand-to-metal mole ratios ranging from 0.1 to 4 were produced, Table 2.1.

Table 2.1 – Method used to produce various ratios of reactants to study the formation of Fe complexes of 8-HQ, CQ and DCHQ.

Mole Ratio (Ligand:Fe)	Volume of ligand (*x* mL)	Volume of methanol (*y* mL)	Volume of Fe (mL)
0.1	0.1	3.9	4
0.5	0.5	3.5	4
1	1	3	4
1.5	1.5	2.5	4
2	2	2	4
2.5[a]	2.5	1.5	4
3	3	1	4
3.5[a]	3.5	0.5	4
4	4	0	4

[a] These ratios were prepared and analysed for CQ only.

Note that an appropriate volume of methanol is added to the methanolic ligand solution to achieve a volume of 4 mL in each case. To this is added, with gentle stirring, 4 mL of the aqueous iron solution. This procedure ensures that each reaction mixture has a 50/50 methanol/water solvent mixture and, due to the metal being added to the ligand, encourages 3:1 ligand:metal complex formation. All solutions are left to incubate for *at least* 15 minutes. Samples were then directly infused into the ESI-MS.

2.2.2.2 ESI-MS analysis method

Each solution, prepared as described in Table 2.1, was directly infused into the mass spectrometer, via electrospray ionization, using a flow rate of 13 μL/min. Typical ESI source conditions used were: spray voltage of approximately 5kV, a capillary temperature of 275.4^{o}C, nitrogen sheath pressure of 10-30 (arbitrary units). The capillary voltage and tube lens offset were tuned, the values of which were 26.2V and 40.0V respectively.

The spectra for each molar ratio solution were recorded, with an m/z range of 150-1000 m/z. Each peak in these spectra were analysed for the appropriate

isotopic fingerprint, as represented for one species type, in Fig. 2.4. Those peaks with matching fingerprints were then identified according to the m/z values.

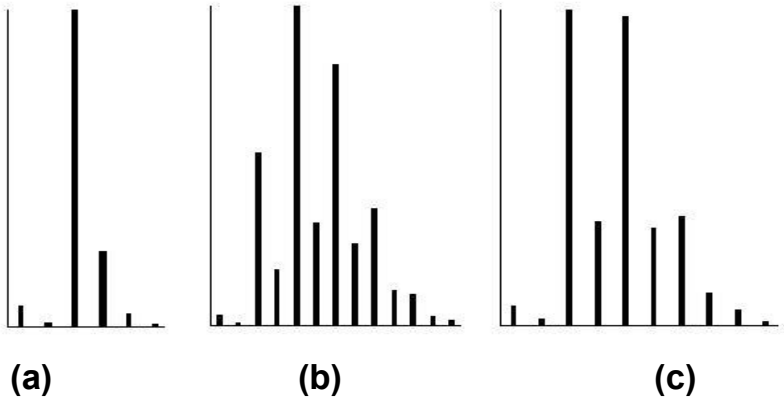

Figure 2.4 – The isotopic fingerprints expected for the $[Fe(L)_2(L\text{-}OH)]^+$ species, where L = (a) 8-HQ (b) DCHQ and (c) CQ

2.2.3 Computational methodology

Preliminary geometry optimisations on all relevant species were performed under the PM3 semi-empirical method, as utilised in Spartan '06[98]. Where appropriate, prior conformer searching, using molecular mechanics with the MMFF parameter set also within Spartan '06, was carried out to ensure that global minima optimisation was achieved.

PM3 and RM1 calculations were utilized to examine the steric influences of the addition of a third ligand (L = 8-HQ, DCHQ or CQ) into the coordination sphere of iron(III). Thus RM1 equilibrium geometry calculations were carried out for the free ligands (L), and PM3 equilibrium geometry calculations were carried out for the $2{:}1^+$ complex ($[Fe(L)_2]^+$) and the $3{:}1H^+$ complex ($[Fe(L)_2(L\text{-}OH)]^+$)[b]. The binding energy of the third ligand (BE_3) was estimated as follows:

$$BE_3 = E_{3:1H}{}^+ - (E_{2:1}{}^+ + E_L) \qquad \textbf{(2.1)}$$

[b] $[Fe(L)_2(L\text{-}OH)]^+$ is referred to in the text as a "protonated" species, although it might be more appropriately described as an "un-deprotonated" species.

The E values are the calculated energies of formation for the respective species. The nature of this "estimation", in terms of ignoring the effects of electron correlation in these calculations, is discussed later.

PM3 equilibrium geometries were calculated for all the relevant 2:1 and 3:1 species between Fe^{3+} and the ligands 8-HQ, DCHQ and CQ. This includes the $[Fe(L)_2(L\text{-}OH)]^+$ (protonated 3:1 cation) and the $[Fe(L)_3]^{+\bullet}$ (hydrogen-abstracted 3:1 radical cation) species[c]. Spin density maps were also calculated under PM3 for the latter species. Scalar relativistic effects due to the heavier elements iron and iodine are assumed to be accommodated under PM3.

As discussed elsewhere in this thesis, the discovery of the [Fe(III)(DCHQ or $CQ)_3]^{+\bullet}$ radical cations in the ESI-MS spectra has important implications for the mechanism of action of hydroxyquinoline derivatives towards neurodegenerative diseases such as Parkinson's disease. Therefore, it is essential to fully characterize such species computationally. Given that such species are likely to be formed from the abstraction of the hydrogen atom of the exocyclic O-H moiety of the third ligand in the "protonated" species $[Fe(L)_2(L\text{-}OH)]^+$, it is desirable to demonstrate with some confidence that the O-H bond in such species is weakened with respect to homolytic cleavage compared to the free ligands. Therefore, high level *ab initio* quantum chemical calculations have been assigned to this task.

Consequently, geometry optimisation calculations have been carried out on all relevant Fe-containing species using Density Functional Theory (DFT) methodology[d]. The B3LYP hybrid functional was used in conjunction with the SDD basis set as implemented by Gaussian '03[148]. The resulting structures were then subjected to single point energy calculations using the post-Hartree-Fock

[c] $[Fe(L)_3]^{+\bullet}$ could also be written as $[Fe(L)_2(L\text{-}O)]^{+\bullet}$ or $[Fe(L)_2(L\text{-}O^{\bullet})]^+$. $[Fe(L)_3]^{+\bullet}$ was chosen since the modelling suggests that the $-O^{\bullet}$ is consolidated into the coordination sphere and subsequently delocalised over the whole complex.

[d] All Gaussian 03 calculations were carried out in conjunction with a collaborator, Dr. David Wilson, of La Trobe University, Melbourne, using the APAC National Supercomputer Facility at ANU.

method MP2, again with the SDD basis set. This basis set was selected as it employs a double-zeta treatment to the valence shell, so is not an overly expensive basis set in terms of computational cost, and it includes the addition of relativistic effects to the heavier atoms, Fe and I. From these single-point energies, the homolytic BDE's were calculated, equation 2.2.

$$BDE = (E_{3:1}^{\cdot +} + E_{H}^{\cdot}) - E_{3:1H}^{+} \quad \textbf{(2.2)}$$

For comparison purposes, the homolytic BDE's of the free ligands themselves were also calculated, to determine the effects of Fe-N-coordination of the third ligand on the O-H bond. The equilibrium geometries of these ligands were calculated using the same method as the Fe-species, DFT/B3LYP/SDD. Again, single-point energies were also calculated, at both MP2/SDD as well as using a coupled-cluster method, CCSD, again with the SDD basis set. The O-H homolytic bond dissociation energies for the free ligand and for the N-coordinated third ligand are calculated as per equation 2.3:

$$BDE = (E_{ArO}^{\cdot} + E_{H}^{\cdot}) - E_{ArOH} \quad \textbf{(2.3)}$$

2.3 RESULTS AND DISCUSSION

2.3.1 ESI-MS Investigations

With respect to all spectra collected as part of these investigations, a mass-to-charge ratio (m/z) range of 150-1000 m/z units was used. The instrument set this lower limit, given that the upper mass cut-off needed to be 1000 m/z, due to the large mass-to-charge ratios of the singly cationic complexes of general type $[Fe(L_3)]^+$. Due to this inability to detect species below 150 m/z, aquated Fe^{3+} cations, such as $[Fe(OH_2)_6]^{3+}$ (m/z = 55.34) and $[Fe(OH_2)_5(OH)]^{2+}$ (m/z = 82.00)

are undetectable. Whilst the detection of such species may be possible with further analyses utilising a reduced m/z range, such speciation was not of major concern in this work; the speciation of Fe^{3+} with selected 8-hydroxyquinoline based ligands was the major focus.

2.3.1.1 8-hydroxyquinoline

For the complexation of Fe^{3+} by 8-HQ, a *representative* spectrum, demonstrating the isotopic signatures and accuracy of the m/z values for the key peaks identified, is shown in Fig. 2.5. The collection of 8-HQ-Fe spectra over the whole range of 8-HQ-Fe mole ratios (R = 0.1 to 4) is displayed in Appendix I. For all seven of these spectra, the relative abundances of the major species are given in Table 2.2.

Five 8-HQ species have been identified as being present in each of the above spectra, albeit in different relative abundances. These are: the protonated free ligand (LH^+), the methanol adduct of $[Fe^{II}(8\text{-HQ})]^+$ (i.e. 1:1 – MeOH), $[Fe(8\text{-HQ})_2]^+$ (i.e. $2:1^+$), the methanol adduct of $[Fe(8\text{-HQ})_2]^+$ (i.e. $2:1^+$- MeOH) and the protonated 3:1 complex $[Fe(8\text{-HQ})_2(8\text{-HQ-OH})]^+$ (i.e. $3:1H^+$). It can be seen that, in a hydrophilic environment across a wide range of mole ratios, the 8-HQ ligand shows a strong propensity to complex with Fe^{3+}.

With respect to the 1:1 and 2:1 complexes, where 8-HQ-based ligands do not occupy all 6 coordination sites of the Fe^{3+}, it is assumed that solvent molecules, (such as methanol or water), or ionic species in solution, (such as hydroxyl (OH^-) ions) would weakly occupy these sites in solution. In the gas-phase, however, there is a total lack of detectable *aqua*-containing complexes in all spectra. With such comprehensive discrimination against *aqua* as a gas-phase ligand, the conclusion that must be drawn is that any weakly coordinating water molecules must be lost as a consequence of the ionisation process.

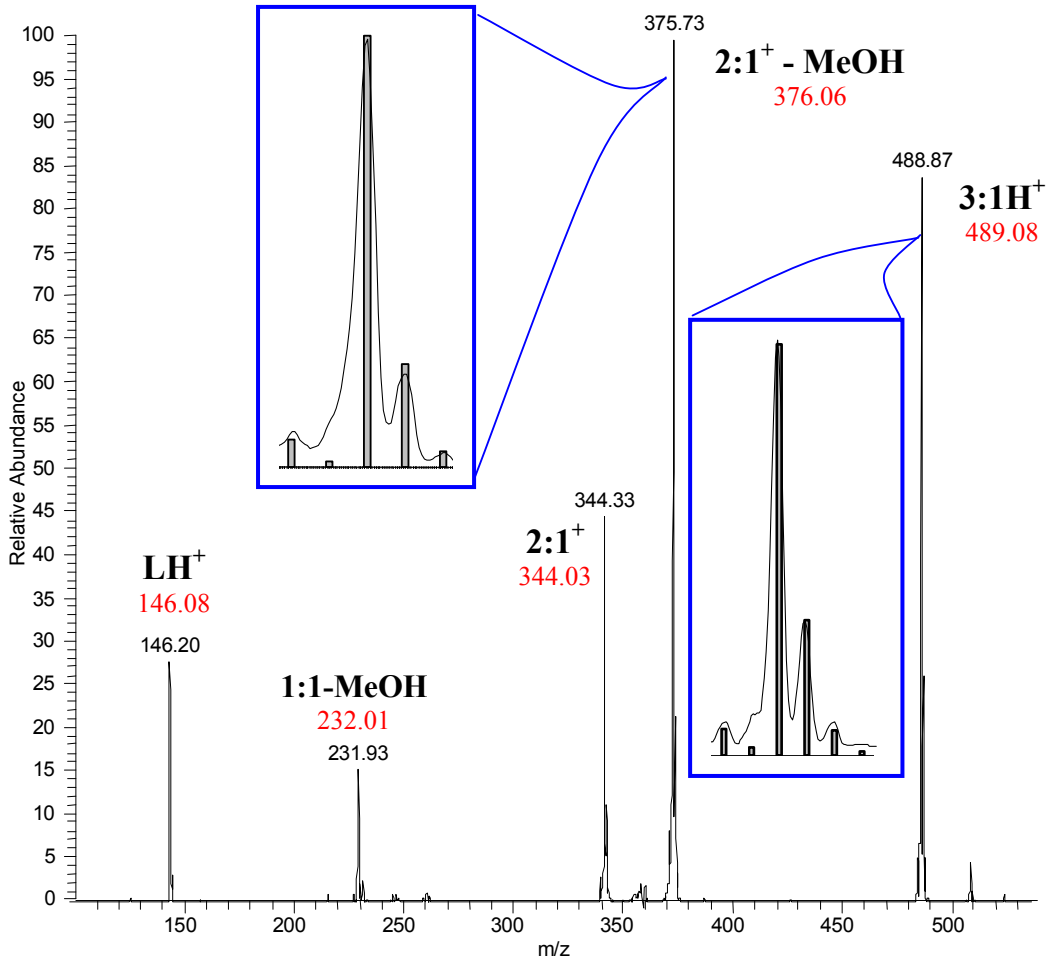

Figure 2.5 – The spectrum obtained for 8-HQ at a representative ligand:Fe mole ratio of 4:1. The speciation of the 8-HQ-Fe containing peaks is indicated in bold type and the theoretical m/z in red. Insets are magnifications for the 2:1-MeOH species and the $3{:}1H^+$ species, with the theoretical isotopic distribution overlayed.

Table 2.2 – Relative abundances for all Fe-containing 8-HQ species, and protonated free ligand, for ESI-MS spectra obtained at different mole ratios R (8-HQ:Fe).

R	LH^+	1:1 (Fe^{II})	2:1	2:1-MeOH	3:1
0.1	11	26	17	100	7
0.5	5.5	16.5	23	100	11.5
1	1	16	31.5	100	27
1.5	22	18	37.5	100	53
2	20.5	15.5	34	100	56
3	27	16	44	100	85
4	28	15.5	45	100	84

It is informative to consider the change in the relative abundance of the 3:1 complex compared to that of the 2:1 species as the 8-HQ:Fe ratio changes, Fig. 2.6. This plot shows a near-linear increase in the ratio of the 3:1 complex

compared to 2:1 species on going from R = 0.1 to 3, with a plateau becoming evident around R = 3. This is not unexpected, as an increase in ligand concentration would encourage more 3:1 complexation.

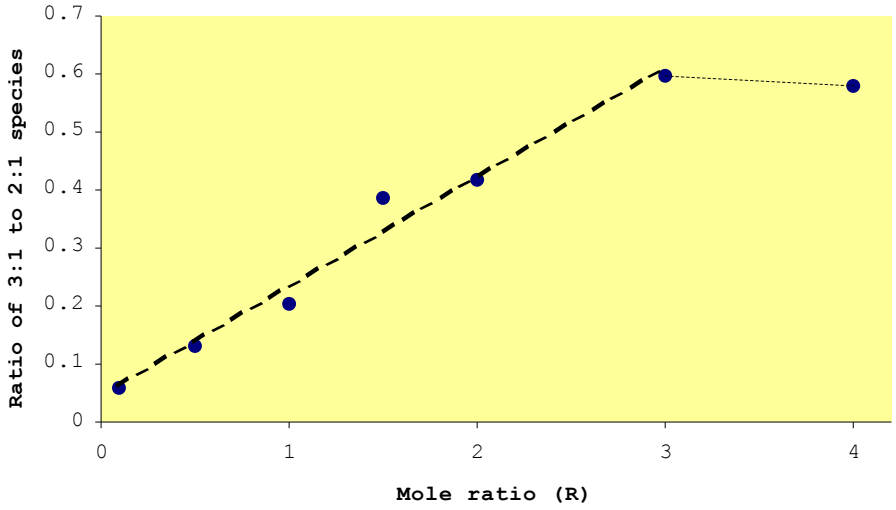

Figure 2.6 – Plot of ratio of relative abundances of 3:1 species to 2:1 species for 8-HQ across the range of HQ:Fe mole ratios (R). The dashed line highlights the ascending portion of the graph, and the dotted line indicates a plateau.

Therefore, given that these spectra were produced at a relatively low cone voltage of 40 volts, and given that it has been previously demonstrated that a speciation distribution in solution can be represented with some fidelity in the ESI spectrum (certainly at lower energies)[149], an equilibrium between the species observed in Fig. 2.5, might be expected to exist in solution. In this regard, the identification of methanol adducts in all spectra is also of relevance, since this interaction is expected to be quite delicate, yet the ionization process is "soft" enough to allow it to persist.

This equilibrium, in solution, could be represented as:

$$[Fe(OH_2)_6]^{3+} + \text{8-HQ} \rightleftharpoons [Fe(\text{8-HQ})(OH_2)_4]^{2+}$$

$$[Fe(\text{8-HQ})(OH_2)_4]^{2+} + \text{8-HQ} \rightleftharpoons [Fe(\text{8-HQ})_2(OH_2)_2]^{+}$$

$$[Fe(\text{8-HQ})_2(OH_2)_2]^{+} + \text{8-HQ} \rightleftharpoons [Fe(\text{8-HQ})_3H]^{+}$$

Figure 2.7 – Aqueous solution equilibrium scheme proposed for all identified 8-HQ-Fe species from the ESI-MS results.

Whilst a 1:1 Fe-HQ complex is identified in all spectra at all mole ratios, the oxidation state of the Fe in this complex is consistent with ferrous, rather than ferric, i.e. $[Fe(HQ)]^{+}$. This suggests that some reduction of the ferric reagent has occurred. Whether this represents an impurity in the reagent, or whether reduction occurs as part of the coordination chemistry or as an artefact of the ESI-MS process, is unclear. Notably, a 1:1 ferric-HQ complex, $[Fe(HQ)]^{2+}$ $(-H^{+})$ cannot be detected in the ESI spectra. Possibly, such a complex is only fleeting and is rapidly reduced, either in solution or in the instrument. From Table 2.2 it can be seen that the abundance of the ferrous species is highest at the highest mole ratio of Fe:ligand (R = 0.1). Interestingly, this is the mole ratio where 3:1 Fe(III) radical cations involving the ligands DCHQ and CQ have been detected – this will be discussed later in this Chapter. In this regard, a large excess of ferric ions could be associated with enhanced redox activity.

As alluded to previously, from the data presented in Table 2.2, there is obviously a significant equilibrium implied between 2:1 and 3:1 species, even in the presence of a large excess of Fe^{3+}. This, perhaps, reflects a relative hindrance to the entry of the third ligand. In this regard, it is worth noting that the protonated 3:1 species does not have a consolidation of N/O bidentate coordination. There are, in fact, two possibilities for the structure of the 3:1 protonated cation, both of which have the same m/z values. These are depicted in Fig. 2.8.

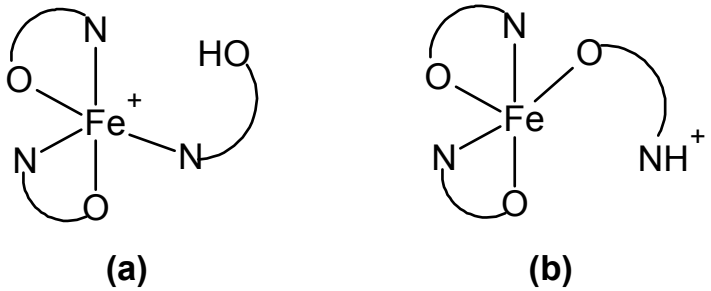

Figure 2.8 – Two possible schemes for the protonated 3:1 8-HQ:Fe complex, i.e. $[Fe(8\text{-}HQ)_2(8\text{-}HQ\text{-}OH)]^{+}$ (i.e. $3{:}1H^{+}$), with the third ligand complexing through either (a) the endocyclic nitrogen (oxygen protonated) or (b) the oxygen of the hydroxy moiety (nitrogen protonated).

To determine the most likely alternative, a rigorous PM3 semi-empirical geometry optimisation calculation was performed on both structures. The results of these calculations are depicted in Fig. 2.9.

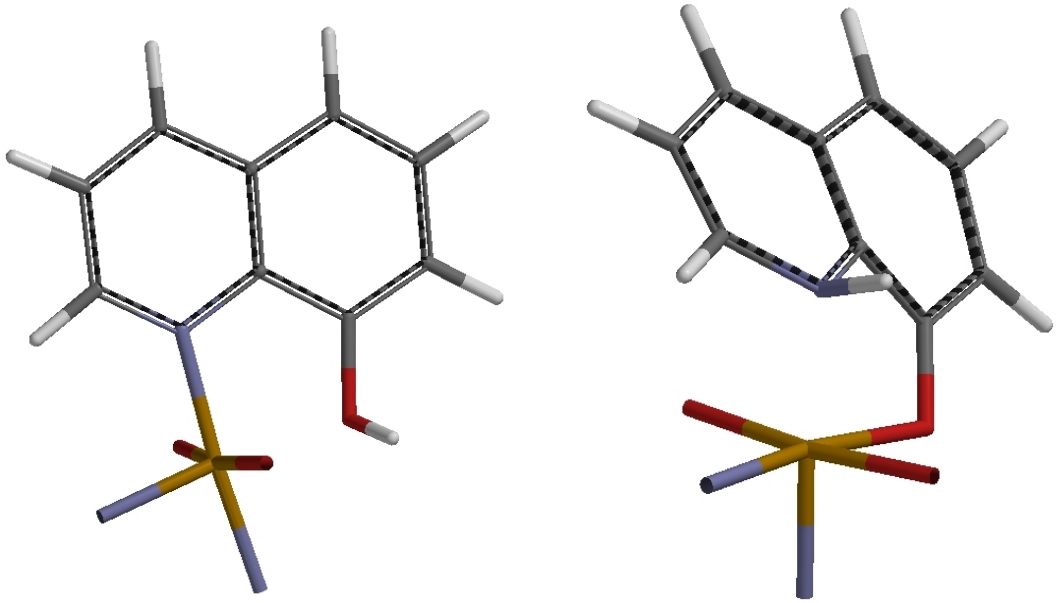

(a) **(b)**

Figure 2.9 – PM3 optimised structures of the two alternative structures for the $[Fe(8\text{-}HQ)_2(8\text{-}HQ\text{-}OH)]^+$ (i.e. $3{:}1H^+$) species as identified in the ESI-MS spectra. The other two HQ ligands have been removed for clarity.

It is clear that structure (a) refines with an acceptable geometry, whereas (b) becomes severely distorted. This is also reflected in their relative formation energies (as calculated using PM3) of -234.85 and -198.22 kcal/mol respectively. As $[Fe(8\text{-}HQ)_2(8\text{-}HQ\text{-}OH)]^+$ was identified in all ESI-MS spectra for 8-HQ, it is reasonably assumed that this would correspond to the most stable alternative i.e. (a). Therefore, according to these results, the species with protonation of the hydroxy group rather than the endocyclic nitrogen atom appears to be the appropriate choice for the mono-coordinated third ligand. It is also worth noting that endocyclic nitrogen atoms are generally preferred over exocyclic substituents with respect to transition metal ion coordination[150, 151].

This also supports the notion that the coordination of the third ligand is hindered by the bulk of the other two ligands and it is suggested that the

coordinatively unsaturated cationic 3:1 species might also be present in solution. Further evidence to support this argument is that no other Fe-containing species that are protonated have been identified, such as $[Fe(8\text{-}HQ)_2H]^{2+}$, the protonated 2:1 species. This indicates that consolidation of N/O-bidentate coordination occurs more readily when crowding is not present.

2.3.1.2 5,7-dichloro-8-hydroxyquinoline (DCHQ)

For the complexation of Fe^{3+} by DCHQ, a *representative* spectrum, demonstrating the isotopic signatures and accuracy of the m/z values for the key peaks identified, is shown in Fig. 2.10. The collection of DCHQ-Fe spectra over the whole range of DCHQ-Fe mole ratios (R = 0.1 to 4) is displayed in Appendix I. For all seven of these spectra, the relative abundances of the major species are given in Table 2.3. For clarity, the most abundant species DCHQ-H^+, which is observed in all the spectra, has been omitted from this table and the relative abundances have been related to the next most abundant, Fe-containing species.

Three different kinds of Fe-containing DCHQ species have been observed. These are the methanol adduct of $[Fe(DCHQ)_2]^+$ (i.e. $2{:}1^+$-MeOH), $[Fe(DCHQ)_2(DCHQ\text{-}OH)]^+$ (i.e. $3{:}1H^+$) and, notably, the radical cation $[Fe(DCHQ)_3]^{+\bullet}$. For any given ratio, however, only two Fe-containing species are present. The radical cation $[Fe(DCHQ)_3]^{+\bullet}$ is the only 3:1 species to be represented for R = 0.1. With increasingly lower relative proportions of iron (R > 0.1) the only 3:1 species to be represented is the protonated form $[Fe(DCHQ)_2(DCHQ\text{-}OH)]^+$.

The most noticeable result from Table 2.3 is the postulation of the 3:1 cationic radical species $[Fe(DCHQ)_3]^{+\bullet}$. A comparison of the peak at m/z = 693.87 in the R = 0.1 spectrum to the peak at m/z = 694.87 in the R = 0.5 spectrum clearly indicates a difference of exactly one m/z unit, Fig. 2.11. This is a significant discovery in the light of possible modes of action of

hydroxyquinolines towards neurodegenerative disease and will be discussed in more detail later, especially given that CQ exhibits the same phenomenon.

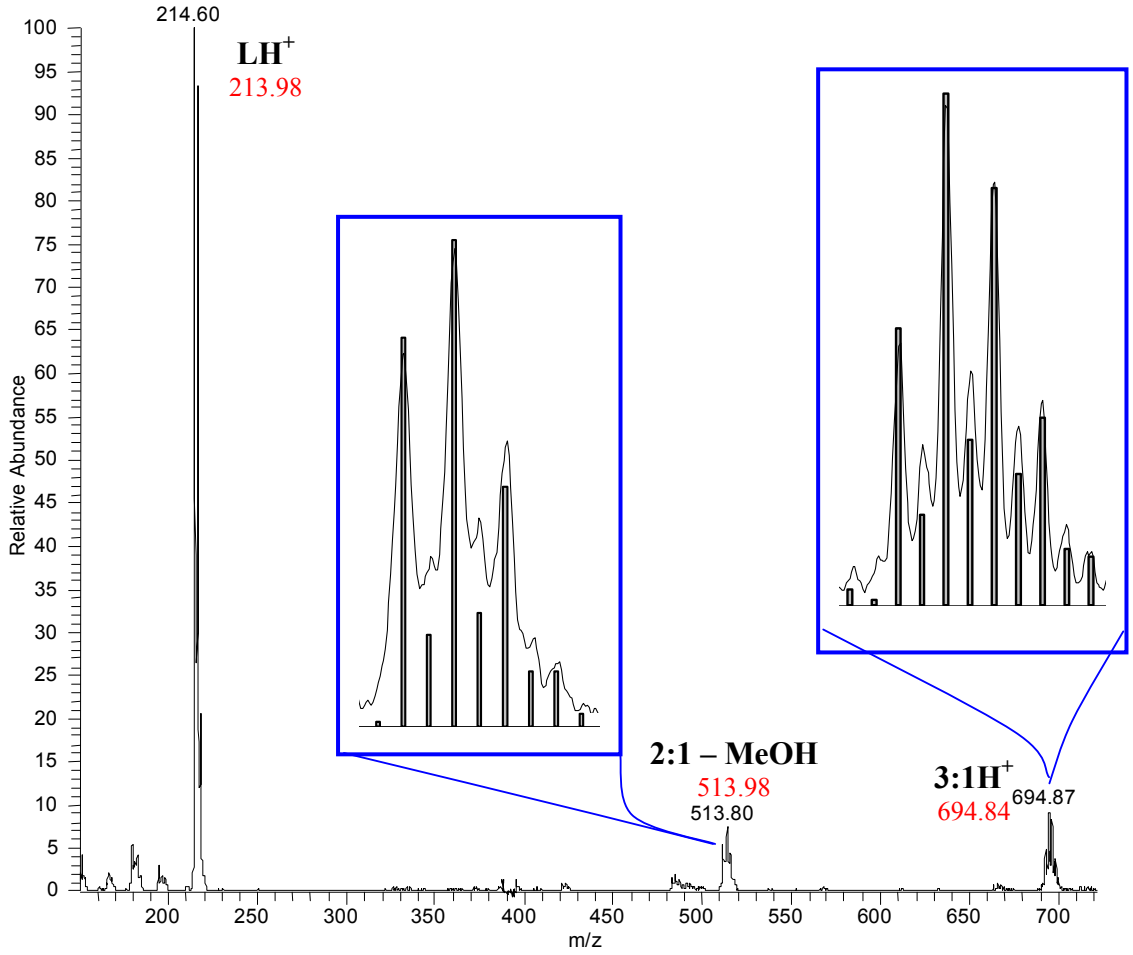

Figure 2.10 - The spectrum obtained for DCHQ at a mole ratio of 2:1. Note the speciation of the DCHQ-Fe containing peaks are shown in bold and the theoretical m/z in red. Insets are magnifications of the 2:1-MeOH species and the 3:1H$^+$ species, with the theoretical isotopic distributions overlayed.

Table 2.3 – Relative abundances for all Fe-containing DCHQ species, for all ESI-MS spectra obtained. Due to the size of the peaks for the DCHQ-H$^+$ species, the relative abundance of the protonated free ligand has been removed.

R	2:1-MeOH	3:1$^{+\bullet}$	3:1H$^+$
0.1	100	43	Absent
0.5	100	Absent	43.5
1	100	Absent	36.5
1.5	100	Absent	79
2	100	Absent	123
3	100	Absent	130
4	100	Absent	138.5

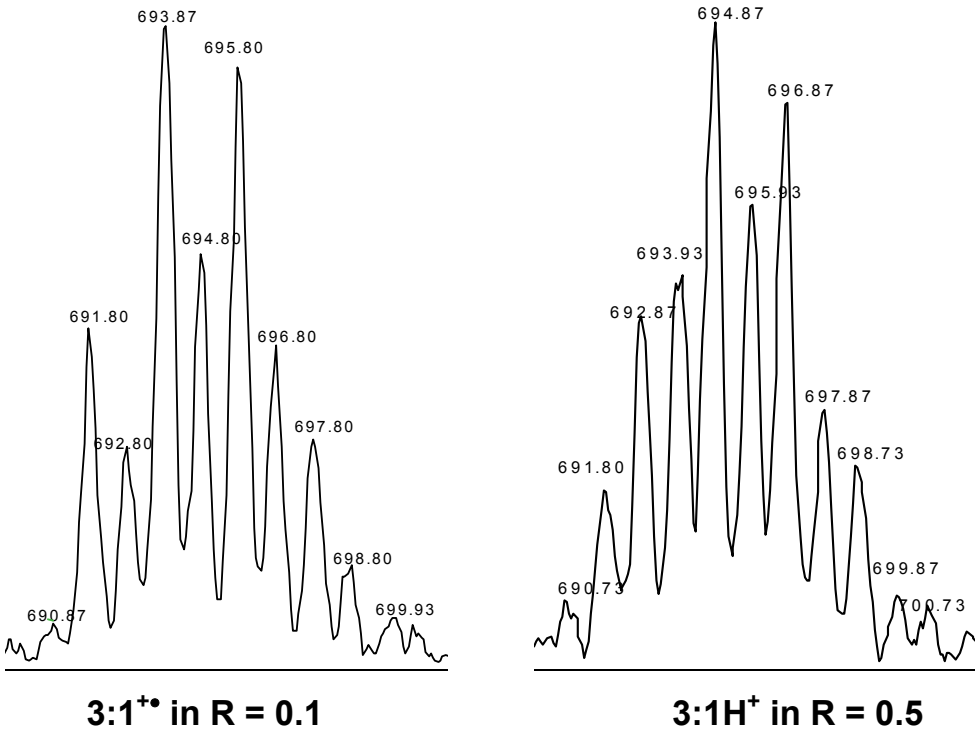

Figure 2.11 – Magnifications of the 3:1 species identified in the lowest mole ratio, R = 0.1 and the next smallest mole ratio, R = 0.5.

Fig. 2.12 compares the relative proportions of 3:1 to 2:1 species as a function of the ligand to Fe ratio. This has a different profile to that produced for the HQ ligand, Fig. 2.6, due to the presence of the chloro groups. With DCHQ as the ligand, there appears to be an initial plateau up to a value of R = 1. Therefore, compared to HQ, it would appear that the DCHQ system is more resistant to the addition of a third ligand than HQ, at least until a critical mole ratio of R = 1 has been achieved.

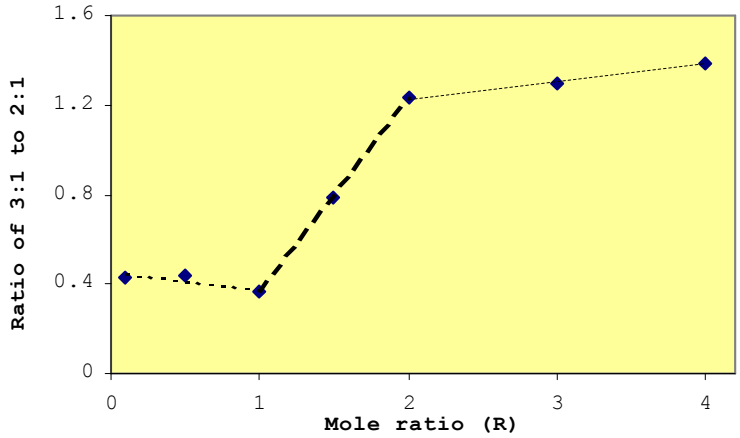

Figure 2.12 – Plot of ratio of relative abundances of 3:1 species to 2:1 species for DCHQ across the range of DCHQ:Fe mole ratios (R).

Therefore, if this mechanism were responsible for the shape of the graph in Fig. 2.12, it would be expected that an increase in this critical mole ratio of ligand to Fe could be achieved by subtly adding more steric bulk. Studying a bulkier ligand, CQ, shall test this hypothesis.

2.3.1.3 5-chloro-7-iodo-8-hydroxyquinoline (CQ)

For the complexation of Fe^{3+} by CQ, a *representative* spectrum, demonstrating the isotopic signatures and accuracy of the m/z values for the key peaks identified, is shown in Fig. 2.13. The collection of CQ-Fe spectra over the whole range of CQ-Fe ratios (R = 0.1 to 4) is displayed in Appendix I. For all nine of these spectra, the relative abundances of the major species are given in Table 2.4. For clarity, the most abundant species, $CQ\text{-}H^+$, which is observed in all the spectra, has been omitted from this table and the relative abundances have been related to the next most abundant (Fe-containing) species.

Five different kinds of Fe-containing CQ species are observed. These are $[Fe(CQ)_2]^+$ (i.e. $2{:}1^+$), the water adduct of $[Fe(CQ)_2]^+$ (i.e. $2{:}1^+$ - H_2O), the methanol adduct of $[Fe(CQ)_2]^+$ (i.e. $2{:}1^+$ - MeOH), $[Fe(CQ)_2(CQ\text{-}OH)]^+$ (i.e. $3{:}1H^+$) and, notably, the radical cation $[Fe(CQ)_3]^{+\bullet}$. The radical cation $[Fe(CQ)_3]^{+\bullet}$ is the only 3:1 species to be represented for R = 0.1, R = 0.5 and R = 1. Note that this species was only observed for R = 0.1 for the DCHQ ligand and was not observed at all for HQ. As the proportion of iron decreases, the 3:1 species reverts to the protonated form $[Fe(CQ)_2(CQ\text{-}OH)]^+$, suggesting a role for excess iron in the abstraction of the hydrogen atom (i.e. in creating a more redox active environment).

Notably, the occurrence of the 3:1 radical cation has again been identified at the higher relative concentrations of Fe^{3+}. However, unlike the DCHQ radical cation discussed previously, the $[Fe(CQ)_3]^{+\bullet}$ species seems to be more persistent, as positive identifications have been made up to a mole ratio of R = 1 (Table 2.4).

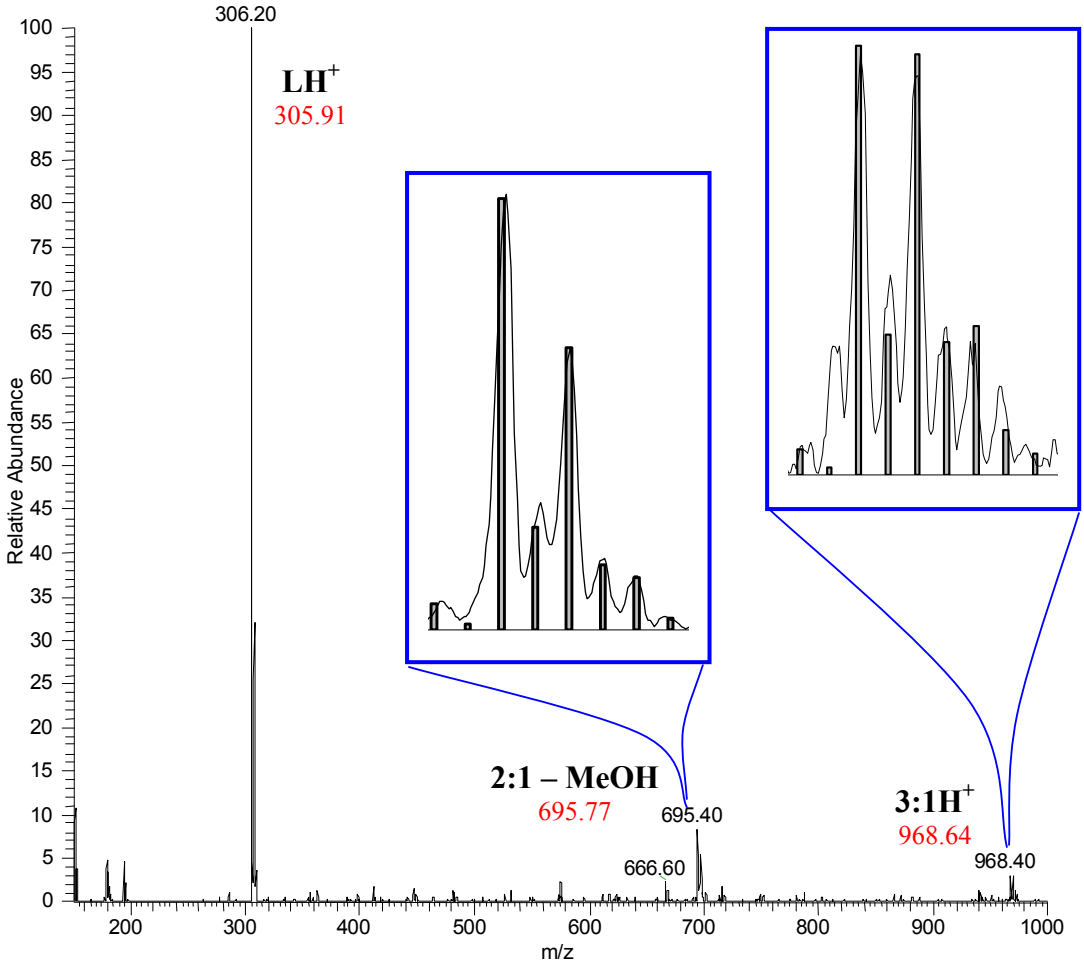

Figure 2.13 - The spectra obtained for CQ at a mole ratio of 4:1. Note the speciation of the CQ-Fe containing peaks in bold and the theoretical m/z in red. Insets are magnifications of the 2:1-MeOH species and the $3{:}1H^+$ species, with the theoretical isotopic distribution overlayed.

Table 2.4 - Relative abundances for all Fe-containing CQ species, for all ESI-MS spectra obtained. Due to the size of the peaks for the CQ-H^+ species, the relative abundance of the protonated free ligand has been removed.

R	2:1	2:1-H_2O	2:1-MeOH	$3{:}1^{+\bullet}$	$3{:}1H^+$
0.1	4.5	11	100	4.5	Absent
0.5	2	8	100	8	Absent
1	Absent	8	100	11	Absent
1.5	Absent	11	100	Absent	19
2	Absent	11	100	Absent	18
2.5	Absent	9.5	100	Absent	12
3	Absent	Absent	100	Absent	32
3.5	Absent	Absent	100	Absent	49
4	Absent	Absent	100	Absent	42.5

A comparison of the peaks assigned to $[Fe(CQ)_3]^{+\bullet}$ ($3{:}1^{+\bullet}$) and $[Fe(CQ)_2(CQ\text{-}OH)]^{+}$ ($3{:}1H^{+}$) are displayed in Fig. 2.14, again showing a displacement in m/z values of 1 unit.

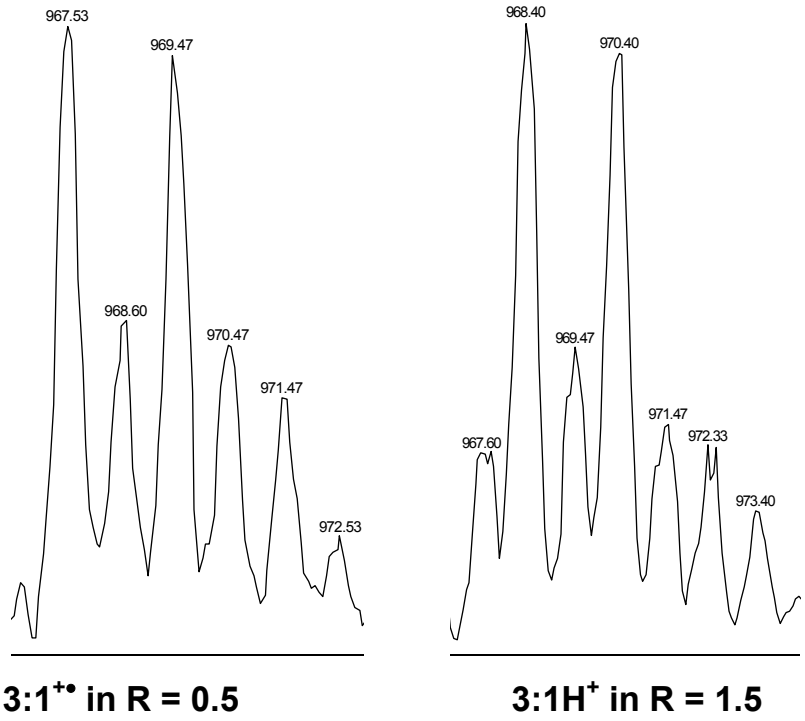

Figure 2.14 - Magnifications of the 3:1 species identified in the R = 0.5 and R = 1.5 spectra respectively.

The more sustained appearance of the radical cation through a wider range of CQ:Fe mole ratios is an important finding. This suggests that the third CQ ligand is more prone to oxidant attack, either through an enhancement of O-H homolytic bond dissociation and/or due to a prolonged failure of the third ligand to consolidate N/O coordination. This observation appears to reinforce the concept mooted previously in the DCHQ discussion regarding a hindrance to complexation of the third ligand. As the difference between the DCHQ and CQ ligands is the identity of the halogen on the carbon adjacent to the hydroxy moiety, the additional steric bulk of the iodine atom in CQ could also influence the relative ease of hydrogen abstraction. It is also worthy of notice at this point that the appearance of a ligand-specific mole ratio dependency on the identification of the radical cation reinforces the idea that these species are present in solution, rather than being artefacts of the ESI-MS process. Were these

species artificially produced via ESI-MS, it would be reasonable to expect to see the radical cation species, either DCHQ- or CQ-based, to be identified *irrespective* of ligand:Fe concentrations.

Fig. 2.15 compares the relative proportions of 3:1 to 2:1 species as a function of the ligand to iron ratio. As observed with DCHQ, this has a different profile to that produced for the HQ ligand, Fig. 2.4. However, the initial plateau that suggests a resistance to the addition of a third ligand is more pronounced in the case of CQ with the plateau extending to a mole ratio of 2.5 rather than 1.0, as seen with DCHQ as the ligand. This is perhaps not surprising since CQ is a bulkier ligand and, again, this is supportive of the argument that hindrance of the third ligand with respect to consolidation of oxygen N/O bidentate coordination is a feature that helps to promote the 3:1 radical cation formation.

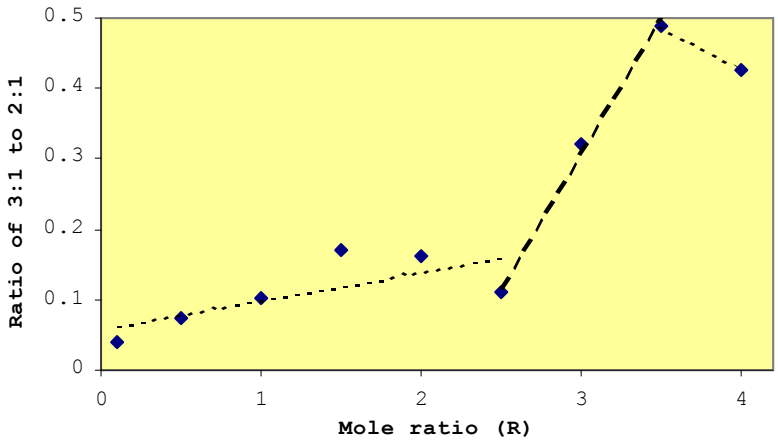

Figure 2.15 - Plot of ratio of relative abundances of total 3:1 species to total 2:1 species for CQ across the range of CQ:Fe mole ratios (R).

As alluded to previously, the discovery of the $[Fe(DCHQ)_3]^{+\bullet}$ and $[Fe(CQ)_3]^{+\bullet}$ radical cations has specific implications for the possible mode of action of CQ in the treatment of Parkinson's disease[110]. Iron overload in the substantia nigra (SN) region of the brains of Parkinson's sufferers is associated with elevated oxidative stress. The ability of a CQ ligand to coordinate an embedded iron(III) site in the SN matrix via the endocyclic N alone, leaving an uncoordinated –OH free to act as a radical scavenger, possibly with the O-H

bond labilised with respect to homolytic dissociation by the coordination of the metal to the nitrogen, is an attractive proposition. Not only would the CQ be acting as an iron sequestering agent, but it would also act as a powerful antioxidant *upon coordination* with the metal complex becoming charged (and mobilized) in the process. Notably, this antioxidant activity does not need to invoke the redox chemistry of the metal. This notion is further supported by our observation that the formation of radical cations such as $[Fe(CQ)_3]^{+\bullet}$ are favoured by an environment where there is excess iron.

2.3.2 Computational investigations

To further support these ideas, a detailed semi-empirical and *ab initio* quantum chemical computational investigation of all relevant hydroxyquinoline species has been undertaken and summarized in Table 2.5.

Table 2.5a – Entries are the relative energies of formation of the relevant hydroxyquinoline species. All structures were optimised using DFT/B3LYP/SDD. Single point energies as per appropriate column headings. All values are in kcal/mol.

Species	PM3	MP2/SDD	CCSD/SDD
3:1H^+ 8-HQ	-234.85	-970881.97	-
3:1H^+ DCHQ	-264.26	-2698647.71	-
3:1H^+ CQ	-169.84	-1854726.30	-
2:1$^+$(aq) 8-HQ	-301.47	-	-
2:1$^+$(aq) DCHQ	-322.48	-	-
2:1$^+$(aq) CQ	-255.89	-	-
3:1$^{\bullet+}$ 8-HQ	-	-970451.58	-
3:1$^{\bullet+}$ DCHQ	-	-2698254.30	-
3:1$^{\bullet+}$ CQ	-	-1854335.45	-
8-HQ	-1.61	-298094.60	-298152.07
8-HQ$^\bullet$	-	-297642.99	-297749.73
DCHQ	-15.30	-874041.63	-874102.50
DCHQ$^\bullet$	-	-873586.03	-873699.96
CQ	8.85	-592729.75	-592788.30
CQ$^\bullet$	-	-592273.49	-592385.66
H$^\bullet$	-	-312.27	-312.27

Table 2.5b - The estimated relative binding energies (BE) for the third ligand in the three 3:1 systems. All values are in kcal/mol.

Addition of the third ligand (2.3.2.1)	BE	BDE	
	PM3	MP2/SDD	CCSD/SDD
$2{:}1^{+}(aq) \rightarrow 3{:}1H^{+}$ 8-HQ	68.23	-	-
$2{:}1^{+}(aq) \rightarrow 3{:}1H^{+}$ DCHQ	73.52	-	-
$2{:}1^{+}(aq) \rightarrow 3{:}1H^{+}$ CQ	77.20	-	-

Table 2.5c - The relative O-H bond dissociation energies (BDE) for the N-coordinated third ligand in the three 3:1 systems, and the relative O-H bond dissociation energies for the three isolated ligands. All values are in kcal/mol.

Homolytic BDE (2.3.2.2)	BE	BDE	
	PM3	MP2/SDD	CCSD/SDD
$3{:}1H^{+} \rightarrow 3{:}1^{\bullet+}$ 8-HQ	-	109.36	-
$3{:}1H^{+} \rightarrow 3{:}1^{\bullet+}$ DCHQ	-	72.23	-
$3{:}1H^{+} \rightarrow 3{:}1^{\bullet+}$ CQ	-	70.33	-
8-HQ $\rightarrow$ 8-HQ$^{\bullet}$	-	137.86	88.88
DCHQ $\rightarrow$ DCHQ$^{\bullet}$	-	133.31	89.18
CQ $\rightarrow$ CQ$^{\bullet}$	-	133.82	89.25

The various metal-containing species that have been identified in the ESI spectra have also been characterized computationally, in order to confirm sensible geometries and to investigate the influence on the homolytic O-H bond dissociation energy of iron coordination at the endocyclic nitrogen of the hydroxyquinoline derivatives. Calculations have also been carried out in order to gain some information on the relative degree of hindrance to the entry of the third ligand in all three 3:1 systems.

2.3.2.1 Semi-empirical PM3 characterization of the 2:1 and 3:1 iron hydroxyquinoline systems

The structures of the 2:1(diaqua) and 3:1 ligand:iron(III) complexes of 8-HQ, DCHQ and CQ that have been refined under PM3 are depicted in Fig. 2.16.

The geometries of all of these structures are reasonable in terms of their bond lengths and angles. This data is accessible via Appendix IV.

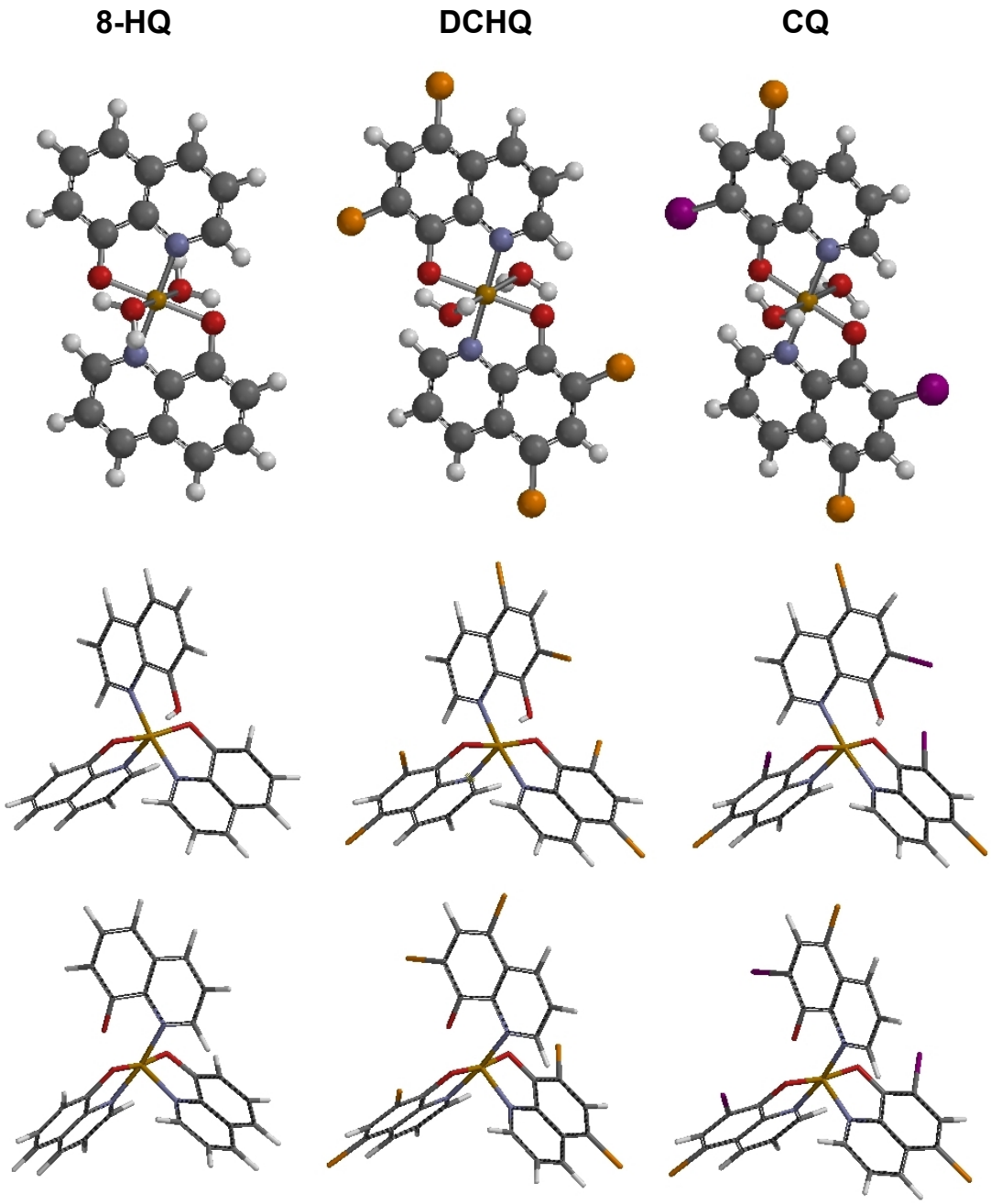

Figure 2.16 – Optimised structures of (from top to bottom) 2:1^{+}(diaqua), 3:1H^{+} and 3:1$^{+\bullet}$ ligand:Fe complexes, for each ligand as labelled across the top.

It is of interest to consider the spin density distribution in all three of the possible radical cation species, Fe(III)(8-HQ)$_3^{+\bullet}$, Fe(III)(DCHQ)$_3^{+\bullet}$ and Fe(III)(CQ)$_3^{+\bullet}$ as calculated under PM3, Figs 2.17. All calculations show

extensive spin delocalization with well-behaved geometries. There appears to be an implicit coordination between the $O^{\bullet}$ atom and the metal in each case. For the CQ system, scalar relativistic effects are assumed to be accounted for in the semi-empirical calculations.

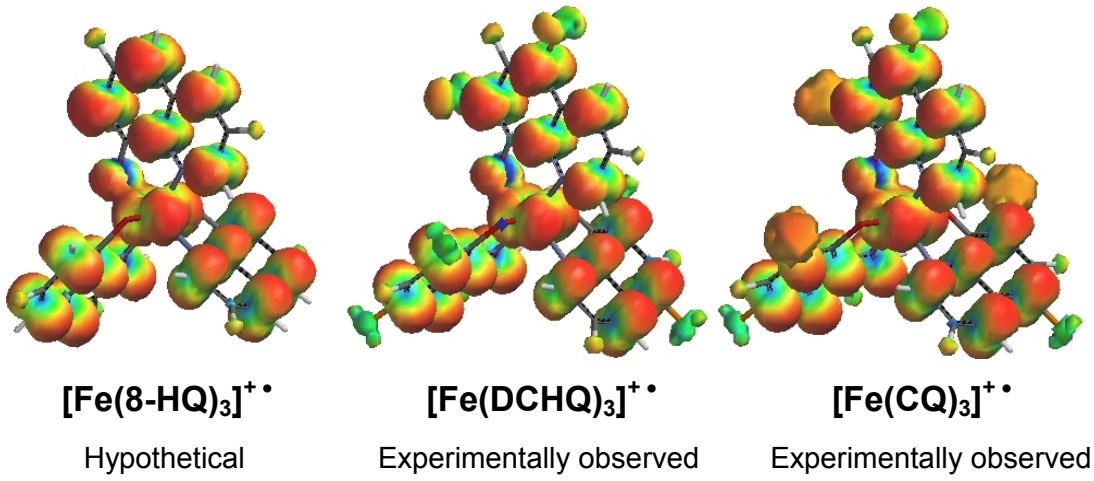

Figure 2.17 – Spin density maps of the 3:1 radical cations for all three ligand systems.

2.3.2.2 Hindrance to the addition of a third ligand

To estimate the steric hindrance of the addition of a third ligand, as discussed previously, PM3 and RM1 calculations were carried out to determine the binding energy of the third ligand. This was achieved by using the PM3 optimised geometries of the $2{:}1^{+}$(diaqua)[e], $3{:}1H^{+}$ and RM1 optimised geometries for the free ligand species for all three ligand systems used, using PM3 in the Spartan '06 package[98]. The binding energies were calculated according to the method described in Section 2.2.3 and the results are presented in Table 2.6.

The results shown in Table 2.6 are consistent with the steric hindrance of the addition of the third ligand being in the order of CQ > DCHQ > 8-HQ. This is

[e] As this investigation involves the formation of the 3:1 species from the 2:1 species, this formation occurs in solution rather than the gas phase environment of the ESI-MS. As mentioned previously, solvent molecules would occupy any coordination sites not occupied by 8-HQ-based ligands in solution. Therefore, the estimated binding energies presented here intrinsically include ligand exchange, rather than just 'binding energy'.

expected since the relative bulk on the ligands increases in this order. Also, the sign of the BE_3 results are positive, indicating that the process of adding a third ligand to the solvated $2:1^+$ species is energetically unfavourable. This supports the conclusion drawn from the ESI results, Figs. 2.4, 2.11 and 2.15, where the ratio of the relative abundances of the 3:1 to 2:1 peaks suggest that the process of adding the third ligand to a 2:1 complex is hindered as the ligand being added increases in steric bulk at the 7-position.

Table 2.6 – Third ligand binding energies, BE_3, for the three 3:1 systems. All energies are in kcal/mol.

Ligand	E(3:1H$^+$)	E(2:1$^+$)	E(L)	BE_3
8-HQ	-234.85	-301.47	-1.61	**68.23**
DCHQ	-264.26	-322.48	-15.30	**73.52**
CQ	-169.84	-255.89	8.85	**77.20**

It is acknowledged here that caution has to be exercised when using the PM3 method to calculate reaction energy where bonds are being broken or formed, since the effects of electron correlation are not taken into account. However, it is reasonably assumed that the differences in reaction energy between the three systems are primarily due to steric effects and that, since the three ligands in question are chemically very similar, the effects of electron correlation would effectively cancel.

2.3.2.3 High level quantum chemical calculations

2.3.2.3.1 Iron species

With the notion that ligand-specific steric hindrance may play a part in 3:1 radical cation formation - by allowing prolonged availability of an uncoordinated O-H group, the next step in our computational investigations is to describe the energetics related to the homolytic cleavage of the O-H bond in such situations. Specifically, it is of interest to enquire whether the O-H bond of a third ligand in species of the type $[Fe(L)_2(L\text{-}OH)]^+$ is significantly labilised with respect to

homolytic bond dissociation (due to metal coordination at the endocyclic nitrogen) compared to the O-H bond in the uncoordinated free ligand. This requires the computation of the homolytic bond dissociation energy at a high level of theory (see Section 2.2.3).

The Fe-containing species involved in the calculation of the BDE's, namely $[Fe(L)_2(L\text{-}OH)]^+$ ($3{:}1H^+$) and $[Fe(L)_3]^{+\bullet}$ ($3{:}1^{+\bullet}$), were subjected to geometry optimization in Gaussian 03 using DFT under B3LYP/SDD. These complexes were treated as low-spin, as iron(III) complexes with ligands of this type usually are[152] and as such were calculated as cationic doublets ($3{:}1H^+$) and cationic triplets ($3{:}1^{+\bullet}$). This method was selected as SDD invokes a Dunning/Huzinaga valence double-zeta basis set (D95V) for the elements of the first two rows (up to Ar), and relativistic Stuttgart/Dresden Effective Core Potentials (ECP's) for the rest of the periodic table[153]. This was selected as the most appropriate theoretical method to obtain good geometries of these large systems, without becoming prohibitively computationally expensive.

Single-point energies of these structures using MP2/SDD in Gaussian 03 were then calculated, in order to achieve improved treatment of electron correlation, and hence reaction energies. Zero-point energy (ZPE) corrections were then made to these single-point energies. The appropriate results of these DFT/B3LYP/SDD//MP2/SDD calculations are summarized in Table 2.7.

Table 2.7 – Results for the homolytic BDE calculations for **O-H** in $[Fe(L)_2(L\text{-}OH)]^+$. All values are in kcal/mol.

$$\mathbf{[Fe(L)_2(L\text{-}OH)]^+}\,(3{:}1H^+) \rightarrow \mathbf{[Fe(L)_3]^{+\bullet}}\,(3{:}1^{+\bullet}) + \mathbf{H^\bullet}$$

L	$E(3{:}1H^+)$	$E(3{:}1^{+\bullet})$	$E(H^\bullet)$	BDE_3
8-HQ	-970881.97	-970451.58	-312.27	**109.36**
DCHQ	-2698647.71	-2698254.30		**72.23**
CQ	-1854726.30	-1854335.45		**70.33**

The BDE values in Table 2.7 shows a clear energetic preference for the production of the 3:1 cationic radical of order CQ > DCHQ >> 8-HQ. These BDE results are encouraging, and appear to agree with experimental data obtained via ESI-MS, where the 3:1 CQ system appeared to be the most likely to undergo hydrogen abstraction, given the prevalence of the radical up to a mole ratio of R = 1. The DCHQ BDE result indicates that this $3{:}1H^+$ complex would undergo hydrogen abstraction to a lesser extent than the CQ system. This is also consistent with what is observed in the ESI-MS experiments where the radical species is found only at R = 0.1. The BDE results suggest a relative reluctance of the 8-HQ $3{:}1H^+$ species to homolytically release the hydrogen from the unconsolidated hydroxy moiety. Again, these results are consistent with the experimental ESI-MS results, where the 8-HQ radical cation is not detected at all.

2.3.2.3.2 Free ligands

In order to determine whether metal coordination to the N position of the third ligand has a weakening effect on the O-H bond with respect to hydrogen atom abstraction, the BDEs in Table 2.7 need to be compared to those of the uncoordinated free ligands. In order to achieve this, the geometries of the free ligands were optimised, and single-point energies were calculated, as described in Section 2.2.3, the results of which are summarized in Table 2.8.

Table 2.8 – Calculated homolytic BDE values for the free ligands, L. All values are in kcal/mol.

L	DFT/B3LYP/SDD//MP2/SDD	DFT/B3LYP/SDD//CCSD/SDD
8-HQ	139.34	88.88
DCHQ	143.32	89.18
CQ	143.98	89.25

An interesting aspect of these results is the disparity between the homolytic BDE values as calculated by MP2 and CCSD. In results shown in Appendix IV, as the order of Möller-Plesset perturbations increases (MPn, where n = 2, 3 or 4) the BDE values for the free ligands converge towards the CCSD results, suggesting that all MPn results (especially MP2) fail to fully account for

the electron correlation, and hence fail to properly account for the bond energies. With such convergence apparent, the CCSD/SDD results are taken here as the most accurate homolytic BDE values for the free ligands. These values are compared to the Fe-complex BDE's and summarized in Table 2.9.

Table 2.9 – Comparison of Fe-complex BDE values and free ligand BDE values, with the difference between the two processes (Δ). All values are in kcal/mol.

L	$[Fe(L)_2(L\text{-}OH)]^+$ BDE	Free ligand BDE	Δ
8-HQ	109.36	88.88	**+20.48**
DCHQ	72.23	89.18	**-16.95**
CQ	70.33	89.23	**-18.92**

In may be seen from Table 2.9, that monodentate coordination of the $Fe(L)_2^+$ species to the nitrogen of the third ligand L-OH, does not result in labilisation of the $H^\bullet$ atom in the case of HQ. However, it strongly activates the O-H bond in this regard for DCHQ and CQ (in that order). This is entirely consistent with what is observed in the ESI-MS data, *vide supra*.

The PM3 results describing the steric barrier to N/O bidentate consolidation of the third ligand, combined with the labilisation of the O-H bond of the third ligand as described by the DFT/MP2 calculations presents a comprehensive view of the formation of the 3:1 radical cations. As shown in Fig 2.18, not only is the O-H bond of the third ligand available for homolytic dissociation for an extended period due to the steric barrier present in CQ and DCHQ, but that this bond is more likely to be broken in such a manner.

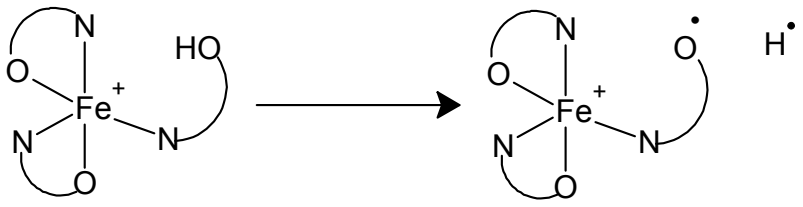

Figure 2.18 – Stages of radical cation formation. In CQ, and to a lesser extent DCHQ, the unconsolidated complex (left) is sterically hindered, allowing this species to exist in solution longer, with a weakened, available O-H bond to be homolytically broken.

2.3.3 Significance of the discovery of the radical cation

With both experimental evidence and theoretical modelling strongly supporting the formation of the Fe-CQ 3:1 radical cation, especially at relatively low concentrations of CQ, comments on the significance of this finding can be made with respect to previous literature findings.

2.3.3.1 Possible explanation of Fe-CQ toxicity

As mentioned in the introduction to this Chapter (Section 2.1.2.1), CQ has a relatively shady past as a pharmaceutical. Cases of the neurological disorder SMON have been previously related to the oral intake of CQ, with Fe-CQ chelates of particular interest given the identification of such species from patients diagnosed with SMON. As such, several previous studies have focused on the Fe-CQ system, with interesting outcomes on which this work might elaborate.

Previous work by Yagi *et al* indicated that Fe-CQ chelates have an increased toxicity profile when applied to cultured nerve cells, compared to CQ and Fe(III) when tested alone[154, 155]. The damage caused to these cultured nerve cells *in vitro* was shown to be via lipid peroxidation, a process that is initiated by free radicals. The conclusions of this paper were that the Fe-CQ chelates were initiating the redox chemistry of the Fe, however no definitive proof of this hypothesis was supplied[155].

One suggestion that combines this *in vitro* neurotoxicity profile with the presence of the 3:1 radical cation would be the possibility of *pro*-oxidant behaviour. With the decrease in the homolytic BDE of the O-H bond of the third CQ ligand suggested by the computational results above, it is possible that the protonated 3:1 complex could become a pro-oxidant under certain conditions, by spontaneously releasing the hydrogen atom as $H^{\bullet}$. These conditions may include

possible photo-dissociation during the previously discussed *in vitro* experiments, as the cultured neuronal cells were not incubated in a dark environment.

Another possibility is that the lipid of the membranes of the cultured neural cells provides a "substrate" for the $[Fe(CQ_2)(CQ\text{-}H)]^+$ species to oxidize, meaning that the radical formation is not an auto-homolytic process, but requires an "acceptor" for the $H^{\cdot}$ species. This corresponds with the identification of the radical cation only at relatively high levels of Fe^{3+} in the ESI-MS. In the ESI-MS solutions, the Fe^{3+} would act as a "substrate" for oxidation, and that once the amount of free Fe^{3+} in solution dropped below a particular threshold, the radical was no longer produced.

A third possibility is that 3:1 protonated species may be interfering with the electron transport chain of respiration in the mitochondria. This is due to the fact that the previous study found Fe-CQ chelates *within* the neural cells[155]. Therefore, the 3:1 Fe-CQ chelates would act as a specific mitochondrial toxin as a possible mechanism for SMON by disrupting normal respiration, given the number of radical species involved with electron transport.

Recent work that followed on from that of Yagi *et al* described above, examined the toxicity of CQ on monolayers of astrocytes, a type of brain cell, isolated from mice. In this work, an unusual dose-dependent toxicity curve was published, which showed that very low levels of CQ, and very high levels of CQ, displayed a high degree of toxicity[156]. The unusual aspect of this toxicity profile was that this toxicity was reduced at intermediate levels of CQ[156]. An analysis of the MEM10 growth medium showed some Fe to be present. The toxicity was measured as activity of lactate dehydrogenase (LDH), an accurate marker of cellular death.

Upon further investigation, the toxicity was found to be oxidative in nature, as the addition of antioxidants, such as ascorbate (vitamin C) and Trolox

C (a water soluble analogue of vitamin E), was shown to inhibit much of the damage to the cultured cells. This *in vivo* toxicity result, where low concentrations of CQ appear to inflict oxidative damage on cultured cells, seems to correlate with the appearance of the 3:1 radical cation discovered in ESI-MS experiments. This appears to provide further evidence that the 3:1 radical cation may act as a pro-oxidant in such an environment.

However, neither of these previous studies examined cellular toxicity in the presence of pathophysiologically important structures, such as the plaques of AD. These are known to produce free radicals, and as such provide an oxidizing environment. Therefore, in such an environment, the 3:1 protonated species is more likely to react with a free radical, therefore leading to antioxidant behaviour.

2.3.3.2 Impacts on current research in this area

The impact on research into neurodegenerative diseases of a radical cation that is possibly active at the site of disease could be significant. As mentioned in the introduction, the sites of disease for AD and PD especially, show signs of oxidant damage, suggesting an increase in the amount of free radicals generated within the brain. Therefore, molecules that reduce both metal imbalance as well as local ROS concentrations should display greater efficacy in treating the symptoms related to AD and PD.

In the case of CQ, this duality seems to be present, as CQ as a free ligand is not particularly effective as an antioxidant (see Chapter 2) and that an increase in antioxidant activity appears only when in the $3{:}1H^+$ Fe complex. As mentioned in the introduction, CQ has been shown to only be active as a chelator within the brain, given that no systemic depletion of Fe has been seen in patients receiving CQ[123]. This means that CQ, as the potentially antioxidative $3{:}1H^+$ species, is most active at the site of Fe-complexation, which also happens to be the site of oxidative damage. Therefore, this environment is similar to that obtained at low

molar ratios within the ESI-MS experiments; both environments are relatively high in potential oxidants and so the 3:1H^+ species would not be expected to be pro-oxidant *in vivo*.

This work also demonstrates a theoretical model for examining this effect *in silico*, with the ability to discriminate between a highly active (i.e. low BDE) 3:1 ligand in CQ and one that does not experimentally form 3:1 radical cations, namely 8-HQ. The fidelity of this model is also demonstrated in the ability to differentiate between CQ and the slightly active DCHQ.

Further work may include a computational investigation of a variety of substituents in the 7-position, as well as other positions that may display steric hindrance, such as the 2-position, with experimental investigations of promising ligands.

Chapter 3

“Magic Numbers” for Metal-Nucleoside Clusters – Molecular Dynamics Simulation of ESI-MS/MS Results

3.1 INTRODUCTION

3.1.1 Metal ion interactions with nucleic acid constituents

Nucleic acids, and their constituents, are amongst the most fascinating of biological molecules. In order to perform their primary function as the building blocks of life, they exhibit the full range of non-covalent interactions[157, 158], including hydrogen bonding, stacking, ionic and steric interactions. As a consequence, they are highly versatile ligands, for both 'hard' and 'soft' metal species[157]. Such interactions of metals with biological molecules in general, and nucleoconstituents specifically, has been a topic of intense scrutiny, using a wide range of techniques, since the 1950s[36].

Early studies examined the effect of Hg^{2+} on DNA, with reversible physico-chemical changes observed[159] with this effect being due to direct binding to the Hg^{2+} to the nucleobases[160]. Complexation of Ag^{+} with RNA followed soon after[161], and by the mid 1960's, binding patterns of CH_3Hg^{+} [162], Cu^{2+} [163] and Zn^{2+} [164] were known. The effects of many other divalent metal cations on DNA were also studied at this time, namely Mg, Co, Ni, Mn, Zn, Cd and Cu[36]. With the advent of routine single crystal X-ray crystallography, a large amount of detailed structural information on metal-nucleobase interactions was produced[36].

In 1969, Rosenberg published work describing the antitumor activity of *cis*-$[Pt(NH_3)_2Cl_2]$[38], commonly known as cisplatin. Further work showed that the inhibitory effects of certain Pt complexes were predominantly related to DNA synthesis, with only a small effect on RNA and proteins[165]. The binding patterns of cisplatin to DNA were soon proposed to be DNA interstrand cross-linking[166], DNA intrastrand cross-linking[167], and DNA-protein cross-linking[168]. Further work shows that adjacent guanine cross-linking was the most prevalent reaction with *cis*-platinum complexes[169], with the *trans* isomer showing no activity[170] (these binding interactions will be discussed in more detail in the next Chapter).

How these various metal species interact with nucleoconstituents is a plentiful area for investigation. Such enquiries can result in sophisticated, and occasionally exotic, structural outcomes consistent with the fundamental role that such molecules play in living systems. An example of such outcomes is the formation of clusters, both in the presence and absence of ionic species (such as metal ions), which is an essential function that relates structure to function.

3.1.2 Clusters

The study of such aggregates allows specifically for a greater understanding of non-covalent interactions within DNA and RNA[34]. Non-covalent interactions are central to biological self-assembly[158], with hydrogen bonding and stacking interactions prevalent in DNA and RNA. Such self-assembling aggregates have been previously identified in solid, liquid and gaseous states and are often reflective of systems found in the biological milieu[29, 34, 171]. An example of this is the discovery of a construct known as the G-quartet.

The G-quartet, a hydrogen-bonded ionophore, was first reported in 1962[171]. This consisted of four hydrogen bonded guanosine moieties, in a planar arrangement, stabilized by a central cation, Fig. 3.1.

In the studies that followed, the cations most frequently investigated were the alkali metals. K^+ and Na^+ have been shown to have a stabilising effect on the hydrogen-bonded quartet, whilst Li^+ and Cs^+ does not form this quartet[29], due to the larger ionic radii of these ions distorting the preferred planar conformation of the ionophore. This stabilisation has been attributed to the cation balancing the electron-rich oxygen atoms in the centre. As a result of this work, given the abundance of K^+ and Na^+ ions in the body, these quartets were thought to possibly have a biological relevance[29, 172].

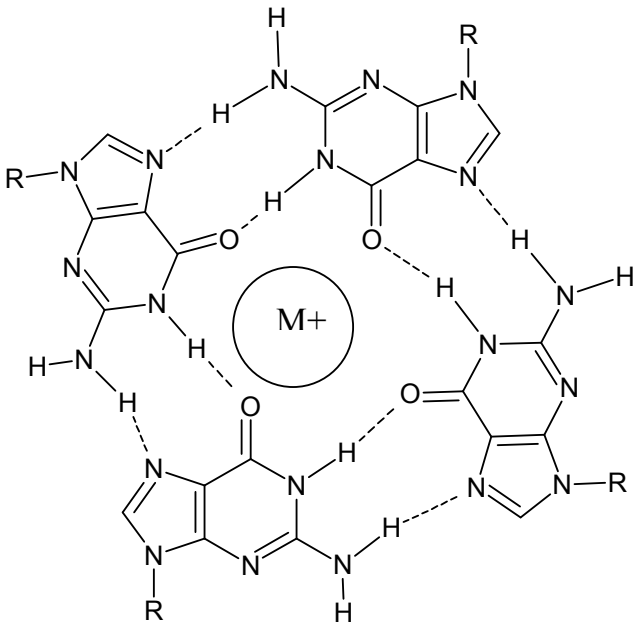

Figure 3.1 – Structure of the G-Quartet, bound to a generic cation.

Indeed, further work indicated that G-quadruplexes (stabilised by Na^+ and K^+ ions), as a DNA secondary structure, are present *in vivo*. These G-quadruplexes have since been found to be present in chromosomal telomeres, gene promoter regions, recombination sites, RNA packaging sites, and RNA dimerization sites[30-32].

The rules that govern such assemblages are still unclear and appear to emerge from the complex interplay of non-covalent (and occasionally covalent) interactions. Of particular interest in this regard is the gas-phase formation, and fragmentation, of clusters based on significantly larger metal ions than those discussed previously, for which the observation of "magic numbers" have previously been made.

3.1.3 Concept of "magic numbers" in mass spectrometry

The general concept of magic numbers, with respect to ESI-MS/MS gas-phase studies, refers to "the appearance of unusually stable clusters compared to their neighbours"[33]. Unusually stable clusters are those that appear to be favoured in the spectra when compared to other clusters of the same type[33], as these are the

most abundant post-collision cluster, irrespective of the size of the pre-collision cluster.

Magic numbers are studied in many different fields of research, from catalyst development, to studying non-bonding interactions of nucleobases. It is the latter that this work focuses on. In fact, since the discovery of the self-assembling G-quartet, studies of nucleobase interactions with cations have rapidly increased. Several enquiries have found that, regardless of the number of guanine residues in the starting cluster, four residues are preferred per metal ion after fragmentation using tandem mass spectrometry, for the alkali metal cations Na^+, K^+, Li^+ and Cs^+[33-35].

The scope of the ESI-MS section of this work is to combine two areas of metallo-nucleoconstituent interactions. With the knowledge that (a) Pt(II), with amine-containing ligands, interacts with nucleoconstituents, specifically at guanine-rich sections of DNA, and (b) guanosine is well documented to produce magic numbers in ESI-MS experiments with cations, this work aims to rationalise the appearance of magic numbers in the ESI-MS/MS results, by exploring this area with computational methods, principally molecular mechanics.

3.1.4 Overview of molecular mechanics

Unlike the quantum mechanical (QM) approaches discussed in previous chapters, molecular mechanics (MM) deals with chemical problems using nuclear positioning. By ignoring the electronic environments, MM can be applied to far larger systems than QM methods. As such, MM is the leading technique today that is applied to problems involving proteins, enzymes and nucleic acid derivatives, with the latter applying to this work. Minimised geometries and molecular dynamics simulations are generally well calculated with this theory; however, properties that rely on electron position cannot be calculated using MM.

MM theory is based upon the Born-Oppenheimer approximation, which allows for the elucidation of ground-state geometry by nuclear coordinates only. This allows for the potential energy function to be reduced to a relatively simple set of interactions. These interactions are bond stretching, angle bending, rotation around a single bond, as well as non-bonding interactions. All force fields have these four interactions; some of the more complex force fields may include more terms.

The four main interactions can be summarised to equation 3.1, where E_{tot} is the potential energy of the system, as a sum of the individual interactions. E_b is the bond stretching term, angle movement is E_a, E_t is the torsional term describing rotation, and the non-covalent and electrostatic interactions are symbolized by E_{vdW} and E_e respectively.

$$\boldsymbol{E_{tot} = E_b + E_a + E_t + E_{vdW} + E_e} \qquad \textbf{(3.1)}$$

The MM algorithm is designed to find nuclear coordinates where E_{tot} is minimised. These are achieved differently depending on the parameter, the details of which are as follows.

Bond stretching (Equation 3.2) and **angle bending** (Equation 3.3) are treated similarly, as harmonic potentials described by Hooke's law.

With the bonding interaction, the harmonic potential increases as the sum of all bond lengths, l_i, departs from the reference values, $l_{i,0}$. The bond angle energy term is similar, as it is the harmonic potential of all valence angles between three bound atoms (θ_i) and the corresponding reference angles ($\theta_{i,0}$). The reference lengths and angles are empirically determined depending on atom types, with any departure from these values increasing the potential energy of the molecule. The units for E_b are kcal/(mol×Å^2) and E_a are kcal/(mol×rad^2).

$$E_b = \frac{k_i}{2}(l_i - l_{i,0})^2 \qquad \textbf{(3.2)}$$

$$E_a = \frac{k_i}{2}(\theta_i - \theta_{i,0})^2 \qquad \textbf{(3.3)}$$

The bond rotation, or **torsion**, term in Equation 3.1, models energy change as a bond rotates. The modelling of this potential is expressed as a cosine series expansion. A functional representation of this is below.

$$E_t = \sum_{n=0}^{N} \frac{V_n}{2}\left[1 + \cos(n\omega - \gamma)\right] \qquad \textbf{(3.4)}$$

where ω is torsion angle, *n* refers to the multiplicity, which is the minimum number of points in the function as the bond is rotated through 360°. V_n is the torsional force constants, in kcal/mol, commonly referred to as the 'barrier height' and γ is the *phase factor* that determines where the angle passes through its minimum value, which is analogous to the reference values in the previous two expressions.

The **van der Waals** (vdW) interactions (Equation 3.5) require an expression that can model the interatomic potential curve quickly and accurately. The best-known function for achieving this is the *Lennard-Jones 12-6 function*, as described below.

$$E_{vdw} = 4\varepsilon\left[\left(\frac{\sigma}{r}\right)^{12} - \left(\frac{\sigma}{r}\right)^{6}\right] \qquad \textbf{(3.5)}$$

where σ refers to collision diameter, and ε refers to the potential well depth. The collision diameter corresponds to the separation between nuclei that corresponds to a potential energy of zero.

The final term in Equation 3.1 to be described is the **electrostatic** energy, E_e. There are several different methods of applying this interaction, depending on the distribution of partial charge through the molecule. One approach is to assign dipole moments to each bond, with the overall electrostatic potential being the sum of these dipole-dipole interactions. However, this method becomes cumbersome with formally charged species. The *point-charge model* more naturally deals with the charged species examined in this work.

The *point-charge model* is used with molecules where the charges are restricted to the nucleus, rather than across a bond. In this model, Coulomb's law is used as such –

$$E_e = \sum_{i=1}^{N_A} \sum_{j=1}^{N_B} \frac{q_i q_j}{4\pi\varepsilon_0 r_{ij}} \qquad \textbf{(3.6)}$$

where q_i and q_j are the point charges, and N_A and N_B are the numbers of point charges in each of the two molecules. r_{ij} is the interatomic separation between atoms i and j, and ε_0 is the dielectric constant.

All of these equations, 3.1 to 3.6, coupled with appropriate atom type parameters, constitute the required elements to describe the energy surface of a molecule, referred to as an MD force field. Atom types are required to describe the individual atomic environments that constitute the molecule. Parameters such as reference bond lengths and angles, torsional force constants and well depths are required for each atomic environment. Each atom type takes into account hybridisation and connectivity, and as such, most force fields will have more than one atom type for the more common atoms, such as C, N, H and O to name a few. Other parameters, such as partial charges required for electrostatic energy terms, are molecule-specific, and can be calculated via auxiliary algorithms within the software, or added separately.

3.1.5 The AMBER force field

The AMBER (Assisted Model Building and Energy Refinement) force field is a specialised force field, as mentioned earlier. AMBER was developed specifically for the modelling of proteins and nucleic acids. In order to achieve this, two more terms were added to the general force field expression (Equation 3.1). Equation 3.7 is a representation of the AMBER force field.

$$E_{tot} = E_b + E_a + E_t + E_{vdW} + E_e + E_{Imp} + E_{HB} \qquad (3.7)$$

All terms described above (Equations 3.2 to 3.6), are as employed by the AMBER force field. E_{Imp} is the energy of *improper torsion*, where not all four atoms are formally bound, and is described with the identical expression as the *torsion angle* energy is, with a different parameter set for each atom type. In AMBER, the cosine expansion expression used for the torsion energy usually only contains one cosine term, but may be expanded to three for certain torsions.

The most significant addition to the AMBER force field is the *hydrogen-bonding* energy term, E_{HB}. In simple force fields where hydrogen bonding is not explicitly described, the *van der Waals* and *electrostatic* terms are required to reproduce these interactions. Given the significance of hydrogen bonding interactions to the biological systems that AMBER was designed to model, a separate term was added to accurately reproduce this bonding interaction.

In order to model these hydrogen-bonding interactions, the *Lennard-Jones 6-12* expression (Equation 3.5, *vide supra*), used previously to model van der Waals interactions, is replaced for most atoms pairs displaying hydrogen bonding. Therefore, the explicit hydrogen bonding term, E_{HB}, is described by a *10-12 Lennard-Jones potential*, below.

$$E_{HB} = \sum \left[\frac{A}{r^{12}} - \frac{C}{r^{10}} \right] \qquad \textbf{(3.8)}$$

In the above expression, A and C refer to the coefficients for suitable donor-acceptor pairs. Where hydrogen bond parameters are defined for any non-covalent atom pairs, this expression is used to calculate the potential of this interaction; otherwise the *van der Waals* expression is used for that atom pair. An exception to this is 1,4-interactions, which are calculated using only the *van der Waals* expression. More recent versions of AMBER, such as AMBER96 and AMBER99, as developed by Cornell *et al* and implemented in HyperChem, have removed this explicit hydrogen-bonding term.

The above equations, as well as a detailed discussion of the processes of MM, have been supplied as this work involved adjusting several parameter sets to accommodate unparameterised atoms.

3.1.6 Missing parameters

As powerful as these force fields are, if an unparameterised atom, bond or interaction is found within the system under study, the entire simulation can either fail or result in unrealistic geometries and/or energies. In this work, molecular dynamics simulations were carried out for systems consisting of platinum(II) complex/nucleoside aggregates (described in more detail later). As the AMBER family of force fields was designed for simulating proteins and nucleic acids, platinum is not parameterised. There are several approaches to overcoming this shortfall.

The user can add parameters. If the program fails due to missing parameters, those parameters can be derived from either *ab initio* calculations, experimental values, or extrapolated from a similar system that has been

parameterised. This approach was chosen for parameter supplementation in this work, and will be discussed in more depth later in the chapter.

The program may use default parameters. Many modelling suites, including HyperChem, as used in this study, use an algorithm whereby missing parameters are estimated. In HyperChem, this is referred to as the 'Wild Card' approach, and is implemented with AMBER, having been developed for another force field, MM+[173]. The methods of estimating the parameters, such as those relating to bond lengths or torsion angles, are slightly different. However, all tend to make generalisations based on the inputted structure, such as perceived hybridisation, covalent radii and electronegativities. Default parameters were not used in the present study.

User ignores missing parameters. In this approach, a default atom type (symbolically ** in HyperChem) is applied automatically, with a set of parameters that does not reflect the actual atom. This is not recommended, as this will almost certainly lead to unrealistic structures and energies.

3.1.6.1 Adding transition metal complexes to AMBER99

There are several methods available for expanding force fields to accommodate transition metal complexes. The method used to define the metal centre here is known as the *Valence Force Field* (VFF) method. This method treats the metal atom similarly to other atoms, requiring the description of parameters for all expressions that compose the force field (M-L bonds, L-M-L and M-L-X angles, etc.). Different atom types describing the geometry around the metal centre is required. Given the generally low rotational barrier that exists around M-L bonds, torsion parameters involving the metal centre need not be defined. The non-covalent interactions involving the metal atom have not been defined in this method either, as these parameters have been shown to have little effect on minimised structures[174].

The other two methods for expanding a force field to include metal complexes are *Point-on-a-sphere* (POS) and the *Ionic method*. POS assumes that atoms tend to be located so as to minimise repulsions from other atoms. Ignoring L-M-L bond angles, and describing L···L vdW interactions instead achieves this. Using this method, all complexes of general formula $[M(L)_4]$ would be tetrahedral in nature. Whilst generally a better method than VFF, as fewer parameters are required, this method requires additional measures where the metal centre under study requires a square planar conformation[175]. Platinum(II), as used in this study, requires square planar geometry.

The ionic method requires no parameters other than M···L non-covalent terms. Whilst simple to parameterise, these interactions are overly sensitive to partial charges and the vdW parameters of the ligand(s). As a result, the accuracy of structures produced with this method can be dubious[176].

Aspects of the above theoretical discourse shall be used throughout this Chapter, where appropriate, in the discussion of the modelling of the interactions between guanosine and two chemically-diverse platinum(II) species.

3.2 METHODS

This work was a collaborative venture designed to marry ESI-MS/MS data with *in silico* calculations and involved a study of the gas-phase clustering of deoxyguanosine (dG) around a ternary platinum(II)-dG complex cation. The tridentate carrier ligands employed were diethylenetriamine (dien) and 2,6′:2′,6″-terpyridine (terpy), Fig. 3.2. These carrier ligands were chosen due to their contrasting non-covalent binding abilities; the dien ligand can only hydrogen bond to nearby dG molecules, whilst the terpy ligand can interact only via π-stacking.

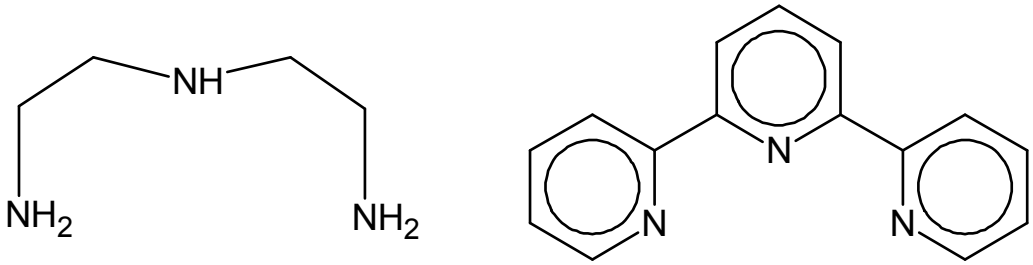

Figure 3.2 – Structures of dien (left) and terpy (right), respectively.

$[Pt^{II}(L)(dG)]^{2+}$, L = dien and terpy were studied for gas-phase clustering with excess dG using Electrospray Ionisation Mass Spectroscopy (ESI-MS). Tandem Mass Spectroscopy (MS/MS) was used to further dissociate the clusters that were observed. Both processes were then modelled using molecular dynamics calculations implementing the AMBER force field as applied in HyperChem 7.52 [177].

3.2.1 ESI-MS/MS

Samples were prepared via mixing appropriate ratios of $[Pt^{II}(dien)Cl]^{+}$: dG (1:5) and $[Pt^{II}(terpy)Cl]^{+}$: dG (1:3) in $MeOH/H_2O$[a]. These samples were then incubated for 24 hours and diluted to a final Pt concentration of 0.03mM. The collaborators at Bio21 had previously characterized both platinum complexes.

All experiments were performed on a Finnigan LTQ-FTMS instrument equipped with electrospray ionisation (ESI). The ESI solution, prepared as described above, was introduced into the mass spectrometer via electrospray ionisation using a flow rate of 4.0 μL/min. Typical ESI source conditions used were: spray voltage 4-5 kV, capillary temperature 275 ^{o}C, nitrogen sheath pressure, 10-30 (arbitrary units), and capillary voltage/tube lens offset adjusted to maximize the intensities of the desired peaks. The injection time was set using

[a] Sample preparation and ESI-MS/MS work was carried out in collaboration with Professor R. O'Hair and Dr. G. Khairallah, Bio21 Molecular Science and Biotechnology Institute, University of Melbourne, Australia, and Dr. Y. Xu, School of Chemistry and Chemical Engineering, Guangxi University, Nanning, China. Ratios were chosen by the collaborators at time of solution preparation. The difference in reactant ratios will not affect the tandem MS results, therefore will not adversely affect the final outcome.

the AGC function. Collision Induced Dissociation (CID) was carried out by mass selection of the desired ions with a 1-4 *m/z* window and subjecting them to the following typical conditions: activation energy 10-25 %; activation (Q) 0.25, and activation time 30 ms for analysis in the ion-trap.

3.2.2 Computational methods

All MD simulations described here were performed using the HyperChem modelling program, version 7.52[177], on a Windows-based Personal Computer. AMBER99 was the MM force field used in all simulations. The AMBER99 force field was modified as necessary.

The choice of force field was as a direct consequence of previous work completed within the Orbell group. In this regard, Yuriev[174, 178] has previously modelled platinum complexation with various nucleic acid derivatives, using both a general organic molecule force field, MM+, as well as a specialised force field, AMBER. Given that AMBER is specifically designed to model nucleic acids, this was the most effective force field to use, as MM+ lacked many of the parameters that specifically describe the nucleoside ligand.

The AMBER force field was originally developed by the group headed by Kollman[179-181] and was developed specifically for the modelling of molecules of biological origin, mainly proteins and nucleic acids[179]. The AMBER99 force field used in this work is also parameterised in HyperChem to model some inorganic atoms, such as iron, lithium, alkali and alkaline earth metals, as well as the halogens. As the systems of interest in this study contain platinum atoms, parameters were required to be added to the force field so that the characteristics of this metal atom could be included in the simulations.

3.2.2.1 AMBER99 atom types and parameters

Parameters describing the immediate environment of the platinum in complexes of the kind Pt(II)(dien)(Nuc), where Nuc is a nucleoconstituent, have been previously described by the Orbell group[174, 178]. These have been used in the present study, where Nuc = deoxyguanosine. These parameters were developed using the *Valence Force Field* (VFF) method, as this does not require constraints on any atom, and is relatively accurate. The VFF method will be discussed further in section 3.3.2.

The missing parameters that were added to the AMBER parameter files for the dien carrier ligand (i.e. all parameters involving the platinum atom) are shown in Table 3.1, with the atom types of $[Pt(dien)(dG)]^{2+}$ represented in Fig. 3.3. The hydrogen atoms, which were involved in the simulations, have been removed for clarity. All dG residues have the same atom types.

The NTT and NTC atom types are analogous to the NT atom type as defined for the AMBER99 force field in HyperChem. The stereo assignment was required to conserve the planarity of the platinum centre. All parameters involving the NTT and NTC atom types are identical to parameters for the NT atom type already parameterised in AMBER99. For example, the CT-NT* bond stretch parameters, where * = T or C, are identical to the CT-NT values originally deployed in the AMBER99 parameter files. All parameters which include platinum are as previously published[174, 178].

The terpy system also required additional parameters, displayed below (Fig. 3.4 and Table 3.2). In this system, the NCC and NCT atom types represent the NC atom type, with stereo designation to conserve planarity. Again, only the parameters directly involving the platinum atom are tabulated, with all other parameters involving the NCT and NCC atom types as per the AMBER99 force field.

Table 3.1 – AMBER parameters added for the simulations involving dien as the carrier ligand

(a) Atom Type parameters

Atom Type	Mass	Description
PT	195.09	Platinum atom
NTT	14.01	Dien nitrogen atom *trans* to nucleoside
NTC	14.01	Dien nitrogen atom *cis* to nucleoside

(b) Bond Stretch parameters

Bond	$l_{i,0}$	k_i
PT-NTC	2.038	366.0
PT-NTT	2.038	366.0
PT-NB	2.035	366.0

(c) Angle Bend parameters

Angle	k_i	$\theta_{I,0}$
NTT-PT-NTT	42	180
NTC-PT-NTT	42	90
NB-PT-NTC	42	180
NB-PT-NTT	42	90

(d) Non-bonded parameters

Atom Type	σ	ε
NTT	1.824	0.12
NTC	1.824	0.12

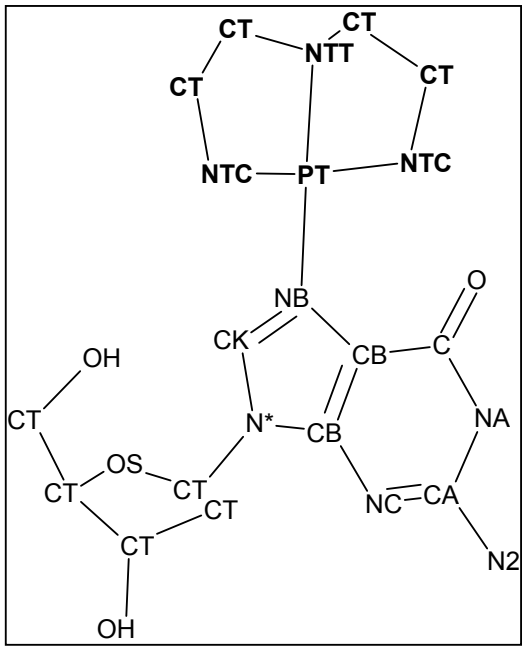

Figure 3.3 - Atom types for [Pt(dien)(dG)]2+. Atom type H describes the hydrogens bound to NTC and NTT atoms. The HC atom type describes the hydrogens bound to CT.

With respect to the parameterisation of the platinum centre of the terpy system, an iterative process was used in order to describe the expected geometry. A semi-empirical PM3 equilibrium geometry structure[98] of $[Pt(terpy)(dG)]^{2+}$ was used as the benchmark and, with the equivalent dien parameters as a starting point, the bond stretch and angle bend parameters for all platinum parameters were iteratively adjusted until a structure equivalent to the PM3 geometry was obtained in HyperChem[173].

Table 3.2 – Additional AMBER parameters added for the simulations involving terpy as the carrier ligand

(a) Atom Type parameters

Atom Type	Mass	Description
PT	195.09	Platinum Atom
NCT	14.01	Terpy nitrogen atom *trans* to nucleoside
NCC	14.01	Terpy nitrogen atom *cis* to nucleoside
CMT	12.01	sp^2 carbon atom bonded to heterocyclic nitrogen in terpy ligand
CBT	12.01	sp^2 carbon atom linking 6-membered rings in terpy ligand

(b) Bond Stretch parameters

Bond	$l_{i,0}$	k_i
PT-NCC	2.038	366.0
PT-NCT	2.038	366.0

(c) Angle Bend parameters

Angle	k_i	$\theta_{I,0}$
NCT-PT-NCT	42	161.4
NCC-PT-NCT	42	80.0
NB-PT-NCC	42	180
NB-PT-NCT	42	90

(d) Non-bonded parameters

Atom Type	σ	ε
CMT	1.908	0.086
CBT	1.908	0.086
NCT	1.824	0.17
NCC	1.824	0.17

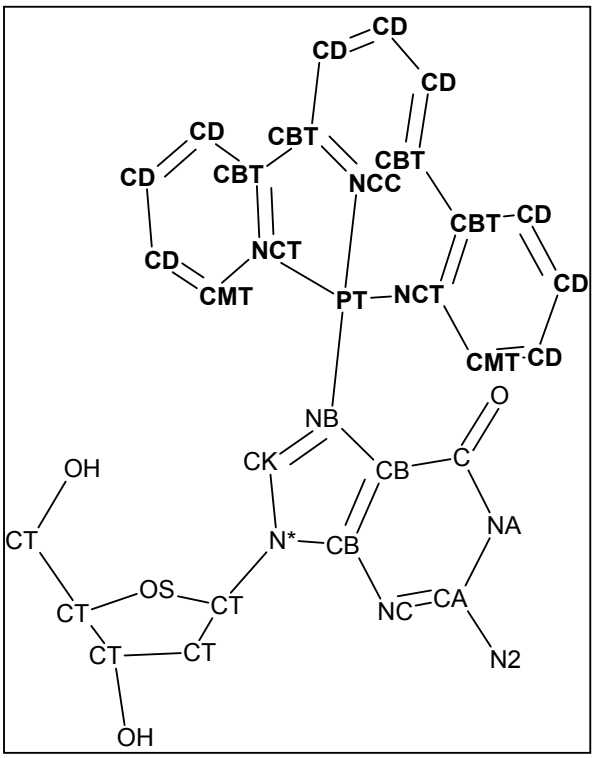

Figure 3.4 - Atom Types for [Pt(*terpy*)(dG)]$^{2+}$. Atom type HC describes the hydrogens bound to CD atoms. H1 is the atom type assigned to the hydrogen bound to the CMT atoms.

3.2.2.2 Cluster construction

3.2.2.2.1 Linear conformation

A linear chain of dG nucleoside residues of the desired length was constructed, using the dG template in HyperChem. This template actually

consists of the 5′-monophosphate nucleotide; therefore the phosphate group was simply removed. The guanosines were hydrogen bonded together as shown, then platinum species was covalently bound to the terminal N(7) position, Fig. 3.5.

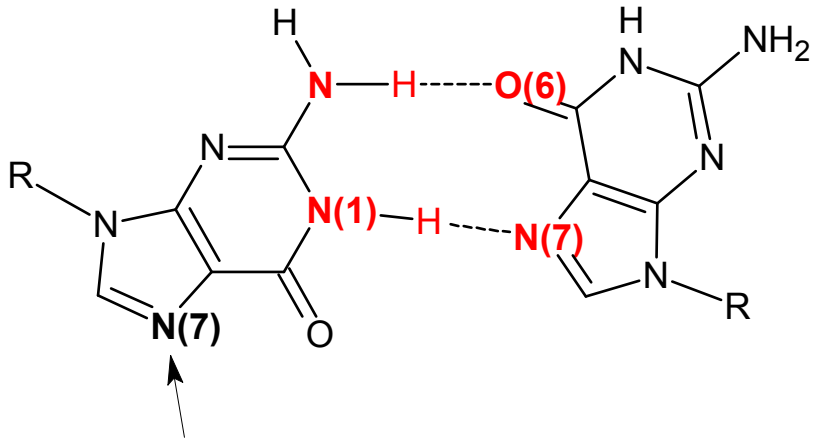

Figure 3.5 – Representation of hydrogen-bonding scheme in linear construct before cluster formation, where R = deoxyribose, (which have been removed here for clarity) and the arrow indicates the terminal N(7).

Atom types for the dG residues were as assigned by HyperChem. The atom types assigned to the platinum carrier ligand systems are described in Figs. 3.3 and 3.4, as shown above, along with a discussion regarding these missing parameters. All electrostatic partial charges were calculated separately, using a semi-empirical method.

3.2.2.2.2 Electrostatic partial charges

Utilising semi-empirical equilibrium geometry calculations using the Spartan ’02 program[182], the electrostatic partial charges were extracted and applied to the corresponding atoms in the linear constructs in HyperChem. The semi-empirical PM3 molecular orbital procedure was used to calculate the partial charges of the $[Pt(L)(dG)]^{2+}$ complexes, whilst AM1 was used to calculate a free dG residue (Fig. 3.6). This is due to the fact that PM3 is parameterised for transition metal-containing species as well as organic atoms, whilst AM1 only deals with organic compounds.

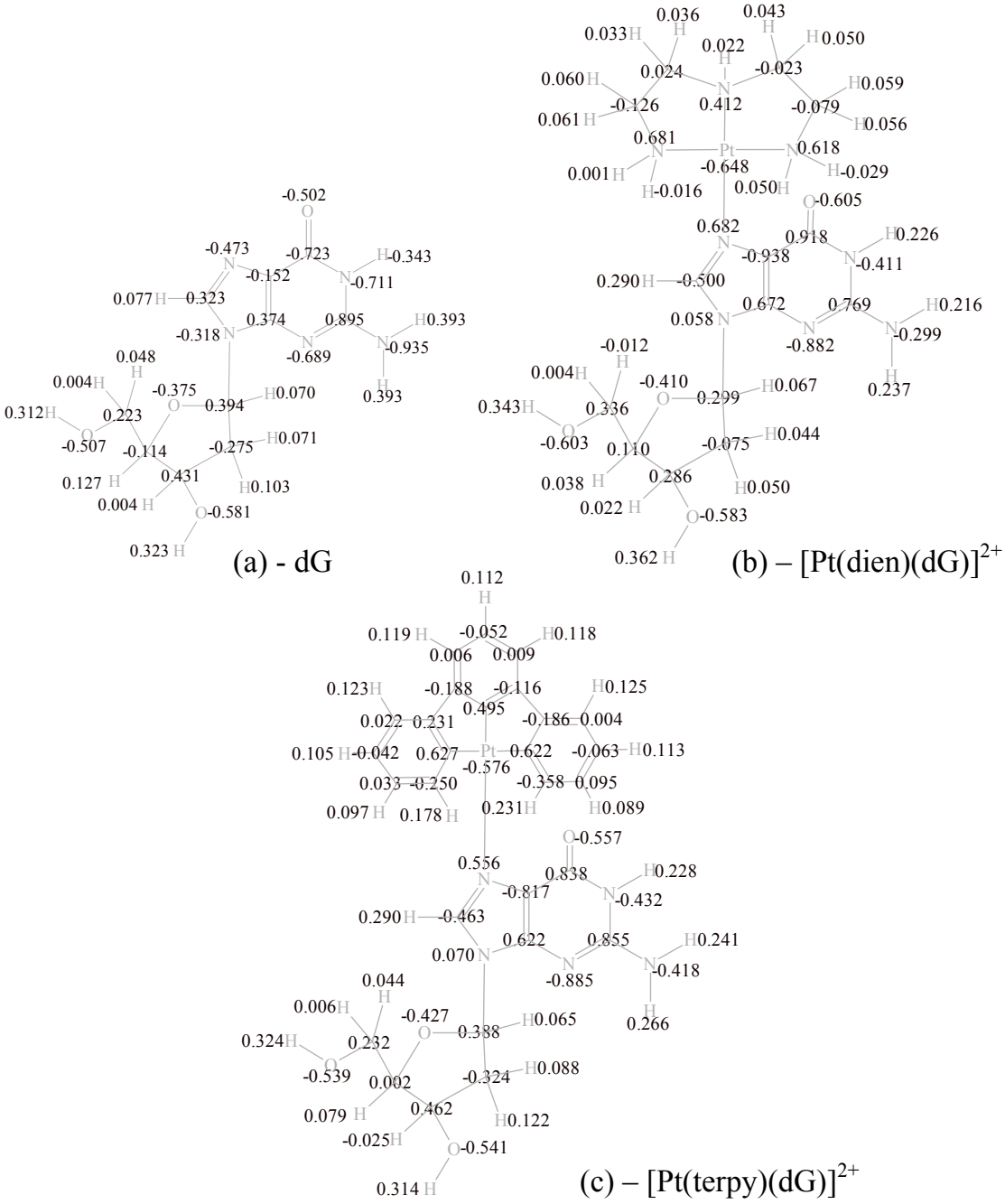

Figure 3.6 – Electrostatic partial charges used for all simulations, as calculated via AM1 (a) and PM3 (b and c).

These semi-empirical methods were used for the electrostatic potentials due to the fact that they are based on measurements of experimental values, such as bond lengths and angles to calculate the wavefunction. This allows for the production of accurate electrostatic partial charges. These charges are important with respect to these clusters, as inter-molecular electrostatic interactions *in vacuo* are of great importance in the formation and dissociation of these clusters.

3.2.2.2.3 Cluster formation

Each linear construct, $(dG)_{n-1}(dG\text{-}PtL)$, n = 3 – 10, was submitted to geometry optimisation using the Polak-Ribière conjugate gradient algorithm *in vacuo* to an RMS gradient of 0.1 kcal/(Å x mol). This ensures that subsequent cluster formation simulations start from an energetically favourable structure. Figs. 3.7a and 3.7b depict structural representations of the starting formation for n = 3.

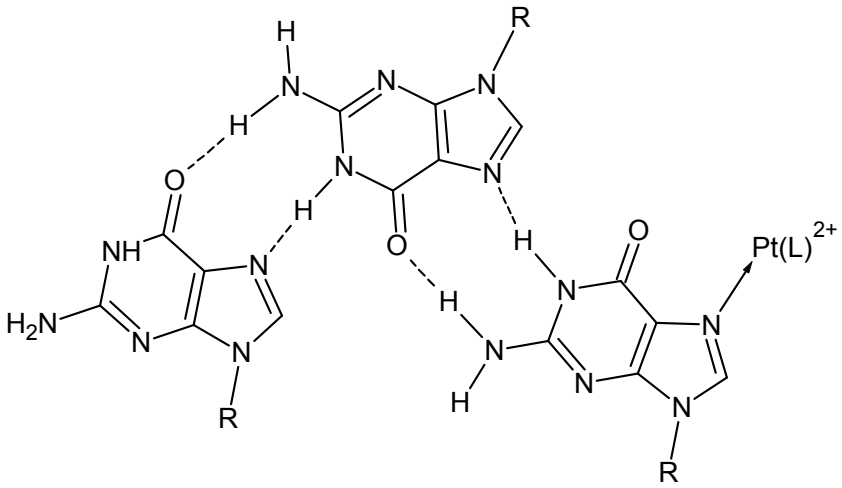

Figure 3.7a – Schematic representation of $(dG)_{n-1}(dG\text{-}PtL)$, n = 3, starting structure for cluster formation. R = deoxyribose groups. L = ligand (dien or terpy)

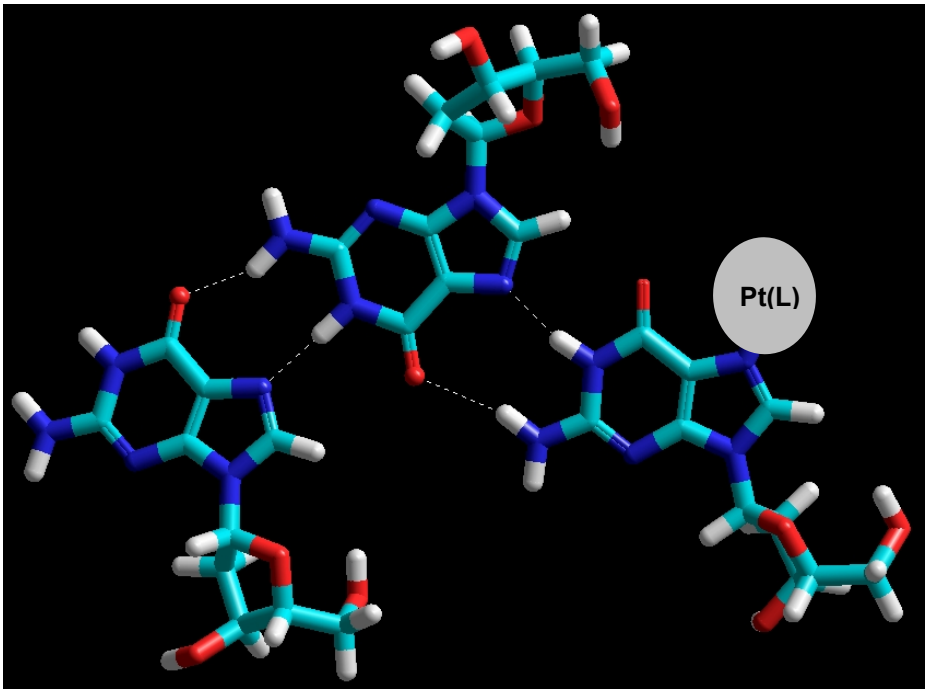

Figure 3.7b – The geometry optimised structure for $(dG)_{n-1}(dG\text{-}PtL)$, n=3.

From the geometry optimised structure, all the atoms of the dG residues *not* bound to the platinum molecule, as well as all the atoms of the *deoxyribose moiety* of the bound dG residue, were selected to be included in the MD simulation. All selected atoms were then simulated at the following conditions, Table 3.3, to induce initial cluster formation.

Table 3.3 – Conditions for cluster formation simulations.

MM Force Field options	
Dielectric (ε)	Constant
1-4 Scale factors - Electrostatic	0.5
1-4 Scale factors – van der Waals	0.5
MD options	
Run Time	1000ps
Step Size	0.0005ps
Simulation Temperature	300K
In vacuo	Checked

3.2.2.3 'Selection' of atoms

Whilst the above parameters were added for both carrier ligands, some precautions were taken when the clusters were 'collided'. Whilst these added parameters reproduce geometries at relatively low temperatures, i.e. room temperature (300 K), the behaviour at higher temperatures was unknown. Coupled with the fact that improper torsions were not parameterised around the platinum centre, the atoms of the carrier ligand as well as the immediately bound dG residue were ignored. This was achieved by selecting the unbound dG residues, as well as the deoxyribose moiety of the bound dG residue.

The effect of this selection was essentially the protection of the geometry of the platinum and the carrier ligand. The atoms that were not selected were removed from the dynamics. However non-bonding parameters and electrostatic potentials were still available, resulting in a stable platform for the analysis of the collisions. This removes the possibility of the simulations failing due to

excessive movement of the carrier ligand upsetting the clusters, as well as the requirement to exhaustively define all torsions relating to the carrier ligand, which would be many with respect to the terpy ligand.

3.2.2.4 Collision simulation and analysis

The following computational method (Table 3.4) was adopted in order to simulate the CID within the ESI instrument. Once parent clusters are obtained, as described previously, these are used as starting points for collision simulations, without further optimisation. This simulates the experimental process, as the gas-phase parent clusters would not be expected to be at an energetic minimum.

Table 3.4 – Collision simulation (molecular dynamics) conditions.

Times (ps)		**Temperatures (K)**	
Heat time	0.5	Starting Temp	300
Run time	25	Run Temp	Varied
Cool time	5	Final Temp	300
Step size	0.0005	Temperature step	15

Collision simulations were carried out by performing molecular dynamics calculations, at a range of run temperatures, on all parent clusters from n = 3 to n = 10, for both ligand systems. These simulations ranged from temperatures where there was no dissociation, through to temperatures where the remaining cluster is approximately 25% of the initial size. This sampling regime led to a wide range of simulation energies, with some parent clusters sampled at more than 20 different energies, all at 50K intervals.

Each collision simulation was analysed individually to determine the size of the daughter (referred to as n`) cluster that remained after each simulation is 'cooled'. Appropriate non-bonding interactions were accounted for when determining the size of the remaining n` cluster, as the dG residues were required to be interacting (directly or indirectly) with the platinum-containing moiety.

This extensive range of internal energies allowed for the accumulation of a sufficient data set for statistical analysis.

3.2.2.4.1 Statistical analysis

A probabilistic analysis was used to determine the relative proportion of each of the different n` clusters arising from all of the simulations of each parent cluster, whereby the most abundant n` cluster (the 'magic number') can be identified. The analysis utilizes a linear approximation of a Gaussian distribution curve, Fig. 3.8.

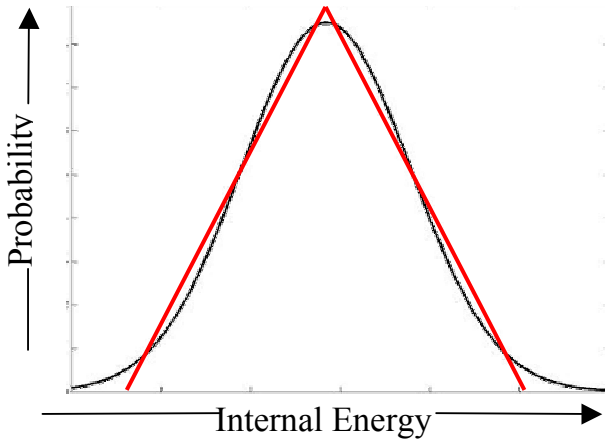

Figure 3.8 – Linear approximation (red) of a Gaussian Probability Curve (black)

The analysis of the simulation results required some assumptions to be made, which were drawn purely from the experimental procedure before the statistical analysis was carried out. The assumptions used were:

1. Due to the degree of randomness regarding the collisions in the ion trap of the ESI-MS/MS, a range of collision energies is produced that would be reasonably expected to follow a standard Gaussian probability curve. Whilst some clusters would receive passing blows and other clusters may be involved in secondary collisions, most clusters would be expected to receive an 'average' amount of energy. As these collisions occur many times in the instrument, an approximation of a Gaussian-type curve would reasonably be expected to arise, Fig 3.9.

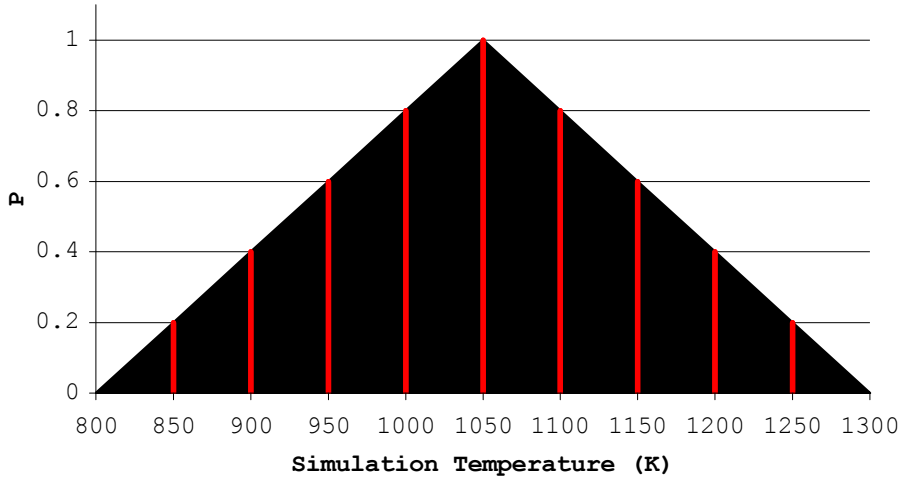

Figure 3.9 – The assignment of P values to simulation temperatures for the n = 5 dien example. The black area estimates the range of energies available in the CID of the ESI-MS/MS, and the red lines represent the discrete sampling by the computational collisions, where the 'Simulation Temperature' is equivalent to the 'Run Temp' in Table 3.4 above.

2. The increase in internal energy experienced by the clusters at the time of, and immediately after, collision in the instrument has been modelled as an appropriate increase in the *in silico* simulation temperature, Fig 3.9. With this assumption, the 'temperature' of simulation is a representation of the internal energy of the cluster, rather than the actual temperatures reached within the ion trap. Also, the relatively long 'run time' of the simulation (25 ps) where the cluster is held at a particular temperature, is designed to account for secondary collisions within the ion trap. Secondary collisions imply that when some clusters, which have collided once, may further collide within the ion trap, hence leading to a delay in energy dissipation.

3. The range of possible internal energies of the clusters within the ion trap increases as the size of the cluster increases. This is due to the fact that a larger cluster has a larger surface to be collided, and therefore has a higher probability of receiving a "passing blow" (a lower amount of energy). Also, a larger surface also increases the probability of secondary or multiple collisions, leading to energies greater than the 'normal' being received.

The value used to define the probability in the remainder of the Chapter is Sum(P), where the probability of that particular energy occurring in the ion trap is P, an arbitrary value representative of an approximation of Gaussian behaviour. Sum(P) is the addition of all P values for like n′ clusters. Fig. 3.10 and Tables 3.5 and 3.6 illustrates an example of this method using the n = 5 collision data for the dien ligand, including a graphical representation of the assignment of P.

Table 3.5 – Probability data for the n = 5 dien collisions, determined computationally.

Simulation Temp. (K)	n′	P
850	5	0.2
900	4	0.4
950	4	0.6
1000	5	0.8
1050	5	1
1100	4	0.8
1150	3	0.6
1200	3	0.4
1250	3	0.2

Table 3.6 – Sum (P) values for the data from the above table. Note the parent cluster size, in this case n′ = 5, is not included in the Sum (P) table.

Cluster size (n′)	Sum (P)
1	0
2	0
3	1.2
4	1.8

At this point, a note regarding the nomenclature used in the following discussion needs to be made. When referring to parent cluster size, i.e. clusters before collisions, n shall refer to the number of dG residues in that particular cluster. For clusters that have been subjected to the collision method, the number of dG residues in that cluster is denoted by n′.

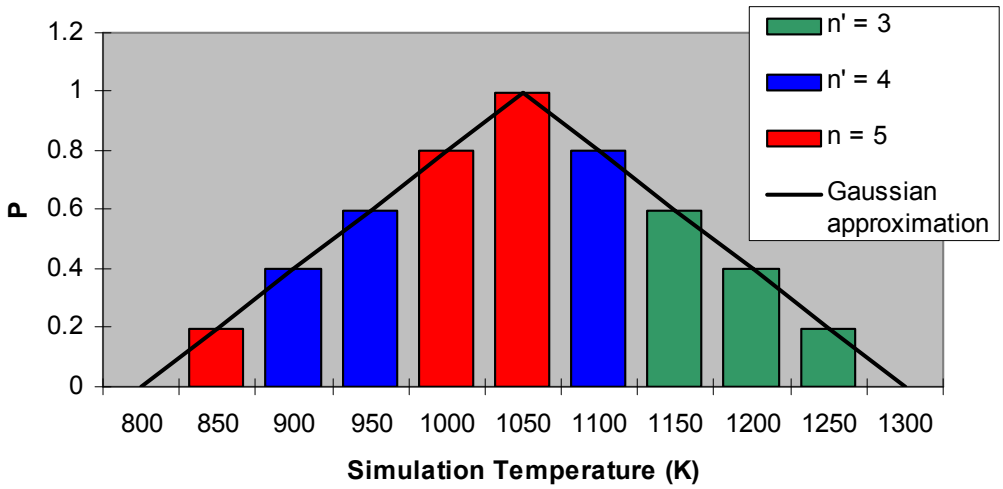

Figure 3.10 – A plot of the data from Tables 3.5 and 3.6, including a representation of the Gaussian approximation. The Sum (P) values for this data are presented below.

This method is repeated for all parent cluster sizes for both carrier ligands. The results of this method, compared to the ESI-MS/MS results, are presented in the results and discussion section.

3.3 RESULTS AND DISCUSSION

3.3.1 Collision induced dissociation of clusters using ESI-MS/MS

The results of the cluster dissociation experiments for the dien carrier ligand are displayed below in Table 3.7. Analogous results for the terpy carrier ligand are given in the following section, 3.3.1.2. This data is represented in terms of relative abundance, compared to the resulting largest cluster. All mass spectra data is given in Appendix I.

3.3.1.1 Relative cluster abundances for the dien system

As can be seen from the table below, an array of different cluster sizes is produced during the collision process involving each parent cluster. Noticeably, and perhaps not unexpectedly, the number of CID-produced clusters increases as the size of the parent cluster increases. From a parent cluster size of n = 5 up to a parent cluster size of n = 10, the appearance of a preferred CID product, defined by n′ = 4 (a magic number), is apparent.

Table 3.7 – ESI-MS/MS results for the [Pt(dien)$(dG)_n$] system showing relative cluster abundances and the magic number phenomenon (n = 4 in this case)

	CID Products (n′)									
n	**1**	**2**	**3**	**4**	**5**	**6**	**7**	**8**	**9**	**10**
3	**100**	12	-	-	-	-	-	-	-	-
4	16	10	**100**	-	-	-	-	-	-	-
5	24	10	80	**100**	-	-	-	-	-	-
6	14	6	48	**100**	26	-	-	-	-	-
7	20	8	48	**100**	36	11	-	-	-	-
8	18	5	41	**100**	53	25	9	-	-	-
9	31	7	43	**100**	58	32	12	18	-	-
10	26	6	38	**100**	72	60	20	8	11	-

The phenomenon of magic numbers (specifically for n′ = 4) has also been observed in previous ESI-MS/MS investigations[33-35] of the clustering of nucleobases and nucleosides in the presence of various cations, including alkali earth cations and NH_4^+. Unlike these previous studies, however, the results around the dominant cluster appear to be distributed in a fashion similar to a normal probability curve, rather than appearing as conspicuous spikes. This observation appears to suggest that the clusters being formed *in vacuo* are not rigid structures similar to the G-quartet, but more transient structures, with the ability to fit slightly more, or slightly fewer, residues around the central cation.

This idea is somewhat supported by the greater-than-expected abundances of the n` = 1 clusters in Table 3.7. This suggests that, in regards to this particular

system, more clusters are formed *in vacuo* that are inherently unstable, such that with a small amount of force, those clusters rapidly disintegrate. Both of these possible outcomes are almost certainly due to the increased bulk around the cation, as well as the potential non-covalent interactions occurring between the dG residues and the carrier ligand. This hypothesis has been further examined with MD simulations, as described later.

3.3.1.2 Relative cluster abundances for the terpy system

Again, as with the dien results, a clear magic number is present, as seen in Table 3.8. However, unlike the magic number obtained for the dien system, this magic number is at n′ = 5 for parent clusters with n > 5. Notably, a magic number of 5 has not been previously reported in other studies of similar systems.

Table 3.8 – ESI-MS/MS results for the [Pt(terpy)$(dG)_n$] system showing relative cluster abundances and the magic number phenomenon (n = 5 in this case)

	CID Products (n′)									
n	**1**	**2**	**3**	**4**	**5**	**6**	**7**	**8**	**9**	**10**
3	15	**100**	-	-	-	-	-	-	-	-
4	2	17	**100**	-	-	-	-	-	-	-
5	1	6	46	**100**	-	-	-	-	-	-
6	0	3	16	70	**100**	-	-	-	-	-
7	0	0	5	28	**100**	85	-	-	-	-
8	0	5	25	67	**100**	64	23	-	-	-
9	0	4	17	52	**100**	93	67	24	-	-
10	0	7	33	72	**100**	74	40	17	4	-

Therefore, to the best of our knowledge, this represents the first experiment where the magic number for such a system is not 4 or a multiple thereof. Given that no prior systems have been investigated where the cationic moiety invokes stacking interactions, as well as hydrogen bond interactions, with the nucleoconstituents of interest, the discovery of a new magic number may be due to the stacking ability of the terpy carrier ligand. Stacking interactions can exert a powerful structural influence, as in DNA itself. Also of interest is the

reduction of n` = 1 relative abundance, when compared to the dien results discussed immediately proceeding. This observation could be supportive of the idea that the stacking ability of the carrier ligand may assist in stable cluster formation, and to resist dissociation, to a degree, of less stable clusters.

For systems where the cationic moiety is represented by a metal complex (rather than a single metal ion in some previous studies), it would appear that the actual value of the magic number is carrier ligand specific. This suggests that the magic number phenomenon might be tunable by an appropriate choice of carrier ligand. In light of the above discussion, a theoretical examination of the phenomenon via MD simulations was considered warranted.

3.3.2 In search of the origin of magic numbers

Given the detailed structural information yielded by the computer-generated parent clusters (Appendix IV), it is reasonable to enquire whether there might be a special confluence of non-covalent interactions that might give rise to preferred aggregates (magic numbers). Indeed, the fact that the magic number value appears to be dependent on the nature of the carrier ligand would suggest this to be the case. Therefore the structures of the parent clusters have been scrutinized and analysed in detail.

As mentioned earlier, contrasting carrier ligands for the platinum were selected due to the difference in their expected non-covalent interactions. Therefore, in the parent clusters, the dien ligand is expected to interact with the dG residues through hydrogen bonding alone, whilst the terpy ligand is expected to form mainly stacking interactions with the dG residues, although this ligand may also form some limited hydrogen bonding interactions. The dG residues themselves are capable of forming both stacking and hydrogen bonding interactions with each other. Less common interactions such as the “dimple effect”, involving the oxygen of the sugar ring and the π-system of an adjacent

guanine[183], and possible axial interaction(s) between the exocyclic oxo of the guanine and the d_z^2 orbital of the platinum[184], have also been considered. For the two different carrier ligands, the relative contribution of these different types of non-covalent interactions to each parent cluster has been analysed. The results are presented in Figs 3.11 and 3.12.

As can be seen from the plots below, clusters of both systems are dominated by hydrogen bonding interactions. This is to be expected given the prevalence of hydrogen bonding donor and acceptor groups present in the nucleosides, including the deoxyribose moiety and in the carrier ligand, in the case of dien. As expected, clusters of the terpy system show significantly more stacking interactions than the dien system.

It is of interest to consider the nature of the non-covalent interactions in the specific parent clusters defined by n = 4 for the dien system and n = 5 for the terpy system. These structures are shown in Fig. 3.12 and 3.13 respectively.

Notably, from the results displayed in Fig 3.13, the n = 4 aggregate for the dien system is unique in that it involves hydrogen bonding only. The histogrammed results shown in Fig 3.14 for the terpy system, although dominated by hydrogen bonding, also involves some stacking interactions. How these differences in non-covalent interactions influence the behaviour of these clusters in the MD simulations will be examined in the next section.

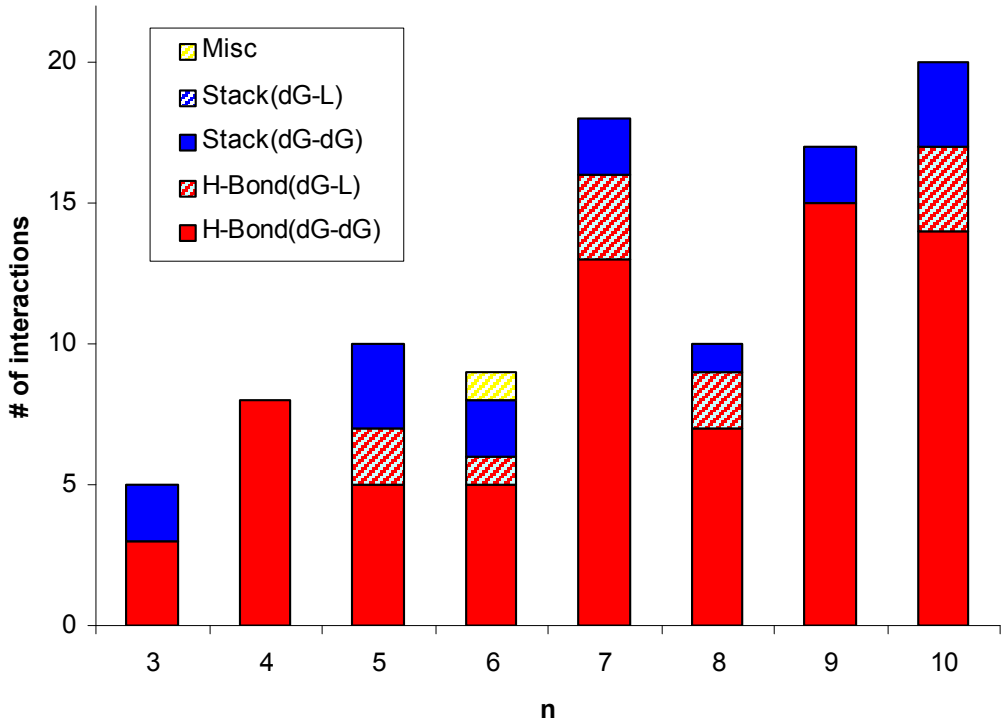

Figure 3.11 – Analysis of specific interactions within each parent cluster of type $[Pt^{II}(dien)(dG)_n]$. Note the influence of the hydrogen-bonding centres in the dien carrier ligand, and the absence of direct stacking interactions with dien.

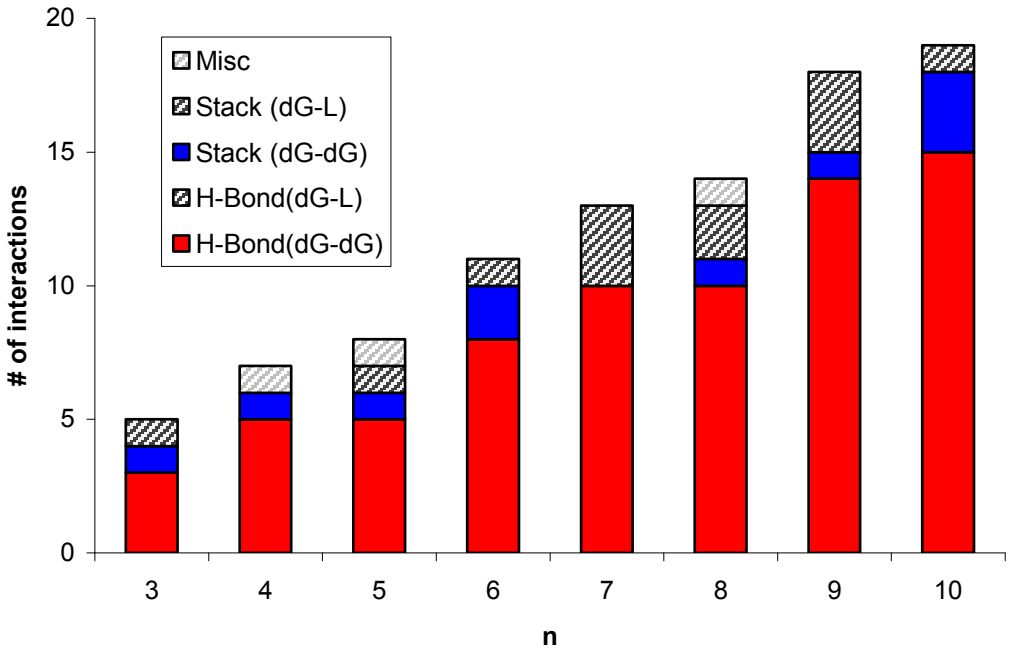

Figure 3.12 – Analysis of specific interactions within each parent cluster of type $[Pt^{II}(terpy)(dG)_n]$. Note the large effect on stacking interactions as a direct result of the aromaticity of the terpy carrier ligand.

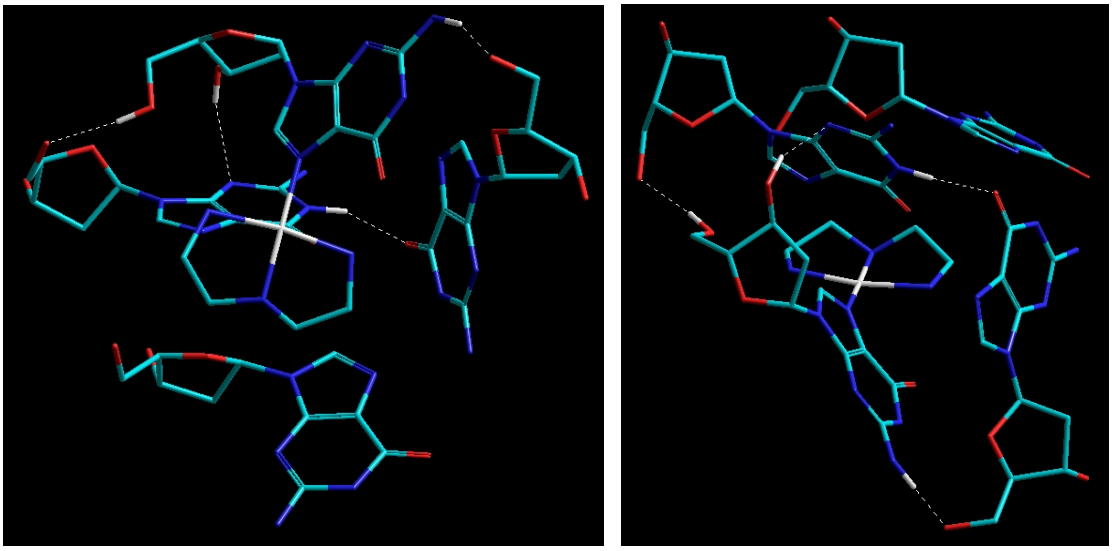

Figure 3.13 – Different views of the dien n = 4 cluster showing hydrogen bonds (dotted lines). This structure is the result of the cluster formation MD simulation. A pdb file of this structure can be found in Appendix IV.

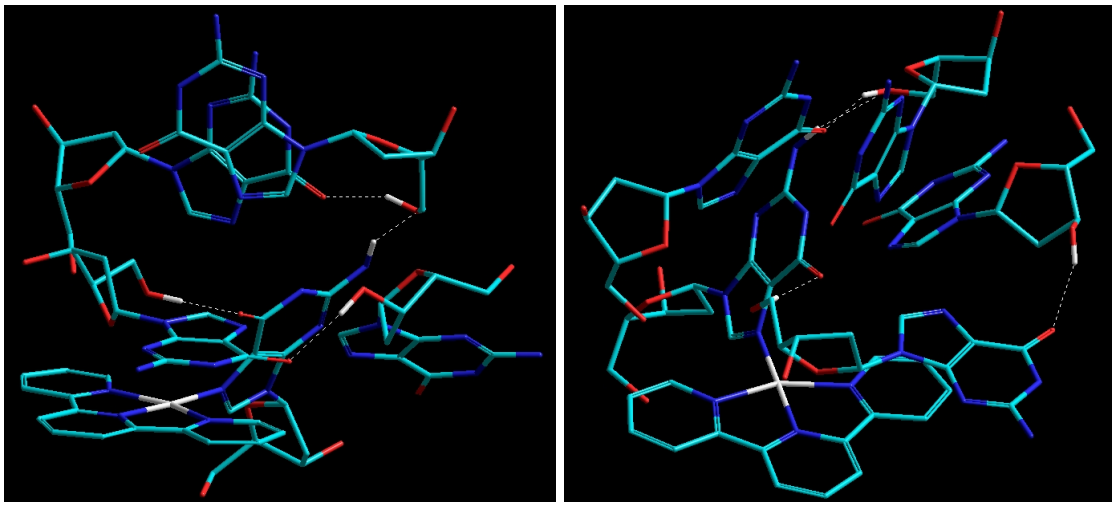

Figure 3.14 – Different views of the terpy n = 5 cluster, as produced from the cluster formation MD simulation method. Hydrogen bonds are represented by dotted lines. Note the stacking interactions in the top image (base-base and base-ligand). A .pdb file of this structure can be found in the Appendix IV.

3.3.3 Analysis of the MM collision simulations

As mentioned previously, in order to fully investigate the 'magic number' phenomenon detected in the ESI-MS/MS results, a computational model of the CID process was developed. This model was designed to duplicate the experimental results, with the aim of elucidating the mechanisms involved.

3.3.3.1 Computational Results

3.3.3.1.1 Dien results

Over the following two pages, plots of the comparison between the computationally derived probability scores are compared to the results obtained experimentally, Fig. 3.15.

All graphs in Fig 3.15 from parent cluster sizes of between 5 and 10, peak at the 'magic number' of n′ = 4, with the smaller starting clusters closely resembling the empirical data. The quality of these plots can be summarised into Table 3.9, which shows the correlation scores for each plot.

Table 3.9 - Summary of the dien computational results

Parent cluster size (n)	Correlation score[1]
3	1
4	0.968
5	0.987
6	0.951
7	0.949
8	0.804
9	0.864
10	1

[1]Correlation score was calculated using the CORREL worksheet function as implemented in Microsoft Excel 2000

These results indicate that the methods used here to simulate the collisions are reflective of actual processes. This is supported quantitatively with the successful identification of a magic number, as well as qualitatively, with the relative abundance profile closely matched.

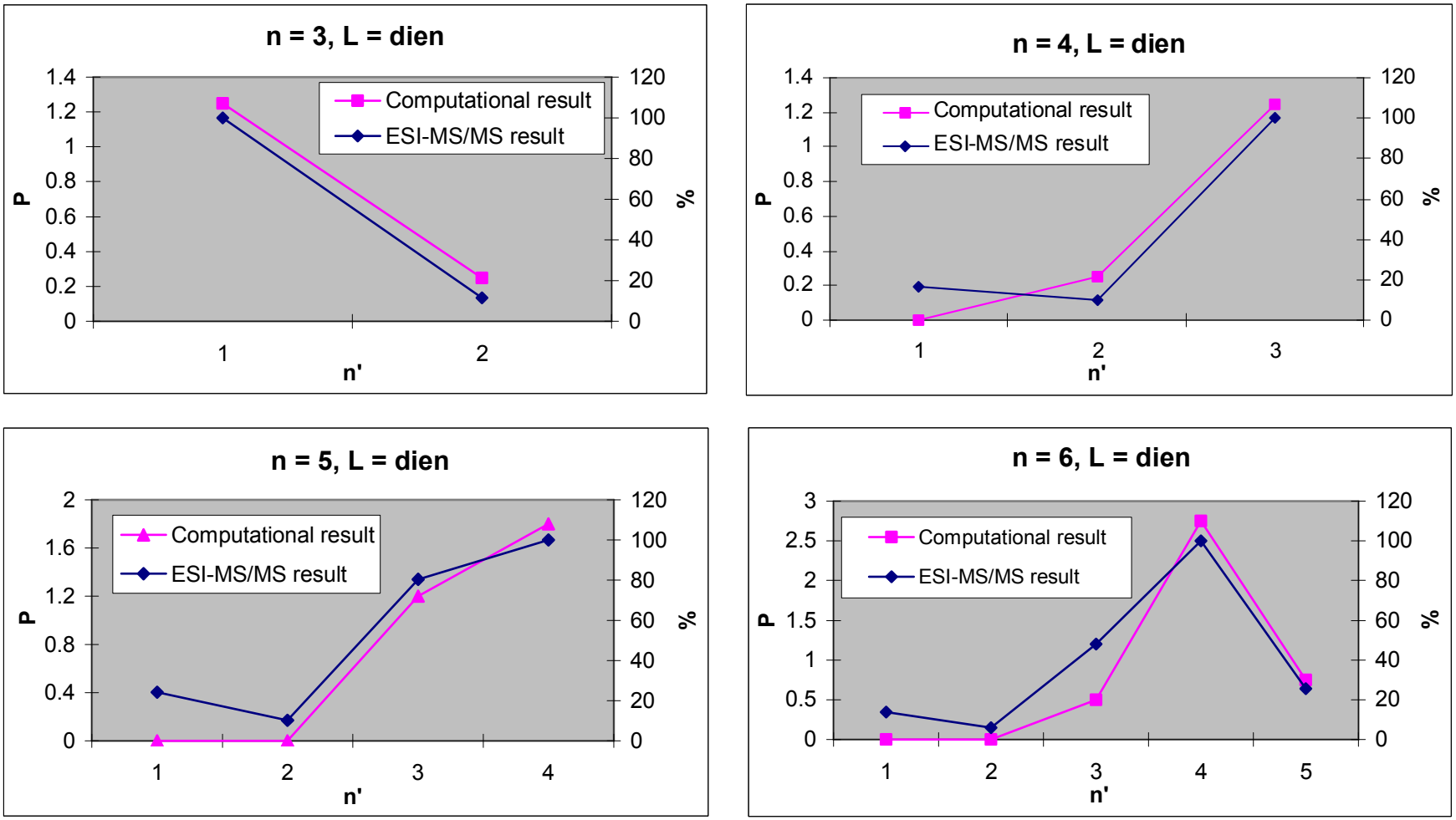

Figure 3.15a – Graphs comparing computationally determined probability scores (P) versus % abundance from ESI-MS/MS spectra (%) for L = dien and parents clusters from n = 3 to n = 6.

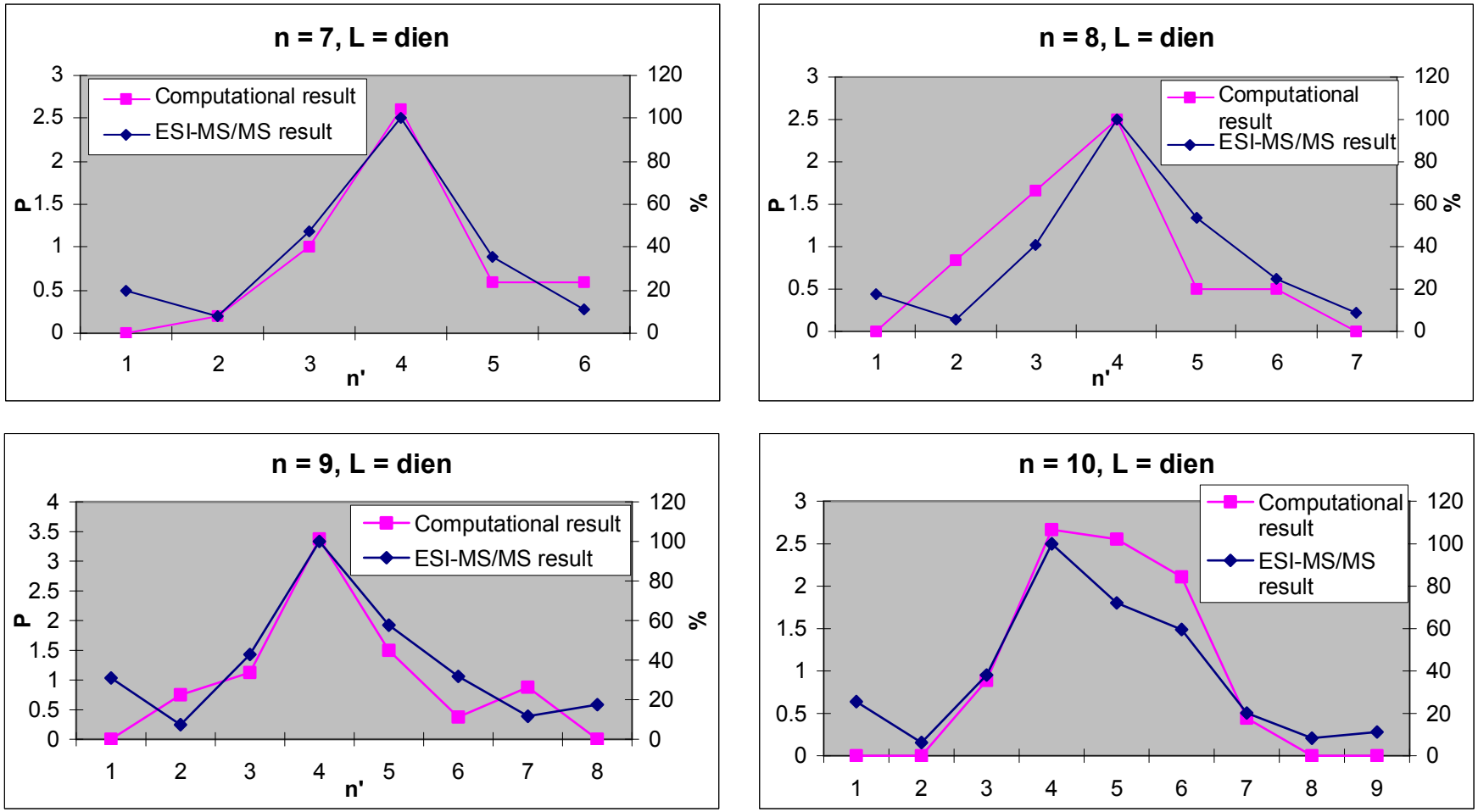

Figure 3.15b – Graphs comparing computationally determined probability scores (P) versus % abundance from ESI-MS/MS spectra (%) for L = dien and parents clusters from n = 7 to n = 10.

The correlation scores in Table 3.9 also indicates that the parameterisation concerning dien as the carrier ligand, which was taken from the literature, is reasonable. This is due to the fact that the resulting behaviour of this ligand system *in vacuo* agrees well with experimentally derived data, insofar as the magic number was reproduced, both quantitatively as well as qualitatively, with the majority of the computational profiles closely resembling the experimental profile. However, one aspect of all of the experimental profiles that were not adequately replicated were those attributed to the n` = 1 clusters.

After due consideration, a possible explanation regarding the failure of the model developed here to duplicate the n` = 1 signals for this ligand system lies somewhat in the assumptions that were used during the model development. In order to simplify the actual processes occurring in the ESI-MS/MS ion trap, a sampling scheme of simulations were used. This sampling scheme simplified two aspects of the experiment; firstly, self-aggregation of only one parent cluster was formed, and this cluster was used as a starting point for all collision simulations of this cluster size and type. Secondly, the internal energy of the clusters during the simulation (i.e. the run temperature) was sampled at 50K intervals.

This differs from the experimental procedure, as both the parent cluster conformation, as well as the internal energies of all clusters before, during and after collision(s) would reasonably be expected to be continuous, rather than the discrete samples that were used for this model. In this regard, it is likely that, in the experimental procedure, less stable (i.e. higher energy) parent clusters are formed in the gas-phase of the instrument. Given the relative inherent instability of these parent clusters, during the collision process these would be expected to fragment easier than the more stable structures. This would lead to an increase in the signal for n` = 1 in the experimental procedure, yet not in the model, as these less stable starting structures were not examined. Therefore, the inability of this model to predict n` = 1 magnitude is merely a sampling (i.e. computational time) issue, rather than an inherent failure of the simulation.

3.3.3.1.2 Terpy results

Again, as with the corresponding plots describing the dien results above, a generally good agreement between experimental and computational results was obtained. Table 3.10, below, shows the quantifying of this agreement. These plots are shown over the following pages, Fig. 3.16.

Table 3.10 - Summary of the terpy computational results

Parent cluster size (n)	Correlation score[1]
3	1
4	0.989
5	0.998
6	0.940
7	0.773
8	0.876
9	0.727
10	0.856

[1]Correlation score was calculated using the CORREL worksheet function as implemented in Microsoft Excel 2000

As can be clearly seen from this data, the agreement between the computational and experimental results is generally very good, with the magic number identification at all increments of n. This is an excellent outcome, as the methodology used for this ligand system is exactly the same as that used for the dien ligand, yet both systems interact non-covalently in significantly different ways. This demonstrates the inherent strength of this model, even at the relatively course sampling intervals employed through this study. However, it must be noted that, whilst these correlation scores are still high enough to determine that a very good correlation exists, the scores for clusters of size n = 7 and greater are not quite as good as those achieved for the dien.

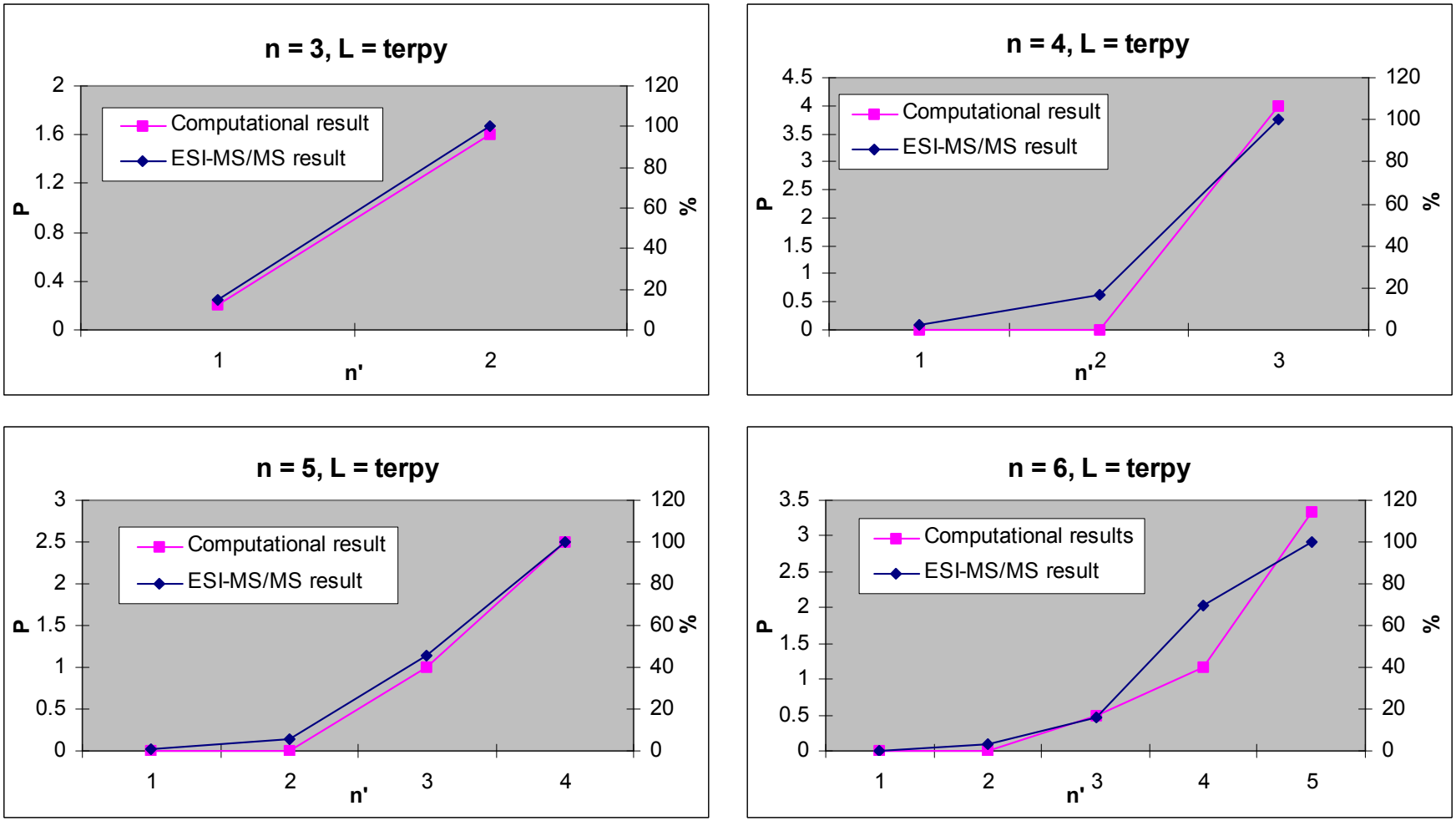

Figure 3.16a – Graphs comparing computationally determined probability scores (P) versus % abundance from ESI-MS/MS spectra (%) for L = terpy and parents clusters from n = 3 to n = 6.

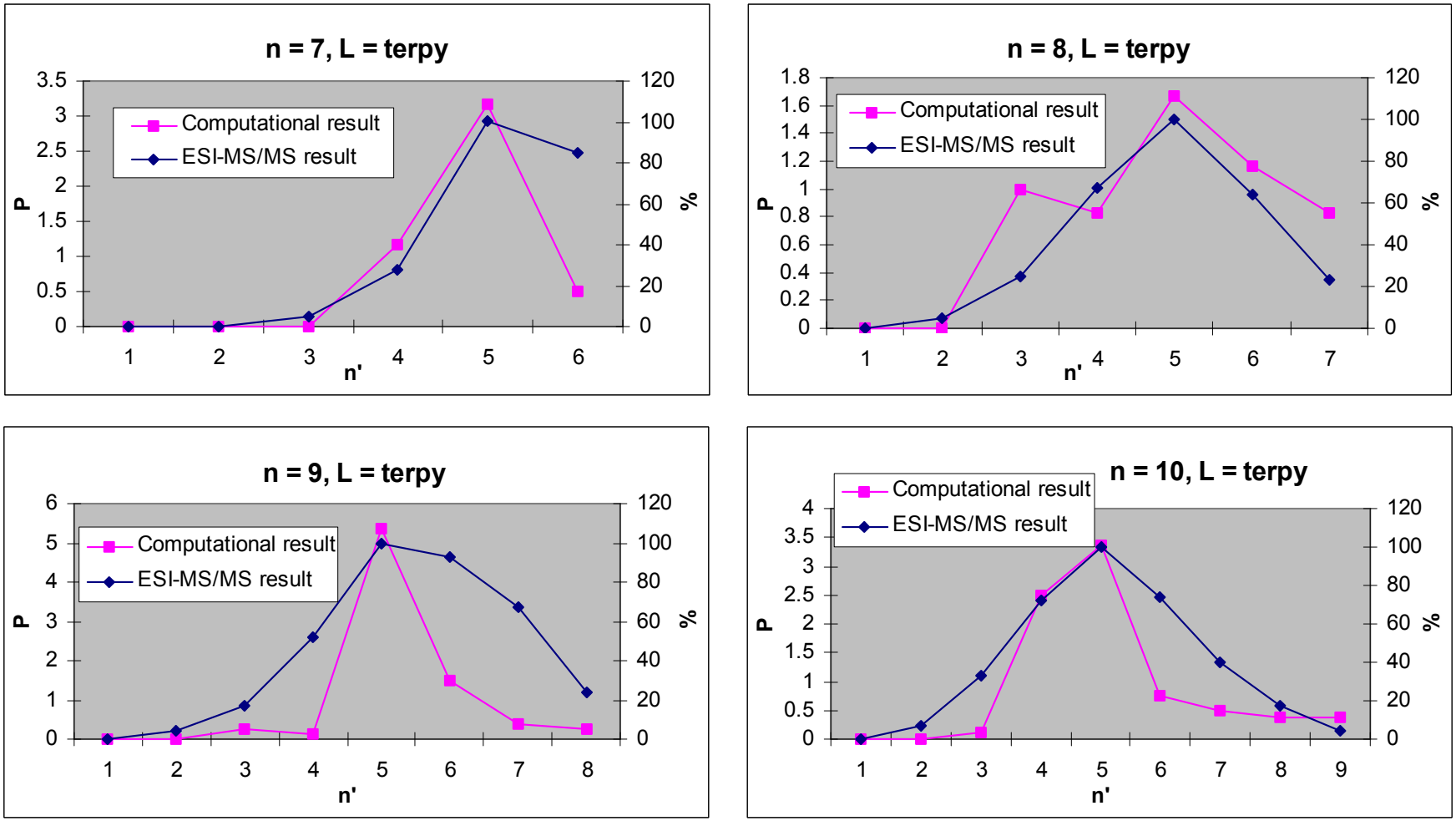

Figure 3.16b – Graphs comparing computationally determined probability scores (P) versus % abundance from ESI-MS/MS spectra (%) for L = terpy and parents clusters from n = 7 to n = 10.

The reason for this greater departure from perfect correlation, compared to the dien ligand results, is difficult to identify, as any problems with the parameterisation should have also affected the results of the smaller clusters as well. One possibility may be an inherent sensitivity to temperature.

Given the relatively weak, transient nature of pi-stacking interactions, any slight movement in the terpy ligand, or the dG residue, could disrupt these interactions. Such movement may occur during the collision simulations, where the parent clusters are excited through an increase in the run temperature. This would affect the accuracy of the simulations, especially at larger cluster sizes. Further factors that are common to both ligands will be discussed in 3.3.3.3 below. This effect would be complementary to the same sampling constraints discussed for the dien ligand above, given that the same modelling methodology was used for both ligand systems.

3.3.3.2 Comparison of both ligands

The results above show that this method stands up well to the simulation of physical processes that occur within the gas-phase of the ESI-MS/MS technique. However, the quality of the correlation decreases above n = 8 for dien and n = 7 for terpy. The reasons behind this may be due to the same factors, rather than being ligand specific.

Sampling size – For both carrier ligands, the same method was applied, which involved simulating collisions every 50K, and measuring the size of the platinum-containing cluster that resulted. Given that the processes of the CID within the ESI-MS/MS would effectively generate a continuum of internal energies, the method used here samples only a small fraction of potential energies. The effective error associated with the results as more residues are added to the parent cluster would increase. This would result in a decrease in accuracy at higher values of n, appearing as a decrease in correlation score.

Starting conformation - As the number of residues in the parent clusters increases, the possible number of conformations of the parent clusters would rapidly increase. However, the collision simulations were performed on a single starting parent cluster conformation. Any differences between the computational starting cluster and the multitude of possible experimental parent cluster conformations would be amplified when these two data sets are compared, which in turn would increase the error of the simulations carried out at larger values of n. This source of error may be reduced if the collision methodology were carried out on a range of starting conformations, however this would also rapidly increase the calculating time, whereas greater sampling may increase correlation scores with a smaller time investment.

Parameterisation – Another possibility as to the departure of the terpy results from near-perfect correlation may be related to the parameterisation of the ligand. Whilst care was taken during parameterisation, this process was not necessarily exhaustive. As such, several force constants or non-covalent interaction parameters may not have been as accurate as the dien parameters.

3.3.3.3 Summary

This Chapter aimed to develop a model, based on molecular dynamics simulations as well as statistical analysis, to replicate the ESI-MS/MS process used to experimentally study fragmentation patterns of $[Pt(L)(dG)_n]^{2+}$ clusters. This model was developed not just to reproduce experimental results, but to also give insights into the formation and dissociation of these clusters, given their unusual fragmentation profiles.

As seen in Figs. 3.15 and 3.16, the model described here gives an excellent representation of the experimental results. This allows for some confidence to be placed in this model, especially concerning the identity of the magic numbers for different ligands. An analysis of the parent clusters suggests

that the non-covalent interactions are important regarding the formation (and reformation) of these clusters, and that hydrogen bonding seems to have a stabilising effect, whilst stacking interactions appear to introduce rigidity to the clusters, which may have a destabilizing effect.

Chapter 4

ESI-MS and computational investigations of the interaction of sterically restrictive platinum(II) and palladium(II) complexes with nucleobases and nucleosides

4.1 INTRODUCTION

4.1.1 Preamble

As mentioned in the previous Chapter, the role of metal ion interactions with biological molecules in general, and nucleic acids in particular, has been scrutinised for many years[36]. Whilst the previous Chapter focuses on aggregation via non-covalent interactions, this Chapter investigates possible ways of influencing the covalent binding of metal species to nucleic acid constituents, specifically via the judicious manipulation of steric effects.

Such metal ion – nucleic acid interactions are a rich area of investigation in coordination chemistry. Nucleotides may interact with a metal ion through either the phosphate group(s), the sugar moiety or the base itself[185]. Further to this, the base itself may covalently interact through various sites, e.g. adenine normally offers N1, N3 or N7 for coordination[185], Fig 4.1, and various modes of co-ordination are also possible.

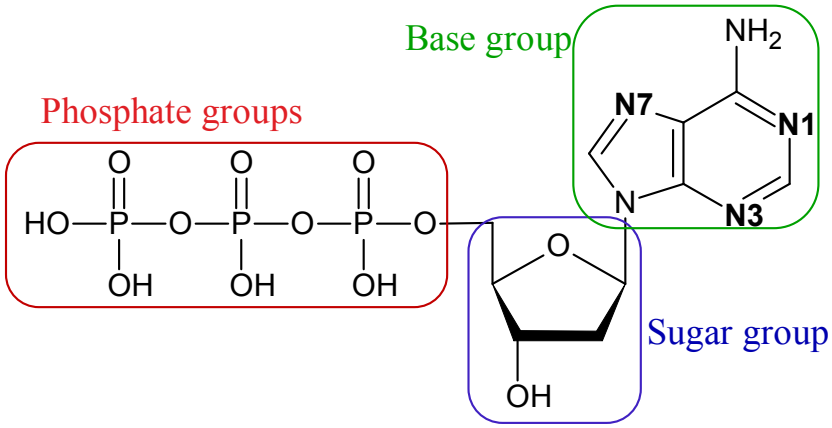

Figure 4.1 – Structure of 5'-adenosinetriphosphate (5'-ATP). Coordination sites are numbered and marked in Bold.

With such a vast backdrop of possible interactions to discuss, some focussing is required. Therefore, this chapter will be concerned with species involving platinum(II) and palladium(II), since their square planar geometries are

well defined and carrier ligands, with a variety of structural attributes, are relatively easily introduced. In addition, a large body of work has been carried out on the interaction of such complexes with nucleic acid constituents in relation to their mechanism of action as anti-tumour agents[186-197]. The role of steric effects in their mechanism of action has also been explored[178, 198-200] and such effects can have a profound effect on their biological profiles[201-203].

4.1.2 Platinum(II) – DNA interactions

Research into interactions between non-essential metal ions and nucleic acids generally focuses on chemotherapeutic agents[36]. The discovery of the famous DNA-binding anti-tumour platinum complex, cisplatin (*cis*-diamminedichloroplatinum(II), Fig 4.2) in 1969[38] has driven much research in this area[37].

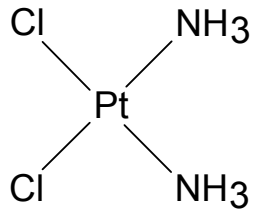

Figure 4.2 - Schematic representation of *cis*-diamminedichloroplatinum(II), Cisplatin.

A comprehensive review of the voluminous amount of work surrounding cisplatin and related complexes will not be repeated here. Rather, the discussion will focus on the modes of platinum(II) and palladium(II) binding to nucleic acids and constituents, with a particular consideration of the steric influences of the carrier ligands.

4.1.2.1 Binding modes

Platinum(II) complexes are known to bind to duplex DNA and this is proposed to give rise to cytotoxic effects[165]. The precise details of *how* such

binding elicits anti-tumour activity has been the subject of considerable enquiry in the past, and is still subject to ongoing investigation and conjecture.

Given the complexity of nucleic acids and their constituents as ligands, the multitude of possible binding motifs is substantial. Not only are there three general types of platinum(II)-nucleotide binding[166-168] (Fig 4.3), but any combination of three different nucleobases, at a range of binding sites on those bases (Fig 4.4), can be involved.

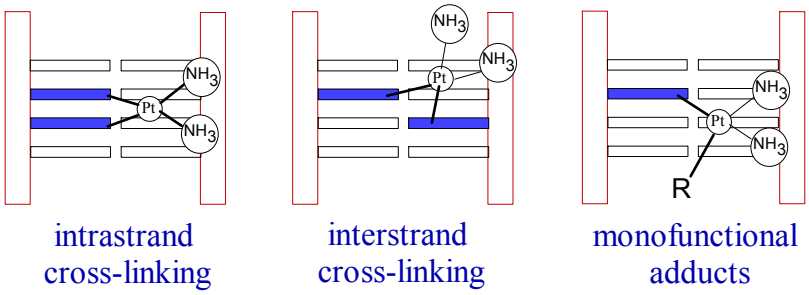

Figure 4.3 – Modes of binding of Cisplatin to double-stranded DNA. With the monofunctional adducts, R can be either be a halogen, or a protein. Where R = protein, this is also referred to as DNA-protein cross-linking. Figure is adapted from Ref. [204].

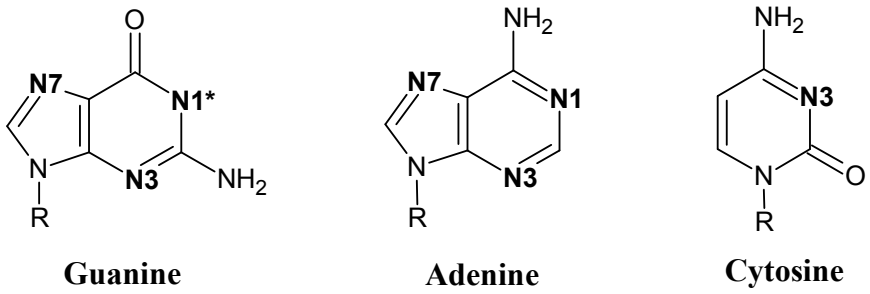

Figure 4.4 – Possible nucleobase binding sites (bold) for platinum(II) complexes. Asterisk indicates deprotonation required.

Whilst several studies have quantified many of the specific interactions that are likely to occur in DNA[205-210], the frequencies of such interactions alone are not necessarily indicative of their biological outcomes. For example, numerous studies[205, 206, 211, 212] have reached the conclusion that cisplatin prefers guanine-guanine intrastrand cross-linking, as a large percentage of these bis-functional adducts of cisplatin are identified in such studies. However, whether

these adducts are *functional* in terms of cytotoxicity cannot be directly inferred from such studies. Less frequent adducts could equally well be responsible for the desirable biological outcomes.

An approach towards determining the activities of specific interactions would be to design a carrier ligand that either cannot form an interaction under scrutiny, or that can only form a certain type of adduct. Subsequent biological testing could then provide information that relates certain adducts, or the absence of certain adducts, to various biological outcomes. This approach is illustrated by the following example from the literature, where the steric bulk of a carrier ligand is used to preclude intrastrand cross-linking.

In order to investigate the relative anti-tumour activity of *interstrand* cross-linking interactions (Fig 4.3), a carrier ligand without the ability to form *intrastrand* linkages was described and studied by Ling *et al* [213], Fig 4.5.

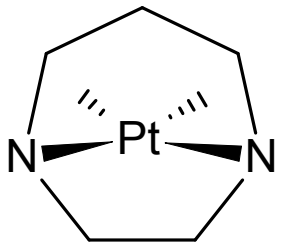

Figure 4.5 – Structure of [Pt(hpip)Cl_2], where hpip = homopiperazine = 1,4-diazacycloheptane.

This platinum complex satisfies the established Structure-Activity Relationship (SARs) requirements of a cytotoxic agent, as it contains a square-planar platinum(II) atom with both *cis* amines, which possess at least one hydrogen atom, as well as *cis* leaving groups and yet does not display anti-tumour activity. Furthermore, this complex was shown to behave as expected, as only interstrand cross-linkages were identified *in vitro*; cytotoxic intrastrand adducts are not observed[213]. The interaction selectivity displayed by [Pt(hpip)Cl_2] in this study is due to the repulsive aliphatic chains within this ligand[213].

4.1.3 Manipulation of the steric features of carrier ligands

With the steric features of the carrier ligand having been shown, *vide supra*, to be able to dictate the general type of interaction displayed by platinum(II) complexes (i.e. *inter* versus *intrastrand* crosslinking), interest is warranted as to whether actual binding site selectivity can be sterically tuned. Such site selectivity requires steric influence over the immediate environs of the coordination site, rather than interacting with the macromolecular DNA structure, as achieved for the hpip system above.

Influences relating to the steric environment of a specific binding site could allow for possible steric discrimination between such sites by a judiciously designed (through the steric attributes of the carrier ligand) metal complex. In this regard, various steric influences may be identified, Fig 4.6.

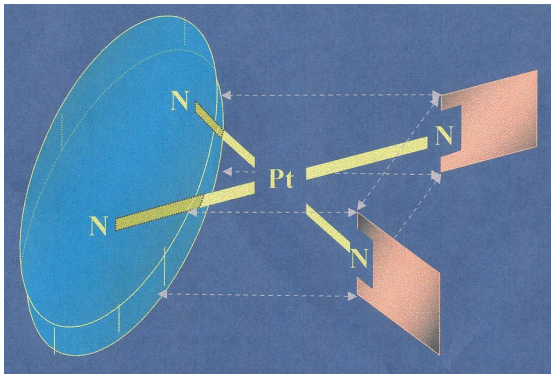

Figure 4.6 – Illustration indicating possible sources of steric influence, either the nucleobase (orange) or carrier ligand (blue). Adapted from Ref. [178].

Thus, the steric influence exerted by a particular nucleobase is usually characteristic of that ligand and is determined by the nature and number of exocyclic substituents in the vicinity of the binding site[214, 215]. Such nucleobases may sterically influence each other in the case of cis/bis coordination, even to the extent of enforcing mono coordination or, for two cis bound nucleobases, enforcing head-to head (HTH) rather than head-to tail (HTT) coordination[216]. In this regard, the influence of the steric bulk of the carrier ligand on the

coordination of the nucleobases may be manipulated to be asymmetric or may favour one side of the coordination plane over the other.

4.1.3.1 Steric influences of nucleobases

Before considering the influence of any proposed carrier ligand, the steric environment provided by the nucleobases themselves must first be carefully considered. Such work has previously been carried out within the Orbell group, where relative ligand repulsive energies (LRE) for the interaction of a standard metal probe with nucleobase binding sites have been calculated[214]. In this regard, Fig 4.7 shows the calculated Steric Indices (I_S) relating to each nucleobase binding site for coordination by a spherically symmetrical metal species.

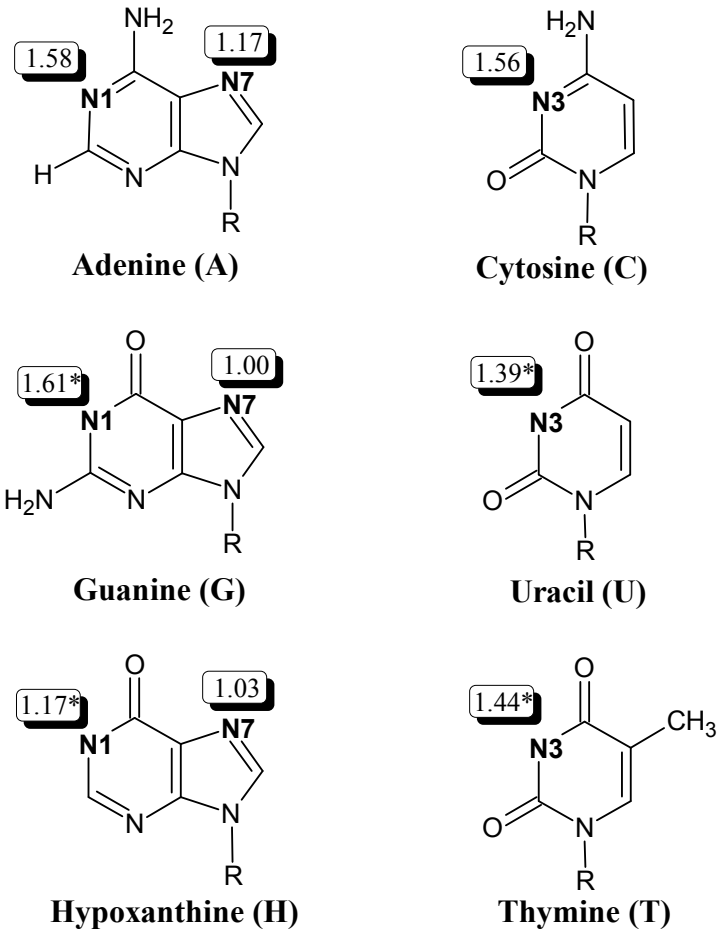

Figure 4.7 – Steric Indices (I_S) for a range of bases, where R = methyl. Asterisk indicates I_S for the deprotonated site. Reproduced with permission from Ref. 214.

Fig. 4.7 clearly shows the variability in the different steric presentations of the binding sites both within and between different nucleobases. This work was extended to include the steric effects of metal complex "flatness", as would be observed in square planar complexes involving platinum(II) and palladium(II)[215].

Therefore, with a wide range of steric environments available, the possibility of selecting for a specific binding site through steric influences alone seems promising. To determine how such steric effects might relate to complex formation in solution, a program was undertaken within the Orbell group to investigate the speciation of various judiciously designed platinum(II) and palladium(II) nucleobase and nucleoside complexes via ESI-MS.

4.1.3.2 Initial investigations – $[Pt^{II}(bpe)Cl_2]$ and $[Pt^{II}(bmpe)Cl_2]$

Two ligands were judiciously designed to provide specific hindrance to the platinum(II) coordination sphere, 1,2-bis(pyridin-2-yl)ethane (bpe) and 1,2-bis(6-methylpyridin-2-yl)ethane (bmpe), Fig 4.8.

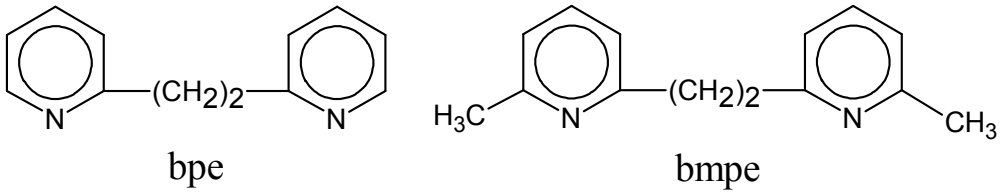

Figure 4.8 – Structures of ligands used in this case study.

As shown in Fig 4.9 below, the bpe ligand displays a certain amount of steric hindrance on both sides of the coordination plane. The bmpe ligand was designed to build up the steric bulk preferentially above the plane[a] compared to bpe. These arrangements would be expected to have significant steric effects with

[a] The reference to 'above' or 'below' the plane of these complexes is arbitrary, however the use of these terms are consistently used throughout this Chapter. "Below the plane" shall refer to the location of the alkyl linker, whilst "above the plane" shall be the opposite side, whereas the axis has been formed by the coordination sites of the platinum or palladium.

respect to their coordination of various nucleobases. This has been explored using ESI-MS at energy settings that are expected to reflect solution speciation[149].

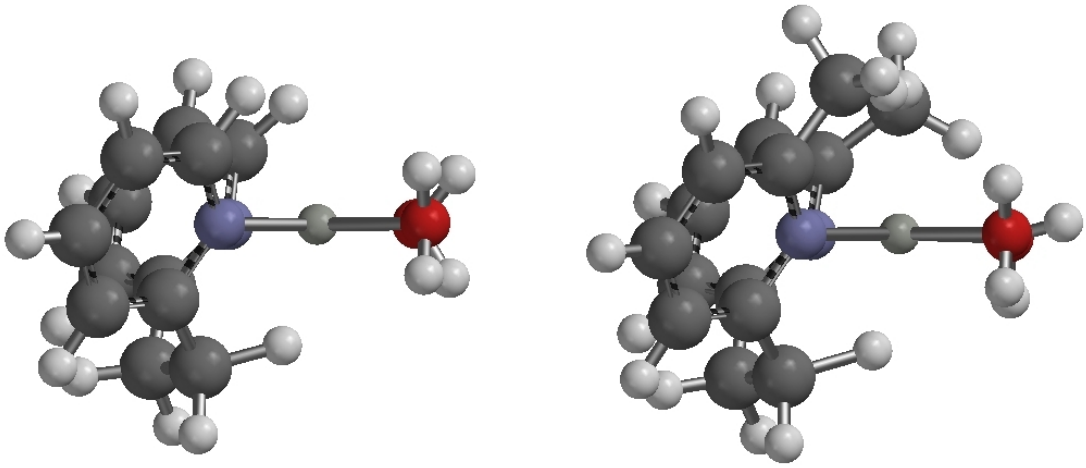

$[Pt(\mathbf{bpe})(\mathbf{H_2O})_2]^{2+}$ $[Pt(\mathbf{bmpe})(\mathbf{H_2O})_2]^{2+}$

Figure 4.9 – Side views of both complexes showing the enhanced steric encroachment above the plane in the bmpe complex.

It is important to emphasize that these ligands have been judiciously designed to sterically hinder both sides of the coordination plane, albeit one side more than the other. This is expected to hinder the formation of a five coordination transition state in relation to the reaction of both platinum (II) and palladium (II) species. Note that for the purpose of these experiments, whilst an attempt to hinder the binding sites may inadvertently affect the transition state, this was not the intended outcome, as empirical rather than mechanistic information is being sought.

Indeed, the intention to affect only the *thermodynamic* stability of certain complexes (in order to preclude formation of certain complexes and hence demonstrate the selective activity of the designed carrier ligands) rather than the *kinetic* stability, remains the objective throughout this Chapter. Therefore, thermodynamically-based influences will dominate complex formation, especially with respect to the palladium complexes discussed later in this Chapter.

4.1.3.2.1 ESI-MS Methodology and Results

As the work involved in these initial investigations forms the basis for the enquiries that follow on later in this Chapter, evidence that the use of ESI-MS in this way can successfully determine selectivity is important. This is due to the fact that the use of ESI-MS to study such selectivity of platinum(II) complexes for nucleobases in this way appears to be a novel approach. Therefore, the results presented here are a validation that this approach can be used to discriminate between carrier ligands.

Using an ESI-MS methodology analogous to that described in later in this Chapter, a preliminary experimental investigation of platinum(II) complexes (with the sterically restrictive bpe and bmpe as carrier ligands) and their relative selectivity towards the nucleobases inosine, 3-methyladenine and 1-methylcytosine (Fig. 4.10), was carried out[b]. These nucleobases were reacted individually with each ligand system, and analysed with respect to a comparison between monofunctional and bifunctional coordination. The results of these investigations are summarised in Table 4.1, with all spectra available in Appendix I.

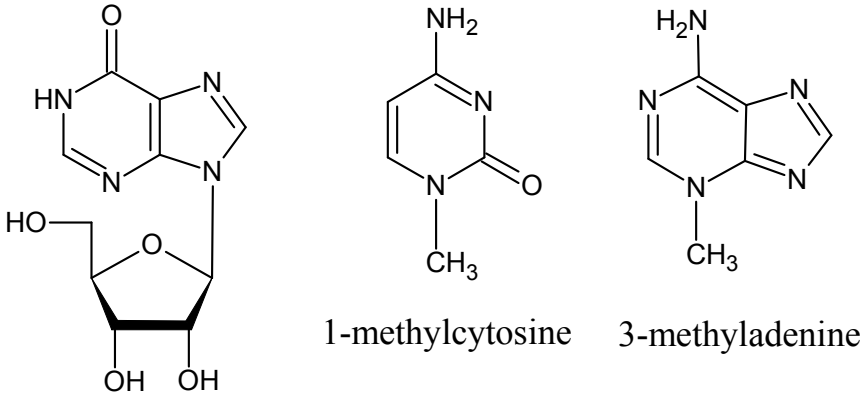

Figure 4.10 – The selected nucleobases reacted with $[Pt^{II}(bpe)Cl_2]$ and $[Pt^{II}(bmpe)Cl_2]$ and analysed by ESI-MS for selectivity.

[b] The data for this work was collected by Professor John Orbell as part of a collaboration with A/Professor David McFadyen at the School of Chemistry, University of Melbourne.

Table 4.1 – Summary of selectivity displayed by each ligand with each nucleobase. Values are relative abundances specific to that nucleobase. *Mono* refers to 1:1 Nuc:Pt binding, *Bis* refers to 2:1 Nuc:Pt binding.

	Total Relative Abundances					
	Inosine		**3-methyladenine**		**1-methylcytosine**	
Ligand	*Mono*	*Bis*	*Mono*	*Bis*	*Mono*	*Bis*
bpe	15.5	100	100	14	100	0.6
bmpe	100	11.1	100	0	100	1

As can be seen from the summary table above, both ligands vary with respect to proportions of nucleobases being coordinated. The results for each ligand system will be discussed separately.

4.1.3.2.2 Analysis of bpe results

The results for the least sterically hindered ligand system, bpe, are in accord with what might be expected for this ligand since the bis (head-to-tail) complex with 9-hypoxanthine has been isolated and characterized crystallographically[217]. Thus this system is seen in the ESI-MS to overwhelmingly prefer bis coordination to two inosine ligands, Table 4.1 and Fig. 4.11a.

The results for the two other nucleic acid constituents, 1-methylcytosine and 3-methyladenine, Table 4.1, are consistent with the theoretical I_S results discussed previously, Fig. 4.7. These results suggest that the N(7) position of adenine derivatives are 17% more sterically restrictive with respect to metal coordination (albeit with a spherical metal species as a probe) than the N(7) position of inosine, and that the N(3) position of a cytosine derivative is 56% more sterically restrictive than the N(7) position of inosine. This is consistent with the prevalence of the mono rather than the bis coordinated species in the ESI-MS spectra, Table 4.1. It is likely that the preference for mono coordination in these systems is dictated primarily by the steric crowding brought about by the exocyclic substituents contiguous to each binding site.

4.1.3.2.3 Analysis of bmpe results

The bmpe ligand has been designed to exhibit enhanced steric influence over the coordination sphere of the platinum(II), Fig. 4.9. As a result, the speciation pattern upon coordination to the above nucleic acid constituents changes dramatically compared to the bpe system, Table 4.1 and Fig 4.11b.

The most drastic change was observed for inosine coordination, where the relative proportions of the mono- and bis-substituted species become inverted compared to the bpe system. This is entirely expected and is a pleasing experimental outcome.

Indeed, for all three nucleobases examined, none prefer bis-coordination with the bmpe system, with the mono-species being by far the most abundant in all cases. In the case of the 3-methyl adenine system, bis coordination appears to be precluded entirely and, although bis coordination for 1-methylcytosine is detectable, it is in very poor abundance. These are also satisfying outcomes that demonstrate the proof of principle that a judicious design of carrier ligand can allow some adducts to form but can preclude others. Thus a biological profile of the $[(bmpe)Pt]^{2+}$ moiety compared to the $[(bpe)Pt]^{2+}$ moiety might allow some deductions to be made about the relevance of the precluded adduct or the preponderance of one adduct over another.

This suggests that there is considerable scope for the steric tuning of carrier ligands in order to affect the nature of adduct formation, *either by making certain adducts more likely, by precluding certain adducts entirely* or *by enforcing a specific adduct*. These results also highlight the power of ESI-MS to investigate the design of site-specific reagents, particularly for nucleic acid binding species

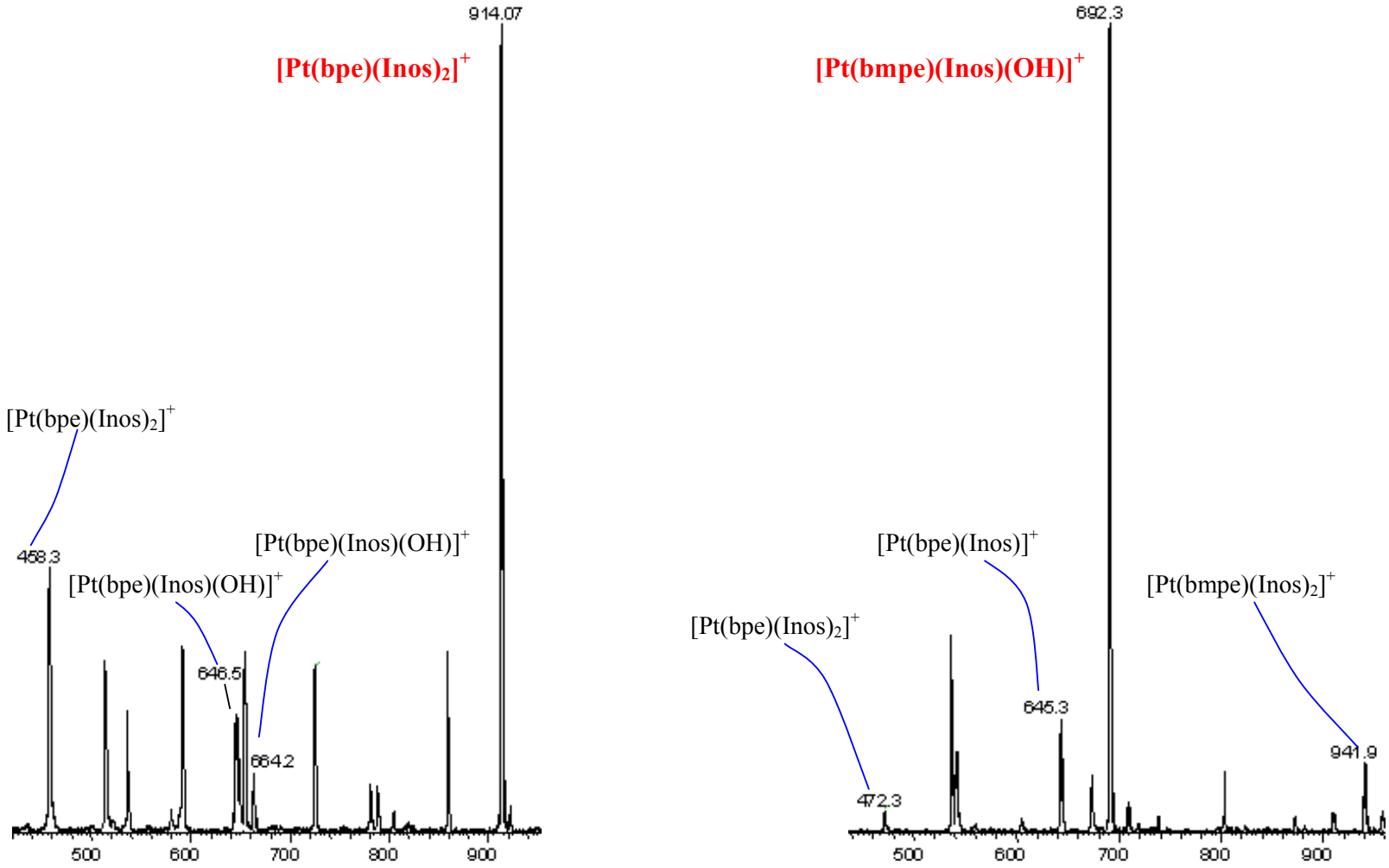

Figure 4.11 – Spectra of inosine coordination to **(a)** the least-restrictive Pt-bpe system, and **(b)** the more restrictive Pt-bmpe system.

The following work extends these initial ESI-MS studies to a broader range of carrier ligands that exhibit a variety of subtle steric characteristics. For these investigations, platinum(II) has been replaced with the structurally analogous palladium(II) [218, 219].

4.2 METHODS

The experimental procedure for this work was carried out in two stages. Initially, the complexes were prepared for reaction with the nucleotides by removing the halogens. Finally, the prepared, purported "di-aqua", complexes[c] were reacted with the chosen nucleic acid derivatives. Atomic Absorption Spectroscopy was performed to quantitate the amount of palladium recovered, and Electrospray Ionisation-Mass Spectroscopy (ESI-MS) was carried out to identify the palladium species present.

4.2.1 Preparation of the Palladium species

The compounds were obtained from collaborators[d] in the form of $[Pd^{II}(L)(Cl)_2]$, L = a bidentate ligand with similar attributes to bpe and bmpe. Specifically, these attributes involve two coordinating aromatic ring systems bridged by an alkyl chain of variable length. As with bpe and bmpe, the ligands are designed to create different steric environments above and below the coordination plane. However, whereas bpe and bmpe are quite dramatically different in this regard, these ligands present a range of more subtle steric differences.

[c] Whilst, with the removal of the halogens from these complexes, pure di-aquo species should, theoretically, be produced, the actual occupiers of the free coordination sites are quite different. This speciation will be discussed later in this Chapter, with the analysis of the prepared ligands via ESI-MS.
[d] Prof. Anthony T. Baker and Dr. Jeffery K. Crass, material from University of Technology Sydney, Australia.

The specific ligands chosen for investigation were bis(benzimidazol-2-yl)methane (bbmm), 1,2-bis(benzimidazol-2-yl)ethane (bbme) and 1,3-bis(benzimidazol-2-yl)propane (bbmp). Structures are given in Figure 4.12 below. These ligands are bidentate and were selected for the similarity of structure, yet with subtle steric changes within the series.

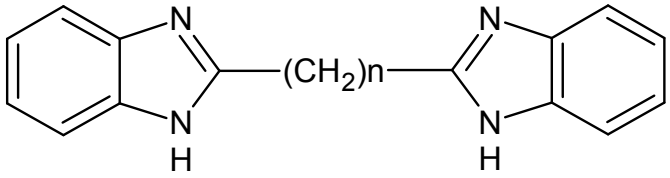

Figure 4.12 – General structure of ligands used, where n = 1 (bbmm), n = 2 (bbme) or n = 3 (bbmp).

A known amount of the di-halogenated compound was weighed and suspended in a minimal volume of deionised water. This suspension was gently heated and stirred. A slight deficiency of $AgNO_3$ (obtained from BDH) dissolved in a minimal amount of deionised water was then added. This was left with gentle heat (~ 60 °C) and stirring in a brown glass bottle for three hours.

After this time, the reaction liquor is filtered over a filtering agent (Celite 5.2.1) and the filtrate collected. The reaction vessel is rinsed several times with a small amount of deionised water, as is the precipitate on the filter agent. The filtrate contains the water-soluble, purported, “di-aqua” species.

4.2.1.1 Determination of metal concentration and speciation

Once collected, the aqueous filtrate for each ligand system was sampled and analysed for palladium content. In order to quantitatively control the stoichiometry of the competition studies, the amount of palladium species present in solution was required. Given the relatively large volume (80 – 140 mL) of filtrate collected, flame Atomic Absorption Spectroscopy (AAS) was used.

A palladium SpectrAA hollow cathode lamp was used, in conjunction with a Varian SpectrAA-400 AAS, utilising an air/acetylene flame. The lamp settings used were the Pd resonance line at 244.8 nm, 0.3 nm slit width, and 5 mA lamp current.

A standard solution of 1000 mg/L was obtained from Aldrich and working solutions of 2.5, 5 and 10 mg/L were prepared. Once a calibration curve was established, the samples were aspirated undiluted at first. Two solutions, involving the ligands bbme and bbmp, required five-fold dilution to fall within the prescribed calibration range of the instrument.

Once the overall palladium content was established for each solution, ESI-MS spectra were collected, in order to investigate the speciation of the palladium. Small samples (1 mL) were taken and diluted with methanol to a solvent composition of 50:50 methanol\water. The ESI-MS spectra were collected using a Finnigan LCQ Deca XP MAX instrument, running Xcalibur LCQ Tune Plus software.

Typical conditions used for the ESI-MS as follows: spray voltage of approximately 5 kV, a capillary temperature of 275.4^{o}C, nitrogen sheath pressure of 10-30 (arbitrary units). The capillary voltage and tube lens offset were tuned, the values of which were 26.2 V and 40.0 V respectively. From these “di-aqua” spectra, palladium-containing peaks were then identified through its isotopic signature (Fig. 4.13), and assigned likely identities via the m/z values.

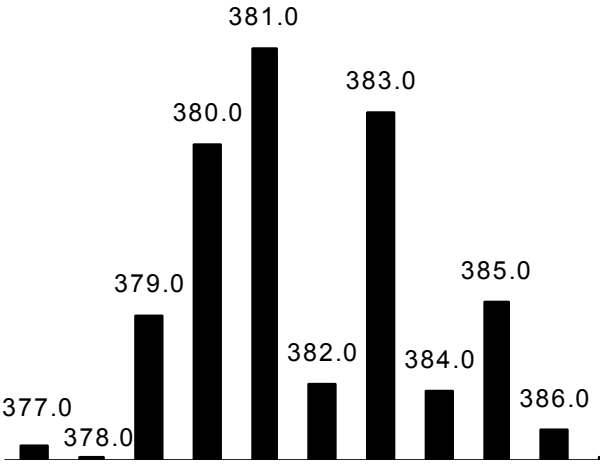

Figure 4.13 – Isotopic signature of $[Pd^{II}(bbmp)]^{+}$ $(-H^{+})$. This signature is typical of palladium-containing species.

4.2.2 Analysis of binding selectivity to nucleic acid constituents

In order to evaluate the binding selectivity for each ligand, competition experiments were carried out. These experiments used three combinations of nucleic acid derivatives; namely, inosine-cytidine, inosine-3-methyladenine and inosine-cytidine-3-methyladenine. The structures of these nucleic acid constituents are shown in Fig 4.14.

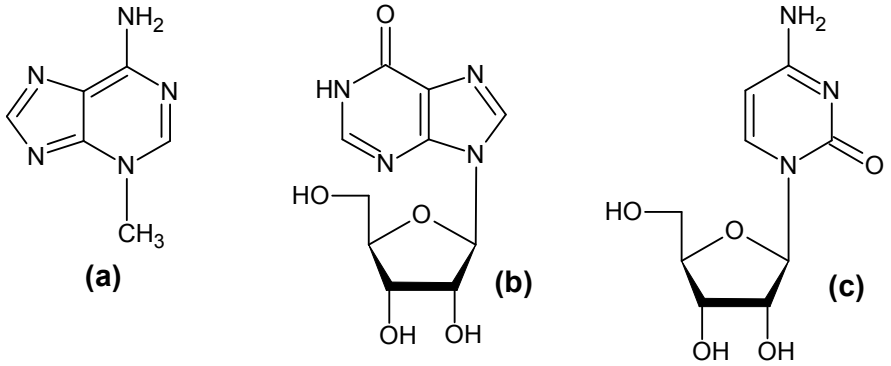

Figure 4.14 – Structure of nucleic acid constituents used in competition studies, (a) 3-methyladenine, (b) inosine, and (c) cytidine.

For each competition experiment, a mixture containing stoichiometrically equal amounts of each nucleoside was produced in 100 mL of 50:50 methanol/water (given the poor aqueous solubility of inosine). This nucleotide

solution was added slowly to the palladium species, with stirring. The volume of nucleotide solution was such that the molar amount of palladium was slightly less than that of the nucleotides. These reactants were mixed in a brown glass bottle, and left with stirring and mild heat for three hours, after which the reaction milieu was adjusted to 50:50 methanol/water, and analysed using ESI-MS. The ESI-MS conditions were identical to those used for the "di-aqua" solutions.

4.2.3 Computational methodology

In an attempt to structurally rationalize the interaction of these sterically restrictive palladium systems with the various nucleobases, all possible mono- and bis-substituted Pd structures of all three carrier ligands have been optimised and examined using semi-empirical PM3 calculations as applied in Spartan '06[98]. Bond lengths and angles within the refined structures have been benchmarked, where possible, to crystallographic data. The PM3 level of calculation allows for a rapid approximation of geometries for a large set of complexes, in a relatively short time. Higher methods (*ab initio*, DFT, MP2, etc.) were not considered necessary for these computations, as only approximate geometries and relative energies were required. Also, PM3 is specifically parameterised for transition metals, whereas pseudopotentials need to be employed for higher calculations.

Specifically, the structures that were optimised include the di-aqua species ($[Pd(L)(H_2O)_2]^{2+}$), species of the type ($[Pd(L)(nuc)]^{2+}$), and various combinations of all three nucleic acids of general formula $[Pd(L)(nuc_1)(nuc_2)]^{2+}$. All structures were initially subjected to MMFF (Molecular Mechanics Force Field) equilibrium conformer searching, so that the semi-empirical optimisation began from a favourable starting position. These structures were then optimised using PM3, without constraints on the angles around the palladium centre. Given the steric nature of the ligands, it was decided that some deformation of the square

planar geometry that typically surrounds the palladium centre might reasonably occur.

In order to obtain an estimate[e] of the relative stabilities of the mono- or bis-substituted complexes, a quantity, referred to here as the binding energy (BE), was calculated. This is used as a measure of the likelihood of bond formation. The equation used is shown below (Eqn. 4.1).

$$BE = (E_{Pd\text{-}Nuc} + E_{H2O}) - (E_{Pd} + E_{Nuc}) \qquad \textbf{(4.1)}$$

where E_{Pd} is the energy of the palladium-containing species before addition of the nucleobase, E_{Nuc} is the energy of the free nucleobase being added, $E_{Pd\text{-}Nuc}$ is the energy of the final complex and E_{H2O} is the energy of the water which is replaced in the complex by the nucleoconstituent. The E_{Pd} species can either be $[Pd(L)(H_2O)_2]^{2+}$ (for monofunctional BE) or $[Pd(L)(nuc)(H_2O)]^{2+}$ (for bisfunctional substitution BE).

4.3 RESULTS AND DISCUSSION

4.3.1 Experimental ESI-MS results

4.3.1.1 Characterisation of the "di-aqua" solution

The removal of halides with $AgNO_3$ in complexes of this kind is usually considered to be quantitative[174]. However, for these complexes this was not observed, as assessed by the AAS data. With all complexes being treated under the same conditions, the ligands, bbme and bbmp, demonstrated 57% and 48%

[e] The term 'estimate' is used here, due to the poor electron correlation applied in PM3. Therefore, caution is required where energetics of a reaction are calculated using PM3. This is discussed in more detail in Section 4.4.2, *vide infra.*

yields respectively and the ligand bbmm (considered to be the most sterically restrictive of the three) returned a yield of approximately 1%. The yields were calculated based on the initial mass of $AgNO_3$, the limiting reagent.

This inertness of the halogens is certainly controlled, in one way or the other, by the various properties of the carrier ligand. This effect may possibly be wielded by the carrier ligand by affecting either the partial solubility of the "di-chloro" complexes, allowing for the reaction to occur in solution, or the kinetic stability of these "di-aqua" species after halide removal. Even if a slight increase in solubility were achieved, the effect on the reaction rate and outcomes would be significant, given the relatively large amount of $Ag^{+}_{(aq)}$. However, whether the differences between these closely-related carrier ligands are significant enough to affect the solubility is doubtful.

Regarding the kinetic stability of the di-aqua complexes, this may influence the very low yield of the bbmm system. In the modelling discussed in section 4.3.2.2.1 below, the $[Pd(bbmm)(H_2O)_2]^{2+}$ complex does contain a considerable steric hindrance between the bulky benzimidazole rings and the two 'free' coordination sites, which may reduce the likelihood of halide removal. A similar reasoning may be applied to the other two systems, as the bbme system yielded 57% and the bbmp system yielded 48%. Were such kinetic influences the dominating influence on reaction outcomes, these results would be as expected, as the bbme ligand is less hindered. In the same modelling mentioned above, the bbmp "di-aqua" complex contains what appears to be an agostic interaction between the acyl linker and the palladium(II). This interaction causes "below-the-plane" hindrance that would affect the kinetic behaviour of this system.

Another possibility which may be postulated at this point is, given that the halogenated compound is in the form of a suspension and must have one or both of the halogens removed by $Ag^{+}_{(aq)}$ in order to be solubilized, the $Ag^{+}_{(aq)}$ species could react with the palladium complex suspended in the solid state (i.e.

heterogeneously). Therefore, it would have to interact directly in the vicinity of the metal to halogen bond. Such a close encounter would necessarily involve some steric resistance from carrier ligands such as the ones used in these experiments. It might also be expected that the steric hindrance to halogen abstraction would also be influenced by the size of the halogen leaving group (Cl, Br or I). The exact mechanism, whist kinetic in nature, is unknown and is of no further consequence to the wider scope of this work.

Spectroscopically, given the yield of 1% achieved for the bbmm system, the concentration of $[Pd(bbmm)]^{2+}$ that was obtained in the filtrate was significantly lower than that obtained for the bbme and bbmp systems. Therefore, the ESI-MS spectra obtained for the di-aqua Pd-bbmm solution was quite noisy compared to those obtained for the bbme and bbmp ligands. A summary of the major peaks found in all three ligand systems is in Table 4.2, with the spectra located in Appendix I.

Table 4.2 – Major Pd species identified from the "di-aqua" spectra, values are relative abundances, with the most abundant peak = 100

Pd (bbmm)	
$[Pd(bbmm)(CH_3OH)]^+ \cdot H_2O$ $(-H^+)$	**100**
$[Pd(bbmm)(NO_3)]^+$	28.8
$[Pd(bbmm)(NO_3)]^+ \cdot H_2O$	72.6
$[Pd(bbmm)(CH_3OH)(CH_3CN)]^+ \cdot H_2O$ $(-H^+)$	27.3
$Na_3[Pd(HP_3O_{10}^{4-})]^+ \cdot 2H_2O$	63.5
Pd (bbme)	
$[Pd(bbme)]^+$ $(-H^+)$	12.5
$[Pd(bbme)(NO_3)]^+$	**100**
$Na_3[Pd(HP_3O_{10}^{4-})]^+ \cdot 2H_2O$	3.4
$[Pd(bbme)_2]^+$ $(-H^+)$	49.5
$[Pd_2(bbme)_2]^+$ $(-3H^+)$	27.5
$[Pd_2(bbme)_2(NO_3)]^+$ $(-2H^+)$	10.3
$[Pd_3(bbme)_2]^+$ $(-5H^+)$	17.2
$[Pd_2(bbme)_2(NO_3)_2]^+$ $(-H^+)$	23.4
Pd (bbmp)	
$[Pd(bbmp)]^+$ $(-H^+)$	51.1
$[Pd(H_4P_3O_{10}^-)(CH_3OH)_2]^+$	10.0
$[Pd(bbmp)(NO_3)]^+$	**100**
$[Pd_2(bbmp)_2(Cl)_2]^+ \cdot 3H_2O$ $(-H^+)$	14.9

An interesting feature of this data is the prevalence of the *nitrato* adducts rather than the *aqua*. This may also be rationalized on the basis of steric effects since the nitro is a flat molecule[215] whereas water (in an sp^3 geometry) is more spherical in shape. This would enable the nitro to "slot in" to the sterically hindered environment[f]. Further analysis of these preliminary spectra also yields further interesting information.

Presence of triphosphate and acetonitrile – Small amounts of triphosphate was identified in all three preparations. The source of this contamination is postulated to be a leftover reactant from the synthesis of the ligands. All ligands were synthesised using polyphosphoric acid, which consists of triphosphate ($H_4P_3O_{10}^-$)[220]. The levels of these triphosphates are relatively small in all three samples, regardless of the high relative abundance in the bbmm spectra (given that only 1% of the bbmm reacted with the $AgNO_3$). The presence of acetonitrile was also noted, again in small amounts relative to the starting material. This contamination was also attributable to the preparation of the ligands, as the ligands and palladium salt were reacted in hot acetonitrile. This contaminant was also detected in the preliminary investigations involving bpe and bmpe where it was also employed in the syntheses.

Nitrated species – The predominant counter anion present in the "di-aqua" preparations, and identified in the ESI-MS data is NO_3^-, as $AgNO_3$ was used to remove the halogens. Therefore, the nitrate ion would be present in solution at concentrations slightly less than two equivalents with respect to palladium. The preferred incorporation of nitrate over water has been discussed above.

Coordinatively unsaturated palladium complexes – As in the preliminary investigations, where [Pt or Pd(bpe)]$^+$(-H$^+$) and [Pt or Pd(bmpe)]$^+$ (-H+), are

[f] Whilst it is recognized that the literature contains various reports of sp^2 hybridised H_2O molecules, these are generally found coordinated to metal species. However, it is postulated here that water molecules are sterically hindered from interacting with the central metal atom, therefore the water molecule(s) would remain in a sp^3 geometry. This, coupled with the inherent charge of the NO_3^-, would mean that nitrato adducts are favoured.

observed (Appendix I), we also observe the species ($[Pd(bbme)]^+$ ($-H^+$) and $[Pd(bbmp)]^+(-H^+)$. Notably, $[Pd(bbmm)]^+(-H^+)$ is not observed, consistent with the rather anomalous behaviour associated with this ligand. It is unlikely these species exist as such in solution, as some weakly interacting groups (such as *aqua* substituents) may be lost during the process of ionisation. To add to the apparent peculiarity of the bbmm system, most Pd(bbmm) species display a single associated (perhaps coordinated) water molecule.

Other palladium species – A 2:1 complex in the case of bbme is observed, namely $[Pd(bbme)_2]^+$ ($-H^+$). Such complexes are not observed with bbmm or bbmp. This is because bbme is more sterically accommodating both above and below the plane than bbmm or bbmp (discussed later). In order to investigate this further, PM3 geometry optimisations were carried out on the 2:1 complexes for all three carrier ligands.

The *trans* isomers of these 2:1 complexes are presented in Fig 4.15, which clearly shows that the bbmm ligand system contains a steric clash due to the above-plane ring bulk, whereas the bbmp ligand system contains some steric clash due to the below-plane propyl linker and, for the bbme system, there is no steric clash. The $[Pd(bbme)_2]^+$ complex appears to be quite stable, as this species is detected in all of the bbme experiments, including the reactions involving nucleic acids constituents.

Due to the steric hindrance that these carrier were designed to display, the lowest energy conformation of these complexes were as the *trans* isomers as displayed in Fig 4.15. The energy differences between *cis* and *trans* isomers of these ligands ranged from 5.19 kcal/mol for the bbme system, to 13.9 and 15.19 kcal/mol for both bbmp and bbmm respectively, as calculated using PM3.

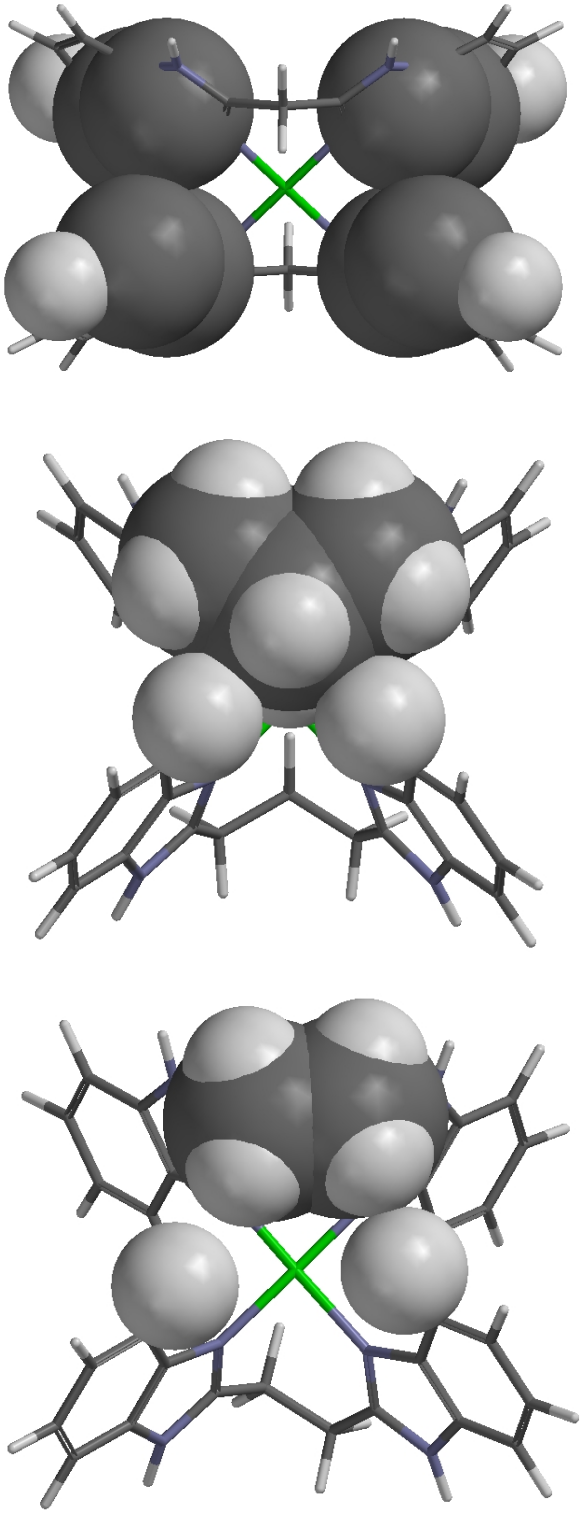

Figure 4.15 – Representations of the PM3[g] geometry optimised structures of $[Pd(L)_2]^{2+}$, where L = bbmm (top), bbmp (centre) and bbme (bottom). The enlarged selections are space-filling graphics (van der Waals radii) showing the steric clash in bbmm and bbmp, with the analogous selection to bbmp highlighted on bbme for comparison.

[g] The PM3 method has been benchmarked against similar complexes, in order to validate this method with respect to reproducing respectable geometries. This benchmarking is discussed later.

The species involving the $Pd_2(bbme)_2$, $Pd_3(bbme)_2$ and $Pd_2(bbmp)_2$ units could arise as polymeric constructs, due to the potential dual coordination of each five membered ring of the benzimidazole systems, Fig. 5.16.

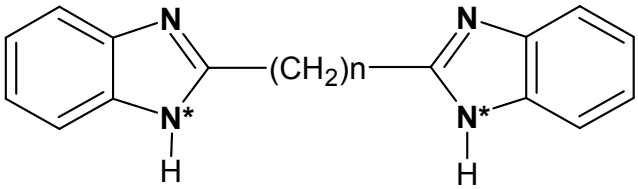

Figure 4.16 – General formula of the carrier ligands, where n = 1 (bbmm), 2 (bbme) or 3 (bbmp). Possible coordination sites are in bold. * denotes deprotonation prior to coordination.

Whether these units are formed by the ionisation process within the ESI-MS, and hence only exist in the gas-phase, or whether they occur in solution, is unclear. To further examine these species, two possible structures are proposed here and studied via PM3 geometry optimisation. These species are a "polymerised" complex and a dimerised complex.

Polymerisation: A proposed general structure, $[Pd_2(L)_2]^{2+}$, where L = bbme, bbmp or bbmm, is shown in Fig. 4.17. PM3 optimisations for the three systems are well behaved computationally, although only the bbme and the bbmp systems are observed experimentally (with bbme being more abundant than bbmp). These results are readily explained by considering the relative strains that are operative in these systems, Fig. 4.18.

It is interesting to note from examining the relative abundances of the clusters (Table 4.2), that there are differing amounts of polymerisation occurring. In this regard, of the ligand systems examined, the bbme system appears to favour clustering more so than bbmp. Again, the bbmm system behaves in a unique way in this series, *vide supra*, with no evidence of polymerisation.

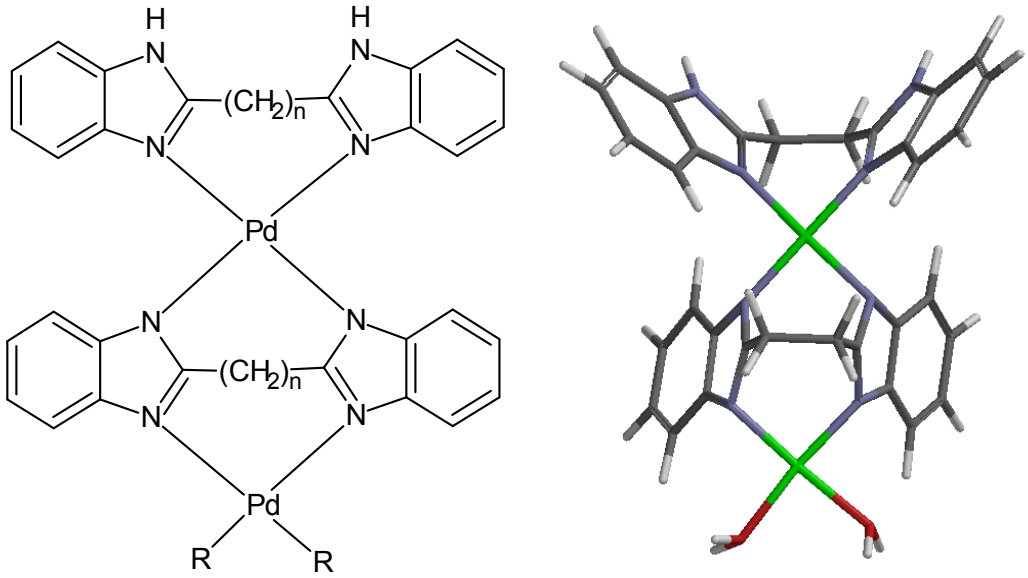

Figure 4.17 – Proposed structure for the formation of $[Pd_2(L)_2]$, where L = bbmm, bbme or bbmp.

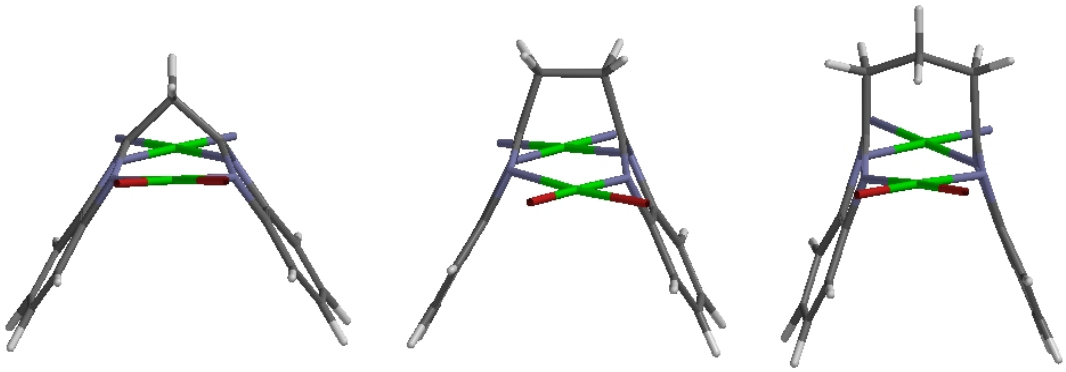

Figure 4.18 – View of the $[Pd_2(L)_2(H_2O)_2]^{2+}$ complexes, where L = bbmm (left), bbme (centre) and bbmp (right). The second carrier ligand has been removed for clarity. Note the strain in the methyl linker in bbmm (C-C-C angle = 92.46°) as well as the distortion in the benzimidazole rings of the bbmp ligand caused by the larger propyl linker. Whilst some distortion appears in the bbme system, it is not to the degree as that in the bbmp system.

Dimerization. Another interesting species worthy of note is the appearance of $[Pd_2(bbme)_2(NO_3)_2]^+$ $(-H^+)$. Although the $[Pd_2(L)_2]$ unit is present in both the "polymer" and the dimer, they are postulated here to be *structurally* different. Thus the dimer appears to be formed from the association of two $[Pd(bbme)(NO_3)]^+$ species (the most abundant in the ESI-MS results, Table 4.2), Fig 4.19.

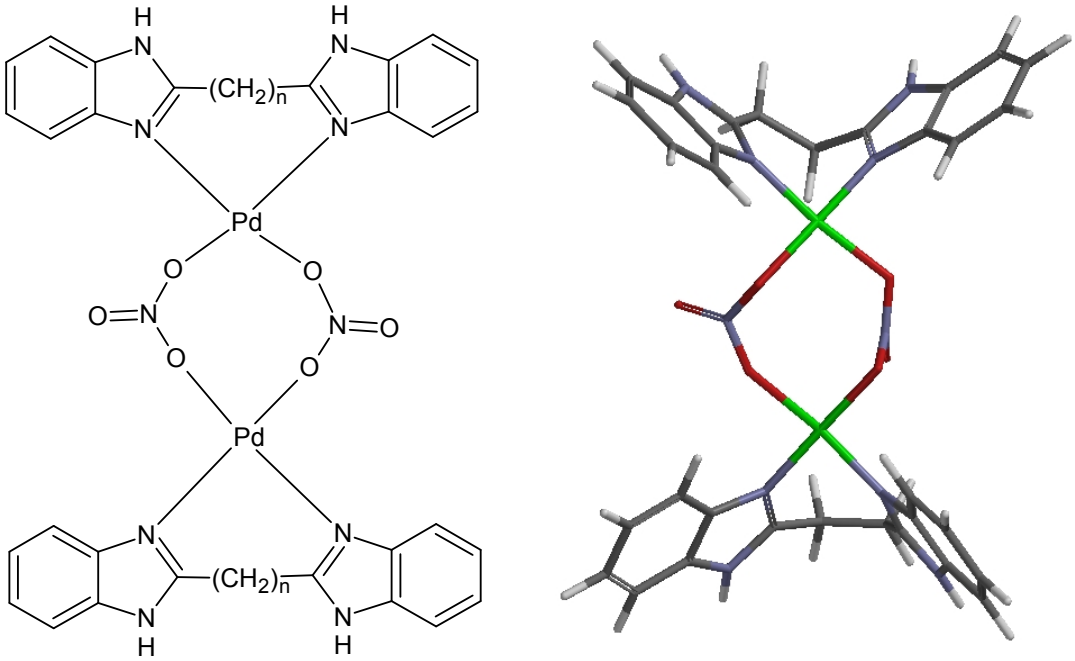

Figure 4.19 – Schematic representation (left) and PM3 geometry of the bbme system (right) of the proposed dimer structure, incorporating nitro-bridging.

PM3 optimizations of the dimers for all three carrier ligands have been carried out, although only the bbme system is observed experimentally. In this regard, the bbmm system displayed distorted Pd-O-N angles as a result of the steric environment provided by this carrier ligand, Fig. 4.20.

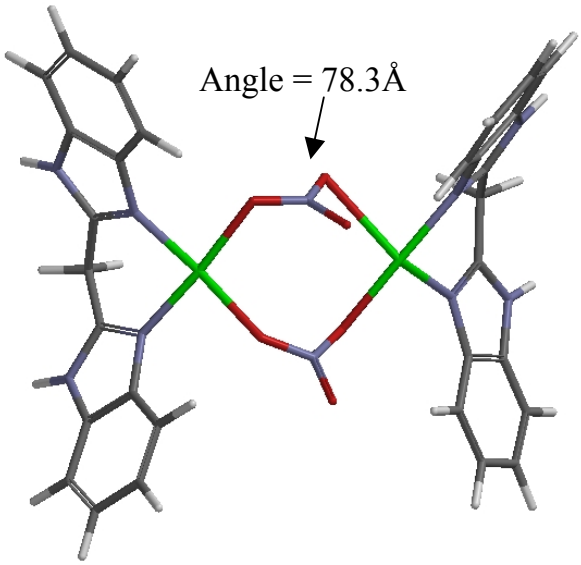

Figure 4.20 – Optimised structure of the hypothetical $[Pd_2(bbmm)_2(NO_3)_2]^{2+}$, with the strained bond angle noted.

A possible reason as to why the bbme ligand system forms such dimers, yet the bbmp system does not, is not evident from the modelling studies. One explanation is the possible restrictive role that agostic interactions play in systems of this type. Both the bbme and bbmp systems display agostic bonds of varying strengths, Fig. 4.21. Notably, the bond for bbmp is the strongest. The strength of this interaction could mitigate against the reorganization required to form a dimer.

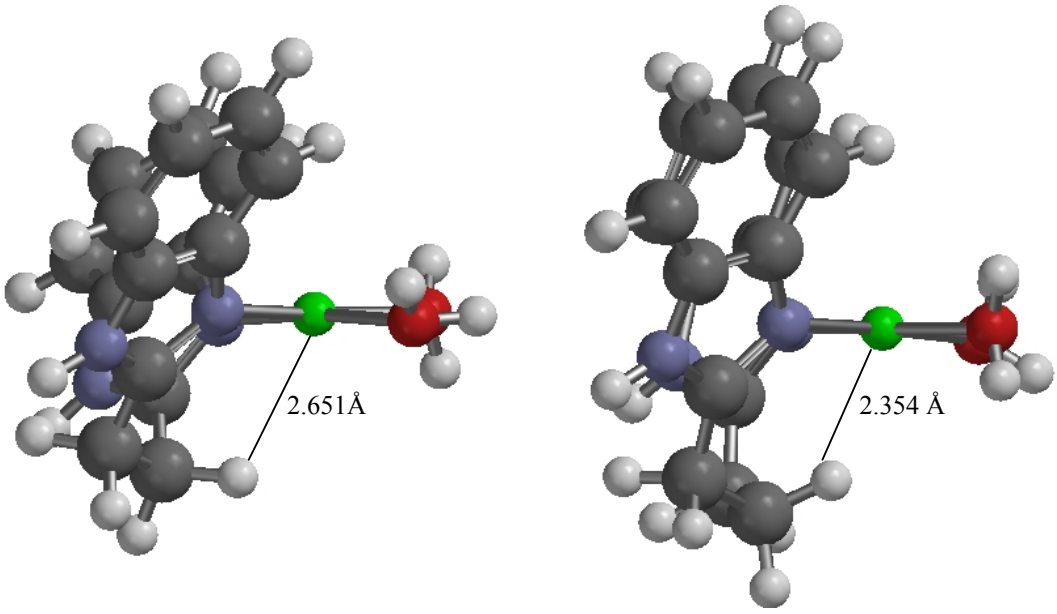

Figure 4.21 – Side views of [Pd(bbme)(H_2O)$_2$] (left) and [Pd(bbmp)(H_2O)$_2$] (right), with the length of the agostic interaction involving the acyl linkers indicated. The bbmm system does not display an agostic interaction.

Identification of chloro species – The discovery of clustering that seems to have incorporated chlorides, ([Pd_2(bbmp)$_2$(Cl)$_2$]$^+$.3H_2O (-H^+)), was a surprise in the bbmp spectrum, although some chlorinated species may be expected, given the slight deficiency of $AgNO_3$ used. The appearance of this structure suggests that a dimer of the mono-chloro species of Pd(bbmp) is being formed via halogen bridging, a phenomenon long known to palladium(II) chemistry[221]. PM3 optimisation of this structure (Fig. 4.22) confirms such halogen bridging is likely.

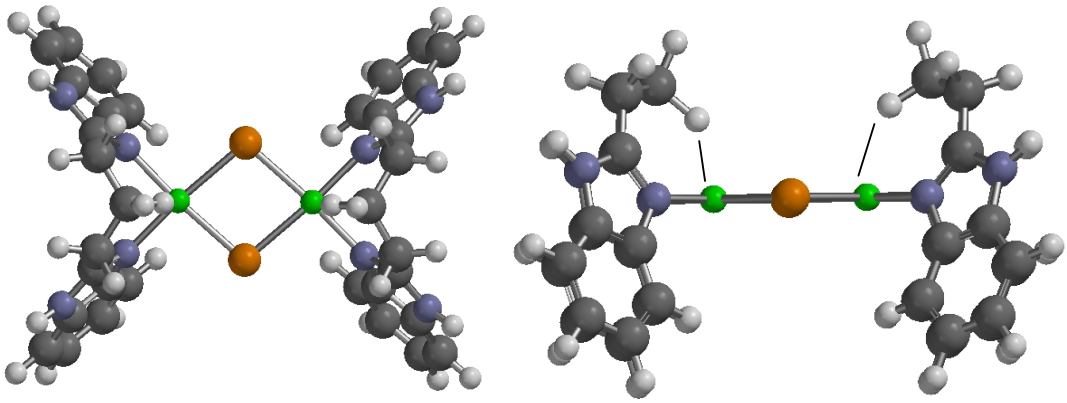

Figure 4.22 – Top view (left) and side view (right) of $[Pd_2(bbmp)_2Cl_2$. Note that agostic bonds are operative in this dimer. Also note that only one isomer is shown (*cis*). The trans isomer is energetically equivalent, also with agnostic interactions.

4.3.1.2 Competition experiments – ESI-MS

As described in the methodology section above, each "di-aqua" system was subjected to two or three equivalents of nucleic acid derivatives. Specifically, three competition experiments were performed for each ligand system. These involved: inosine and cytidine (Inos/Cytid), inosine and 3-methyladenine (Inos/3-MeA) and (Inos/Cytid/3-MeA). Accompanying spectra can be found in Appendix I and tables containing data relating to all palladium-containing species that were identified can be found in Appendix II. It must be noted at this point that that the use of the terms 'cytosine' and 'hypox' (abbreviation of hypoxanthine) refers to the relevant substituents which have lost the ribose moiety, to become nucleobases.

4.3.1.2.1 Pd-bbmm

The results obtained for the Pd-bbmm system show a resistance of binding to the nucleic acid constituents to the "di-aqua" species. The major palladium species of interest are listed in Table 4.3.

The remaining ESI-MS competition experiments utilising this ligand system were conducted several days after the reaction mixtures had been made

up. Even though the di-aqua-Pd-bbmm solution was stored alongside the other ligand systems, the spectra obtained from these experiments seem to be littered with degradation products, indicating an inherent instability in this system, at least in aqueous solution. As such, no further experimental results for this system will be discussed, however all spectra are available in Appendix I. In order to shed light on this observation, the computational results for this system will be discussed alongside the other systems.

Table 4.3 – Species identified in the Inos/Cytid Competition experiment for $[Pd(bbmm)(H_2O)_2]^{2+}$.

Theoretical formula	Relative Abundance
$[Pd(bbmm)(CH_3OH)]^{2+}$	100
$[Pd(bbmm)(CH_3OH)(CH_3CN)]^{+} \cdot H_2O$ $(-H^+)$	14.3
$[Pd(bbmm)(NO_3^-)]^{+}$	5.6
$[Pd(bbmm)(Hypox.)]^{+}(-H^+)$	8.8
$[Pd(bbmm)(Cytosine)]^{+} \cdot 3H_2O$ $(-H^+)$	18.5
$[Pd(bbmm)(Cytosine)_2]^{+} \cdot H_2O$ $(-H^+)$	18.3
$[Pd(bbmm)(Cytosine)(Hypox.)]^{+} \cdot H_2O$ $(-H^+)$	46.0
$[Pd(bbmm)(Cytosine)(Hypox.)]^{+} \cdot H_2O$ $(-H^+)$	20.1
$[Pd(bbmm)(Cytidine)]^{+} \cdot 3H_2O$ $(-H^+)$	36.3

4.3.1.2.2 Pd-bbme

For each competition experiment, all identified Pd(bbme)-nucleoconstituent species are summarised in Table 4.4.

As can be seen from Table 4.4, the most abundant species in all three experiments is a mono-functional inosine adduct. This is not unexpected, given the calculated I_S values (Fig. 4.6) show that the N7 position of inosine is the least hindered, coupled with the fact that unhindered systems involving platinum and palladium, such as cisplatin, show a preference for 6-oxo purines.

Regarding the binding selectivity of the other identified mono-functional adducts, it would appear as though 3-methyladenine was favoured slightly over cytidine, again in line with I_S values. This conclusion was made on the basis of the third competition experiment, containing all three nucleic acid bases. Whilst

the results of the other two experiments cannot be disregarded, it is likely that the mono-3-methyladenine adduct is decreased in the second competition experiment because these were sequestered for bis-binding (to produce the inosine-3-methyladenine mixed adduct) more readily than the mono-cytidine species in the first competition experiment.

Table 4.4 – Summary of ESI-MS results for all $[Pd(bbme)]^{2+}$ competition experiments. Values are relative abundances for each experiment. Relative abundances may consist of more than one peak where various forms exist.

	Competition Experiment		
Nucleic acid complexation	**Inos/Cytid**	**Inos/3MeA**	**Inos/Cytid/ 3-MeA**
Inosine	**100**	**100**	**100**
Cytidine	17.5	-	7.5
3-methyladenine	-	7.3	9.6
Inosine – 3-methyladenine	-	10.4	12.5
Inosine – Cytidine	8.7	-	9.5
Inosine – Inosine	9.8	7.2	2.5
Cytidine – 3-methyladenine	-	-	0
Cytidine – Cytidine	0	-	0
3-methyladenine – 3-methyladenine	-	0	0

More insight into the steric environment of the bbme ligand can be garnered from these ESI-MS results by considering the bis-functional binding patterns. Whilst a thorough analysis of these species may not be available due to constantly changing concentrations of reactants at this stage of the reaction, some qualitative conclusions can be reached. The most interesting insight concerns the apparent selection for the inosine-3-methyladenine mixed adduct. As mentioned earlier, the unhindered cisplatin greatly prefers 6-oxo purines to adenine. Therefore, this appears to be evidence of a sterically active ligand, bbme, influencing the binding patterns of the palladium complex. The conclusion that cytidine is the least favoured base, either in mono- or bis-functional binding, is also reasonable.

As is often the case with many areas of science, some of the best quality information to be gained from these spectra is not what is identified, but what is

not identified. Interestingly, three possible combinations of coordinated nucleic acid bases to this ligand have not been identified in any spectra; namely the bis-cytidine, bis-3-methyladenine and the mixed adduct of these two bases. Whilst, with further experimentation, these 'missing' complexes could be forced to exist through a large excess of reactants, this would be of no consequence when developing biologically active compounds. Any platinum or palladium species being developed for biological activity would need to compete with 6-oxo purine bases. If certain combinations of nucleobases exist only under certain conditions in the lab, then these combinations become redundant when designing site-specific ligands for biological use, and as such are of no use in this study.

The steric bulk of the ligand appears to have significantly altered the binding selectivity of palladium, as outlined above. Therefore, this system will benefit from detailed computational investigations. Such investigations should illuminate these ESI-MS results, with the aim of dissipating any kinetic effects and clearly defining the site selectivity of this ligand system.

4.3.1.2.3 Pd-bbmp

All identified Pd(bbmp) species bound to nucleoconstituents are summarized in Table 4.5 for each competition experiment. Immediately noticeable is the apparent increase in the relative abundance for all identified bis-species over the equivalent bbme complexes. Whether this is due to a decrease in selectivity towards the cytidine and adenine constituents, or an increase in selectivity *against* mono-inosine, hence affecting the magnitude of the largest peak, is unknown at this point, but will be further investigated with computational modelling.

As with the bbme results previously discussed, the bbmp system shows the inherent preference of palladium for inosine residues as the first nucleobase added. With respect to the other two bases, this system seems to slightly favour cytidine over 3-methyladenine as the choice of nucleobase for the first

coordination site, as evidenced in the third competition experiment. This finding is significant, as this is in stark contrast to the I_S values in Fig. 4.7, *vide supra*. This suggests that the bbmp ligand has a greater steric effect on the coordination site available to 3-methyladenine than cytidine or inosine.

Table 4.5 – Summary of ESI-MS results for all $[Pd(bbmp)]^{2+}$ competition experiments. Values are relative abundances for each experiment. Relative abundances may consist of more than one peak where various forms exist.

	Competition Experiment		
Nucleic acid complexation	**Inos/Cytid**	**Inos/3MeA**	**Inos/Cytid/ 3-MeA**
Inosine	**100**	**100**	**100**
Cytidine	24.3	-	9.0
3-methyladenine	-	11.8	7.9
Inosine – 3-methyladenine	-	22.6	12.0
Inosine – Cytidine	18.3	-	10.9
Inosine – Inosine	14.8	21.8	7.8
Cytidine – 3-methyladenine	-	-	0
Cytidine – Cytidine	6.3	-	0
3-methyladenine – 3-methyladenine	-	0	0

Such discrimination is not as clear regarding the second coordination site. Initial consideration of the bis-functional adducts shows that all identified species are relatively more abundant than in the bbme system. This would indicate a greater ease of coordination to the second site, confirming a relative decrease in steric hindrance. The distinct selectivity noted for the previous ligand system, bbme, does seem to be lost to a degree in the case of this ligand, bbmp. This is evident in the result of the third competition experiment involving all three nucleic acid derivatives. The result of this experiment shows almost no selectivity between cytidine and inosine bases as the second nucleic acid to coordinate, although 3-methyladenine appears less favoured. The assumption that these adducts were mainly formed from mono-inosine complexes is made, however the second competition experiment results, involving inosine and 3-methyladenine, suggests that some mono-3-methyladenine species accept an inosine to produce the mixed bis species, given the relatively low amount of mono-3-methyladenine complex identified.

Perhaps the most interesting aspect of the bbmp spectra is the appearance of the bis-cytidine species in one competition experiment involving this nucleoside, but not the other. The absence of this adduct from the experiment involving all three nucleobases may be due to an increase in competition for the second coordination site, indicating that the result obtained in the inosine-cytidine experiment was perhaps a 'false positive'; given an alternative, this adduct would not normally form. As this bis-species was not identified with the bbme ligand system, this confirms the notion that the bbmp ligand is somewhat selectively hindering 3-methyladenine more so than cytidine, yet is less restrictive than the bbme ligand.

Whilst some tantalising hints of site selectivity have been observed in the ESI-MS spectra, to fully understand and characterise what is occurring with respect to the coordination of these nucleic acid derivatives, a computational investigation was carried out.

4.3.2 Computational results

4.3.2.1 Benchmarking studies

In order to examine these complexes computationally, we needed to benchmark the computational calculations. This is a process where similar complexes, with an elucidated crystal structure, are compared to the optimised geometry. Given that steric effects and inherent strain are present in the ligands examined via ESI-MS, several benchmark structures have been selected which build up both of these aspects. Whilst only the most similar carrier ligand to those investigated is discussed here, further benchmarking is shown in Appendix II.

Given that bbmm, bbme and bbmp consist of bis-benzimidazole moieties, a Pd(II) complex of a similar carrier ligand was modelled using PM3, and bond

lengths and angles were compared to the crystal structure. The complex selected for this benchmarking was [Pd((bmim)$_2$CO)ClMe], Fig. 4.23, is a benzimidazole derivative, similar to the ligands that were analysed via ESI-MS. This compound has a formaldehyde-type linker between the benzimidazole rings.

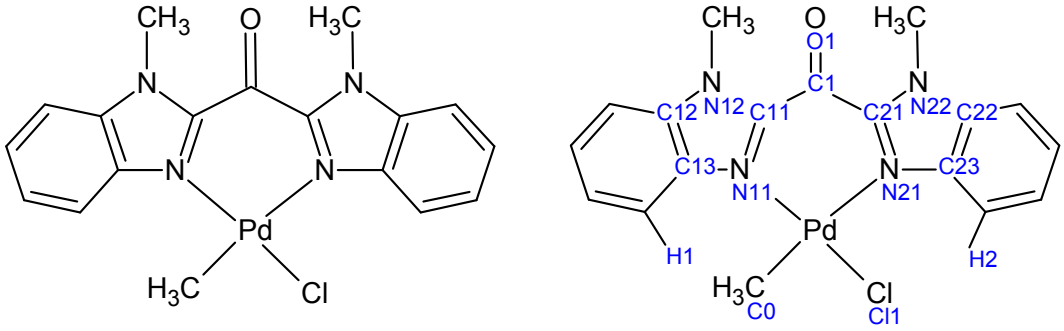

Figure 4.23 – Structure (left) and crystal structure numbering scheme (right) for [Pd((bmim)$_2$-MeCO)Cl].

This complex was selected due to the fact that the linker between the benzimidazole rings consisted of a single carbon, as is the case with the bbmm carrier ligand. The effect of this short linker is a reduction in the bite angle N(11)-Pd-N(21), which increases the inherent strain in this complex. Therefore, this benchmark accommodates the "lowest common denominator" i.e. if the PM3 method can accurately model this inherently strained complex, the less-strained complexes should be calculated equally well.

Literature bond lengths (Table 4.6 and Fig. 4.24) and angles (Table 4.7 and Fig. 4.25) for the [Pd((bmim)$_2$CO)ClMe] system are compared with the theoretical bond lengths and angles as measured from the PM3 equilibrium geometry structure.

With regard to the bond length comparison (Fig 4.24), a generally good comparison was found. As expected, the PM3 optimisation resulted in a very good description of the organic bonds (C-C and C-N, with an R^2 value of 0.8961), and a relatively poorer description of the Pt-L bonds, especially with respect to accounting for the structural *trans* effect present in this complex.

Table 4.6 – Benchmark data – comparison of bond lengths, crystal vs optimised.

Bond	Crystal Bond Lengths (Å)	Calculated Bond Lengths (Å)
Pd-Cl(1)	2.323	2.321
Pd-C(0)	2.030	2.075
Pd-N(11)	2.042	1.978
Pd-N(21)	2.156	2.006
N(11)-C(11)	1.338	1.377
N(21)-C(21)	1.323	1.375
N(11)-C(13)	1.389	1.435
N(21)-C(23)	1.374	1.433
C(11)-N(12)	1.364	1.414
C(21)-N(22)	1.367	1.414
N(12)-C(12)	1.378	1.402
N(22)-C(22)	1.374	1.404
C(12)-C(13)	1.393	1.414
C(22)-C(23)	1.414	1.414
C(11)-C(1)	1.489	1.494
C(21)-C(1)	1.489	1.491
C(1)-N(1)	1.212	1.213

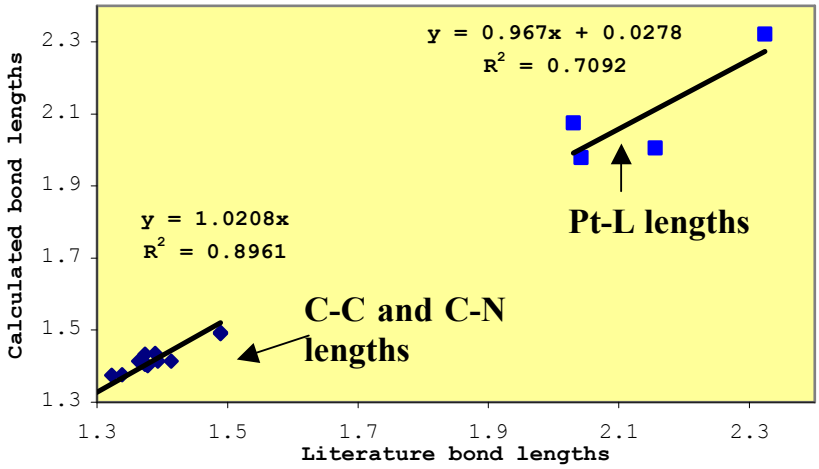

Figure 4.24 – Literature bond lengths (Å) versus theoretical bond lengths as derived from the optimised geometry using PM3 in Spartan '06 for [Pd((bmim)$_2$CO)ClMe],.

Coordinated methyl groups are known to have a greater structural *trans* effect than chloride, which results in an increase in the N-Pd bond opposite[222]. The PM3 method employed here seems to underestimate this *trans* effect. However, this shortcoming in this benchmarking result is redundant, as none of the systems of interest in this study contained a coordinated methyl group.

Table 4.7 – Benchmark data – comparison of bond angles, crystal vs optimised.

Angle	Crystal Bond Angles (°)	Calculated Bond Angles (°)
N(11)-Pd-N(21)	85.6	90.60
Cl(1)-Pd-C(0)	87.9	86.62
N(11)-Pd-C(0)	90.6	92.45
N(21)-Pd-Cl(1)	95.65	90.24
N(11)-Pd-Cl(1)	176.8	178.11
N(21)-Pd-C(0)	173.2	175.85
Pd-N(11)-C(11)	119.6	121.08
Pd-N(21)-C(21)	119.3	121.09
Pd-N(11)-C(13)	131.1	133.37
Pd-N(21)-C(23)	132.6	133.12
C(11)-N(11)-C(13)	105.7	105.45
C(21)-N(21)-C(23)	105.7	105.65
N(11)-C(11)-C(1)	125.3	126.09
N(21)-C(21)-C(1)	124.9	125.63
N(11)-C(11)-N(12)	111.9	110.52
N(21)-C(21)-N(22)	112.7	110.54
C(1)-C(11)-N(12)	122.7	123.28
C(1)-C(21)-N(22)	122.3	123.77
C(11)-N(12)-C(12)	106.7	107.84
C(21)-N(22)-C(22)	106.6	107.75
N(12)-C(12)-C(13)	106.9[1]	106.50
N(22)-C(22)-C(23)	105.9[1]	106.50
C(12)-C(13)-N(11)	108.8	109.60
C(22)-C(25)-N(21)	109.1	109.54
C(11)-C(1)-C(22)	117.5	114.59
C(11)-C(1)-N(1)	121.4	122.54
C(22)-C(1)-N(1)	121.0	122.82

[1] These angles are not as they appear in the Done *et al* paper, however they are the angles as they appear in the CIF raw data as obtained from the Cambridge Crystallographic Database. The angles as published in the literature were 130.7 and 135.9 respectively.

The graphical comparison of these bond angles, Fig. 4.25, shows a very good correlation (R^2 = 0.9918), suggesting that the PM3 method accurately describes the angles in this complex. This, coupled with the bond length data above, shows that PM3 can accurately describe the geometry of strained, bidentate Pd(II) complexes, based on benzimidazole moieties.

However, due to the importance of steric hindrance in this study, further characterisation of this complex was carried out. As the steric hindrance of significance in these investigations specifically influence the palladium environment, some additional measurements were made on the crystal structure

(CCDC number 141684, obtained from the Cambridge Crystallographic Data Centre) and compared these measurements to the computed structure. Specifically, the lengths representing 'above the plane' (Pd···H(1) and Pd···H(2)) and below the plane (Pd-O(1)) hindrances, as well as the H(1)···Pd···H(2) and H(1)···O(1)···H(2) angles. The results of these measurements can be found in Table 4.8 below, which shows a generally good agreement between the crystal structure and the calculated structure.

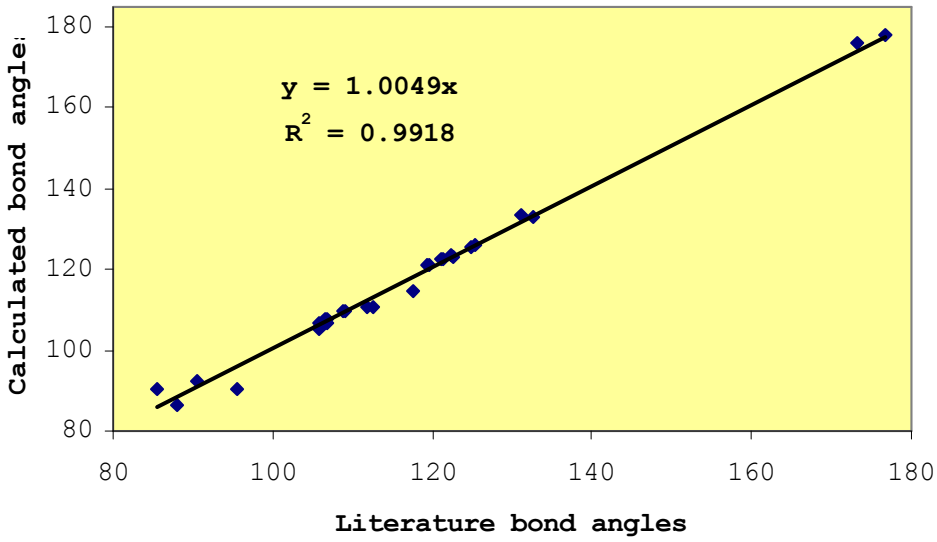

Figure 4.25 – Literature bond angles (˚) versus theoretical bond angles as derived from the optimised geometry using PM3 in Spartan '06 for [Pd((bmim)$_2$CO)ClMe].

Table 4.8 – Supplementary measurements describing the palladium environment.

Length / Angle	Crystal measurement	Calculated measurement	Δ
Pd···O(1)	4.396 Å	4.423 Å	+0.027 Å
Pd···H(1)	3.454 Å	3.424 Å	-0.030 Å
Pd···H(2)	3.530 Å	3.420 Å	-0.110 Å
H(1)···Pd···H(2)	120.8 °	117.9 °	-2.9 °
H(1)···O(1)···H(2)	57.3 °	53.6 °	-3.7 °

An observation of interest here is the verification of the difference between solid state and gas phase structures. Whilst the calculated and crystal structures have been shown to be almost identical, there is a constant difference in all bond lengths and angles. This is evident by the gradient of the above plots

(Figs. 4.24 and 4.25) as both gradients are slightly more than 1, suggesting that the bond lengths and angles are consistently slightly larger in the calculated structures than in the corresponding crystal measurements. This is due to the fact that the crystal structure is influenced by the stacking forces within the crystal; influences that do not exist in the gas phase geometries as calculated using PM3.

In summary, the PM3 method appears to be well suited for producing accurate geometries of palladium(II) complexes that bind through an inherently strained benzimidazole moiety. This suggests that PM3, as utilised in this case by Spartan '06, will accurately represent the systems of interest in this work.

4.3.2.2 Comparison of computational modelling with experimental ESI-MS data

Once the benchmarking process was completed, systems that were studied in the ESI-MS could be probed computationally. With confidence that the PM3 method would accurately describe the geometries of the palladium(II) complexes, displaying various amounts of restriction, the species of interest to this work were modelled.

All complexes required for the calculation of BE values were modelled using PM3. The di-aqua species, $[Pd(L)(H_2O)_2]^{2+}$, where L = bbmm, bbme, or bbmp was modelled first. Secondly, the monofunctional species, where each ligand was modelled with each of the three nucleobases used and a water molecule filled the fourth coordination site, $[Pd(L)(nuc_1)(H_2O)]^{2+}$, where nuc_1 = inosine, cytidine or 3-methyladenine were modelled. Finally, all combinations of bis-nucleotide species for all three palladium systems were modelled, including the combinations that were not identified in the ESI-MS results. The BE values for all species were calculated following adequate equilibrium geometry optimisation.

It must be noted that the use of semi-empirical PM3 methods to calculate any energetic parameter relating to covalent bond formation/ dissociation is rare, given the relative simplicity of these methods compared to the more extensive electronic methods such as DFT. A reason for this caution in using PM3 for any energy calculations is that semi-empirical methods greatly simplify electron-electron interactions. By employing the Neglect of Diatomic Differential Overlap (NDDO) approximation, the number of electron-electron interactions is reduced by two orders of magnitude[223]. This approximation can affect the accuracy of bonding energetics, given the nature of the chemical bond.

However, with respect to the complexes in this study, PM3 was used for estimating the relative BE magnitudes for two reasons. Firstly, the binding sites for all nucleobases added are the same – heterocyclic nitrogen atoms. Therefore, any errors in the estimation of this bond will be roughly equivalent for all nucleobases, essentially cancelling out any inherent errors. Secondly, interactions would be expected to play a large part in influencing the BEs of these complexes, by greatly increasing the calculated energies of structures that contain significant steric repulsion. These steric influences should be clear when comparing relative energies.

The BE's that are obtained using this method are only *relative* values; they are by no means *absolute*. In this regard, it is the *trends* in the PM3 calculated BE's that are being examined, not the *absolute* binding energies. Of importance is whether a particular nucleoconstituent is more or less likely to bind to a particular complex; the magnitude of this difference is largely inconsequential, given the fact that the PM3 method was chosen to optimise these structures. However, as PM3 is computationally inexpensive, this method allows for a large number of large transition metal systems to be calculated in a relatively short period of time, with the view towards developing this method as a screening tool for the future design of ligands with specific binding patterns.

4.3.2.2.1 Di-aqua species – above- and below-the-plane hindrance

After modelling the di-aqua species of the palladium complexes of interest, the subtle steric effects of all three were illustrated. All three palladium(II) systems studied, bbmm, bbme and bbmp, are sterically restrictive to a degree, given the design of the ligands. The source of restriction, however, appears to change across the series. As can be seen in Figures 4.26a and 4.26b below, the steric hindrance with the other two coordination sites essentially move from 'above the plane' in the bbmm, to 'below the plane' in the bbmp. The bbme is somewhat between the two extremes.

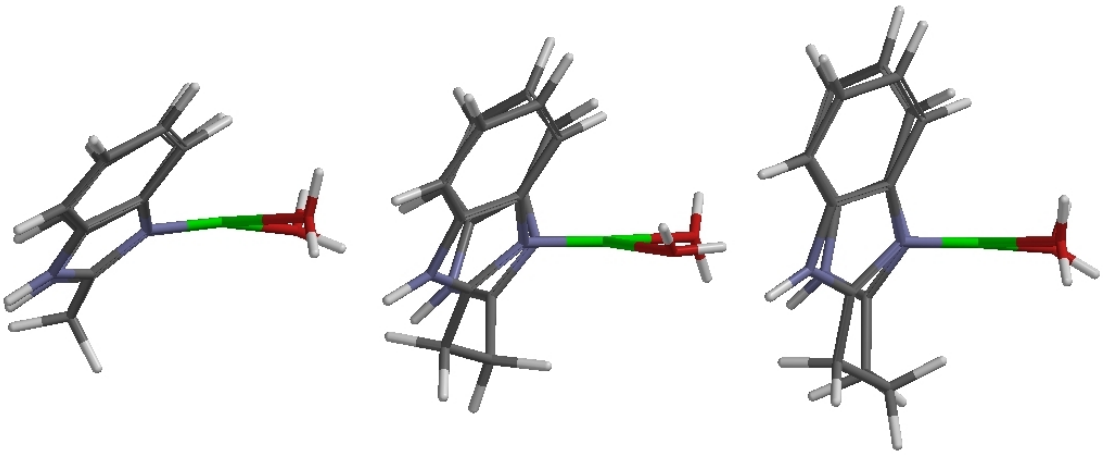

Figure 4.26a – Side Views of di-aqua palladium complexes of bbmm (left), bbme (centre) and bbmp (right), rendered in 'tube' form.

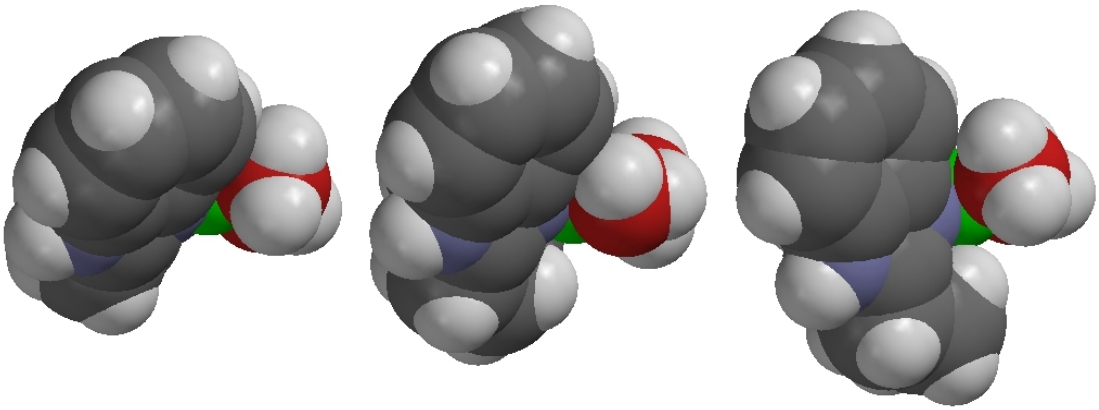

Figure 4.26b – Side Views of di-aqua palladium complexes of bbmm (left), bbme (centre) and bbmp (right), rendered in 'space filling' form, representing atomic radii.

The 'above the plane' restrictions may be expected to wield the most influence, as this hindrance is due to the bulky benzimidazole rings crowding the

coordination sites. The ‘below the plane’ hindrance is due to hydrogen atoms of the acetyl linker attempting to form agostic binding interactions with the palladium. However, this ‘below the plane’ hindrance has some freedom in the bbmp ligand, due to the fact that the benzimidazole rings are connected via a propyl linker. As such, the second CH_2 group that seems to cause the most steric conflict in this ligand has a degree of freedom, allowing for the rotation, and subsequent relaxation, of steric influence.

In order to fully probe these steric environments, the binding energy values for single nucleoside addition to each ligand system will be investigated first. The identification of the expectedly subtle steric effects on the selectivity of nucleobase addition, as a result of PM3 investigations, will be discussed.

4.3.2.2.2 Disclaimer affecting the analysis of the following data

It is important at this point in the discourse to clearly state the aim of the analyses of these systems. Firstly, the original aim of the experimental work was to *qualitatively* identify any complexes, either mono- or bis-substituted, that could be totally excluded depending on the steric properties of the carrier ligand. Due to this aim, an attempt to study these systems mechanistically was not carried out.

Similarly, the aim of the computational work was to identify trends and relative, *qualitative*, differences in the complexes, as well as to test the hypothesis that sterically unsuitable complexes would be identifiable using a semi-empirical PM3 approach. If detailed energetic and mechanistic investigations were sought after, the approach used would be largely different. In this regard, in the following discussions, trends in BE data and precluded complexes in ESI-MS data is paramount.

4.3.2.2.3 Mono-substituted considerations

In order to calculate the BE's for the mono-substituted complexes, the equilibrium geometries and subsequent energies of the di-aqua palladium species, $[Pd(L)(H_2O)_2]^{2+}$, the mono-functional, coordinatively saturated complexes of each ligand, $[Pd(L)(nuc_1)(H_2O)]^{2+}$, the water molecule (aqua ligand) which is replaced and nucleobases were obtained. A summary of these BE values is below in Table 4.9, with the energy values contained in Appendix IV. Each ligand system will be discussed in turn, relating these values to the experimental results.

Table 4.9 - BE values for the addition of each nucleobase to each ligand system, to form a complex of general formula $[Pd(\mathbf{L})(\mathbf{nuc_1})(H_2O)]^{2+}$. All values are in kcal/mol.

(nuc_1) identity	**L = bbmm**	**L = bbme**	**L = bbmp**
Pd-L-Inosine	-66.66	-68.02	-65.60
Pd-L-Cytidine	-52.53	-45.38	-44.43
Pd-L-3-methyladenine	-51.62	-53.18	-52.17

To recap the experimental results, with respect to the mono-functional binding, a strong preference for inosine in all three competition experiments was shown for both the bbme system (Table 4.4) as well as the bbmp system (Table 4.5). This result is reflected in the BE values obtained above, with a strong bias favouring mono-inosine binding. These BE results also seem to reflect the selectivity displayed in the third competition experiment involving bbme and all three nucleobases, with a preference for 3-methyladenine over cytidine. Interestingly, with respect to the bbmp ligand system, the experimental results suggest that the mono-substitution of a cytidine moiety is slightly preferred over the 3-methyladenine. Certainly, the BE results presented above suggest that, in this regard, the bbmp system should behave similarly to the bbme system. Whether this is due to a limitation in the computational methodology, or possibly a limitation in the experimental design with respect to reactant concentrations and the subsequent sequestering of mono-substituted species into bis-substituted species, is unknown. However, this outcome is of limited interest in this study, where the primary aims are to describe what bis-substituted complexes are precluded.

The bbme and bbmp BE results above also seem to qualitatively reflect the relative I_S values as discussed previously, where the N7 of inosine (1.03) was the least hindered site, adenine (1.17) was somewhat hindered, and cytidine (1.56) the most hindered. Interestingly, this is not the case for the bbmm ligand, as the BE values suggest that the cytidine would be as attractive to the first binding site as 3-methyladenine. A comparison of the BE values also suggests that this is due to a *reduction* in steric hindrance against the cytidine, rather than an *increase* in the steric hindrance experienced by a coordinating 3-methyladenine. This is an intriguing outcome, and highlights the possible influence available via prudent ligand design.

To further investigate these intricate steric environments, the bis-nucleotide selectivity will be examined.

4.3.2.2.4 Bis-substituted considerations

As mentioned previously, the major aim of this Chapter is to study what bis-substituted complexes are formed and, perhaps more importantly, which combinations of nucleobases are precluded, depending on the steric environment. This bis-substitution discrimination may inform further drug design studies, due to the mechanism of action of similar chemotherapy agents as discussed in section 4.1.2 above. In the following discussion, bbme and bbmp will be examined first, with appropriate conclusions drawn regarding the possible behaviour of the bbmm system following.

The bbme BE results are presented below, in Table 4.10, alongside the ESI-MS results first presented in section 4.3.1.2.2 for ease of comparison. These BE values were calculated as per Eq. 4.1 in section 4.2.3 above and are presented in kcal/mol. All BE values displayed in the following tables are for the most energetically favourable conformer, given that various possible orientations of the nucleobases around the palladium atom are possible (i.e. head-to-head, etc.). Further, where the complexes contain two different nucleobases, the BE

value presented indicates the lowest energy combination and are presented this way in Table 4.10. For example, the first entry indicates that the [Pd(bbme)(3-methyladenine)(Inosine)]$^+$ complex has a BE of –57.14 kcal/mol when an inosine moiety binds to a [Pd(bbme)(3-methyladenine)(H_2O)]$^+$ mono-substituted complex.

Table 4.10 –Summary of calculated BE values for the most energetically favourable bis-functional adducts of the bbme system, as compared to the equivalent ESI-MS results. All values are in kcal/mol.

		ESI-MS Result (% abundance)		
Complex	**BE**	**Inos.-Cyt.**	**Inos.-3-MeA**	**All three nuc.**
Pd(bbme)**(3-methyladenine)(Inosine)**	**-57.14**	-	10.4	12.5
Pd(bbme)**(Cytidine)(Inosine)**	**-51.51**	8.7	-	9.5
Pd(bbme)**(Inosine)$_2$**	**-49.88**	9.8	7.2	2.5
Pd(bbme)**(Cytidine)(3-methyladenine)**	**-41.08**	-	-	0
Pd(bbme)**(Cytidine)$_2$**	**-27.02**	0	-	0
Pd(bbme)**(3-methyladenine)$_2$**	**+14.74**	-	0	0

The first aspect that is immediately noticed is the relatively greater magnitude in calculated BE values compared to the mono-substituted complexes. This is not unexpected, as the nucleobases themselves provide some steric hindrance, leading to consistently larger binding energies. Also noticeable is the large range of BE values, indicative of the large effect wielded by the sterically active carrier ligand in combination with the nucleobases.

Generally, as can be seen in Table 4.10 above, the computationally derived BE values follow a very similar trend to that observed in the ESI-MS results, with the possible exception of the inosine-cytidine competition experiment. This may be due to the fact that the two complexes are energetically similar, according to the BE values, and as such may be sensitive to experimental stoichiometric ratios. Certainly, where more competition is present, as seen in the final experiment with all three nucleobases, the trend of the experimental results matches the calculated BE values.

Perhaps more interestingly is the absence of three bis-complexes; namely the cytidine-3-methyladenine, bis-cytidine and bis-3-methyladenine adducts. The pleasing aspect of this non-appearance of these adducts in the experimental data is that these particular complexes registered the largest BE values, showing that, in this particular example, the semi-empirical PM3 method is capable of not only describing the trends of *observed* species, but is able to identify *unobserved* species. This discrimination between observed and absent species (in the ESI-MS data) appears to lie somewhere between approximately –50 kcal/mol and –41 kcal/mol (in the computational data). This range is only approximate, given the limitations of the PM3 method and is not designed to form the basis of a steadfast rule; it is merely an observation at this point.

The bbmp results (Table 4.11) display a similar trend to the bbme results, reinforcing the similarity of these ligands. However, closer inspection reveals subtle differences between the bbme system discussed above and the bbmp system described below.

Table 4.11 – Summary of calculated BE values for the most energetically favourable bis-functional adducts of the bbmp system, as compared to the equivalent ESI-MS results. All values are in kcal/mol.

		ESI-MS Results		
Complex	**BE**	**Inos.-Cyt.**	**Inos.-3-MeA**	**All three nuc.**
Pd(bbmp)**(3-methyladenine)(Inosine)**	**-57.61**	-	22.6	12.0
Pd(bbmp)**(Cytidine)(Inosine)**	**-54.21**	18.3	-	10.9
Pd(bbmp)**(Inosine)$_2$**	**-52.69**	14.8	21.8	7.8
Pd(bbmp)**(Cytidine)(3-methyladenine)**	**-45.02**	-	-	0
Pd(bbmp)**(Cytidine)$_2$**	**-23.60**	6.3	-	0
Pd(bbmp)**(3-methyladenine)$_2$**	**+15.14**	-	0	0

Unlike the bbme system above, the trends seen in the ESI-MS for all three experiments with the bbmp ligand match the trends seen in the equivalent BE results, with respect to those species observed, as well as those species which are not observed. This is again a pleasing result that supports the use of PM3 as a possible screening method in the development of cytotoxic agents.

However, what must be noted here is the ambiguity of the bis-cytidine results. According the BE results, which explain all other experimental observations to this point, the bis-cytidine adduct should not form at all, especially given the absence of a cytidine-3-methyladenine complex, which appears to be more energetically favourable. This may again be a stoichiometric artefact from the experimental procedure, especially as this particular complex is not seen in the experiment involving a greater level of competition.

Where competition for the second binding site is greater, energetic considerations would gain more importance. This is consistent with the BE results for the experiment involving all three nucleobases, with the same three adducts precluded as seen in the bbme system. Again, the PM3 results suggest a theoretical cut-off energy whereby that particular combination is less likely to be observed in the ESI-MS results, of somewhere between –53 and – 45 kcal/mol. To cautiously expand on this theme, keeping in mind the energetic limitations of semi-empirical methods, it would appear that this energy cut-off may lie between –50 and –45 kcal/mol if the results for both ligand systems are combined (and the bis-cytidine positive result is discounted).

Whilst, due to unforseen circumstances, the ESI-MS results involving the bbmm carrier ligand did not work as planned, some informed comment can still be made. The BE values for the bbmm ligand in contained in Table 4.12 below.

Table 4.12 – Summary of calculated BE values for all possible bis-functional adducts of Pd-bbmm. All values are in kcal/mol.

Complex	**BE**
Pd(bbmp)**(3-methyladenine)(Inosine)**	**-58.98**
Pd(bbmp)**(Inosine)$_2$**	**-50.58**
Pd(bbmp)**(Cytidine)(Inosine)**	**-43.80**
Pd(bbmp)**(3-methyladenine)(Cytidine)**	**-36.99**
Pd(bbmp)**(Cytidine)$_2$**	**-14.68**
Pd(bbmp)**(3-methyladenine)$_2$**	**+12.49**

Using the results for the two previous studies as a guideline for the interpretation of the BE values above, it would be expected that the more sterically-hindered system, bbmm, would only form the 3-methyladenine-inosine and bis-inosine adducts, with all other nucleobase combinations precluded, including the cytidine-inosine adduct that was identified in all other experiments where this combination was possible. This conclusion is based on the ESI-MS results and the subsequent PM3 BE values obtained for the complexes around the threshold of inclusion and preclusion seen in the two other ligand systems. Whether this prediction holds true can only be realised through further experimental investigation.

Table 4.13 –Summary of calculated BE values for all possible bis-functional adducts of Pd-bbmm. All values are in kcal/mol.

	Nucleobase to be added		
Complex	**Inosine**	**Cytidine**	**3-methyladenine**
Pd(bbmm)**(Inosine)**	19.38	27.60	13.34
Pd(bbmm)**(Cytidine)**	16.72	33.76	12.36
Pd(bbmm)**(3-MeA)**	10.98	20.88	12.50

4.3.3 Summary

Evidence presented here shows that ESI-MS can be used in order to determine site selectivity for platinum(II) and palladium(II) complexes that possess a variety of steric influences on the binding site. This nucleoconstituent selectivity, as well as the vagaries of the "di-aqua" species, have been fully characterised using semi-empirical methods, providing insights into all aspects of the experimental procedure. Further, this study shows that a semi-empirical PM3 methodology may be used to prudently design similar carrier ligands of a more targeted nature, as the systems studied here agreed with the general trends seen in the ESI-MS data.

Scope for further work in this area is extensive, as a variety of carrier ligands may be synthesised, for both platinum(II) and palladium(II), with a variety of influences over the coordination sphere, steric or otherwise, , lead by PM3 calculations, as these are computationally cheap and generally yield good qualitative information. Further competition experiments using ESI-MS can also be envisioned, where short oligonucleotide sequences may be used *in lieu* of the nucleoconstituents, which would provide additional information on the specific binding patterns of the bis-functional adducts of these sterically restricted complexes, as oligonucleotide sequences would have their own unique restrictions.

REFERENCES

(1) Raghavan, V. *J. Phase Equilib.* **2002**, *23*, 437-438.

(2) Jungwirth, T.; Sinova, J.; Masek, J.; Kucera, J.; MacDonald, A. H. *Rev. Mod. Phys.* **2006**, *78*, 809-864.

(3) Stueber, D. *Concepts Magn. Reson.* **2006**, *28A*, 347-368.

(4) Curtarolo, S.; Morgan, D.; Ceder, G. *Calphad* **2005**, *29*, 163-211.

(5) Atkinson, H. V. *Progr. Mater. Sci.* **2005**, *50*, 341-412.

(6) Nelson, B. A.; Kim, C. C.; Cassidy, A. P.; Griffith, S. D.; Milroy, R. D.; Jarboe, T. R. *J. Fusion Energ.* **2007**, *26*, 127-130.

(7) Andreev, M. I.; Afanasiev, V. V.; Belevitin, A. G.; Karaulov, A. V.; Romodanov, V. L.; Sakharov, V. K.; Tikhomirov, G. V.; Vasiliev, A. P.; Kandiev, Y. Z.; Lyutov, V. D.; Sokolov, Y. A.; Terekhin, V. A.; Shmakov, V. M.; Androsenko, P. A.; Semenov, V. P.; Trykov, L. A.; Lopatkin, A. V.; Muratov, V. G. *Fusion Eng. Des.* **2001**, *55*, 373-385.

(8) Jameson, C. J. *ACS Symp. Ser.* **1999**, *732*, 1-23.

(9) Canetta, E.; Lucia, U.; Maino, G. *X-Ray Spectrom.* **1999**, *28*, 357-371.

(10) Anderson, G. Y.; McClinton, C. R.; Weidner, J. P. *Progr. Astronaut. Aeronaut.* **2000**, *189*, 369-446.

(11) Krishnamurthy, R.; Woods, D. A. M.; Chandra, S. *Flow Turbulence Combust.* **2000**, *64*, 29-41.

(12) Prommersberger, K.; Maier, G.; Wittig, S., Applied Vehicle Technology Panel (AVT) Symposium, Lisbon 1998.

(13) Seaton, M. J. *Astronomical Society of the Pacific Conference Series* **1995**, *78*, 1-17.

(14) National Institute of Standards and Technology (NIST), 2006.

(15) Gillet, V. J.; Willett, P. In *Trends in Drug Research III*; van der Groot, H., Ed.; Elsevier: Amsterdam, 2002; Vol. 32, pp 125-133.

(16) Lemmen, C.; Lengauer, T. *J. Comput. Aided Mol. Des.* **2000**, *14*, 215-232.

(17) Loew, G. H. *Mod. Drug Discovery* **1999**, *2*, 24-30.

(18) Nussinov, R.; Ma, B.; Wolfson, H. J. In *Current Topics in Computational Molecular Biology*; Jiang, T., Xu, Y., Zhang, M. Q., Eds.; MIT Press: Cambridge, MA, 2002, pp 503-524.

(19) Pattabiraman, N. *Curr. Med. Chem.* **2002**, *9*, 609-621.

(20) Clark, D. E.; Grootenhuis, P. D. J. *Curr. Opin. Drug Discovery Dev.* **2002**, *5*, 382-390.

(21) Clark, D. E.; Pickett, S. D. *Drug Discovery Today* **2000**, *5*, 49-58.

(22) Pirard, B. *Comb. Chem. High Throughput Screening* **2004**, *7*, 271-280.

(23) Podlogar, B. L.; Muegge, I. *Curr. Top. Med. Chem.* **2001**, *1*, 257-275.

(24) Podlogar, B. L.; Muegge, I.; Brice, L. J. *Curr. Opin. Drug Discovery Dev.* **2001**, *4*, 102-109.

(25) Klein, E.; Lukeš, V. *THEOCHEM* **2006**, *767*, 43-50.

(26) Wright, J. S.; Carpenter, D. J.; McKay, D. J.; Ingold, K. U. *J. Am. Chem. Soc.* **1997**, *119*, 4245-4252.

(27) Wright, J. S.; Johnson, E. R.; DiLabio, G. A. *J. Am. Chem. Soc.* **2001**, *123*, 1173-1183.

(28) Borges dos Santos, R. M.; Martinho Simoes, J. A. *J. Phys. Chem. Ref. Data.* **1998**, *27*, 707-739.

(29) Henderson, E.; Hardin, C. C.; Walk, S. K.; Tinoco, I.; Blackburn, E. H. *Cell* **1987**, *51*, 899-908.

(30) Smirnov, I.; Shafer, R. H. *Biopolymers* **2001**, *56*, 147-194.

(31) Simonsson, T. *Biol. Chem.* **2001**, *382*, 621-628.

(32) Arthanari, H.; Bolton, P. H. *Chem. Biol.* **2001**, *8*, 221-230.

(33) Koch, K. J.; Aggerholm, T.; Nanita, S. C.; Cooks, R. G. *J. Mass Spec.* **2002**, *37*, 676-686.

(34) Aggerholm, T.; Nanita, S. C.; Koch, K. J.; Cooks, R. G. *J. Mass Spec.* **2003**, *38*, 87-97.

(35) Mezzache, S.; Alves, S.; Paumard, J.-P.; Pepe, C.; Tabet, J.-C. *Rapid Comm. Mass Spec.* **2007**, *21*, 1075-1082.

(36) Lippert, B. *Coord. Chem. Rev.* **2000**, *200-202*, 487-516.

(37) Derose, V. J.; Burns, S.; Kim, N.-K.; Vogt, M. *Comprehensive Coordination Chemistry II* **2003**, *8*, 787-812.

(38) Rosenberg, B.; VanCamp, L.; Trosko, J. E.; Masnsour, V. H. *Nature* **1969**, *222*, 385-386.

(39) Halliwell, B.; Gutteridge, J. M. C. *Free Radicals in Biology and Medicine*, 3rd. ed.; Oxford University Press: Oxford, 1999.

(40) Cutler, R. G.; Packer, L.; Bertram, J.; Mori, A., Eds. *Oxidative Stress and Aging*; Birkhäuser Verlag: Basel, 1995.

(41) Pritchard, G., Ed. *Plastics Additives An A-Z Reference*; Chapman and Hall: London, 1998.

(42) Zellner, R. *Oxid. Commun.* **1986**, *9*, 255-300.

(43) Harman, D. *J. Gerontol.* **1956**, *11*, 298-300.

(44) Harman, D. *Proc. Natl. Acad. Sci. USA* **1981**, *78*, 7124-7128

(45) Ames, B. N.; Shigenaga, M. K.; Hagen, T. M. *Proc. Natl. Acad. Sci. USA* **1993**, *90*, 7915-7922.

(46) Jesberger, J. A.; Richardson, J. S. *Int. J. Neurosci.* **1991**, *57*, 1-17.

(47) Adams, J. D. J.; Odunze, I. N. *Free Radic. Biol. Med.* **1991**, *10*, 161-169.

(48) Fraga, C. G.; Motchnik, P. A.; Shigenaga, M. K.; Helbock, H. J.; Jacob, R. A.; Ames, B. N. *Proc. Natl. Acad. Sci. USA* **1991**, *88*, 11003-11006.

(49) Packer, L. In *Oxidative Stress and Aging*; Cutler, R. G., Packer, L., Bertram, J., Mori, A., Eds.; Birkhäuser Verlag: Basel, 1995.

(50) Marnett, L. J.; Hurd, H.; Hollstein, M. C.; Esterbauer, D. E.; Ames, B. N. *Mutat. Res.* **1985**, *148*, 25-34.

(51) Wijtmans, M.; Pratt, D. A.; Valgimigli, L.; DiLabio, G., A.; Pedulli, G. F.; Porter, N. A. *Agnew. Chem. Int. Ed.* **2003**, *42*, 4370-4373.

(52) Rezai-Zadeh, K.; Shytle, D.; Sun, N.; Mori, T.; Hou, H.; Jeanniton, D.; Ehrhart, J.; Townsend, K.; Zeng, J.; Morgan, D.; Hardy, J.; Town, T.; Tan, J. *J. Neurosci.* **2005**, *25*, 8807-8814.

(53) Murcia, M. A.; Jimenez, A. M.; Martinez-Tome, M. *Progr. Nutr.* **2001**, *3*, 31-38.

(54) Dimitrios, B. *Trends in Food Science and Technology* **2006**, *17*, 505-521.

(55) Giugliano, D.; Esposito, K. *Ann. NY Acad. Sci.* **2005**, *1056*, 253-260.

(56) Heinonen, I. M.; Meyer, A. S. *Fruit and Vegetable Processing* **2002**, 23-51.

(57) Yanishlieva-Maslarova, N. V.; Heinonen, I. M. *Antioxidants in Food* **2001**, 210-263.

(58) Kaur, C.; Kapoor, H. C. *Int. J. Food Sci. Tech.* **2001**, *36*, 703-775.

(59) Yang, F.; Lim, G. P.; Begum, A. N.; Ubeda, O. J.; Simmons, M. R.; Ambegaokar, S. S.; Chen, P. P.; Kayed, R.; Glabe, C. G.; Frautschy, S. A.; Cole, G. M. *J. Biol. Chem.* **2005**, *280*, 5892-5901.

(60) Weber, W. M.; Hunsaker, L. A.; Abcouwer, S. F.; Deck, L. M.; Vander Jagt, D. l. *Bioorg. Med. Chem.* **2005**, *13*, 3811-3820.

(61) Barik, A.; Mishra, B.; Shen, L.; Mohan, H.; Kadam, R. M.; Dutta, S.; Zhang, H.-Y.; Priyadarsini, K. I. *Free Radic Biol Med* **2005**, *39*, 811 - 822.

(62) Wright, J. S.; Johnson, E. R.; DiLabio, G. A. *J. Am. Chem. Soc.* **2001**, *123*, 1173-1183.

(63) Sroka, Z.; Cisowski, W. *Food Chem. Toxicol.* **2003**, *41*, 753-758.

(64) Katsube, T.; Tabata, H.; Ohta, Y.; Yamasaki, Y.; Anuurad, E.; Shiwaku, K.; Yamane, Y. *J. Agric. Food Chem.* **2004**, *52*, 2391-2396.

(65) Buge, J.-A.; Aust, S.-D. *Methods in Enzymology* **1978**, *52C*, 302-310.

(66) Dinis, T. C. P.; Madeira, V. M. C.; Almeida, L. M. *Arch. Biochem. Biophys.* **1994**, *315*, 161-169.

(67) Janero, D. R. *Free Rad. Biol. Med.* **1990**, *9*, 515-540.

(68) Kromhout, D. *Lipids* **1999**, *34*, S27-S31.

(69) WHO, 2004.

(70) Ancerewicz, J.; Migliavacca, E.; Carrupt, P.-A.; Testa, B.; Bree, F.; Zini, R.; Tillement, J.-P.; Labidalle, S.; Guyot, D.; Chauvet-Monges, A.-M.; Crevat, A.; Ridant, A. L. *Free Radical Biol. Med.* **1998**, *25*, 113-120.

(71) Karki, S. B.; Treemaneekarn, V.; Kaufman, M. J. *J. Pharm. Sci* **2000**, *89*, 1518-1524.

(72) Moridani, M. Y.; Pourahmad, J.; Bui, H.; Siraki, A.; O'Brien, P. J. *Free Radical Biol. Med.* **2003**, *34*, 243-253.

(73) Oktay, M.; Gulcin, I.; Kufrevioglu, O. I. *Lebensm.-Wiss. U.-Technol.* **2003**, *36*, 263-271.

(74) Saito, S.; Kawabata, J. *Tetrahedron* **2005**, *61*, 8101-8108.

(75) Brand-Williams, W.; Cuvelier, M. E.; Berset, C. *Lebensm.-Wiss. U.-Technol.* **1995**, *28*, 25-30.

(76) Kitts, D. D.; Wijewickreme, A. N.; Hu, C. *Mol. Cell. Biochem.* **2000**, *203*, 1-10.

(77) Valgimigli, L.; Banks, J. T.; Ingold, K. U.; Lusztyk, J. *J. Am. Chem. Soc.* **1995**, *117*, 9966 - 9971.

(78) Thorpe, G. H.; Kricka, L. J. *Methods Enzymol.* **1986**, *133*, 331-353.

(79) Cheng, Z.; Yan, G.; Li, Y.; Chang, W. *Anal. Bioanal. Chem.* **2003**, *375*, 376-380.

(80) Georgetti, S. R.; Casagrande, R.; DiMambro, V. M.; Azzolini, A. E. C. S.; Fonseca, M. J. V. *AAPS Pharm. Sci.* **2003**, *5*, A20.

(81) Cao, G.; Alessio, H. M.; G., C. R. *Free Radic. Biol. Med.* **1993**, *14*, 303-311.

(82) Gomes, A.; Fernandes, E.; Lima, J. L. F. C. *J. Biochem. Biophys. Methods* **2005**, *65*, 45-80.

(83) Ou, B.; Hampsch-Woodill, M.; Prior, R. L. *J. Agric. Food Chem.* **2001**, *49*, 4619-4626.

(84) Naguib, Y. M. A. *Anal. Biochem.* **2000**, *284*, 93-98.

(85) Arts, M. J. T. J.; Dallinga, J. S.; Voss, P.-H.; Haenen, G. R. M. M.; Bast, A. *Food Chem.* **2003**, *80*, 409-414.

(86) Arts, M. J. T. J.; Haenen, G. R. M. M.; Voss, P.-H.; Bast, A. *Food Chem. Tox.* **2004**, *42*, 45-49.

(87) Gliszczyńska-Świgło, A. *Food Chem.* **2006**, *96*, 131-136.

(88) Folin, O.; Denis, W. *J. Biol. Chem.* **1912**, *12*, 239-243.

(89) Folin, O.; Denis, W. *J. Biol. Chem.* **1912**, *12*, 245-251.

(90) Folin, O.; Denis, W. *J. Ind. Eng. Chem.* **1912**, *4*, 680-682.

(91) Singleton, V. L.; Rossi, J. A. *Am. J. Enol. Vitic.* **1965**, *16*, 144-158.

(92) Prior, R. L.; Wu, X.; Schaich, K. *J. Agric. Food Chem.* **2005**, *53*, 4290-4302.

(93) Barbooti, M. M.; Al-Sammerrai, D. A. *Thermochimica Acta* **1984**, *76*, 221-228.

(94) Al-Sammerrai, D. A.; Salih, Z. S. *Thermochimica Acta* **1985**, *88*, 461-466.

(95) Leach, A. R. *Molecular Modelling : Principles and Applications*, 2nd ed.; Pearson Education Limited: Dorchester, 2001.

(96) Tehan, B. G.; Lloyd, E. J.; Wong, M. G.; Pitt, W. R.; Gancia, E.; Manallack, D. T. *Quant. Struct.-Act. Relat.* **2002**, *21*, 473-485.

(97) Hohnenberg, P.; Kohn, W. *Phys. Rev.* **1964**, *B136*, 785-789.

(98) Wavefunction, Inc.: Irvine, CA.

(99) Litwinienko, G.; Ingold, K. U. *J. Org. Chem.* **2002**, *68*, 3433-3438.

(100) Hunt, N.; Tyrrell, S.; Nicholson, J.: www.coventry.ac.uk/ec/~nhunt/regress/good4.html, 2001.

(101) Pierre, J.-L.; Baret, P.; Serratrice, G. *Curr. Med. Chem.* **2003**, *10*, 1077-1084.

(102) Mattson, M. P. *Nature* **2004**, *430*, 631-639.

(103) Cummings, J. L. *N. Engl. J. Med.* **2004**, *351*, 56-67.

(104) McMurray, A. *Community Health and Wellness: A Socioecological Approach*; Harcourt: Melbourne, 2001.

(105) Mukherjee, O.; Kauwe, J. S. K.; Mayo, K.; Morris, J. C.; Goate, A. M. *BMC Genetics* **2007**, *8:3*.

(106) Zhu, X.; Babar, A.; Siedlak, S. L.; Yang, Q.; Ito, G.; Iwatsubo, T.; Smith, M. A.; Perry, G.; Chen, S. G. *Mol. Neurodegeneration* **2006**, *1:17*.

(107) Athey, R. J.; Walker, R. W. *Int. J. Geriatr. Psychiatry* **2006**, *21*, 977-982.

(108) Masters, C. L.; Simms, G.; Weinman, N. A.; Multhaup, G.; McDonald, B. L.; Beyreuther, K. *Proc. Natl. Acad. Sci.* **1985**, *82*, 4245-4249.

(109) Thompson, K. J.; Shoham, S.; Connor, J. R. *Brain Res. Bull.* **2001**, *55*, 155-164.

(110) Kaur, D.; Yantiri, F.; Rajagopalan, S.; Kumar, J.; Mo, J. Q.; Boonplueang, R.; Viswanath, V.; Jacobs, R.; Yang, L.; Beal, M. F.; DiMonte, D.; Volitakis, I.;

Ellerby, L.; Cherny, R. A.; Bush, A. I.; Anderson, J. K. *Neuron* **2003**, *37*, 899-909.

(111) Galbraith, A.; Bullock, S.; Manis, E. *Fundamentals of Pharmacology*, 3rd ed.; Pearson Education Australia Pty. Ltd.: French's Forest, 2001.

(112) Erdö, S. L.; Schäfer, M. *Eur. J. Pharmacol.* **1991**, *198*, 215-217.

(113) Porsteinsson, A. P.; Cosman, K. M. *Aging Health* **2006**, *2*, 891-904.

(114) Rossom, R.; Adityanjee; Dysken, M. *Am. J. Geri. Pharmacother.* **2004**, *2*, 303-312.

(115) Grutzendler, J.; Morris, J. C. *Drugs* **2001**, *61*, 41-52.

(116) Farlow, M. *International Psychogeriatrics* **2002**, *14*, 93-126.

(117) Yankner, B. A.; Duffy, L. K.; Kirschner, D. A. *Science* **1990**, *250*, 279-282.

(118) Bush, A. I.; Multhaup, G.; Moir, R. D.; Williamson, T. G.; Small, D. H.; Rumble, B.; Pollwein, P.; Beyreuther, K.; Masters, C. L. *J. Biol. Chem* **1993**, *268*, 16109-16112.

(119) Bush, A. I.; Pettingell, W. H.; Paradis, M. d.; Tanzi, R. E. *J. Biol. Chem* **1994**, *269*, 12153-12158.

(120) Bush, A. I.; Pettingell, W. H.; Multhaup, G.; Paradis, M. d.; Vonsattel, J.-P.; Gusella, J. F.; Beyreuther, K.; Masters, C. L.; Tanzi, R. E. *Science* **1994**, *265*, 1464-1467.

(121) Atwood, C. S.; Scarpa, R. C.; Huang, X.; Moir, R. D.; Jones, W. D.; Fairlie, D. P.; Tanzi, R. E.; Bush, A. I. *J. Neurochem.* **2000**, *75*, 1219-1233.

(122) Cherny, R. A.; Legg, J. T.; McLean, C. A.; Fairlie, D. P.; Huang, X.; Atwood, C. S.; Beyreuther, K.; Tanzi, R. E.; Masters, C. L.; Bush, A. I. *J. Biol. Chem* **1999**, *274*, 23223-23228.

(123) Cherny, R. A.; Atwood, C. S.; Xilinas, M. E.; Gray, D. N.; Jones, W. D.; McLean, C. A.; Barnham, K. J.; Volitakis, I.; Fraser, F. W.; Kim, Y.-S.; Huang,

X.; Goldstein, L. E.; Moir, R. D.; Lim, J. T.; Beyreuther, K.; Zheng, H.; Tanzi, R. E.; Masters, C. L.; Bush, A. I. *Neuron* **2001**, *30*, 665-676.

(124) Bush, A. I.; Tanzi, R. E. *PNAS* **2002**, *99*, 7317-7319.

(125) Ritchie, C. W.; Bush, A. I.; Mackinnon, A.; Macfarlane, S.; Mastwyk, M.; MacGregor, L.; Kiers, L.; Cherny, R. A.; Li, Q.-X.; Tammer, A.; Carrington, D.; Mavros, C.; Volitakis, I.; Xilinas, M. E.; Ames, D.; Davis, S.; Beyreuther, K.; Tanzi, R. E.; Masters, C. L. *Arch. Neurol.* **2003**, *60*, 1685-1691.

(126) Arbiser, J. L.; Kraeft, S.-K.; Leeuwen, R. v.; Hurwitz, S. J.; Selig, M.; Dickersin, G. R.; Flint, A.; Byers, H. R.; Chen, L. B. *Molecular Medicine* **1998**, *4*, 665-670.

(127) Tateishi, J. *Neuropathology* **2000**, *20*, S20-S24.

(128) Yoshioka, M.; Tamura, Z. *Igaku No Ayumi* **1970**, *74*, 320-322.

(129) Doraiswamy, P. M.; Finefrock, A. E. *Lancet Neurol.* **2004**, *3*, 431-434.

(130) Cole, G. M. *Neuron* **2003**, *37*, 889-890.

(131) Forte, G.; Bocca, B.; Senofonte, O.; Petrucci, F.; Brusa, L.; Stanzione, P.; Zannino, S.; Violante, N.; Alimonti, A.; Sancesario, G. *J. Neural. Transm.* **2004**, *111*, 1031-1040.

(132) Sofic, E.; Riederer, P.; Heinsen, H.; Beckmann, H.; Reynolds, G. P.; Hebenstreit, G.; Youdim, M. B. H. *J. Neural. Transm.* **1988**, *74*, 199-205.

(133) Sofic, E.; Paulus, W.; Jellinger, K.; Riederer, P.; Youdim, M. B. H. *J. Neurochem.* **1991**, *56*, 978-982.

(134) Dexter, D. T.; Wells, F. R.; Agid, F.; Agid, Y.; Lees, A. J.; Jenner, P.; Marsden, C. D. *Lancet* **1987**, *21*, 1219-1220.

(135) Dexter, D. T.; Wells, F. R.; Lees, A. J.; Agid, F.; Agid, Y.; Jenner, P.; Marsden, C. D. *J. Neurochem.* **1989**, *52*, 1830-1836.

(136) Youdim, M. B. H.; Ben-Shachar, D.; Riederer, P. *Mov. Disord.* **1993**, *8*, 1-12.

(137) Gerlach, M.; Ben-Shachar, D.; Riederer, P.; Youdim, M. B. H. *J. Neurochem.* **1994**, *63*, 793-807.

(138) Yantiri, F.; Andersen, J. K. *IUBMB Life* **1999**, *48*, 1-3.

(139) Griffiths, P. D.; Dobson, B. R.; Jones, G. R.; Clarke, D. T. *Brain* **1999**, *122*, 667-673.

(140) Andersen, J. K. In *Ageing Vulnerability: Causes and Interventions*; John Wiley and Sons: New York, 2001; Vol. 253, pp 11-25.

(141) Berg, D.; Gerlach, M.; Youdim, M. B. H.; Double, K. L.; Zecca, L.; Riederer, P.; Becker, G. *J. Neurochem.* **2001**, *79*, 225-236.

(142) Cherny, R. A.; Barnham, K. J.; Lynch, T.; Volitakis, I.; Li, Q.-X.; McLean, C. A.; Multhaup, G.; Beyreuther, K.; Tanzi, R. E.; Masters, C. L.; Bush, A. I. *J. Struct. Biol.* **2000**, *130*, 209-216.

(143) Curtain, C. C.; Ali, F.; Volitakis, I.; Cherny, R. A.; Norton, R. S.; Beyreuther, K.; Barrow, C. J.; Masters, C. L.; Bush, A. I.; Barnham, K. J. *J. Biol. Chem* **2001**, *276*, 20466-20473.

(144) Barnham, K. J.; Masters, C. L.; Bush, A. I. *Nature Reviews*.

(145) Ji, H.-F.; Zhang, H.-Y. *Bioorg. Med. Chem. Lett.* **2005**, *15*, 21-24.

(146) Lynch, S. M.; Boswell, S. A.; Colon, W. *Biochem.* **2004**, *43*, 16525-16531.

(147) Barry, G., Victoria University, Melbourne, 2003.

(148) Frisch, M. J.; Trucks, G. W.; Schlegel, H. B.; Scuseria, G. E.; Robb, M. A.; Cheeseman, J. R.; Montgomery, J., J. A.; Vreven, T.; Kudin, K. N.; Burant, J. C.; Millam, J. M.; Iyengar, S. S.; Tomasi, J.; Barone, V.; Mennucci, B.; Cossi, M.; Scalmani, G.; Rega, N.; Petersson, G. A.; Nakatsuji, H.; Hada, M.; Ehara, M.; Toyota, K.; Fukuda, R.; Hasegawa, J.; Ishida, M.; Nakajima, T.; Honda, Y.; Kitao, O.; Nakai, H.; Klene, M.; Li, X.; Knox, J. E.; Hratchian, H. P.; Cross, J. B.; Bakken, V.; Adamo, C.; Jaramillo, J.; Gomperts, R.; Stratmann, R. E.; Yazyev, O.; Austin, A. J.; Cammi, R.; Pomelli, C.; Ochterski, J. W.; Ayala, P. Y.; Morokuma, K.; Voth, G. A.; Salvador, P.; Dannenberg, J. J.; Zakrzewski, V.

G.; Dapprich, S.; Daniels, A. D.; Strain, M. C.; Farkas, O.; Malick, D. K.; Rabuck, A. D.; Raghavachari, K.; Foresman, J. B.; Ortiz, J. V.; Cui, Q.; Baboul, A. G.; Clifford, S.; Cioslowski, J.; Stefanov, B. B.; Liu, G.; Liashenko, A.; Piskorz, P.; Komaromi, I.; Martin, R. L.; Fox, D. J.; Keith, T.; Al-Laham, M. A.; Peng, C. Y.; Nanayakkara, A.; Challacombe, M.; Gill, P. M. W.; Johnson, B.; Chen, W.; Wong, M. W.; Gonzalez, C.; Pople, J. A.; Gaussian, Inc.: Wallingford, CT, 2004.

(149) Ross, A. R. S.; Ikonomou, M. G.; Thompson, J. A. J.; Orians, K. J. *Anal. Chem.* **1998**, *70*, 2225-2235.

(150) de Sousa, G. F.; Filgueiras, C. A. L. *Transition Met. Chem.* **1990**, *15*, 286-289.

(151) de Sousa, G. F.; Filgueiras, C. A. L. *Transition Met. Chem.* **1990**, *15*, 290-292.

(152) Sugiura, Y.; Kuwahara, J. *J. Am. Chem. Soc.* **1987**, *109*, 5848-5850.

(153) Frisch, Æ.; Frisch, M. J.; Trucks, G. W. *Gaussian 03 User's Reference*; Gaussian. Inc.: Wallingford, CT, 2003.

(154) Ohtsuka, K.; Ohishi, N.; Eguchi, G.; Yagi, K. *Experientia* **1982**, *38*, 120-122.

(155) Yagi, K.; Ohtsuka, K.; Ohishi, N. *Experentia* **1985**, *41*, 1561-1563.

(156) Benvenisti-Zarom, L.; Chen, J.; Regan, R. F. *Neuropharmacology* **2008**, *49*, 687-694.

(157) Sivakova, S.; Rowan, S. J. *Chem. Soc. Rev.* **2005**, *34*, 9-21.

(158) Davis, J. T. *Angew. Chem. Int. Ed.* **2004**, *43*, 668-698.

(159) Katz, S. *J. Am. Chem. Soc.* **1952**, *74*, 2238-2245.

(160) Thomas, C. A. *J. Am. Chem. Soc.* **1954**, *76*, 6023-6034.

(161) Shimizu, R. *J. Pharm. Soc. Jpn.* **1957**, *77*, 676-678.

(162) Simpson, R. B. *J. Am. Chem. Soc.* **1964**, *86*, 2059-2065.

(163) Eichhorn, G. L. *Nature* **1962**, *194*, 474-475.

(164) Butzow, J. J.; Eichhorn, G. L. *Biopolymers 2* **1965**, *3*, 97-107.

(165) Harder, H. C.; Rosenberg, B. *Int. J. Cancer* **1970**, *6*, 207-216.

(166) Roberts, J. J.; Pascoe, J. M. *Nature* **1972**, *235*, 282-284.

(167) Stone, P. J.; Kelman, A. D.; Sinex, F. M. *Nature* **1974**, *251*, 736-737.

(168) Zwelling, L. A.; Kohn, K. W.; Ross, W. E.; Ewig, R. A. G.; Anderson, T. *Cancer Res.* **1978**, *38*, 1762-1768.

(169) Jamieson, E.; Lippard, S. J. *Chem. Rev.* **1999**, *99*, 2467-2498.

(170) Brenner, A.; Hucul, D. A. *J. Am. Chem. Soc.* **1980**, *102*, 2487-2488.

(171) Gellert, M.; Lipsett, M. N.; Davies, D. R. *Proc. Natl. Acad. Sci.* **1962**, *48*, 2013-2018.

(172) Williamson, J. R.; Raghuraman, M. K.; Cech, T. R. *Cell* **1989**, *59*, 871-880.

(173) *HyperChem Release 7 for Windows - User's Manual*; Hypercube, Inc., 2002.

(174) Yuriev, E., Victoria University of Technology, Melbourne, 1997.

(175) Hambley, T. W.; Hawkins, C. J.; Palmer, J. A.; Snow, M. R. *Aust. J. Chem.* **1981**, *34*, 2525-2542.

(176) Hay, B. P. *Coord. Chem. Rev.* **1993**, *126*, 177-236.

(177) HyperChem; Hypercube, Inc., 2003.

(178) Yuriev, E.; Orbell, J. D. *J. Comp.-Aided Mol. Design* **1996**, *10*, 589-606.

(179) Weiner, S. J.; Kollman, P. A.; Nguen, D. T.; Case, D. A. *J. Comput. Chem.* **1986**, *7*, 230-252.

(180) Cornell, W. D.; Cieplak, P.; Bayly, C. I.; Gould, I. R.; Merz, K. M., Jr.; Ferguson, D. M.; Spellmeyer, D. C.; Fox, T.; Caldwell, J. W.; Kollman, P. A. *J. Am. Chem. Soc.* **1995**, *117*, 5179-5197.

(181) Kollman, P. A. *Chem. Rev.* **1993**, *93*, 2395-2395.

(182) Wavefunction, Inc.: Irvine, CA.

(183) Bugg, C., E.; Thomas, J. M.; Sundaralingham, M.; Rao, S. T. *Biopolymers* **1971**, *10*, 175-219.

(184) Khan, B. T.; Kumari, S. V.; Mohan, K. M.; Goud, G. N. *Indian J. Chem., Sect. A.* **1992**, *31A*, 28-33.

(185) Sigel, H. *Chem. Soc. Rev.* **1993**, 255-267.

(186) Beck, D. J.; Brubaker, R. R. *Mutat. Res.* **1975**, *27*, 181-189.

(187) Kohl, H. H.; Firiedman, M. E.; Melius, P.; Mora, E. C.; McAuliffe, C. A. *Chem. Biol. Interact.* **1979**, *24*, 209-215.

(188) Turnbull, D.; Popescu, N. C.; DiPaolo, J. A.; Myhr, B. C. *Mutat. Res.* **1979**, *66*, 267-275.

(189) Kistenmacher, T. J.; Wilkowski, K.; de Castro, B.; Chiang, C. C.; Marzilli, L. G. *Biochem. Biophys. Res. Commun.* **1979**, *91*, 1521-1527.

(190) Kohl, H. H.; Haghighi, S.; McAuliffe, C. A. *Chem. Biol. Interact.* **1980**, *29*, 327-333.

(191) Marzilli, L. G.; Reily, M. D.; L., H. B.; McMurray, C. T.; Wilson, W. D. *FEBS Lett.* **1984**, *176*, 389-392.

(192) Takenaka, T.; Yoshino, I.; Kpusa, H.; Ohba, T.; Yohena, T.; Osoegawa, A.; Shoji, F.; Maehara, Y. *Int. J. Cancer* **2007**, *121*, 895-900.

(193) Colangelo, D.; Osella, D. *Curr. Med. Chem.* **2005**, *12*, 3091-3102.

(194) Kweekel, D. M.; Gelderblom, H.; Guchelaar, H.-J. *Cancer Treat. Rev.* **2005**, *31*, 90-105.

(195) Giandomenico, C. M. In *Abstracts of Papers, 226th ACS National Meeting*: New York, NY, United States, 2003.

(196) van den Berg, H. W.; Roberts, J. J. *Chem. Biol. Interact.* **1976**, *12*, 375-390.

(197) Eriguchi, M.; Nonaka, Y.; Yanagie, H.; Yoshizaki, I.; Takeda, Y.; Sekiguchi, M. *Biomed. Pharmacother.* **2003**, *57*, 412-415.

(198) Holford, J.; Raynaud, F.; Murrer, B. A.; Grimaldi, K.; Hartley, J. A.; Abrams, M.; R., K. L. *Anti-Cancer Drug Des.* **1998**, *13*, 1-18.

(199) Habtemariam, A.; Watchman, B.; Potter, B. S.; Palmer, R.; Parsons, S.; Parkin, A.; Sadler, P. J. *J. Chem. Soc., Dalton Trans.* **2001**, *1*, 1306-1318.

(200) Miller, K. J.; Macrea, J.; Pycior, J. F. *Biopolymers* **1980**, *19*, 2067-2089.

(201) Farrell, N. P. In *Abstracts of Papers, 220th ACS National Meeting*: Washington, DC, United States, 2000.

(202) Guddneppanavar, R.; Saluta, G.; Kucera, G. L.; Bierbach, U. *J. Med. Chem.* **2006**, *49*, 3204-3214.

(203) Mandal, S.; Berube, G.; Asselin, E.; Richardson, V. J.; Church, J. G.; Bridson, J.; Pham, T. N.; Pramanik, S. K.; Mandal, S. K. *Bioorg. Med. Chem. Lett.* **2007**, *17*, 2139-2145.

(204) Liu, S. M.; Imperial College, University of Cambridge, UK: http://www2.mrc-lmb.cam.ac.uk/personal/sl/Html/Frames.html, 1998.

(205) Fichtinger-Schepman, A. M. J.; van der Veer, J. L.; den Hartog, J. H. J.; Lohman, P. H. M.; Reedijk, J. *Biochem.* **1984**, *24*, 707-713.

(206) Eastman, A. *Pharmac. Ther.* **1987**, *34*, 155-166.

(207) Lippert, B.; Raudaschl, G.; Lock, C. J. L.; Pilon, P. *Inorg. Chim. Acta* **1984**, *93*, 43-50.

(208) Schölihorn, H.; Raudaschl-Sieber, G.; Müller, G.; Thewalt, U.; Lippert, B. *J. Am. Chem. Soc.* **1985**, *107*, 5932-5937.

(209) Sherman, S. E.; Gibson, D.; Wang, A. H. J.; Lippard, S. J. *J. Am. Chem. Soc.* **1988**, *110*, 7368-7381.

(210) Coll, M.; Sherman, S. E.; Gibson, D.; Lippard, S. J. *J. Biomol. Struct. Dyn.* **1990**, *8*, 315-330.

(211) Lippert, B.; Lippard, S. J., Ed., 1989; Vol. 37.

(212) Sherman, S. E.; Lippard, S. J. *Chem. Rev.* **1987**, *87*, 1153-1181.

(213) Ling, E. C. H.; Allen, G. W.; Hambley, T. W. *J. Am. Chem. Soc.* **1994**, *116*, 2673-2674.

(214) Yuriev, E.; Orbell, J. D. *Inorg. Chem.* **1996**, *35*, 7914-7915.

(215) Yuriev, E.; Orbell, J. D. *Inorg. Chem.* **1998**, *37*, 6269-6275.

(216) Baker, A. T.; Crass, J. K.; Kok, G. B.; Orbell, J. D.; Yuriev, E. *Inorg. Chim. Acta* **1993**, *214*, 169-176.

(217) Marcelis, A. T. M.; Korte, H.-J.; Krebs, B.; Reedijk, J. *Inorg. Chem.* **1982**, *21*, 4059-4063.

(218) Kasselouri, S.; Garoufis, A.; Lamera-Hadjiliaids, M.; Hadjiliadis, N. *Coord. Chem. Rev.* **1990**, *104*, 1-12.

(219) Pettit, L. D.; Bezer, M. *Coord. Chem. Rev.* **1985**, *61*, 97-114.

(220) Crass, J. K., University of Technology, Sydney, Australia, 1995.

(221) Cotton, F. A.; Wilkinson, G. *Advanced Inorganic Chemistry - A Comprehensive Text*, 2nd ed.; Interscience Publishers: New York, 1967.

(222) Done, M. C.; Rüther, T.; Cavell, K. J.; Kilner, M.; Peacock, E. J.; Braussaud, N.; Skelton, B. W.; White, A. *J. Organomet. Chem.* **2000**, *607*, 78-92.

(223) Hehre, W. J. *A Guide to Molecular Mechanics and Quantum Chemical Calculations.*; Wavefunction, Inc.: Irvine, CA, USA, 2003.

Appendices

Appendix I – ESI-MS spectra

Appendix II – Identification tables for ESI-MS spectra

Appendix III – Auxiliary benchmarking case studies

Appendix IV – Molecular structures and raw data
(located on attached CD)

Appendix I – ESI-MS spectra

Ia. Iron(III) – 8-hydroxyquinoline at various mole ratios (R).

Ia. i - R = 0.1

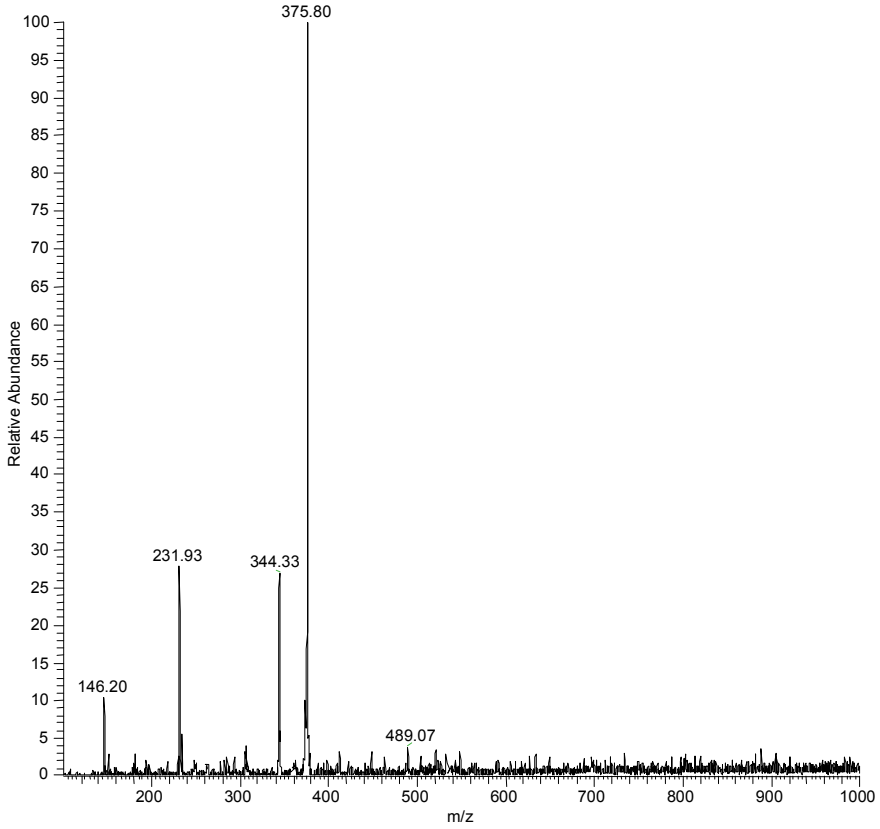

Ia. ii - R = 0.5

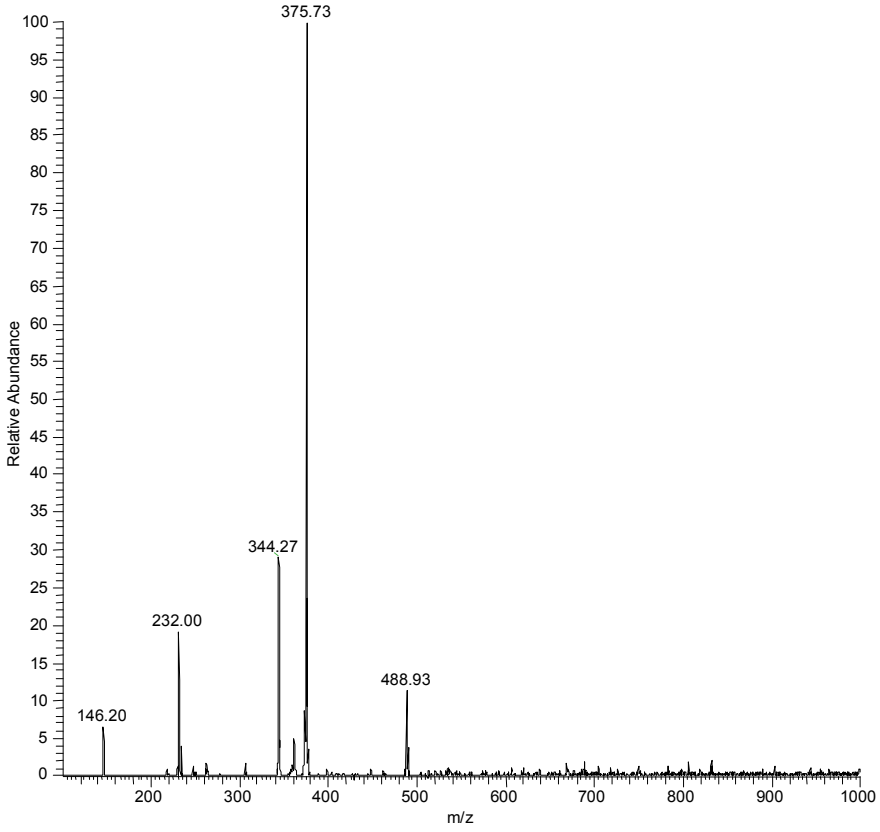

Ia. iii - R = 1

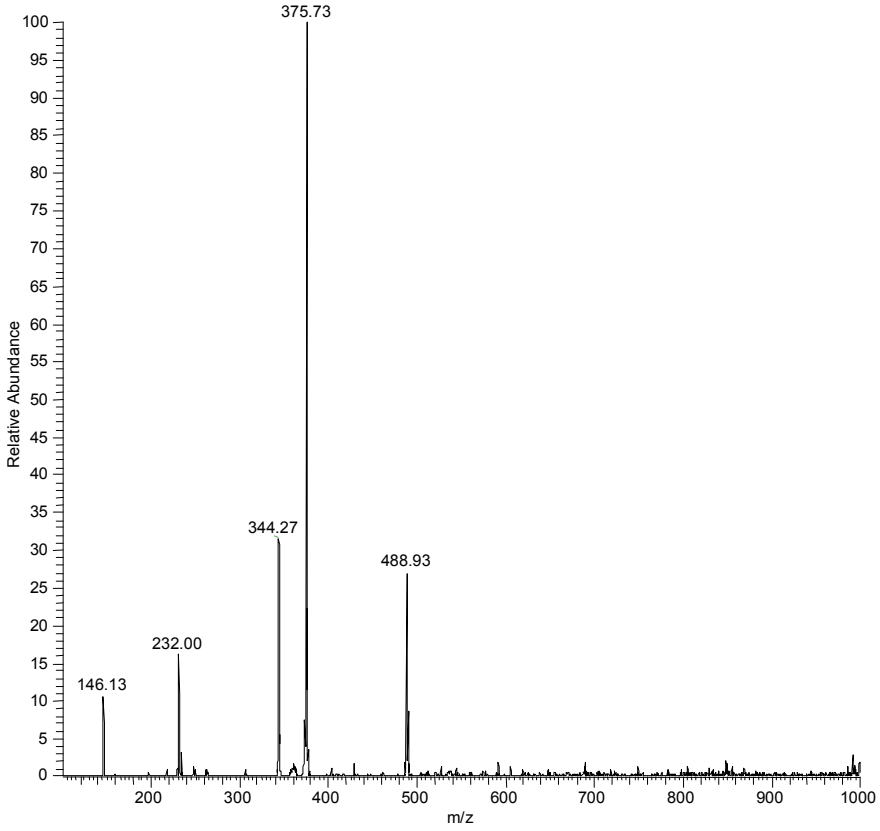

Ia. iv - R = 1.5

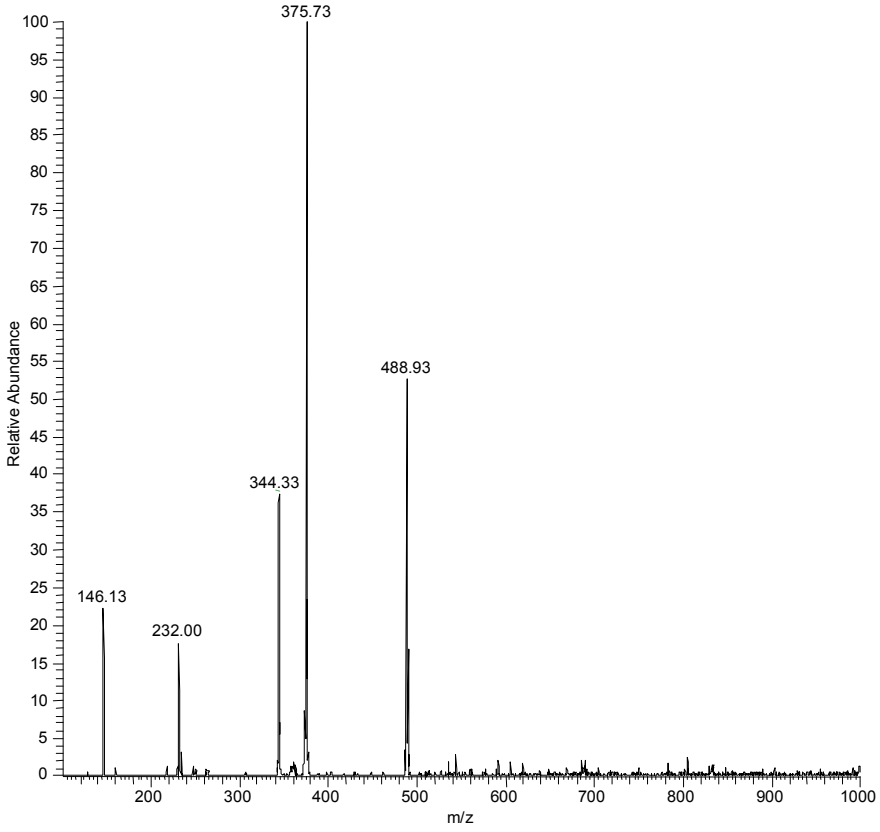

Ia. v - R = 2

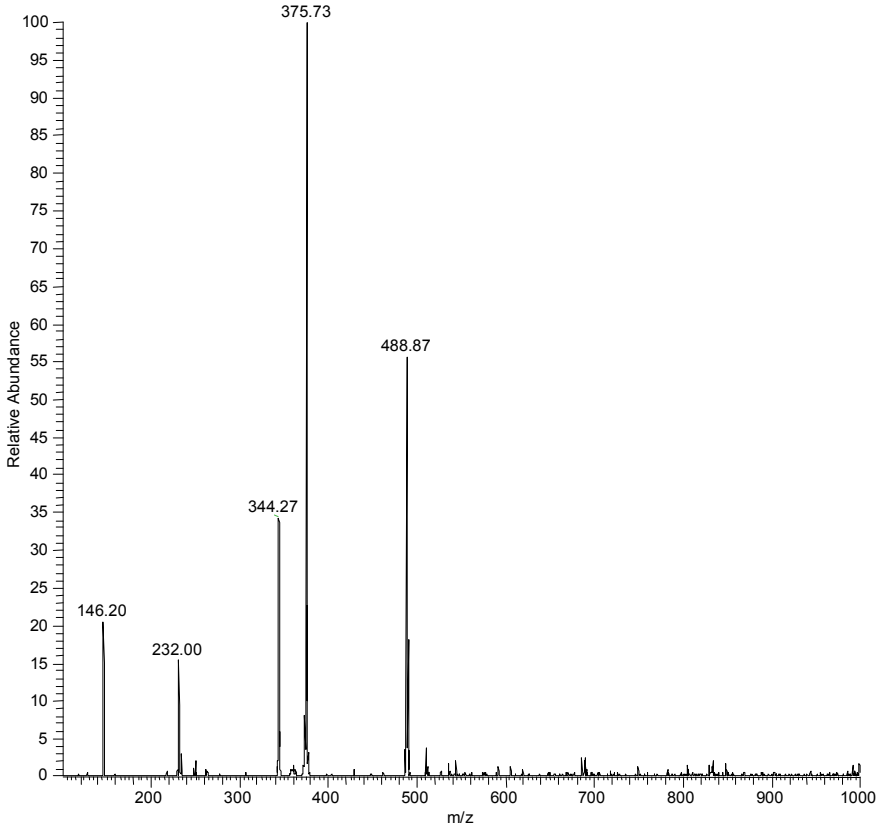

Ia. vi - R = 3

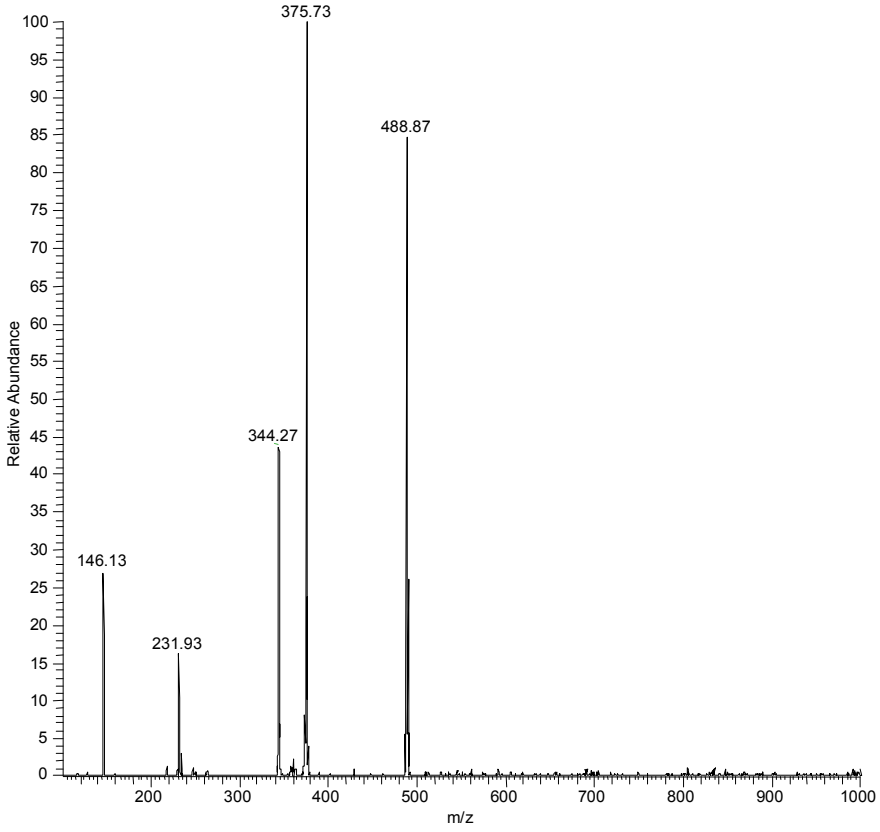

Ia. vii - R = 4

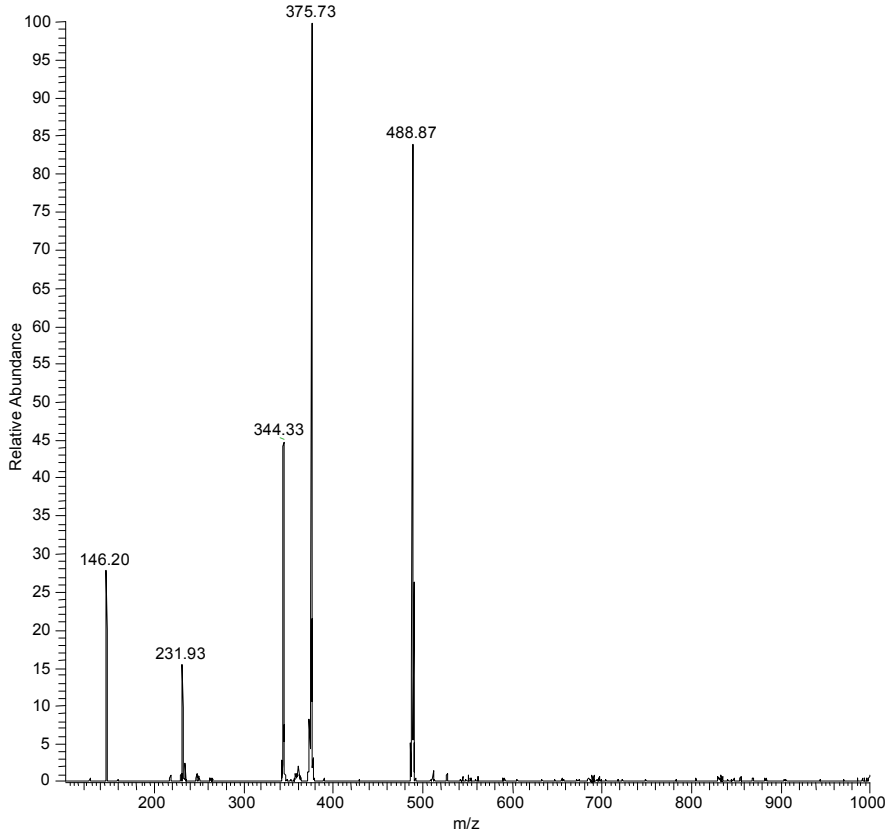

Ib. Iron(III) – 5,7-dichloro-8-hydroxyquinoline at various mole ratios (R).

Ib. i - R = 0.1

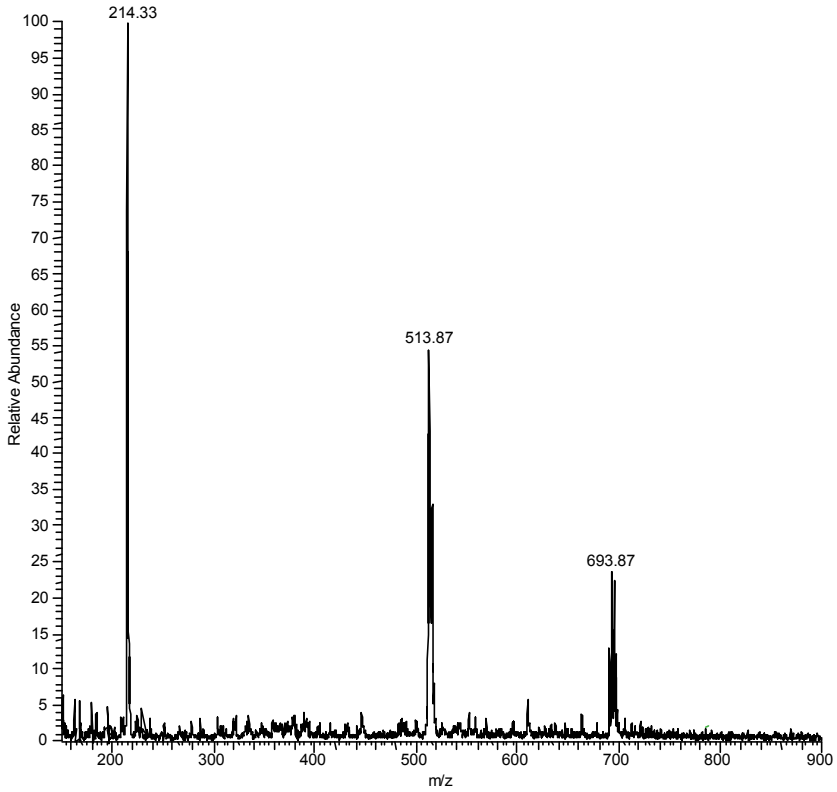

Ib. ii - R = 0.5

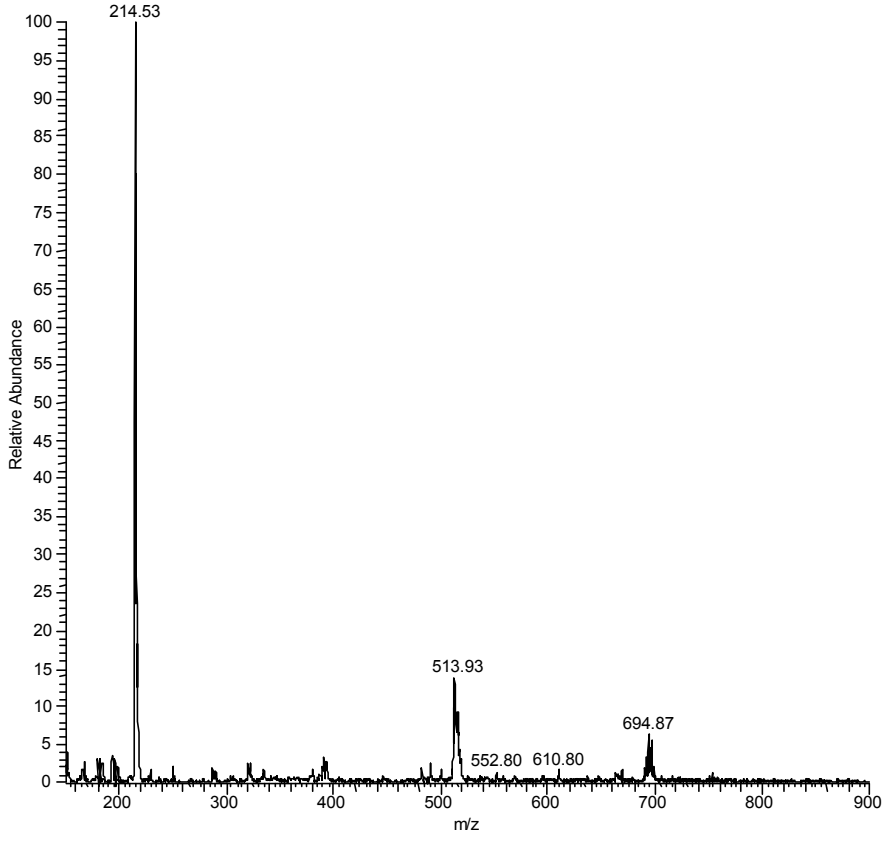

Ib. iii - R = 1

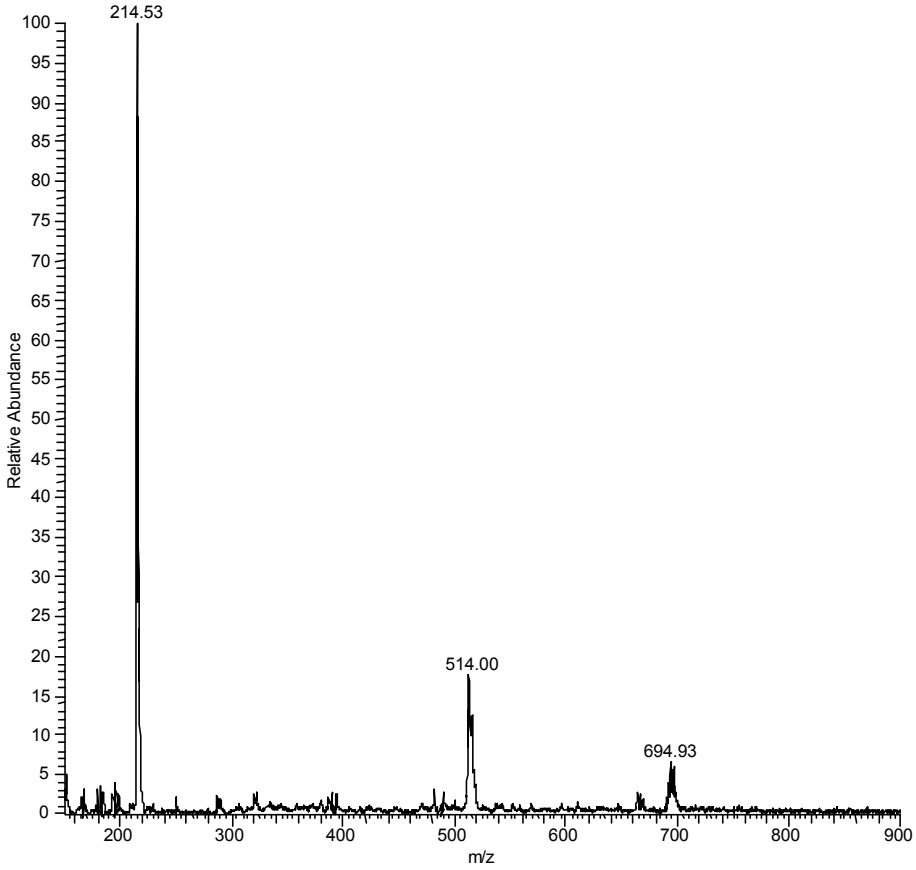

Ib. iv - R = 1.5

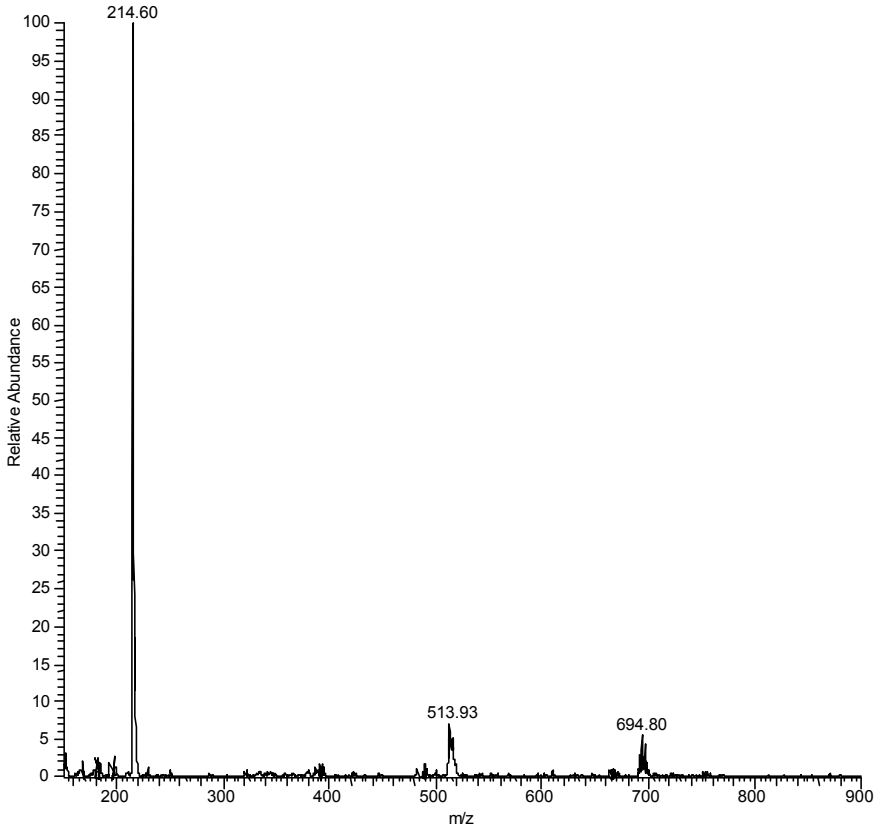

Ib. v - R = 2

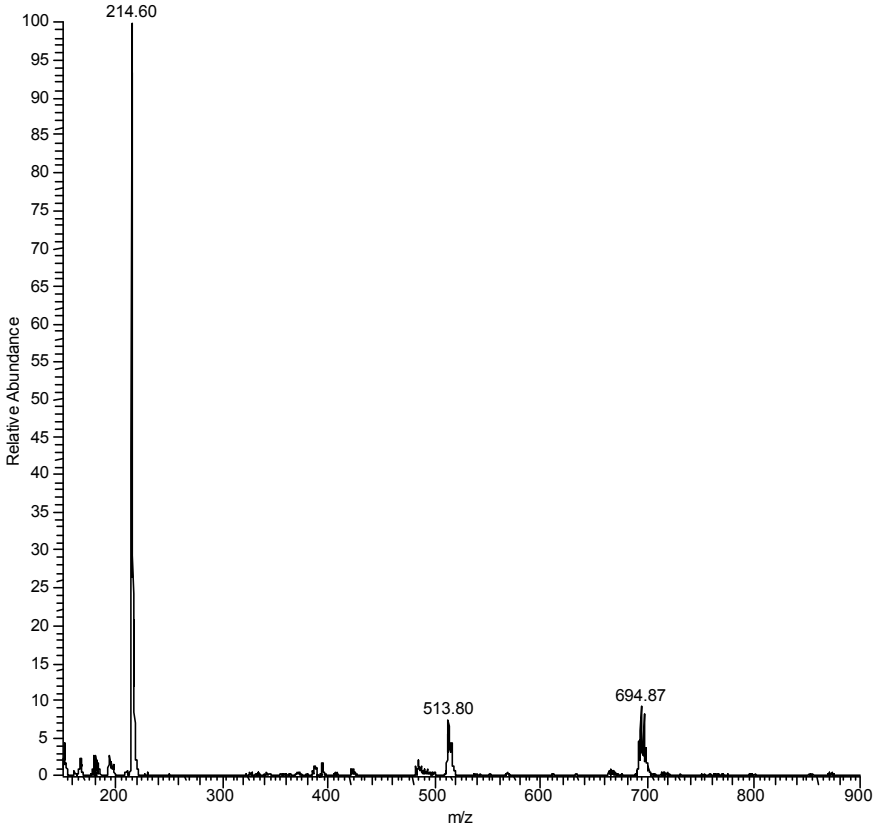

Ib. vi - R = 3

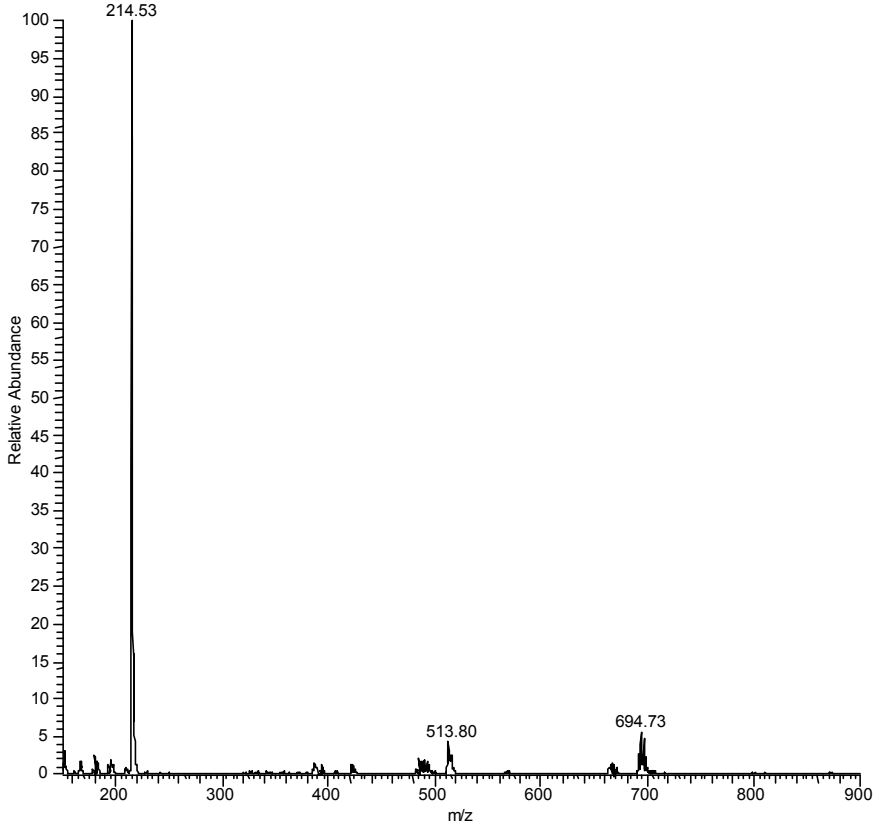

Ib. vii - R = 4

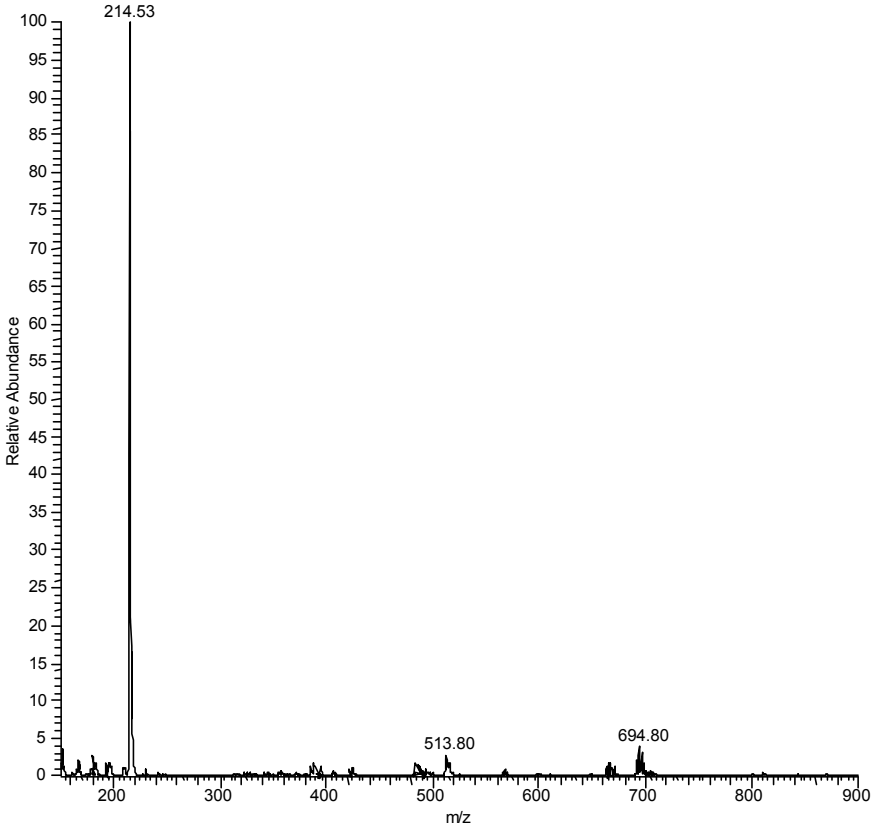

Ic. Iron(III) – 5-chloro-7-iodo-8-hydroxyquinoline at various mole ratios (R).

Ic. i - R = 0.1

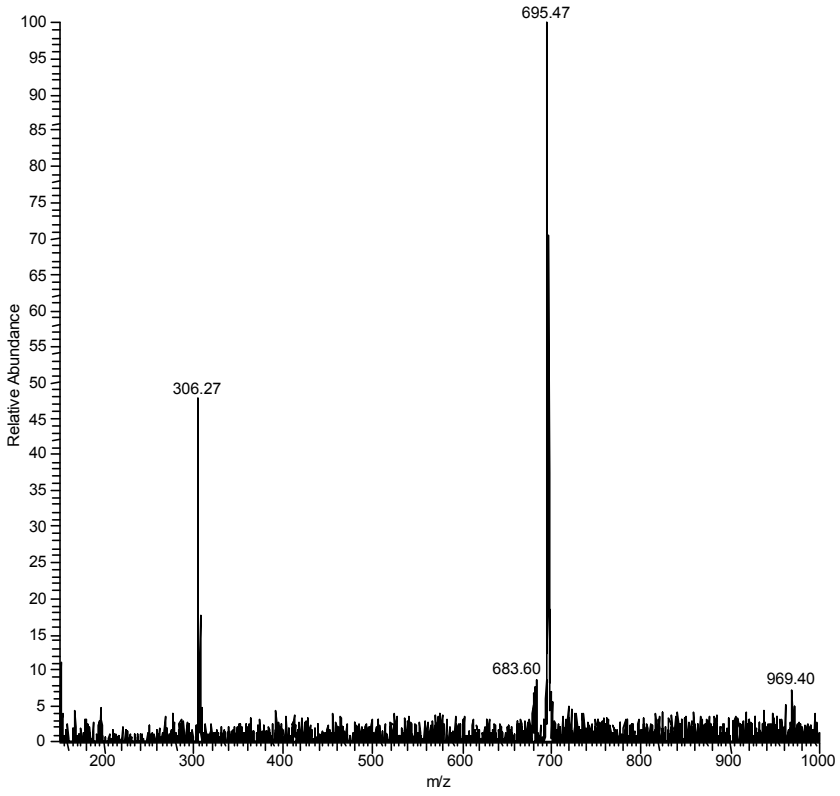

Ic. ii - R = 0.5

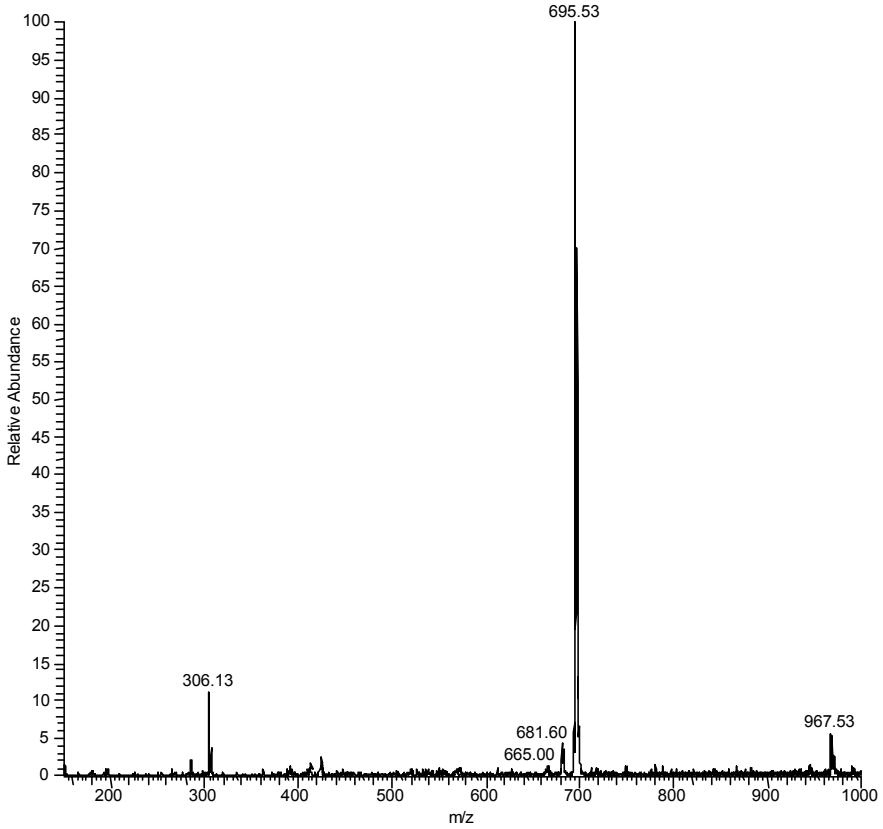

Ic. iii - R = 1

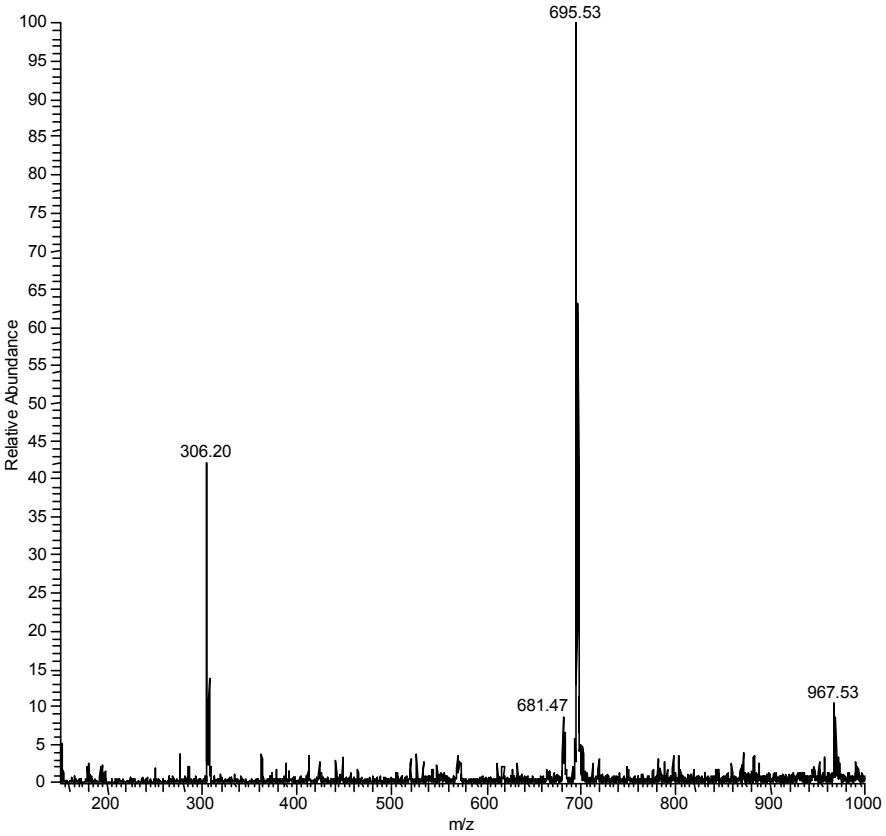

Ic. iv - R = 1.5

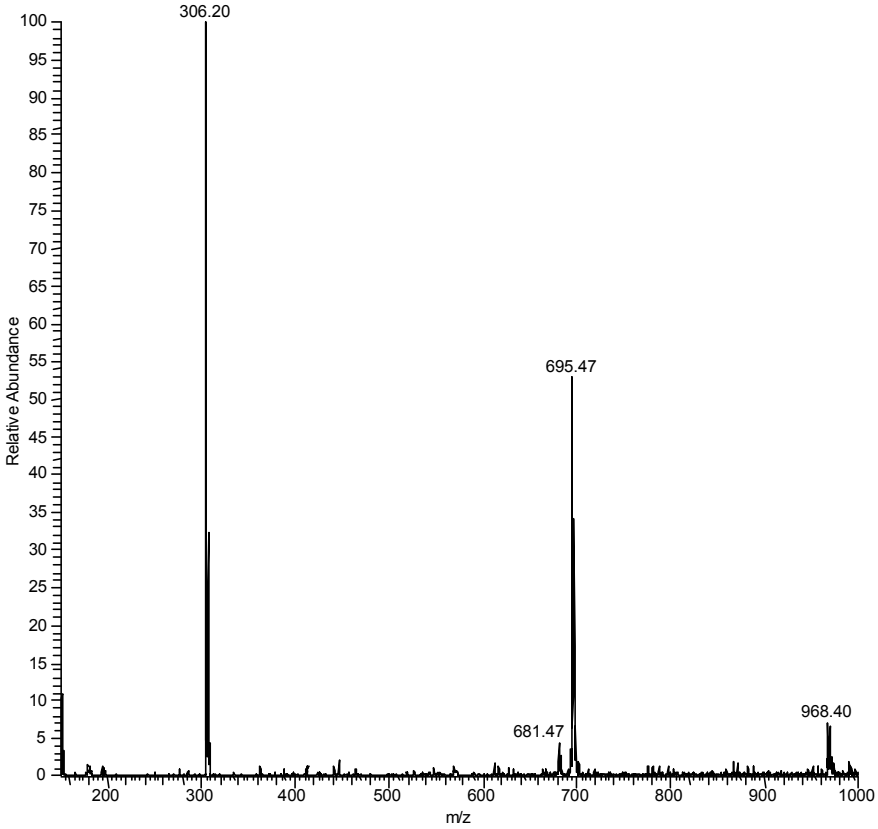

Ic. v - R = 2

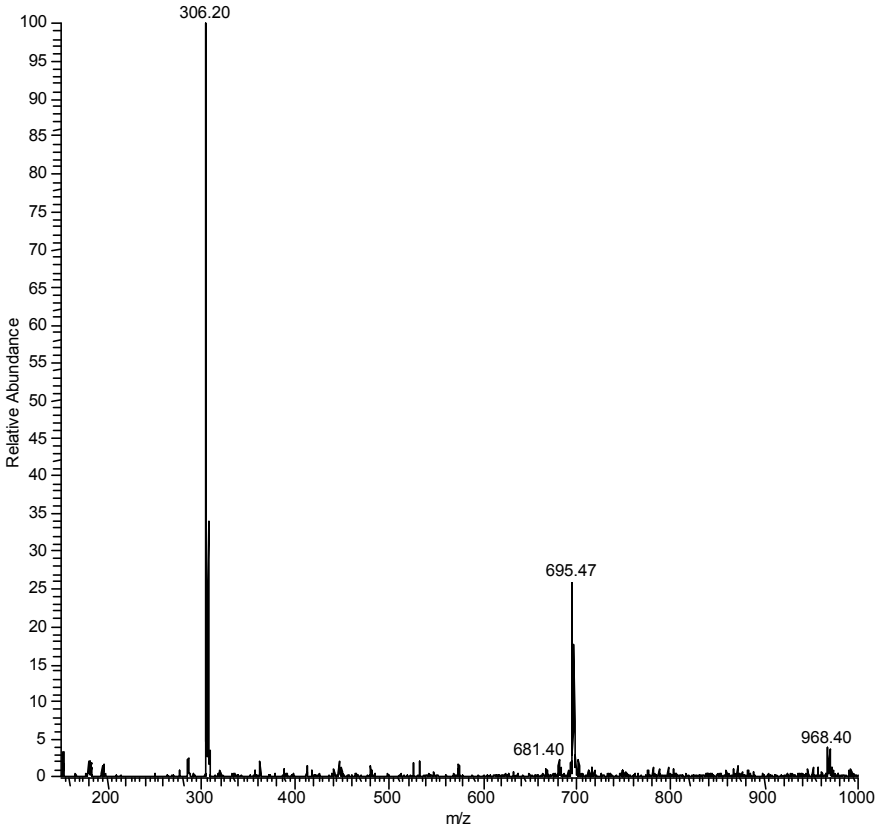

Ic. vi - R = 2.5

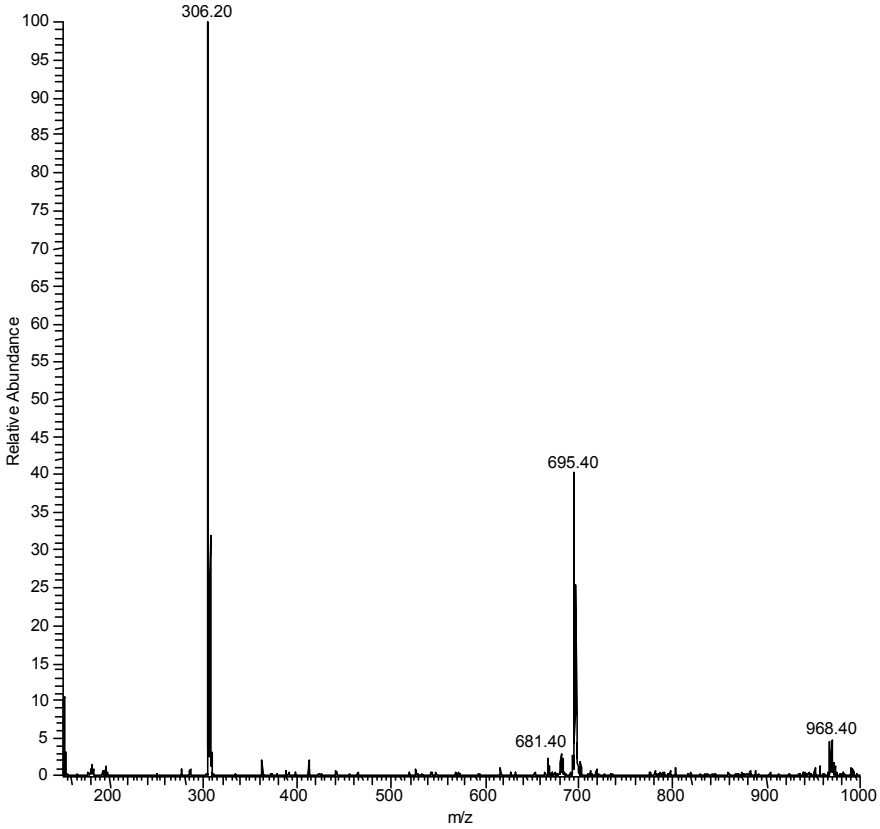

Ic. vii - R = 3

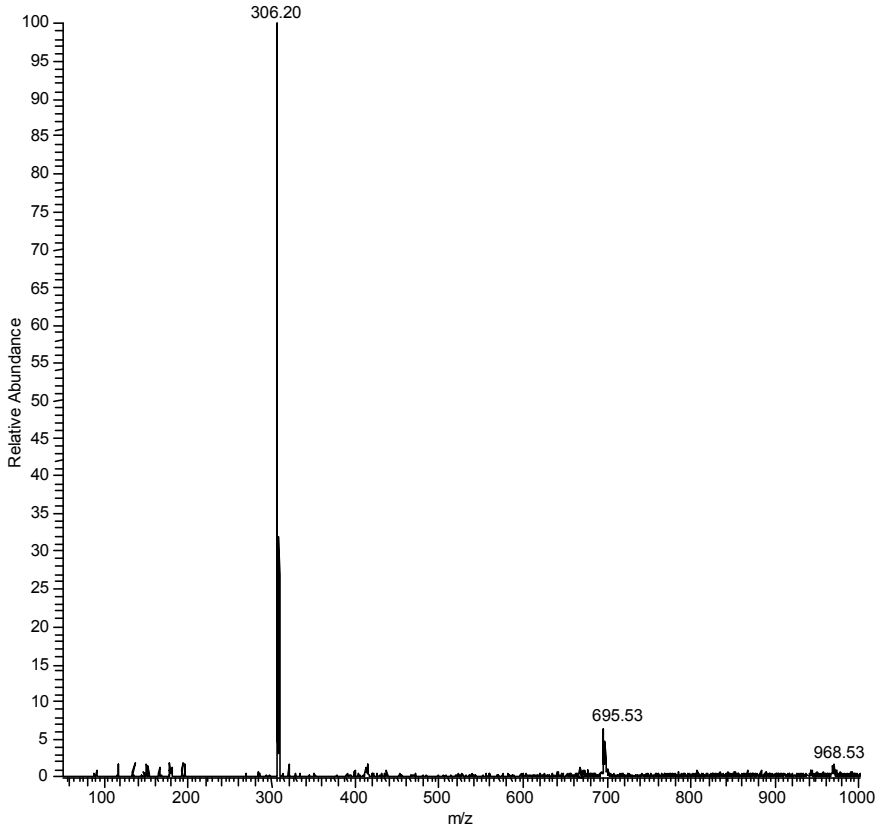

Ic. viii - R = 3.5

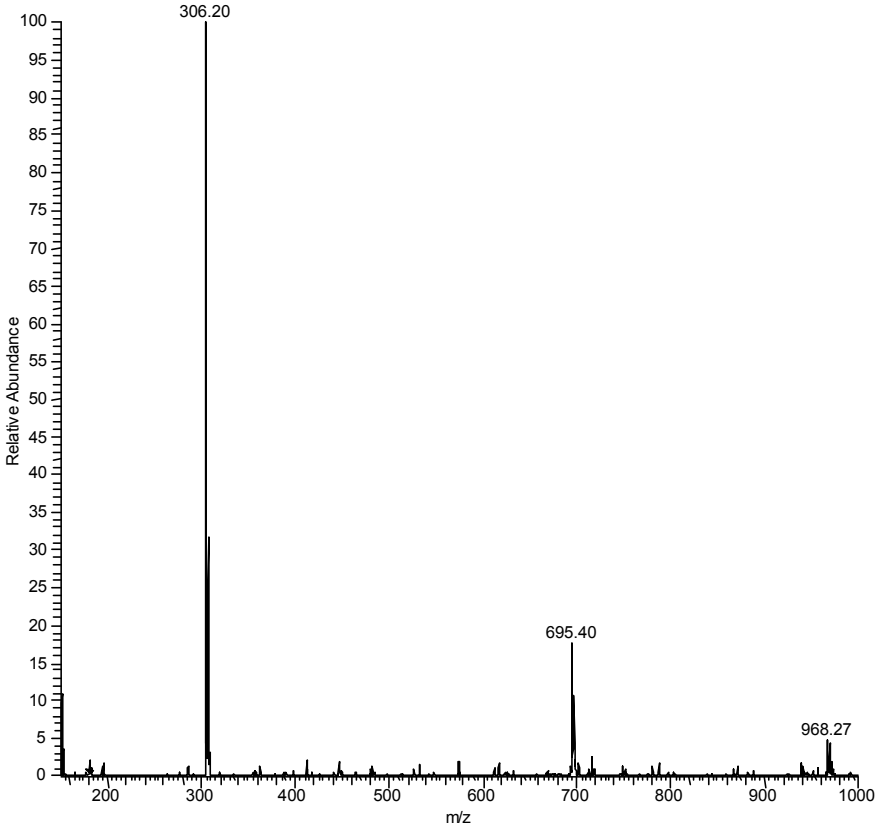

Ic. ix - R = 4

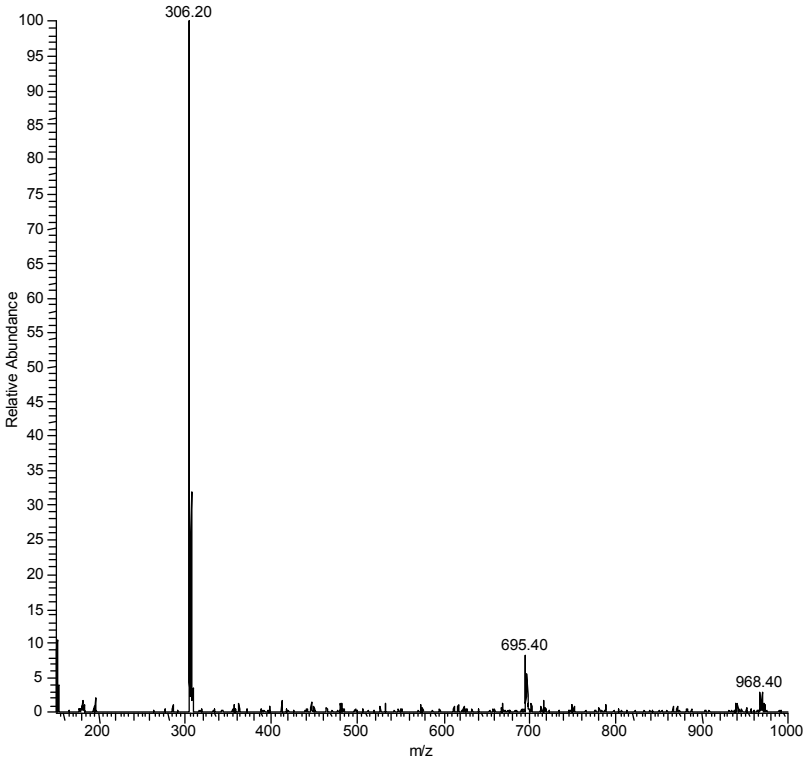

Id. Platinum(II)-dien clusters with deoxyguanosine

Id. i – ESI-MS spectrum of 1:5 $[Pt(dien)Cl]^+$ - dG mixture.

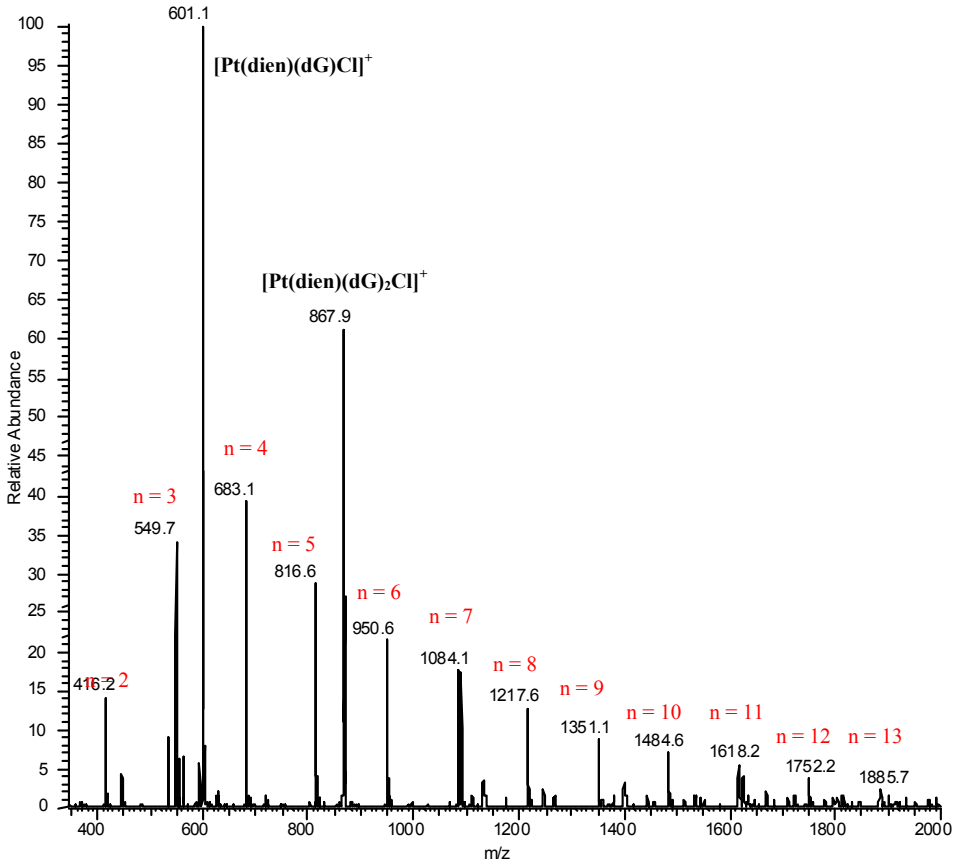

Id. ii - ESI-MS/MS spectrum of n = 2 (m/z = 416.2)

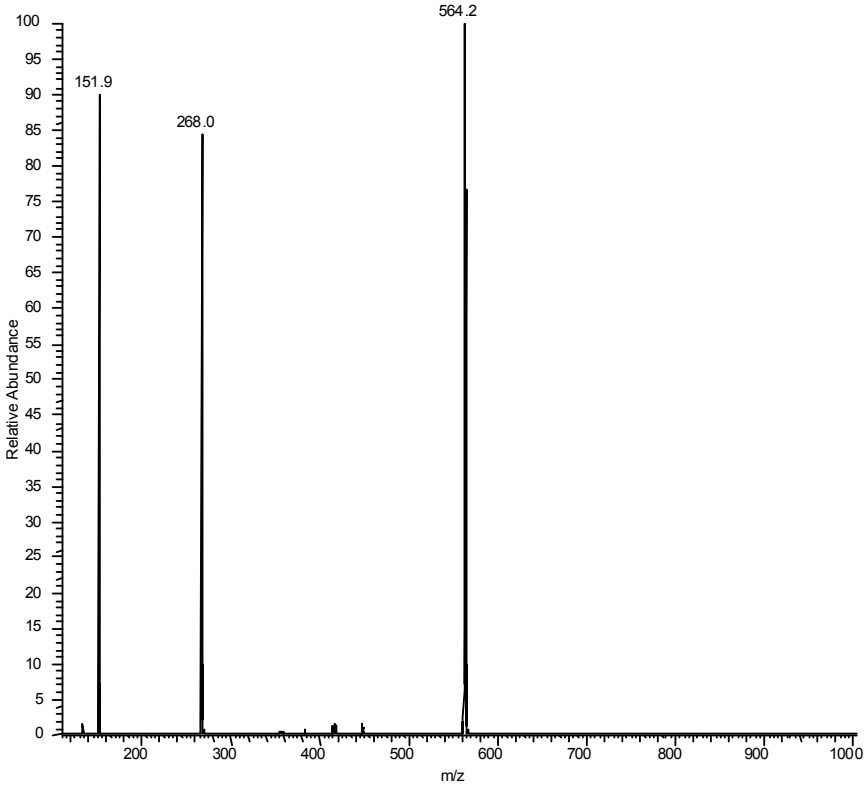

Id. iii – ESI-MS/MS spectrum of n = 3 (m/z = 549.7)

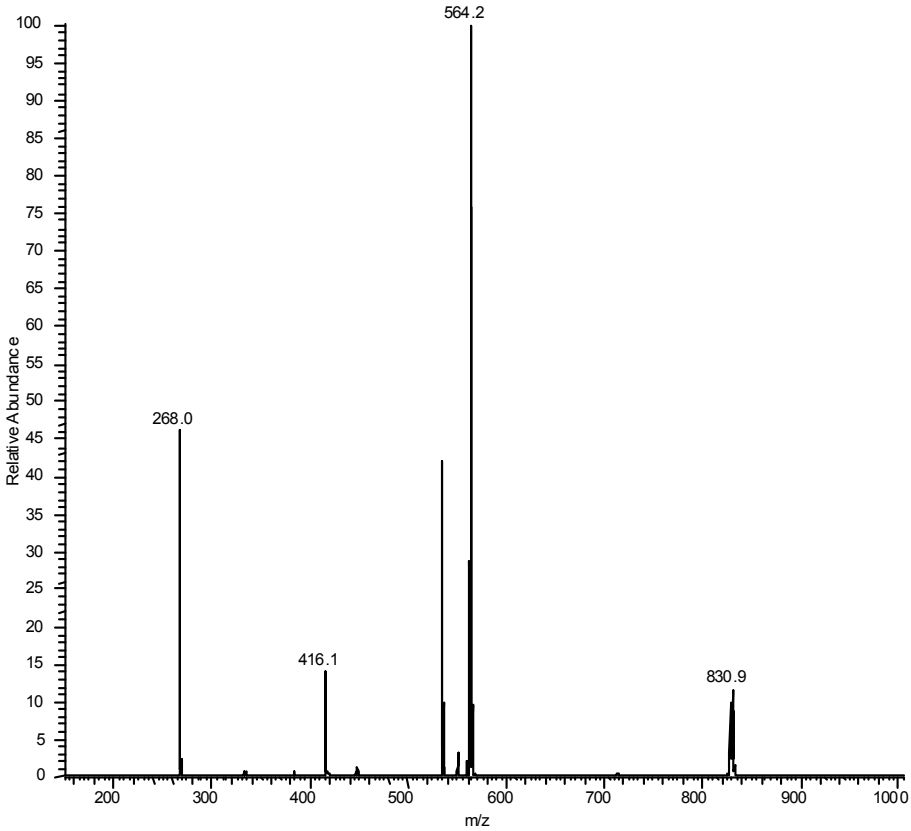

Id. iv – ESI-MS/MS spectrum of n = 4 (m/z = 683.1)

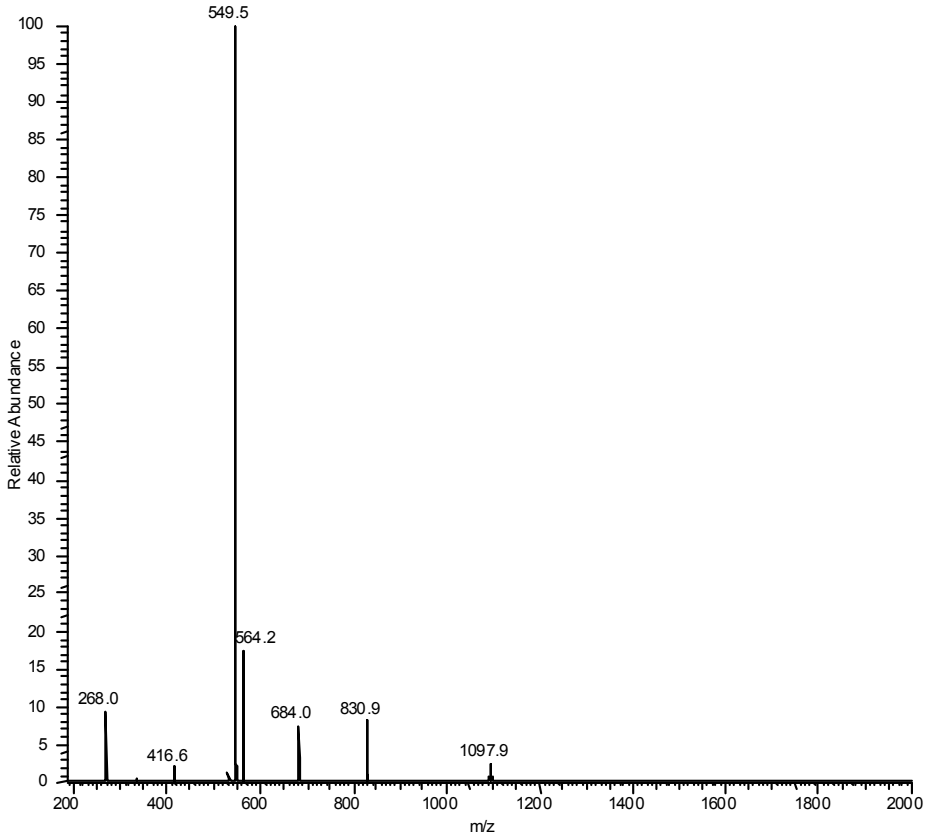

Id. v - ESI-MS/MS spectrum of n = 5 (m/z = 816.6)

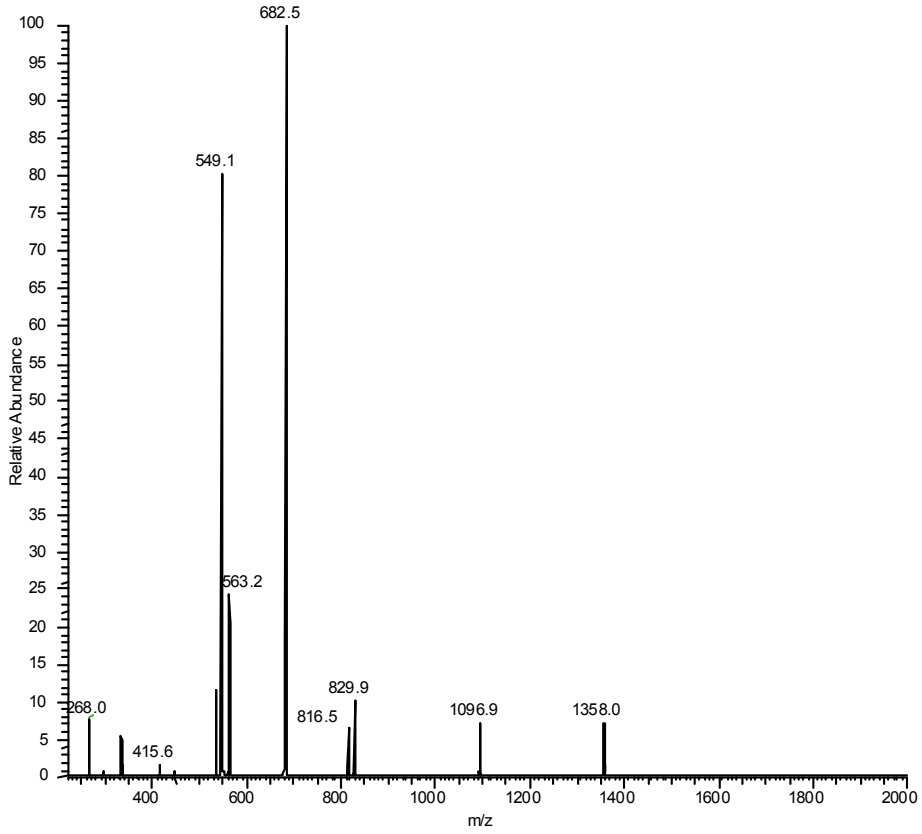

Id. vi – ESI-MS/MS spectrum of n = 6 (m/z = 950.6)

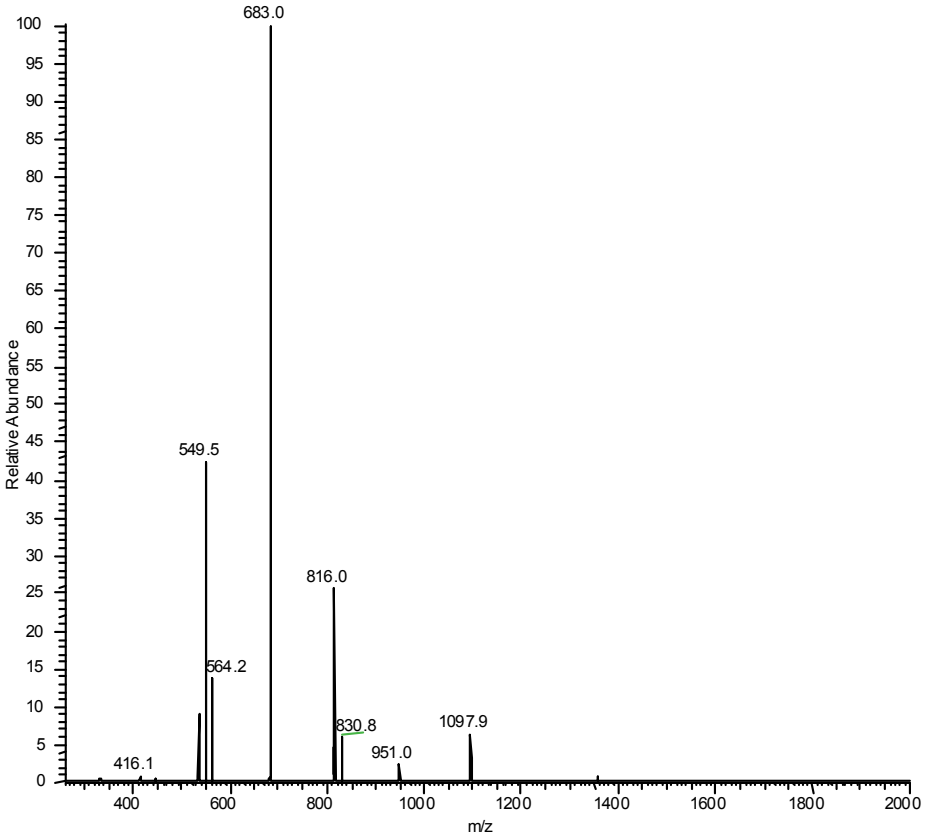

Id. vii – ESI-MS/MS spectrum of n = 7 (m/z = 1084.1)

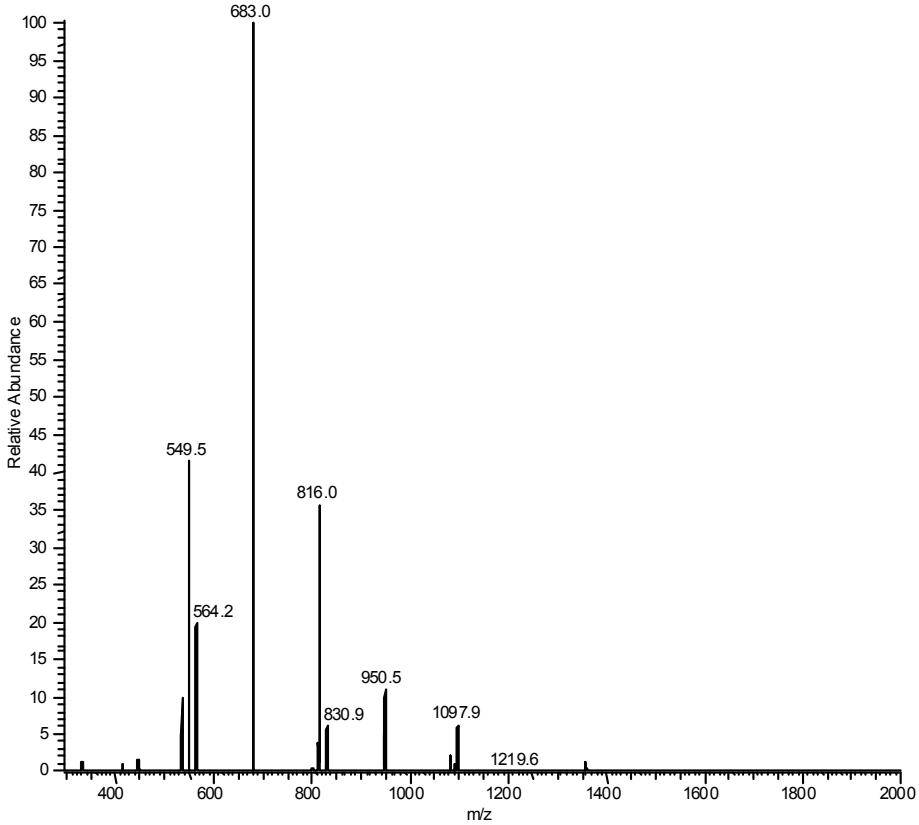

Id. viii – ESI-MS/MS spectrum of n = 8 (m/z = 1217.6)

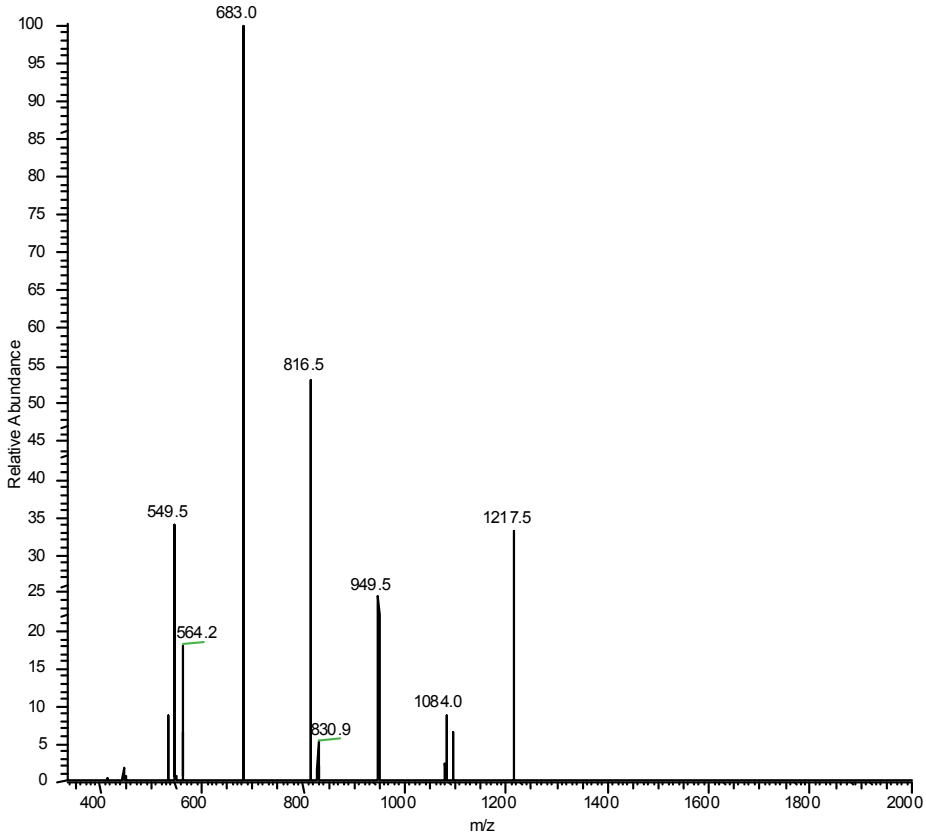

Id. ix - ESI-MS/MS spectrum of n = 9 (m/z = 1351.1)

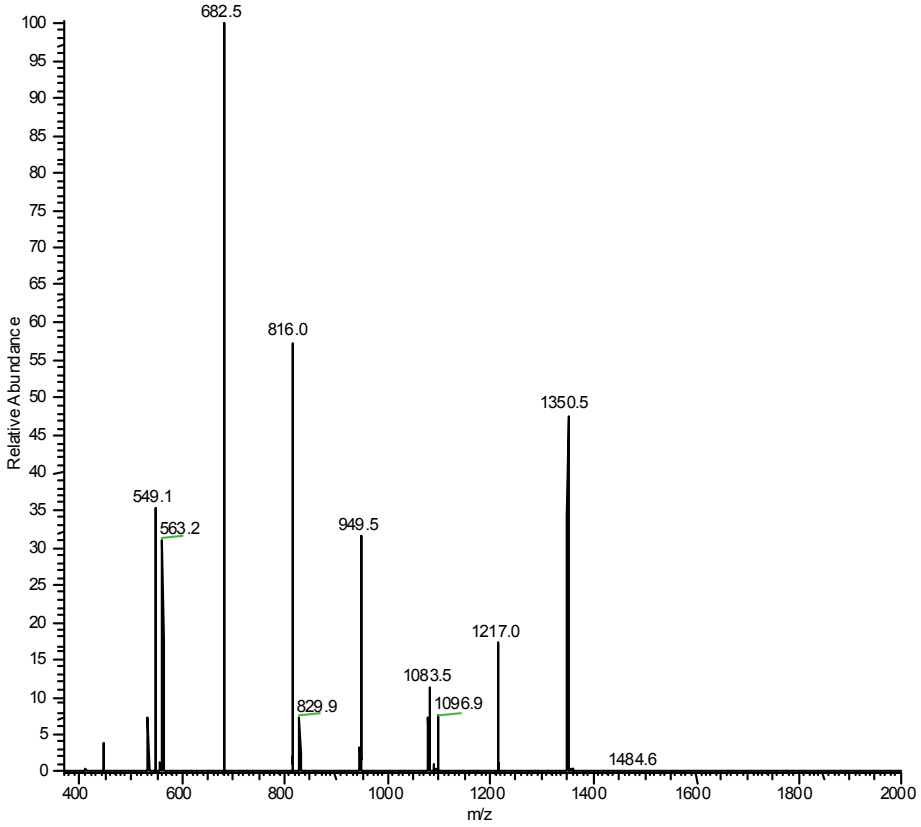

Id. x – ESI-MS/MS spectrum of n = 10 (m/z = 1484.6)

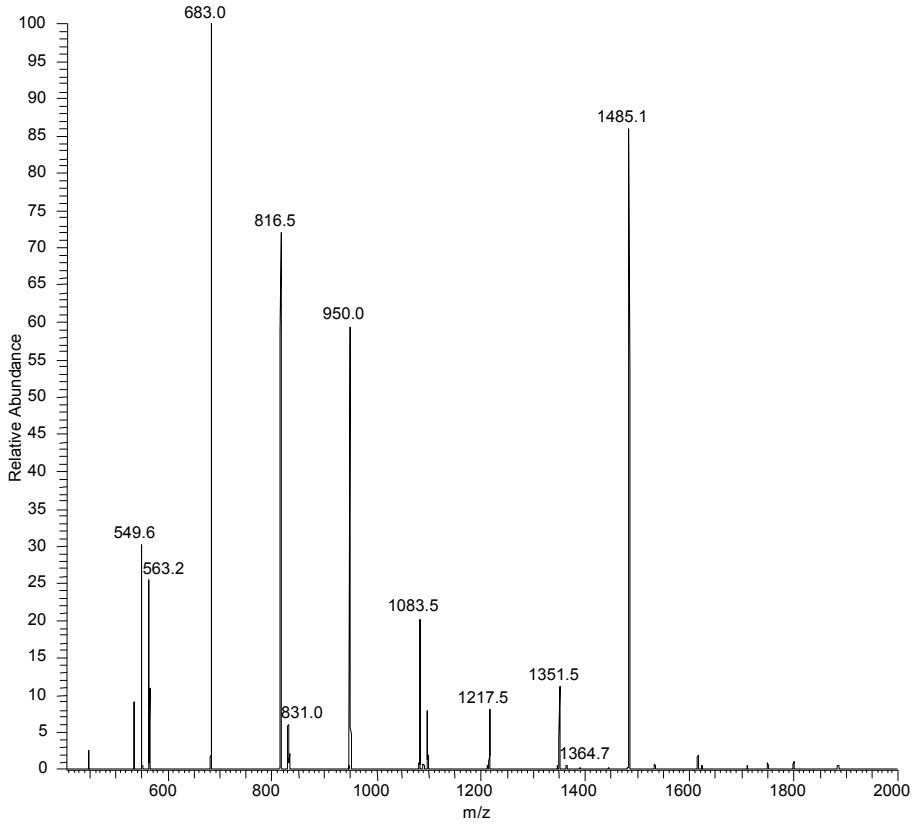

Ie. Platinum(II)-terpy clusters with deoxyguanosine

Ie. i – ESI-MS spectrum of 1:3 $[Pt(terpy)Cl]^+$ - dG mixture.

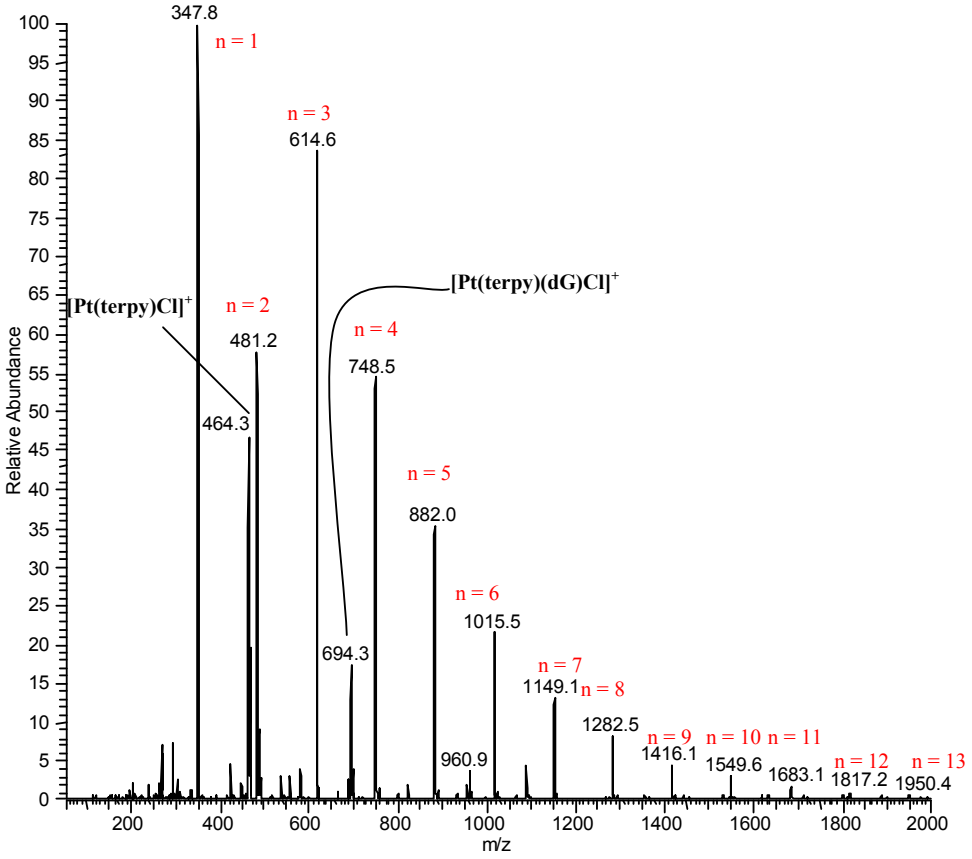

Ie. ii – ESI-MS/MS spectrum of n = 2 (m/z = 481.2)

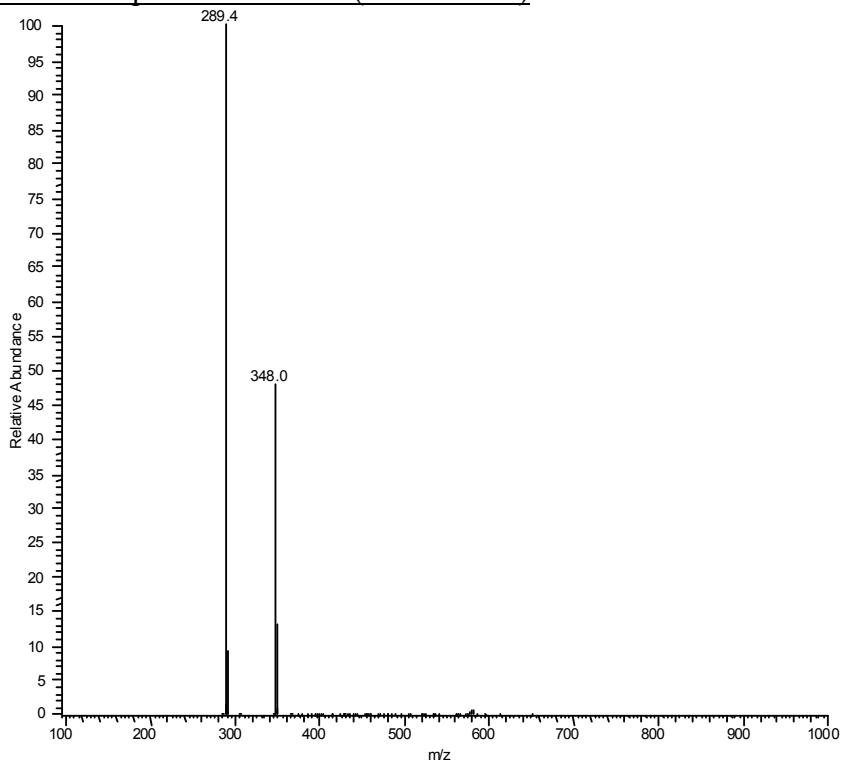

Ie. iii – ESI-MS/MS spectrum of n = 3 (m/z = 614.6)

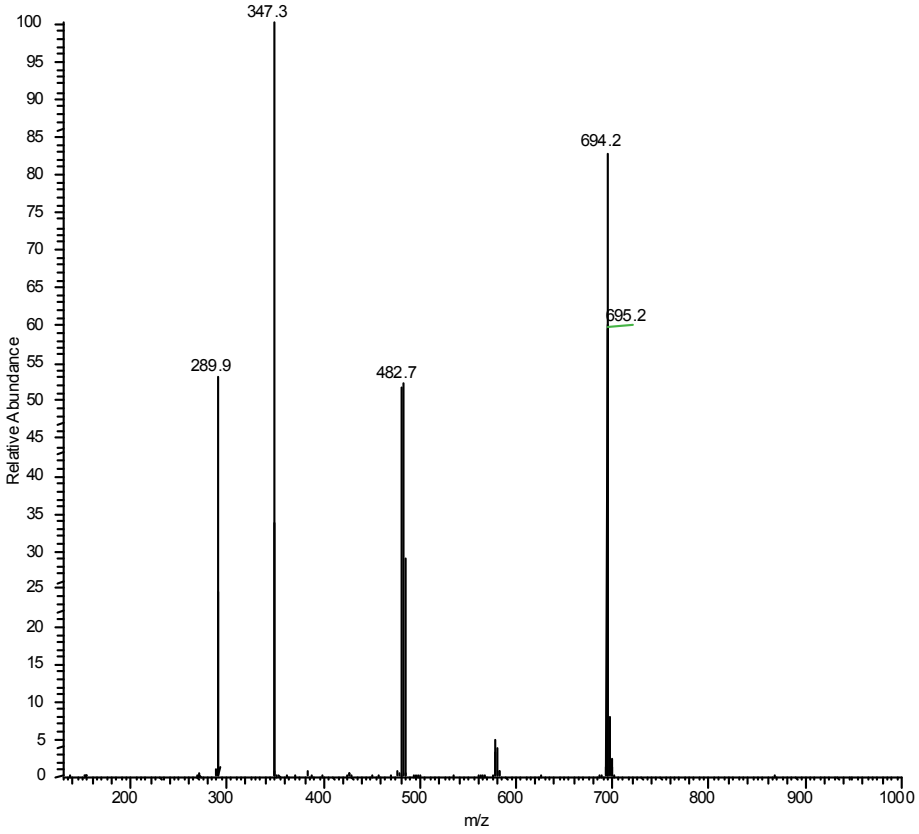

Ie. iv – ESI-MS/MS spectrum of n = 4 (m/z = 748.5)

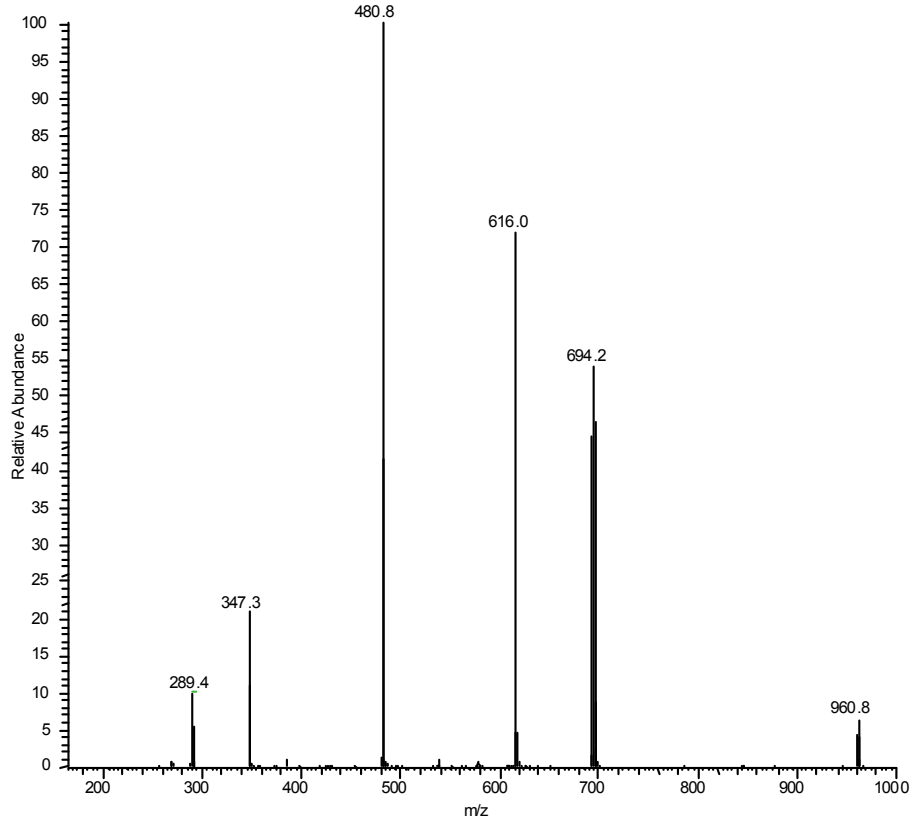

Ie. v – ESI-MS/MS spectrum of n = 5 (m/z = 882.0)

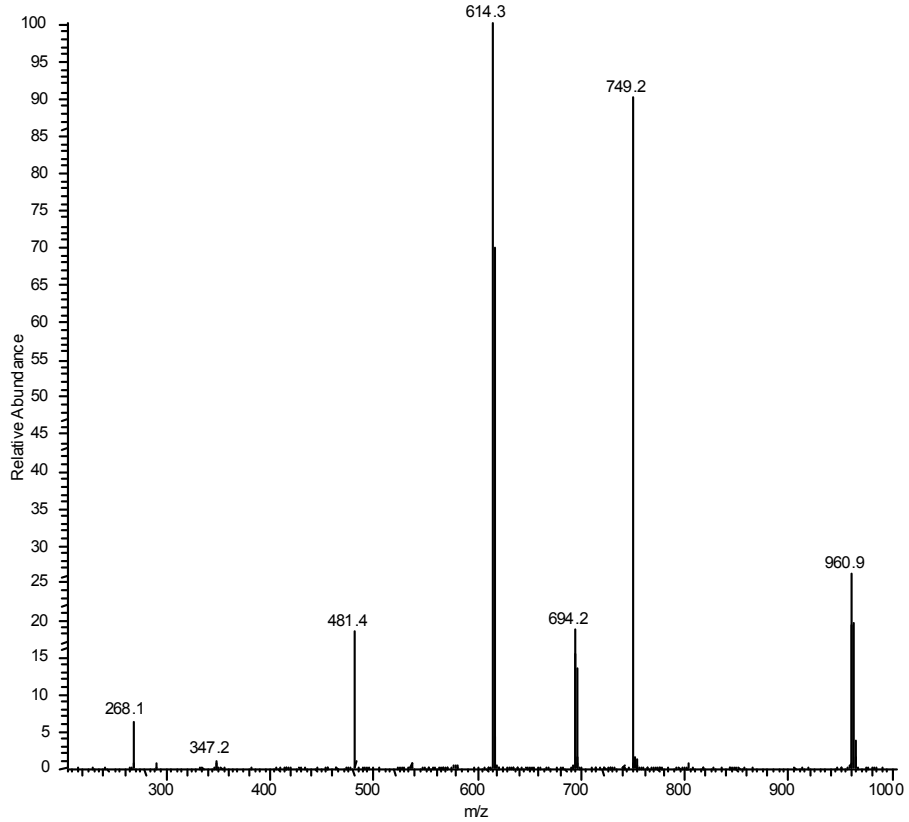

Ie. vi – ESI-MS/MS spectrum of n = 6 (m/z = 1015.5)

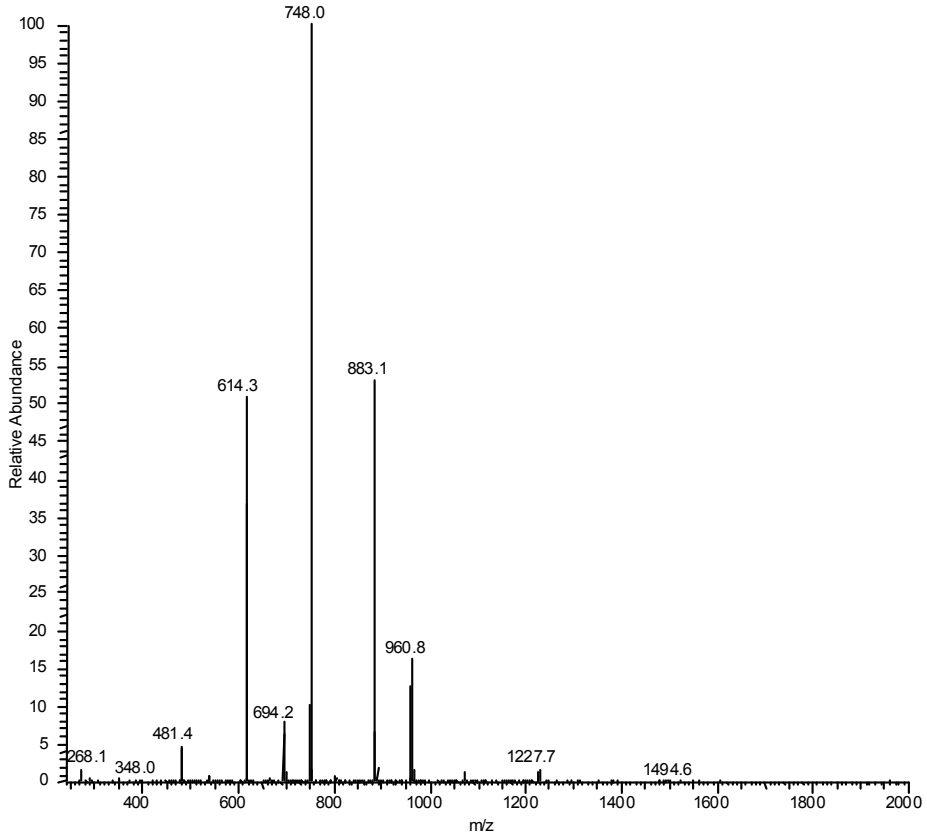

Ie. vii – ESI-MS/MS spectrum of n = 7 (m/z = 1149.1)

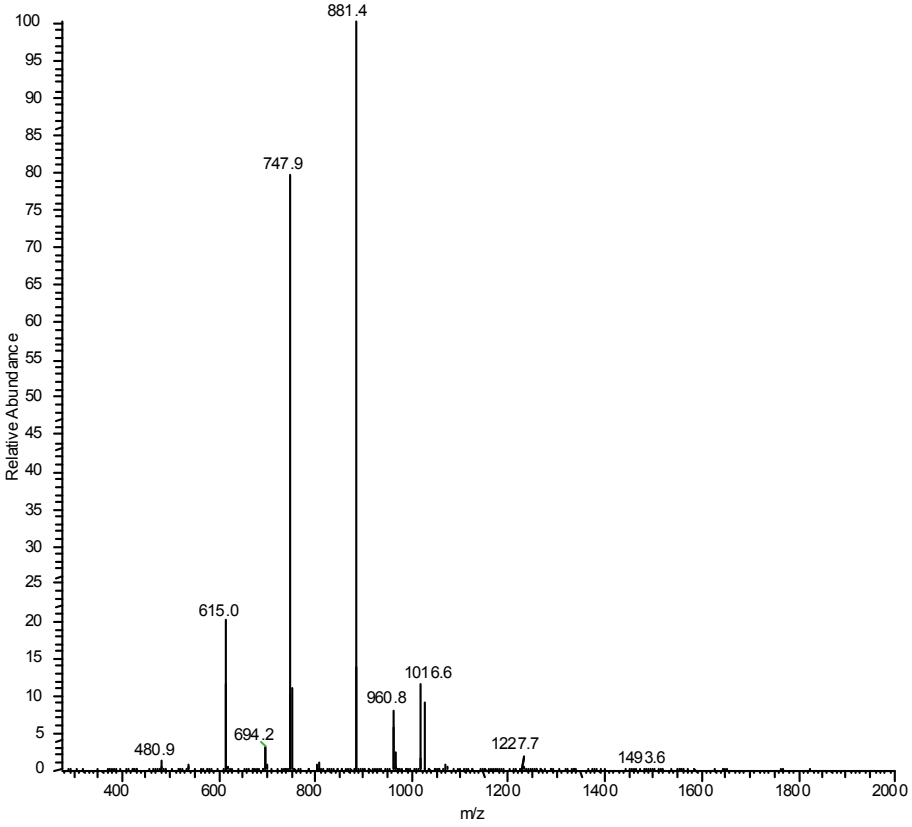

Ie. viii – ESI-MS/MS spectrum of n = 8 (m/z = 1282.5)

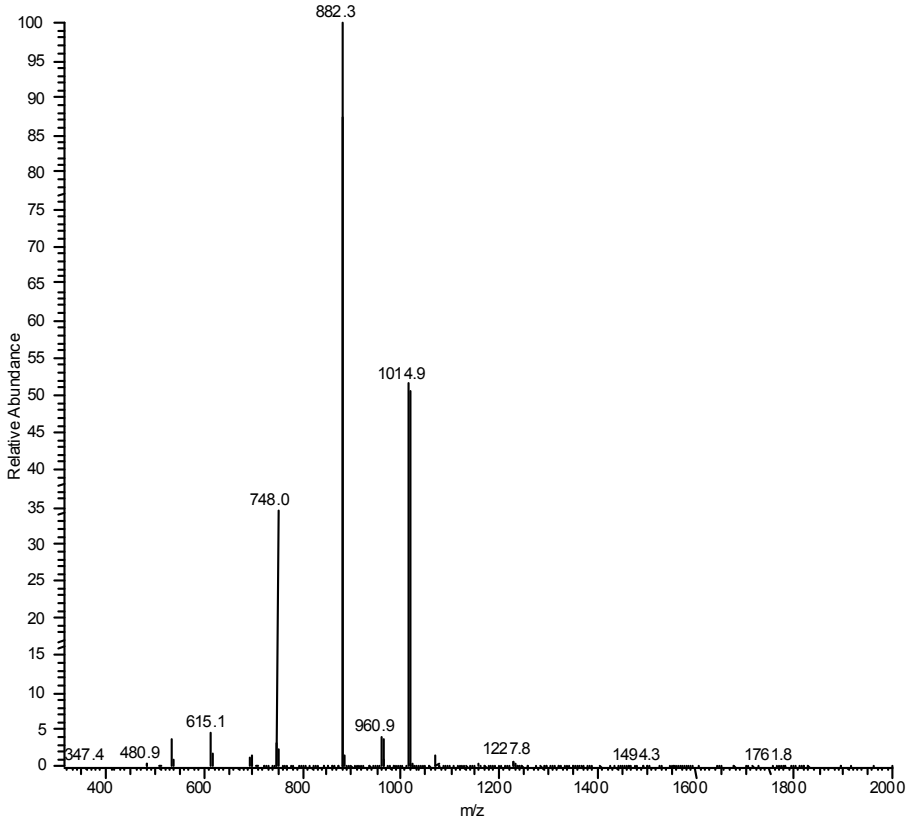

Ie. ix – ESI-MS/MS spectrum of n = 9 (m/z = 1416.1)

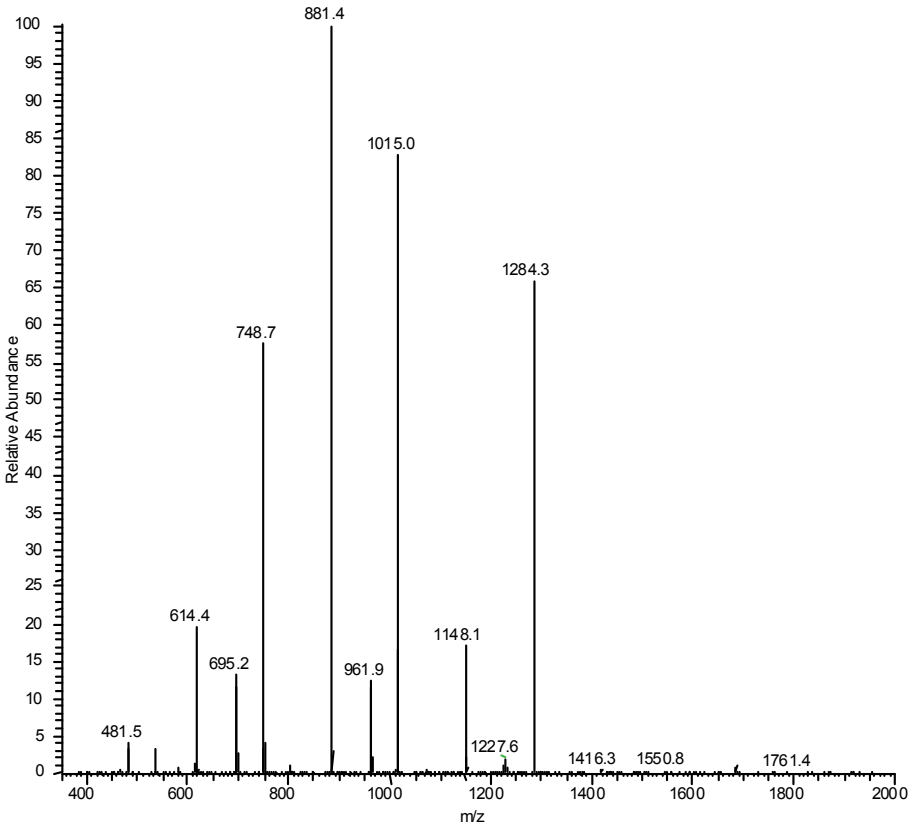

Ie. x – ESI-MS/MS spectrum of n = 10 (m/z = 1549.6)

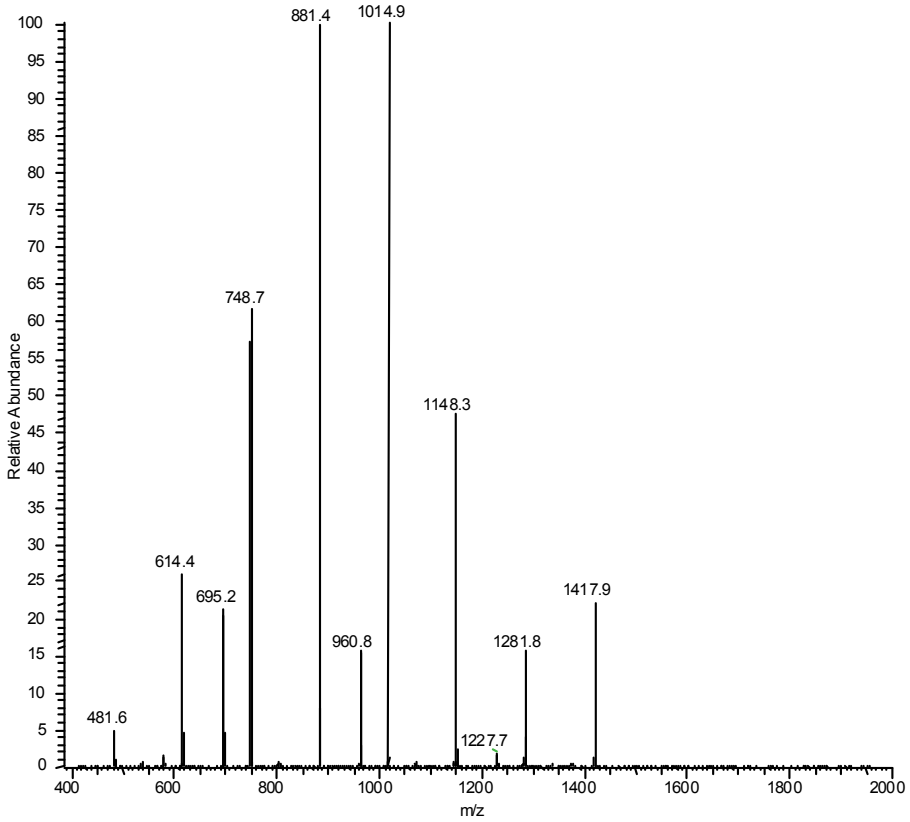

If. Platinum(II)-bpe system with various nucleoconstituents

If. i – Pt(bpe) and Inosine

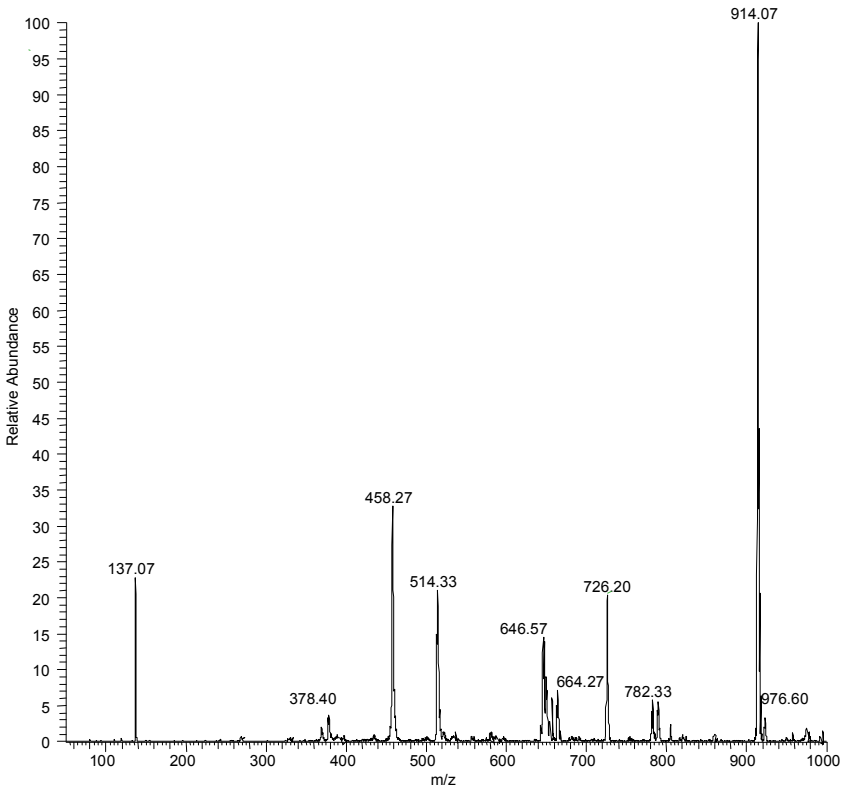

If. ii- Pt(bpe) and 1-methylcytosine

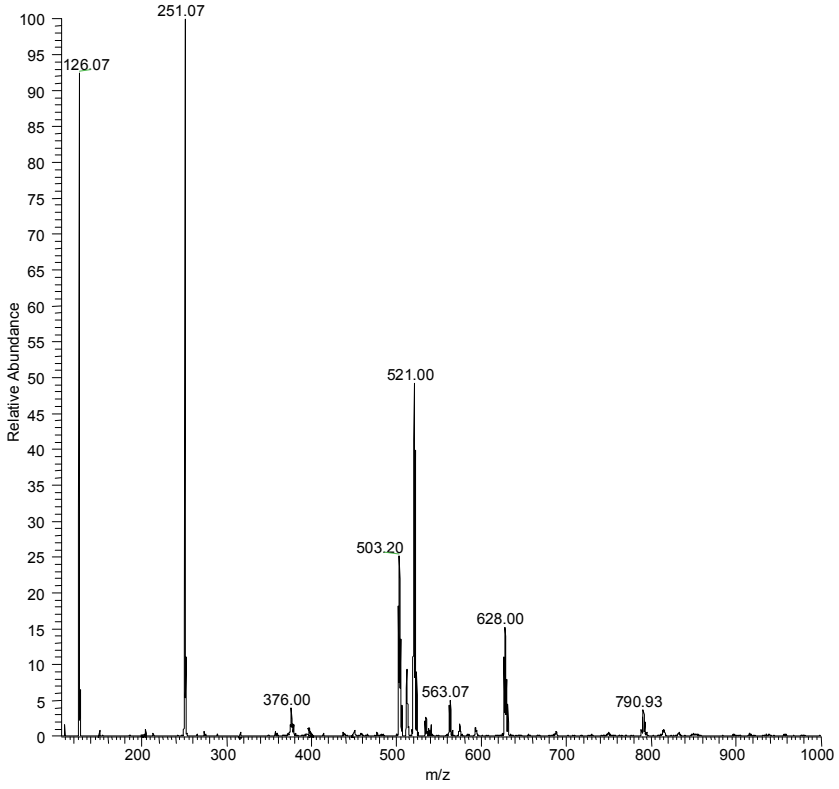

If. iii – Pt(bpe) and 3-methyladenine

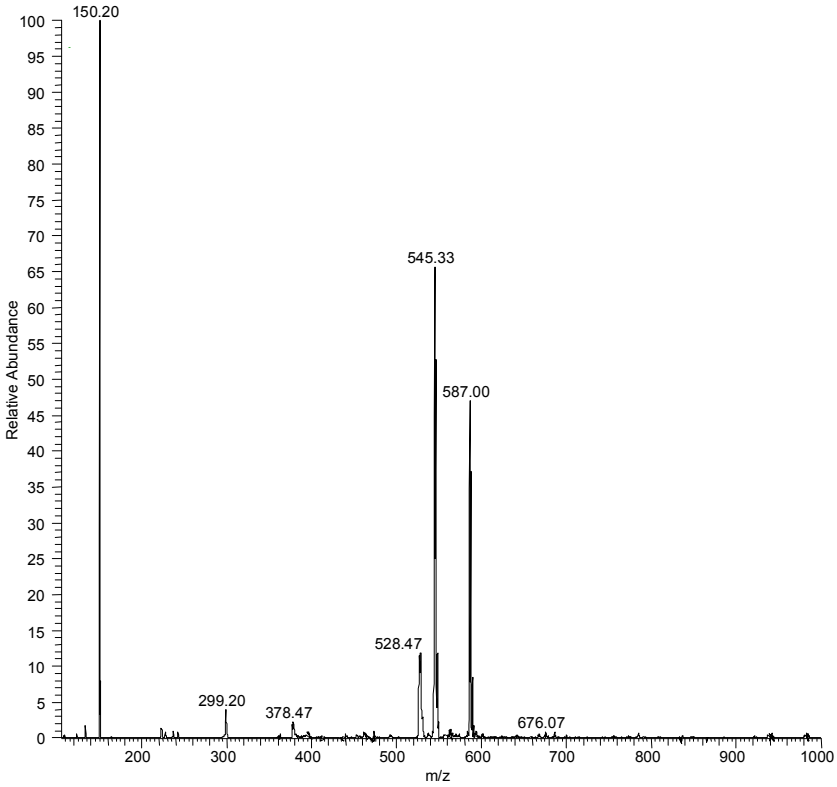

Ig. Platinum(II)-bpe system with various nucleoconstituents

Ig. i – Pt(bmpe) and Inosine.

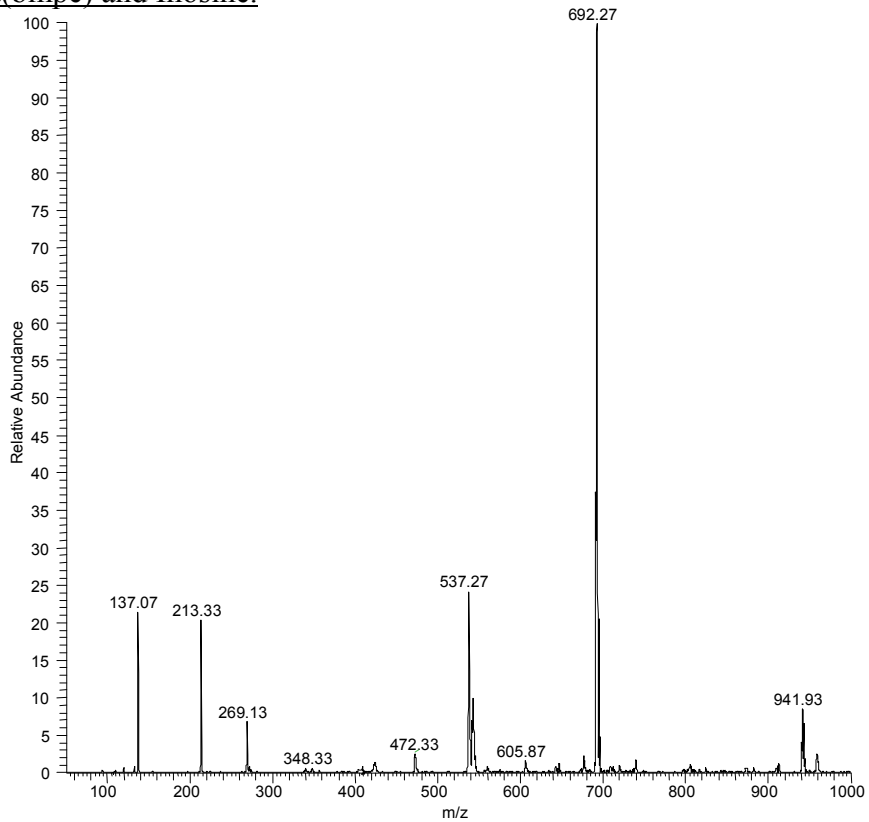

Ig. ii – Pt(bmpe) and 1-methylcytosine

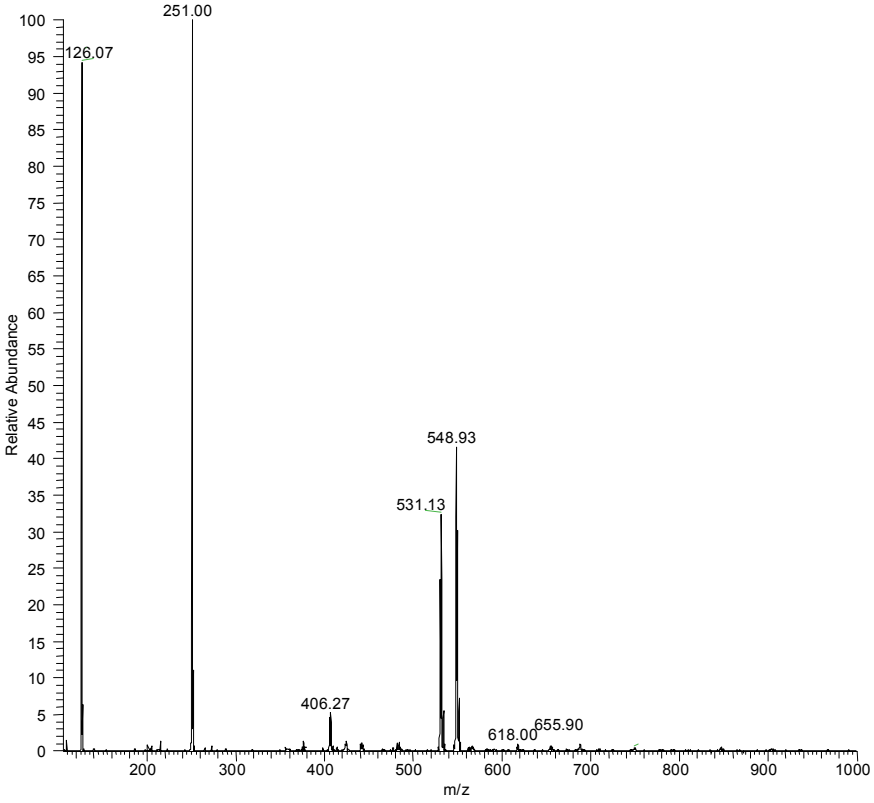

Ig. iii – Pt(bmpe) and 3-methyladenine.

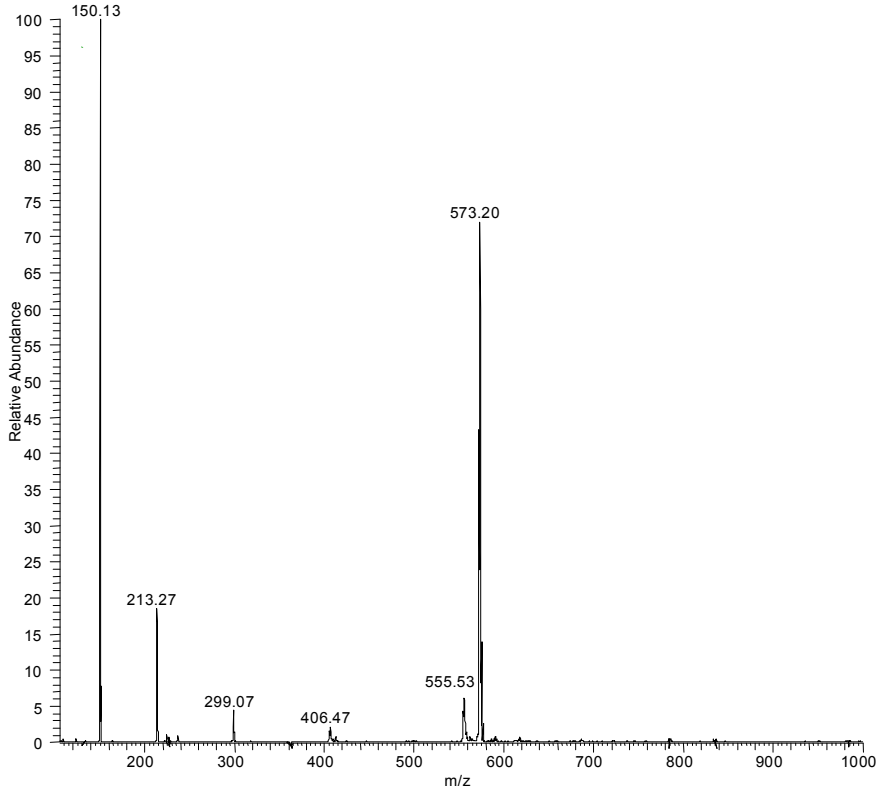

Ih. Palladium(II)-bbmm system with and without competing nucleoconstituents

Ih. i – Pd(bbmm) “diaquo” solution

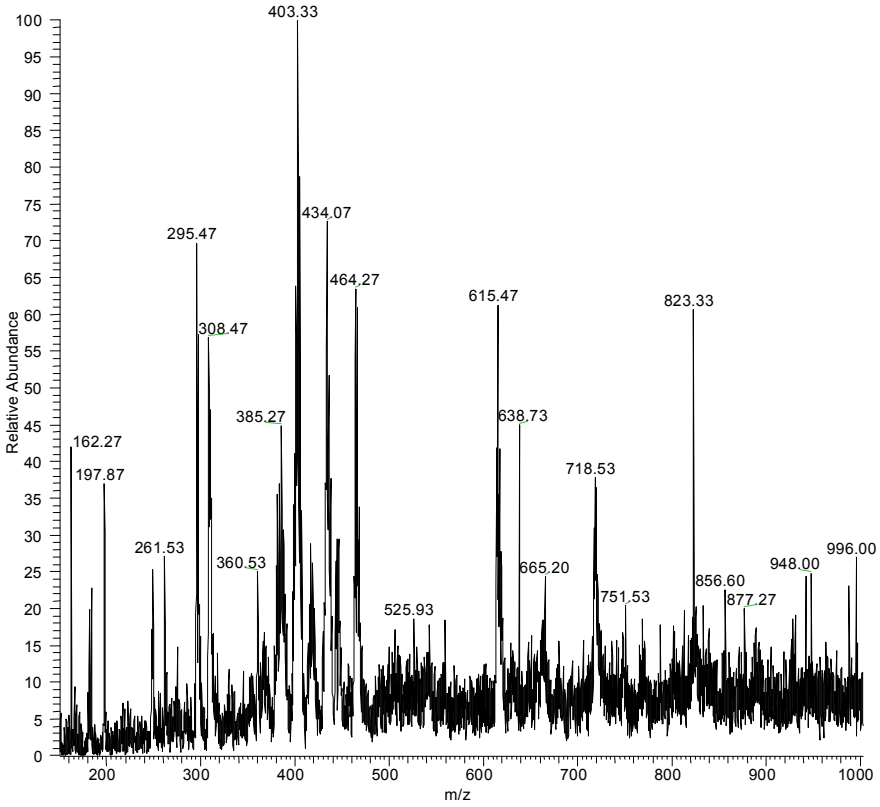

Ih. ii – Pd(bbmm) competition with inosine and cytosine

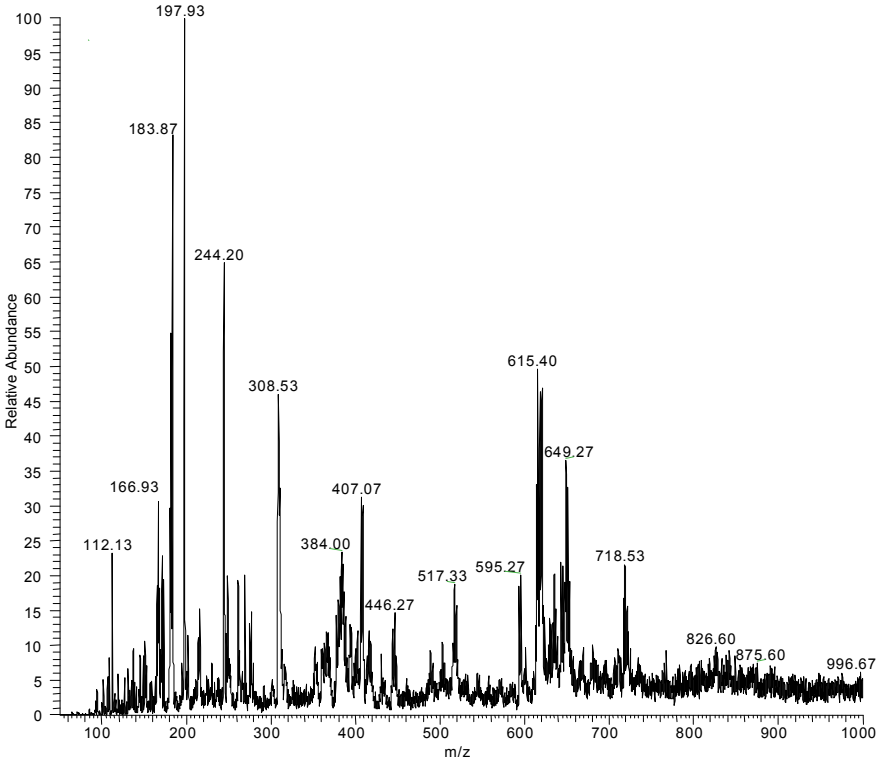

Ih. iii – Pd(bbmm) competition with inosine and 3-methyladenine

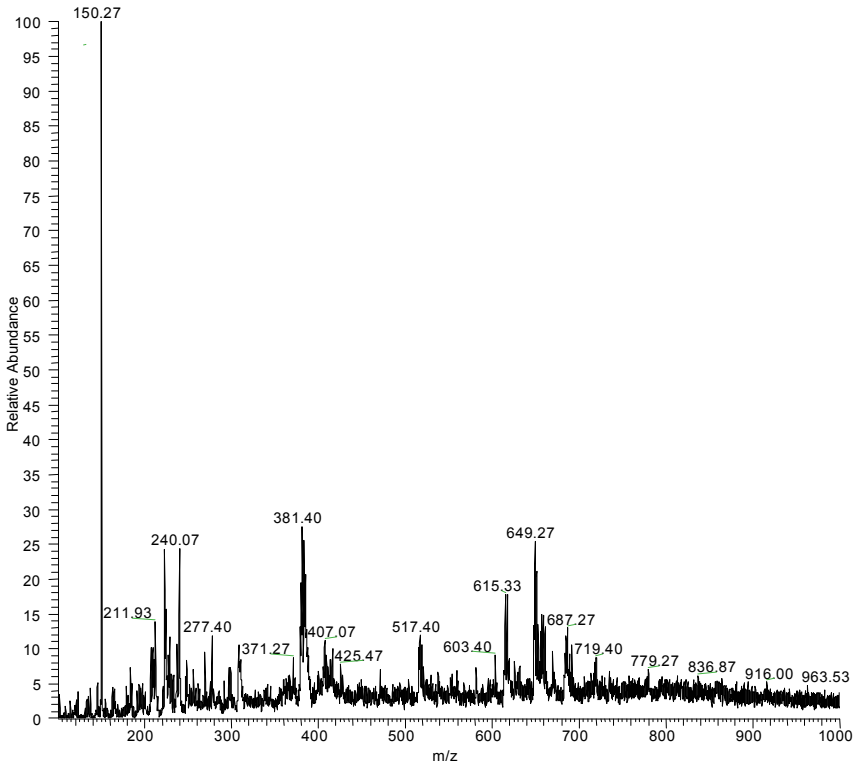

Ih. iv – Pd(bbmm) competition with inosine, cytidine and 3-methyladenine

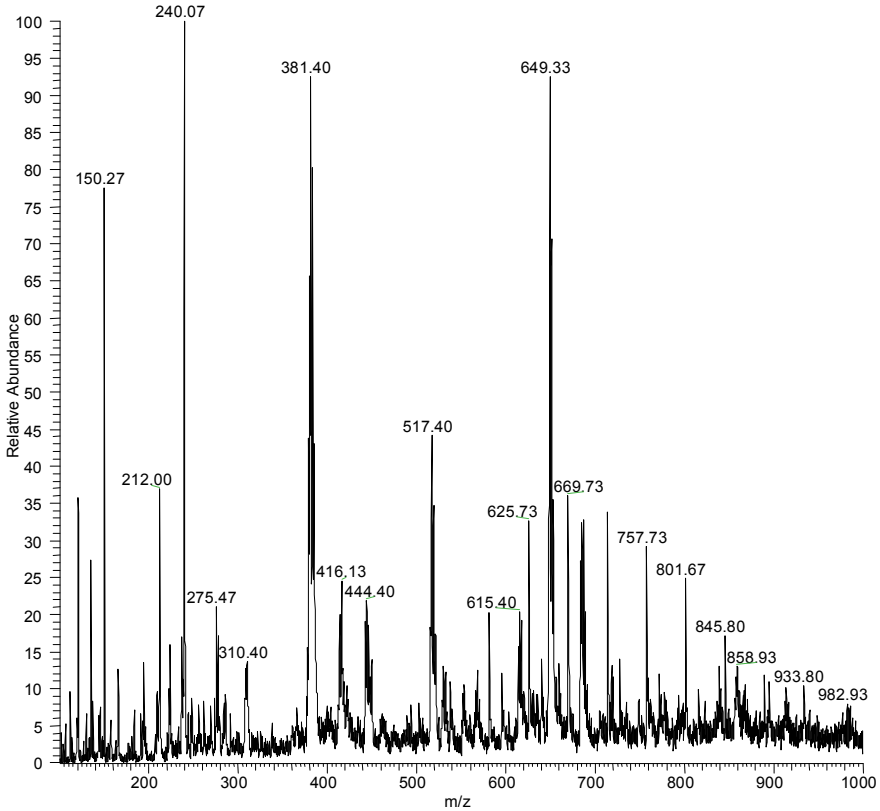

Ii. Palladium(II)-bbme system with and without competing nucleoconstituents

Ii. i – Pd(bbme) "diaquo" solution

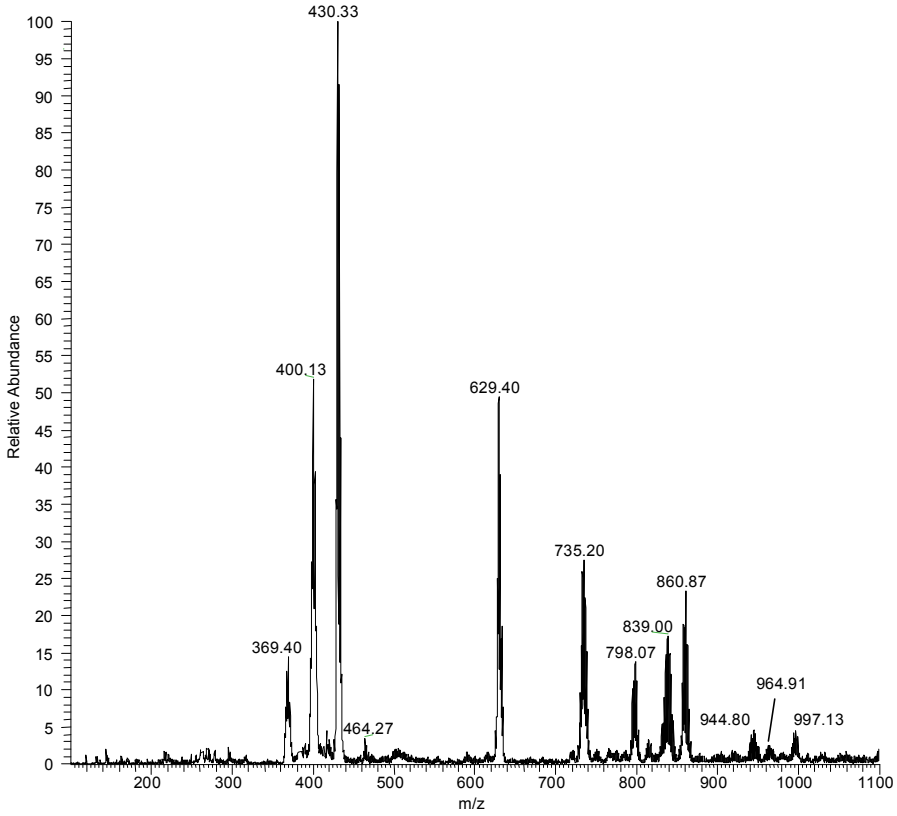

Ii. ii – Pd(bbme) competition with inosine and cytidine

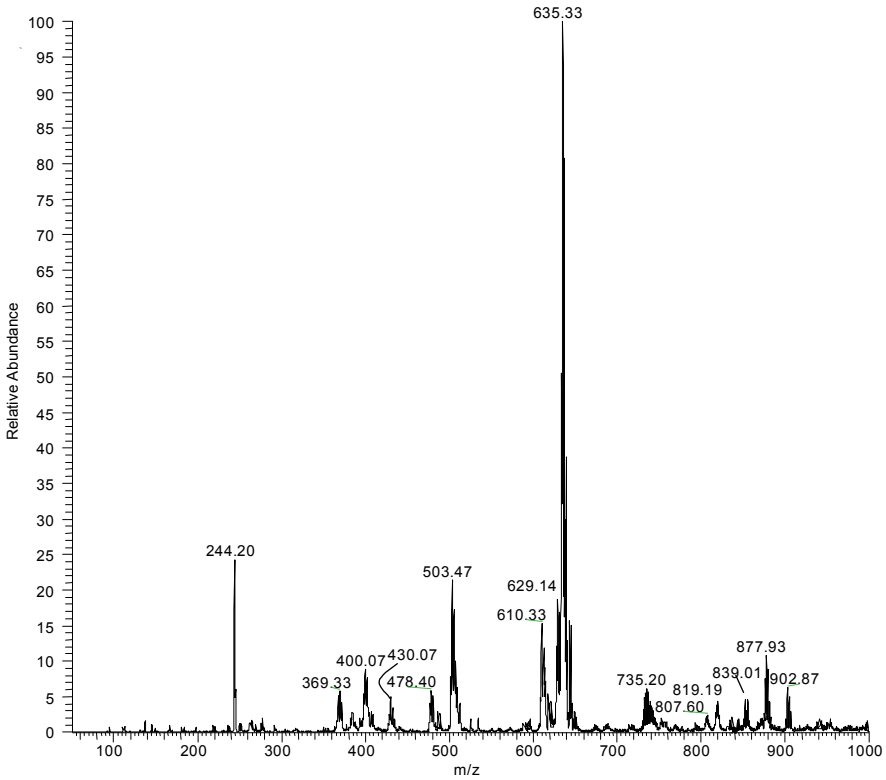

Ii. iii – Pd(bbme) competition with inosine and 3-methyladenine

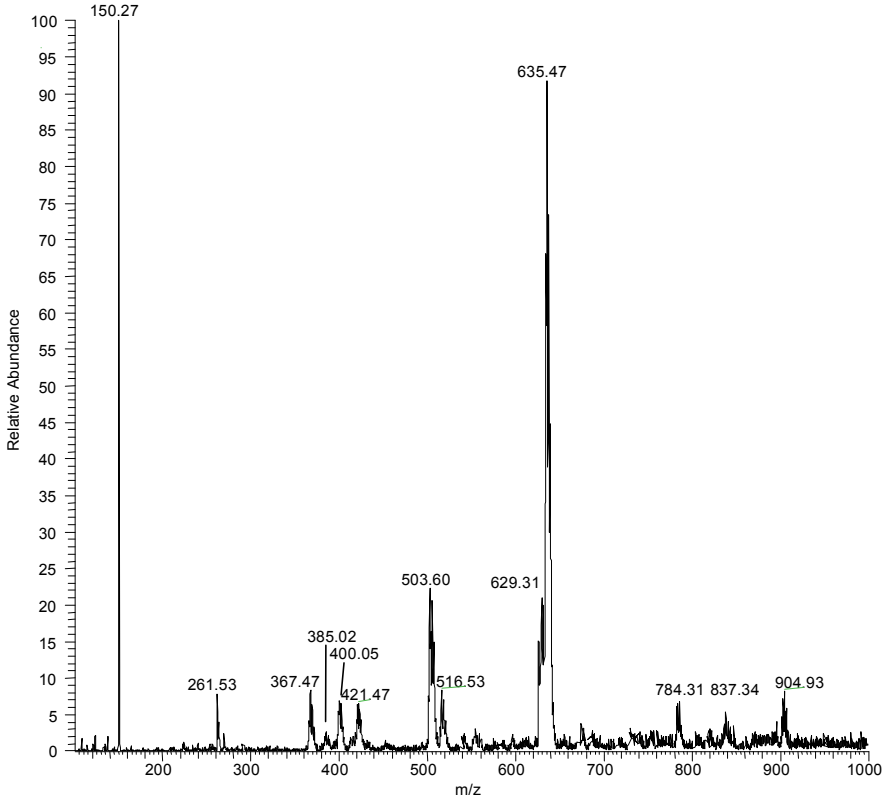

Ii. iv – Pd(bbme) competition with inosine, cytidine and 3-methyladenine

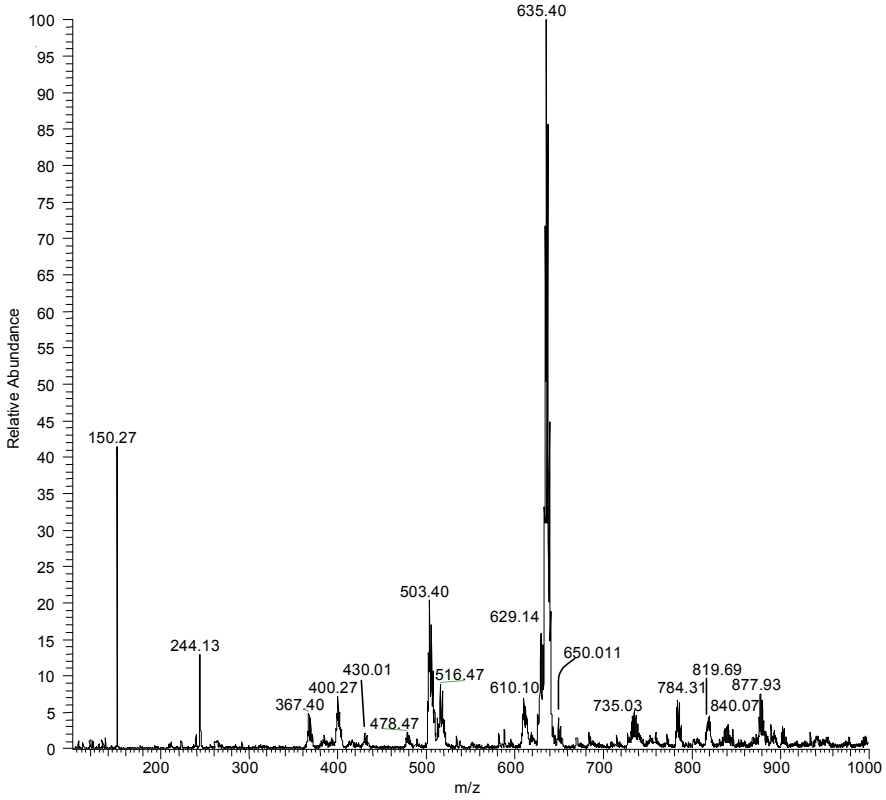

Ij. Palladium(II)-bbmp system with and without competing nucleoconstituents

Ij. i – Pd(bbmp) “diaquo” solution

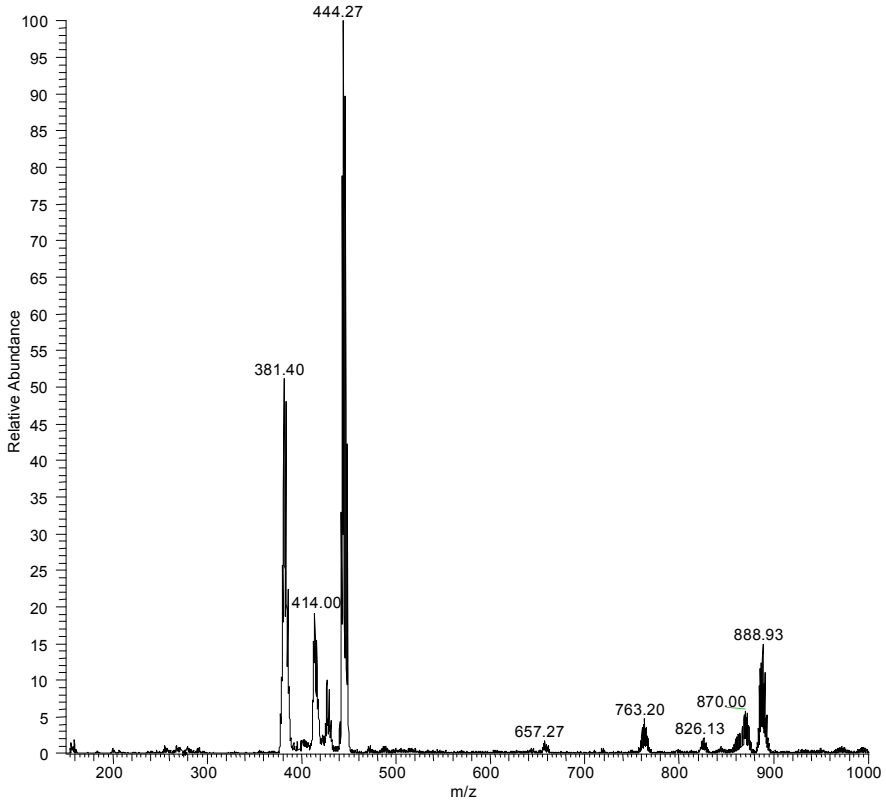

Ij. ii – Pd(bbmp) competition with inosine and cytidine

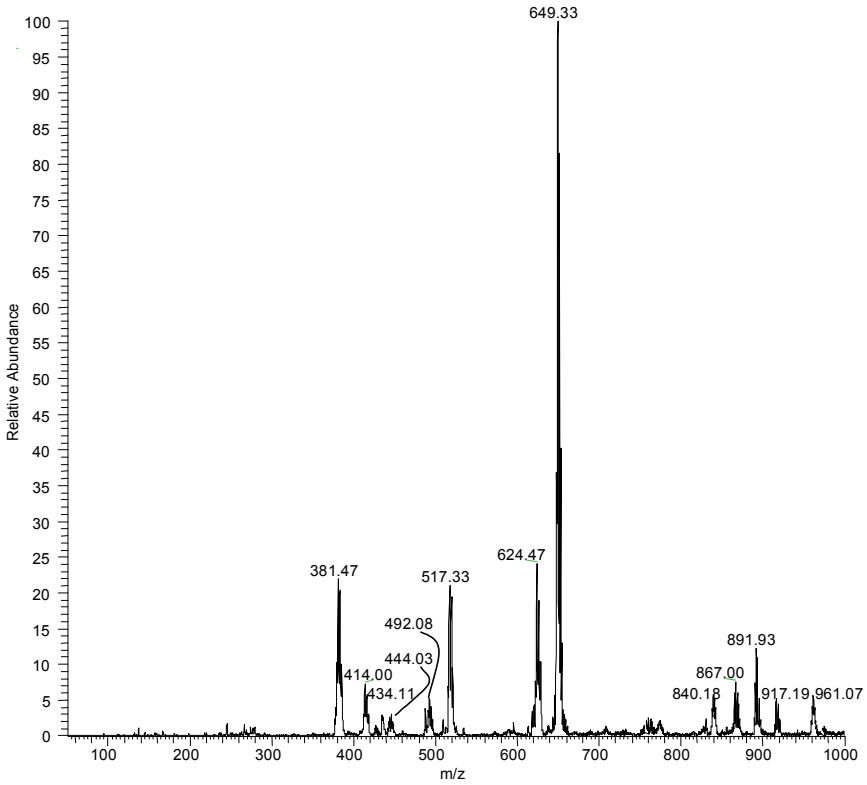

Ij. iii – Pd(bbmp) competition with inosine and 3-methyladenine

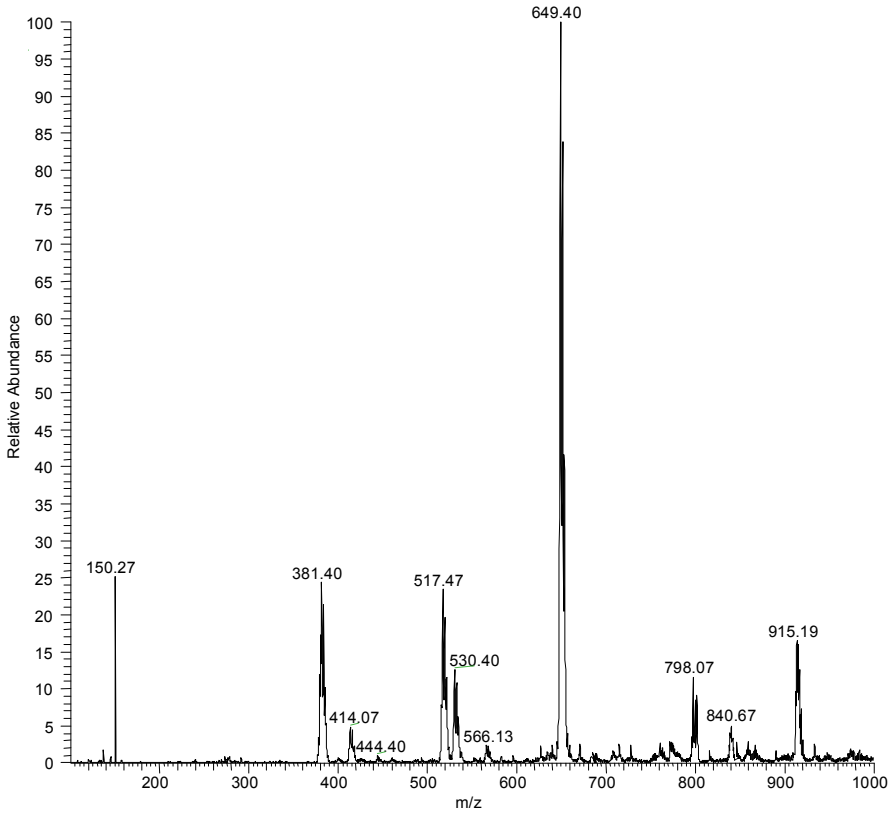

Ij. iv – Pd(bbmp) competition with inosine, cytidine and 3-methyladenine

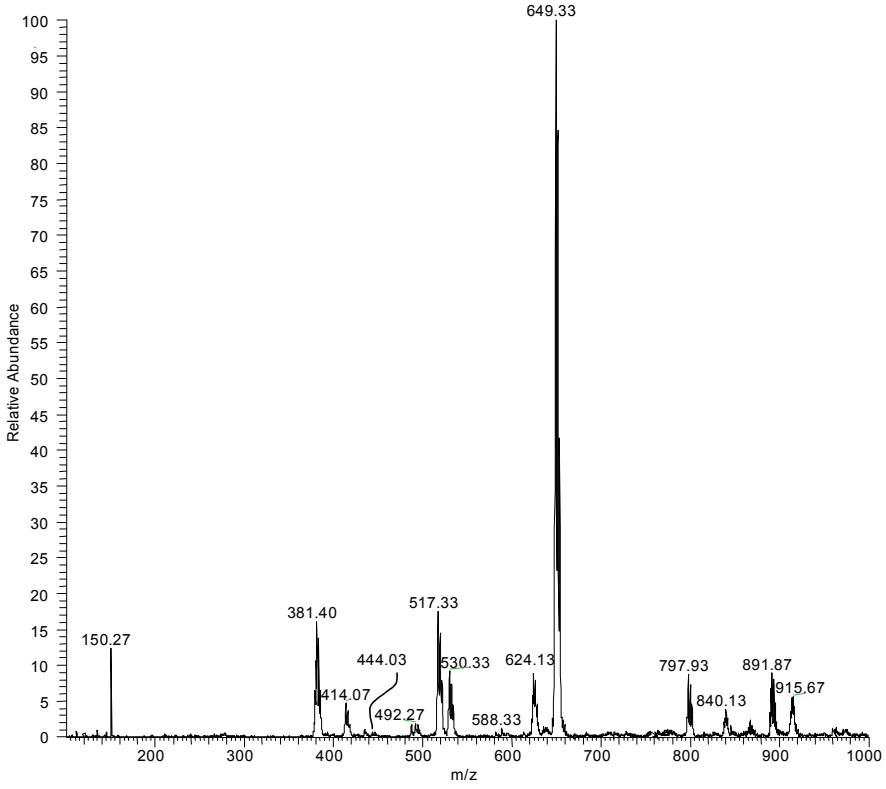

Appendix II – Identification tables for ESI-MS spectra

Pd(bbmm) "diaquo"

M/z	Theoretical formulae	Theor. MWt	Abundance (Rel)
403.33	$[Pd(bbmm)(CH_3OH)]^+ \cdot H_2O$ $(-H^+)$	403.04	473998.3 (100)
416.40	$[Pd(bbmm)(NO_3^-)]^+$	416.00	136623.8 (28.8)
434.07	$[Pd(bbmm)(NO_3^-)]^+ \cdot H_2O$	434.01	344135.1 (72.6)
444.33	$[Pd(bbmm)(CH_3OH)(CH_3CN)]^+ \cdot H_2O$ $(-H^+)$	444.87	129505.0 (27.3)
464.27	$Na_3[Pd(HP_3O_{10}^-)]^+ \cdot 2H_2O$	464.77	300832.0 (63.5)

Pd(bbme) "diaquo"

M/z	Theoretical formulae	Theor. MWt	Abundance
367.40	$[Pd(bbme)]^+$ $(-H^+)$	367.01	1149642.3 (12.5)
430.33	$[Pd(bbme)(NO_3^-)]^+$	430.01	9198789.0 (100)
464.27	$Na_3[Pd(HP_3O_{10}^-)]^+ \cdot 2H_2O$	464.77	310149.8 (3.4)
629.40	$[Pd(bbme)_2]^+$ $(-H^+)$	629.14	4551668.6 (49.5)
735.20	$[Pd_2(bbme)_2]$ $(-3H^+)$	733.03	2527556.9 (27.5)
798.07	$[Pd_2(bbme)_2(NO_3^-)]$ $(-2H^+)$	798.03	947190.6 (10.3)
839.00	$[Pd_3(bbme)_2]^+$ $(-5H^+)$	838.92	1584097.9 (17.2)
860.87	$[Pd_2(bbme)_2(NO_3^-)_2]$ $(-H^+)$	861.02	2148876.1 (23.4)
964.73	$[Pd_3(bbme)_2(NO_3^-)_2]$ $(-3H^+)$	964.91	233053.0 (2.5)
997.13	$[Pd_3(bbme)_2(NO_3^-)_2(MeOH)]$ $(-3H^+)$	996.94	414739.4 (4.5)

Pd(bbmp) "diaquo"

M/z	Theoretical formulae	Theor. MWt	Abundance
381.40	$[Pd(bbmp)]^+$ $(-H^+)$	381.04	9134465.8 (51.1)
427.20	$[Pd(H_4P_3O_{10}^-)(MeOH)_2]$	426.86	1790829.8 (10.0)
444.27	$[Pd(bbmp)(NO_3^-)]^+$	444.03	17868084.4 (100)
657.27	$[Pd(bbmp)_2]$ $(-H^+)$	657.17	320228.7 (1.8)
763.20	$[Pd_2(bbmp)_2]$ $(-3H^+)$	763.02	841344.7 (4.7)
826.13	$[Pd_2(bbmp)_2(NO_3^-)]$ $(-2H^+)$	826.06	375215.6 (2.1)
870.00	$[Pd_3(bbmp)(NO_3^-)_3(Cl^-)]^+ \cdot (3H_2O)$	869.81	1023925.3 (5.7)
888.93	$[Pd_2(bbmp)_2(Cl^-)_2]^+ \cdot 3H_2O$ $(-H^+)$	889.05	2664156.4 (14.9)

Pd(bbmm) Inosine Cytidine competition

M/z	Theoretical formula	Theor. MWt	Abundance (Rel)
416.13	$[Pd(bbmm)(NO_3^-)$	416.00	
489.27	$[Pd(bbmm)(\mathbf{hypox})]^+$ $(-H^+)$	489.04	67020.8 (19.2)
517.33	$[Pd(bbmm)(\mathbf{Cytosine})]^+ \cdot 3H_2O$ $(-H^+)$	518.08	140596.0 (40.2)
593.20	$[Pd(bbmm)(\mathbf{Cytosine})_2]^+ \cdot H_2O$ $(-H^+)$	593.10	138703.3 (39.7)
618.27	$[Pd(bbmm)(\mathbf{Cytosine})(\mathbf{hypox})]^+ \cdot H_2O$ $(-H^+)$	618.10	349486.7 (100)
635.40	$[Pd^{III}(bbmm)(\mathbf{Cytosine})(\mathbf{hypox})]^+ \cdot 2H_2O$ $(-2\,H^+)$	635.10	152739.6 (43.7)
649.27	$[Pd^{III}(bbmm)(\mathbf{Cytidine})]^+ \cdot 3H_2O$ $(-2H^+)$	649.11	275802.9 (78.9)

Pd(bbme) Inosine Cytidine competition

M/z	Theoretical formula	Theor. MWt	Abundance (Rel)
367.40	$[Pd(bbme)]^+ (-H^+)$	367.02	1652964.8 (5.8)
400.07	$[Pd^I(bbme)(CH_3OH)]^+$	400.05	2527472.5 (8.9)
430.33	$[Pd(bbme)(NO_3^-)]^+$	430.01	1418651.6 (5.0)
478.40	[Pd(bbme)(**Cytosine**)]$^+$ $(-H^+)$	478.06	1654686.0 (5.8)
503.47	[Pd(bbme)(**hypox**)]$^+$ $(-H^+)$	503.06	6088379.2 (21.4)
610.33	[Pd(bbme)(**Cytidine**)]$^+$ $(-H^+)$	610.10	4366531.7 (15.4)
629.47	$[Pd(bbme)_2]^+ (-H^+)$	629.14	5328106.7 (18.8)
635.33	[Pd(bbme)(**Inosine**)]$^+$ $(-H^+)$	635.10	28416039.5 (100)
735.20	$[Pd_2(bbme)_2]^+ (-H^+)$	735.04	1758243.6 (6.2)
807.60	$[Pd_2(bbme)_2$(**Inosine**$)_2$(**Hypox**$)_2$(MeOH)$]^+ \cdot 2H_2O$ $(-2H^+)$ 807.67		629655.1 (2.2)
819.13	$[Pd_2(bbme)_2$(**Inosine**$)_2$(**Hypox**)(**Cytosine**)$(MeOH)_2]^+ \cdot 3H_2O$ $(-2H^+)$ 819.19		1241340.3 (4.4)
839.00	$[Pd_3(bbme)_2]^+ (-5H^+)$	839.01	949813.9 (3.3)
877.93	[Pd(bbme)(**Cytidine**)(**Inosine**)]$^+$ $(-H^+)$	878.18	2141165.7 (7.5)
902.87	[Pd(bbme)(**Inosine**$)_2$]$^+$ $(-H^+)$	903.17	1767146.2 (6.2)

Pd(bbme) 3-methyladenine Inosine competition

M/z	Theoretical formula	Theor. MWt	Abundance (Rel)
367.47	$[Pd(bbme)]^+$ $(-H^+)$	367.02	493964.4 (9.1)
385.40	$[Pd(bbme)(H_2O)]^+$ $(+H^+)$	385.02	159972.7 (3.0)
400.27	$[Pd^I(bbme)(CH_3OH)]^+$	400.05	408104.6 (7.5)
421.47	$[Pd(bbme)(H_2O)_3]$ $(-H^+)$	421.04	384574.3 (7.1)
503.60	[Pd(bbme)(**hypox**)]$^+$ $(-H^+)$	503.06	1317995.5 (24.3)
516.53	[Pd(bbme)(**3MeA)**]$^+$ $(-H^+)$	516.08	490024.5 (9.1)
629.47	$[Pd(bbme)_2]^+$ $(-H^+)$	629.31	1237791.4 (22.9)
635.47	[Pd(bbme)(**Inosine**)]$^+$ $(-H^+)$	635.24	5412644.8 (100)
784.20	[Pd(bbme)(**3MeA**)(**Inosine**)]$^+$ $(-H^+)$	784.31	385597.5 (7.1)
838.07	[Pd(bbme)(**3MeA**)(**Inosine**)$(H_2O)_3]^+$ $(-H^+)$	837.34	313889.7 (5.8)
902.87	[Pd(bbme)(**Inosine**$)_2]^+$ $(-H^+)$	903.18	484092.7 (8.9)

Pd(bbme) 3-methyladenine Inosine Cytidine competition

M/z	Theoretical formula	Theor. MWt	Abundance (Rel)
367.40	$[Pd(bbme)]^+$ $(-H^+)$	367.02	1010389.5 (4.9)
430.40	$[Pd(bbme)(NO_3^-)]^+$	430.01	440349.1 (2.1)
478.47	$[Pd(bbme)(\mathbf{Cytosine})]^+$ $(-H^+)$	478.05	459516.1 (2.2)
503.40	$[Pd(bbme)(\mathbf{hypox})]^+$ $(-H^+)$	503.05	4218788.1 (20.4)
516.47	$[Pd(bbme)(\mathbf{3MeA})]^+$ $(-H^+)$	516.08	1824541.5 (8.8)
610.40	$[Pd(bbme)(\mathbf{Cytidine})]^+$ $(-H^+)$	610.10	1436105.6 (7.0)
629.47	$[Pd(bbme)_2]^+$ $(-H^+)$	629.14	3283475.8 (15.9)
635.40	$[Pd(bbme)(\mathbf{Inosine})]^+$ $(-H^+)$	635.24	20642312.6 (100)
649.40	$[Pd(bbme)(\mathbf{hypox})(\mathbf{Cytosine})]^+ \cdot 2H_2O$ $(-H^+)$	650.11	877225.1 (4.2)
735.20	$[Pd_2(bbme)_2]^{2+}$	735.03	1077273.3 (5.2)
784.00	$[Pd(bbme)(\mathbf{3MeA})(\mathbf{Inosine})]^+$ $(-H^+)$	784.31	1366494.1 (6.6)
819.67	$Na[Pd_2(bbme)_2(\mathbf{Insoine})_2(\mathbf{3MeA})_2(EtOH)]^{2+}$	819.69	911082.5 (4.4)
840.07	$[Pd_2(bbme)(\mathbf{hypox})(\mathbf{3MeA})(EtOH)]^{2+} \cdot 2H_2O$ $(-H^+)$	840.07	624029.0 (3.0)
877.93	$[Pd(bbme)(\mathbf{Cytidine})(\mathbf{Inosine})]^+$ $(-H^+)$	878.33	1552732.3 (7.5)
902.92	$[Pd(bbme)(\mathbf{Inosine})_2]^+$ $(-H^+)$	903.47	639842.7 (3.1)

Pd(bbmp) Inosine Cytidine competition

M/z	Theoretical formula	Theor. MWt	Abundance (Rel)
381.47	$[Pd(bbmp)]^{+}$ $(-H^{+})$	381.04	8811796.0 (21.9)
414.00	$[Pd(bbmp)(MeOH)]^{+}$ $(-H^{+})$	414.07	2948478.9 (7.3)
427.40	$[Pd(bbmp)(EtOH)]^{+}$ $(-H^{+})$	427.07	581277.9 (1.4)
434.47	$[Pd(bbmp)(\mathbf{Cytidine})_2]^{2+}$	434.11	1185713.3 (2.9)
444.33	$[Pd(bbmp)(NO_3^{-})]^{+}$	444.03	1046692.7 (2.6)
492.33	$[Pd(bbmp)(\mathbf{Cytosine})]^{+}$ $(-H^{+})$	492.08	2130698.1 (5.3)
517.33	$[Pd(bbmp)(\mathbf{hypox})]^{+}$ $(-H^{+})$	517.07	8467158.9 (21.0)
624.47	$[Pd(bbmp)(\mathbf{Cytidine})]^{+}$ $(-H^{+})$	624.12	9704560.1 (24.1)
649.33	$[Pd(bbmp)(\mathbf{Inosine})]^{+}$ $(-H^{+})$	649.11	40241086.9 (100)
840.13	$[Pd_2(bbmp)_2(\mathbf{Inosine})_3(\mathbf{Cytosine})]^{+}$ $(-2H^{+})$	840.18	2280632.5 (5.7)
867.00	$[Pd(bbmp)(\mathbf{Cytidine})_2]^{+}$ $(-H^{+})$	867.20	3070754.3 (7.6)
891.93	$[Pd(bbmp)(\mathbf{Cytidine})(\mathbf{Inosine})]^{+}$ $(-H^{+})$	892.20	4895162.7 (12.2)
916.93	$[Pd(bbmp)(\mathbf{Inosine})_2]^{+}$ $(-H^{+})$	917.19	2118349.9 (5.3)
961.53	$[Pd_2(bbmp)_2(\mathbf{Inosine})_4(MeOH)(Cl^{-})]^{2+} \cdot H_2O$ $(-H^{+})$	961.71	2262097.2 (5.6)

Pd(bbmp) 3-methyladenine Inosine competition

M/z	Theoretical formula	Theor. MWt	Abundance (Rel)
381.40	$[Pd(bbmp)]^{+}$ $(-H^{+})$	381.04	5187806.4 (24.4)
414.07	$[Pd^{I}(bbmp)(CH_3OH)]^{+}$	414.05	1044619.1 (4.9)
444.40	$[Pd(bbmp)(NO_3^{-})]^{+}$ $(-H^{+})$	444.03	216756.7 (1.0)
459.87	$[Pd(bbmp)(\mathbf{Inosine})_2]^{2+}$	459.60	139239.1 (0.6)
488.87	$Na[Pd(bbmp)(\mathbf{Inosine})_2(Cl^{-})]^{2+}$	488.58	97762.3 (0.45)
517.47	$[Pd(bbmp)(\mathbf{hypox})]^{+}$ $(-H^{+})$	517.07	4994587.7 (23.5)
530.40	$[Pd(bbmp)(\mathbf{3MeA})]^{+}$ $(-H^{+})$	530.10	2682272.7 (12.6)
566.40	$[Pd(bbmp)(\mathbf{3MeA})]^{+} \cdot 2H_2O$ $(-H^{+})$	566.13	513650.9 (2.4)
649.40	$[Pd(bbmp)(\mathbf{Inosine})]^{+}$ $(-H^{+})$	649.12	21254026.8 (100)
798.07	$[Pd(bbmp)(\mathbf{3MeA})(\mathbf{Inosine})]^{+}$ $(-H^{+})$	798.17	2452543.0 (11.5)
840.67	$[Pd_2(bbmp)_2(\mathbf{Inosine})_2(\mathbf{Hypox})_2(NO_3^{-})(EtOH)]^{2+}$ $(-2H^{+})$ 840.67		1053460.3 (5.0)
915.07	$Na[Pd_2(bbmp)_2(\mathbf{Inosine})_3(\mathbf{3MeA})(Cl^{-})(OH^{-})]^{2+} \cdot 2H_2O$ $(-H^{+})$ 915.19		3492532.7 (16.4)

Pd(bbmp) 3-methyladenine Inosine Cytidine competition

M/z	Theoretical formula	Theor. MWt	Abundance (Rel)
381.40	$[Pd(bbmp)]^{+}$ $(-H^{+})$	381.04	7541898.0 (16.2)
414.07	$[Pd^{I}(bbmp)(CH_3OH)]^{+}$	414.05	2179331.2 (4.7)
444.27	$[Pd(bbmp)(NO_3^{-})]^{+}$	444.03	335108.8 (0.7)
492.27	[Pd(bbmp)(**Cytosine**)]$^{+}$ $(-H^{+})$	492.08	856704.0 (1.8)
517.33	[Pd(bbmp)(**hypox**)]$^{+}$ $(-H^{+})$	517.07	8180832.5 (17.5)
530.33	[Pd(bbmp)(**3MeA**)]$^{+}$ $(-H^{+})$	530.10	4342684.9 (9.3)
588.33	$[Pd(bbmp)(\mathbf{Inosine})_2(\mathbf{Cytosine})_2]^{2+} \cdot 2H_2O$	588.66	577136.5 (1.2)
624.40	[Pd(bbmp)(**Cytidine**)]$^{+}$ $(-H^{+})$	624.12	4126194.3 (8.8)
649.33	[Pd(bbmp)(**Inosine**)]$^{+}$ $(-H^{+})$	649.12	46656088.1 (100)
797.93	[Pd(bbmp)(**3MeA**)(**Inosine**)]$^{+}$ $(-H^{+})$	798.17	4046485.1 (8.7)
840.13	$[Pd_2(bbmp)_2(\mathbf{Inosine})_3(\mathbf{Cytosine})]^{2+}$ $(-2H^{+})$	840.18	1775591.4 (3.8)
891.87	[Pd(bbmp)(**Cytidine**)(**Inosine**)]$^{+}$ $(-H^{+})$	892.20	4204221.2 (9.0)
914.53	$Na[Pd_2(bbmp)_2(\mathbf{Inosine})_3(\mathbf{3MeA})(Cl^{-})(OH^{-})]^{2+} \cdot 2H_2O$ 915.19		2514548.1 (5.4)

Appendix III –

Auxiliary benchmarking case studies

IIIa. Non-restricted ligand system – 1-vinylimidazole

The first benchmark structure of interest was a non-sterically hindered complex consisting of four 1-vinylimiadazole molecules (Figure IIIa.1). This structure was chosen given that the three ligands studied in the competition experiment described above are imidazole derivatives. As such, binding to the palladium centre via the heterocyclic nitrogens of an imidazole ring occurs, so this binding interaction was the first to be benchmarked. See Figure IIIa.1 for the numbering scheme and Table IIIa.1 for the benchmark data.

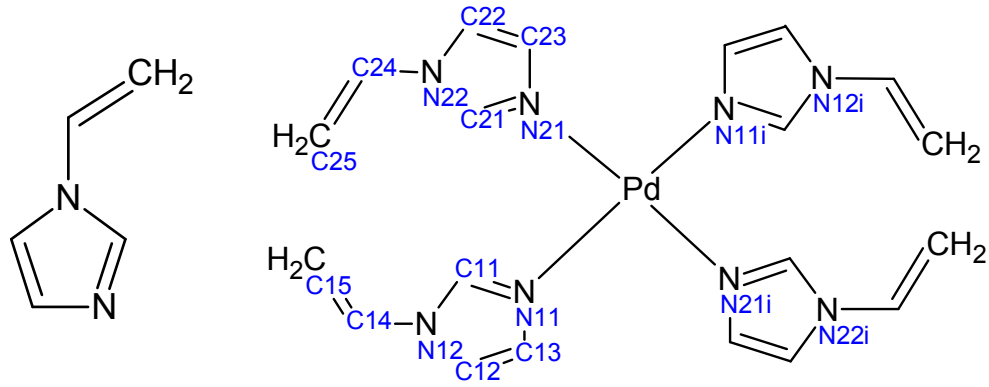

Figure IIIa.1 – Representation of 1-vinylimidazole, in both free ligand (left) and bound forms.

With respect to the bond length data in Table IIIa.1, there is a good correlation (R^2 = 0.9677) between the literature and theoretical results for this complex (Fig. IIIa.2). In the absence of a clear outlier, as well as a good correlation, bond lengths appear to be well described by the relatively simple PM3 calculation method as employed by Spartan '06. Importantly, the calculated lengths between the heterocyclic nitrogen and the palladium centre appear to be well defined, with an average error of less than 0.005Å.

Table IIIa.1 – Non-sterically restrictive benchmark data – crystal data vs optimised geometry. Data is summarised in Figs. IIIa.2 and IIIa.3.

Bond	Crystal Bond Lengths (Å)[1]	Calculated Bond Lengths (Å)
Pd N(11)	1.997	2.005
Pd N(21)	2.022	2.005
N(11) C(11)	1.308	1.385
N(11) C(13)	1.366	1.415
N(12) C(11)	1.322	1.385
N(12) C(12)	1.353	1.398
N(12) C(14)	1.490	1.437
C(12) C(13)	1.343	1.382
C(14) C(15)	1.251	1.333
Angle	**Crystal Bond Angles (°)[1]**	**Calculated Bond Angles (°)**
N(11) Pd N(11i)	180.0	178.67
N(11) Pd N(21i)	90.5	89.98
N(11) Pd N(21)	89.5	90.01
N(21i) Pd N(21)	180.0	178.70
C(11) N(11) C(13)	106.8	106.25
C(11) N(11) Pd	126.5	129.78
C(13) N(11) Pd	126.6	123.97
C(11) N(12) C(12)	108.0	108.86
C(11) N(12) C(14)	145.0	127.69
C(12) N(12) C(14)	107.0	123.45
N(11) C(11) N(12)	110.2	108.81
C(13) C(12) N(12)	106.7	106.59
C(12) C(13) N(11)	108.2	109.50
N(12) C(14) C(15)	113.2	124.48

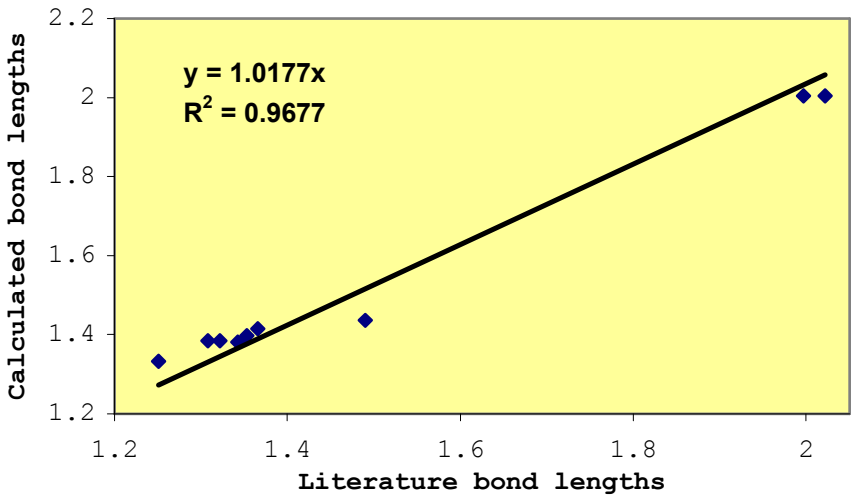

Figure IIIa.2 – Literature bond lengths (Å) versus theoretical bond lengths as derived from the optimised geometry using PM3 in Spartan '06.

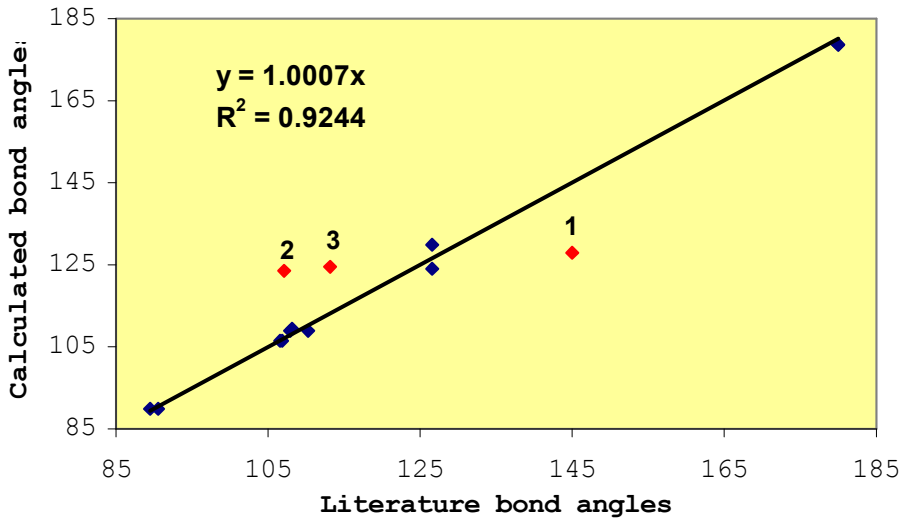

Figure IIIa.3 – Literature bond angles (˚) versus theoretical bond angles as derived from the optimised geometry using PM3 in Spartan '06.

The bond angles (Fig. IIIa.3) seem, on initial inspection of the R^2 value, to be not quite so well described, with three distinct outliers. However, these three points are somewhat irrelevant with respect to this particular benchmarking process. The three angles that appear to be outliers are the three angles that describe the orientation of the vinyl group, Fig IIIa.4. Given that the ligands used in the competition experiments do not contain functional groups with degrees of freedom, as the vinyl group does, these outliers may be discarded. When these outliers are removed, the correlation is significantly improved, as seen in Figure IIIa.5.

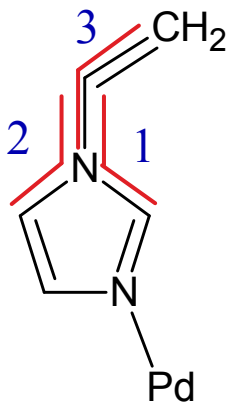

Figure IIIa.4 – Structure of 1-vinylimidazole with the numbered angles referred to as outliers in Fig. 5.14.

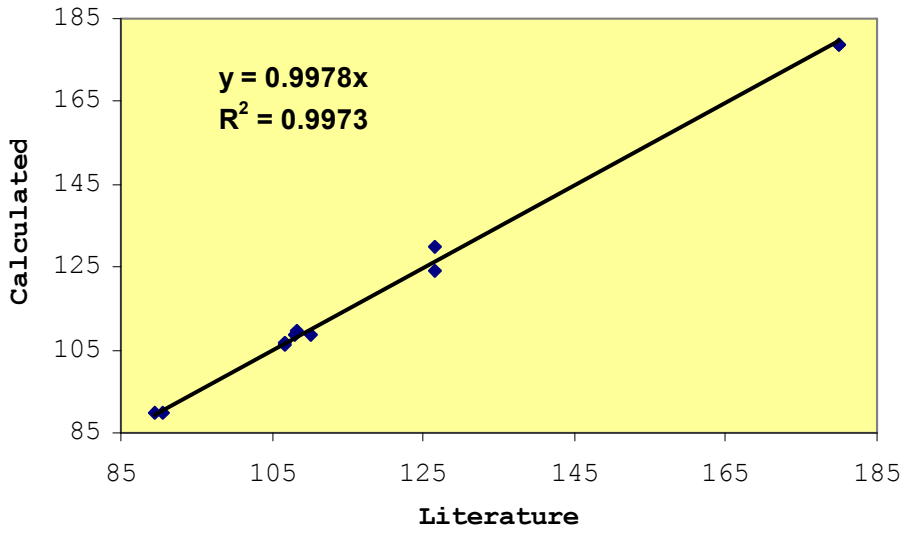

Figure IIIa.5 – Literature bond angles (˚) versus theoretical bond angles as derived from the optimised geometry using PM3 in Spartan '06, with outliers removed.

Again, as with the bond lengths, the immediate environment of the palladium centre is well defined, with a maximum error of 1.33°, and an average error of just 0.89°. These results suggest that the PM3 method used here accurately describes the heterocyclic nitrogen interaction with the palladium centre, as well as the imidazole moiety.

With such good results for a non-strained complex, benchmarking of a strained complex can be completed, to determine if the PM3 method can accommodate an inherently strained structure.

IIIb. Restricted ligand system – bis-*N*-methylimidazole-2-yl (mim) based system

The $[Pd(Cl)_2(mimNPh)]$ system (Fig. IIIb.1) was chosen given the similarities to the 1-vinylimidazole benchmark above, yet this system introduces some restriction, via a single carbon separating the two imidazole rings. This reduces the bite angle (N(11)-Pd-N(21)) of the mim ligand, compared to the analogous angle in the unstrained benchmark system. This decrease in bite angle increases the strain on the system.

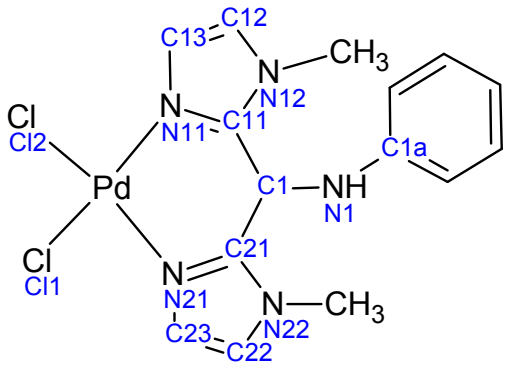

Figure IIIb.1 – General numbering scheme for $[Pd(Cl)_2(mim)NPh]$

Table IIIb.1 – Comparison of literature vs calculated bond lengths for the mim system.

Bond	Literature Bond Lengths (Å)[2]	Calculated Bond Lengths (Å)
Pd-Cl(1)	2.2916	2.309
Pd-Cl(2)	2.2964	2.311
Pd-N(11)	2.020	1.981
Pd-N(21)	2.031	1.975
N(11)-C(11)	1.331	1.393
N(21)-C(21)	1.324	1.391
N(11)-C(13)	1.385	1.406
N(21)-C(23)	1.372	1.406
C(11)-N(12)	1.359	1.397
C(21)-N(22)	1.353	1.400
N(12)-C(12)	1.376	1.390
N(22)-C(22)	1.361	1.391
C(12)-C(13)	1.341	1.386
C(22)-C(23)	1.363	1.385
C(11)-C(1)	1.481	1.479
C(21)-C(1)	1.461	1.476
C(1)-N(1)	1.284	1.292

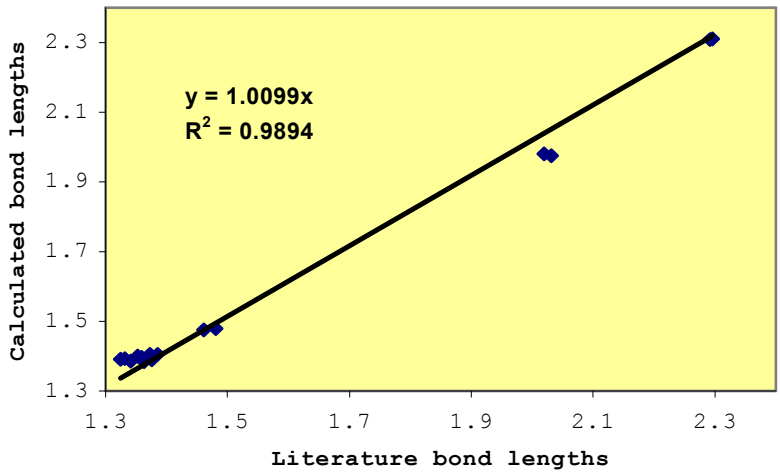

Figure IIIb.2 – Literature bond lengths(Å) versus theoretical bond lengths as derived from the optimised geometry using PM3 in Spartan '06 for the mim system.

Table IIIb.2 – Comparison of literature vs calculated bond angles for the mim system

Angle	Literature Bond Angles (°)[2]	Calculated Bond Angles (°)
N(11)-Pd-N(21)	88.5	91.44
Cl(1)-Pd-Cl(2)	90.57	91.18
N(11)-Pd-Cl(2)	91.03	88.70
N(21)-Pd-Cl(1)	89.95	88.68
N(11)-Pd-Cl(1)	177.50	179.70
N(21)-Pd-Cl(2)	176.93	178.76
Pd-N(11)-C(11)	124.0	124.61
Pd-N(21)-C(21)	125.6	124.98
Pd-N(11)-C(13)	129.5	129.14
Pd-N(21)-C(23)	126.9	128.08
C(11)-N(11)-C(13)	106.0	106.24
C(21)-N(21)-C(23)	107.4	106.54
N(11)-C(11)-C(1)	124.1	124.49
N(21)-C(21)-C(1)	123.2	124.20
N(11)-C(11)-N(12)	110.5	108.52
N(21)-C(21)-N(22)	109.9	108.20
C(1)-C(11)-N(12)	125.4	126.87
C(1)-C(21)-N(22)	126.9	127.58
C(11)-N(12)-C(12)	106.7	108.64
C(21)-N(22)-C(22)	107.4	108.66
N(12)-C(12)-C(13)	107.5	106.87
N(22)-C(22)-C(23)	107.4	106.90
C(12)-C(13)-N(11)	109.2	109.74
C(22)-C(25)-N(21)	107.9	109.62
C(11)-C(1)-C(22)	114.5	113.88
C(1)-N(1)-C(1a)	123.0	127.59
C(11)-C(1)-N(1)	126.7	128.29
C(22)-C(1)-N(1)	118.7	117.47

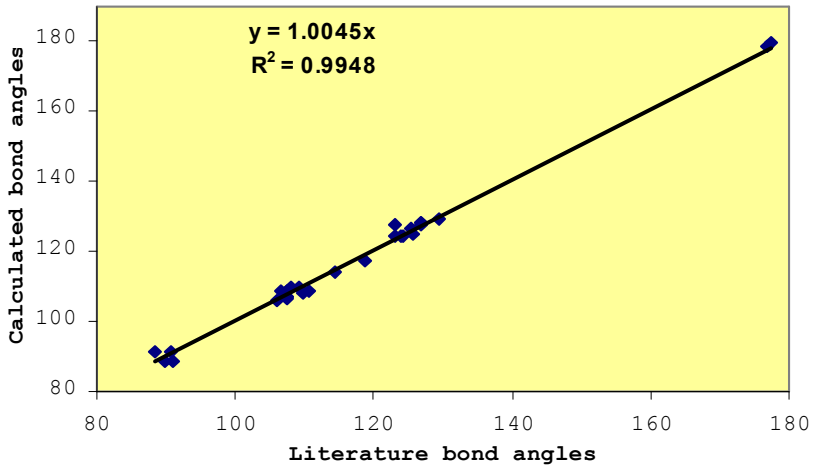

Figure IIIb.3 – Literature bond angles(˚) versus theoretical bond angles as derived from the optimised geometry using PM3 in Spartan ’06 for the mim system.

The bond lengths for this strained benchmark system was well described computationally, with a very strong R^2 value of 0.9894. The bond angle comparisons for the mim system confirms the computationally good behaviour, again with a very good correlation, $R^2 = 0.9948$.

These strong benchmarking results lead into the benchmarking process described in Chapter 4, a restricted bis-benzimidazole based system.

(1) Kurdziel, K.; Glowiak, T. *J. Coord. Chem.* **2002**, *55*, 327-334.
(2) Done, M. C.; Rüther, T.; Cavell, K. J.; Kilner, M.; Peacock, E. J.; Braussaud, N.; Skelton, B. W.; White, A. *J. Organomet. Chem.* **2000**, *607*, 78-92.